

**DISORDERED AND ORDERED DERIVATIVES OF CARBIDES
FOR ACID GAS ADSORPTION**

A Dissertation
Presented to
The Academic Faculty

by

Colton Michael Moran

In Partial Fulfillment
of the Requirements for the Degree
Doctor of Philosophy in the
School of Chemical and Biomolecular Engineering

Georgia Institute of Technology
May 2019

COPYRIGHT © 2019 BY COLTON MICHAEL MORAN

DISORDERED AND ORDERED DERIVATIVES OF CARBIDES
FOR ACID GAS ADSORPTION

Approved by:

Dr. Krista S. Walton, Advisor
School of Chemical and Biomolecular
Engineering
Georgia Institute of Technology

Dr. Pradeep K. Agrawal
School of Chemical and Biomolecular
Engineering
Georgia Institute of Technology

Dr. William J. Koros
School of Chemical and Biomolecular
Engineering
Georgia Institute of Technology

Dr. Christopher W. Jones
School of Chemical and Biomolecular
Engineering
Georgia Institute of Technology

Dr. Gleb Yushin
School of Materials and Science
Engineering
Georgia Institute of Technology

Date Approved: November 28, 2018

To My Family

ACKNOWLEDGEMENTS

First and foremost, I would like to acknowledge my advisor Dr. Krista Walton for bringing me into her group and giving me just the right amount of direction and freedom to pursue a multitude of new and exciting ideas. With unyielding support, there was never a challenge or question too big to surmount. The environment of encouragement, latitude of research exploration provided, and the mysteries of science made for an amazing 4 years at Georgia Tech.

I would also like to thank my committee members, Dr. Agrawal, Dr. Jones, Dr. Koros, and Dr. Yushin, for their valuable insights along my PhD career which greatly improved the quality of my work and broadened my perspective of the scientific world. Additionally, I would like to thank the Center for Understanding and Control of Acid Gas-Induced Evolution of Materials for Energy (UNCAGE-ME) Energy Frontier Research Center (EFRC) for funding this work and opening up a multitude of wonderful collaborations.

Thank you to past and present Walton group members, (Dr. Bogna Grabicka, Dr. Mike Mangarella, Dr. Cody Morelock, Dr. Ian Walton, Dr. Karen Tulig, Dr. Nick Burtch, Dr. Will Mounfield, Dr. Yang Jiao, Dr. Lalit Durante, Dr. Michael Dutzer, Julian Hungerford, Jacob Deneff, Jay Joshi, Eli Carter, and Yutao Gong) for making my time at GT enjoyable and a great learning experience. I'm especially thankful for the collaborative work with Jay Joshi and Dr. Robert Marti which produced great research and even better memories, forged through late hours and long discursions. Last, but far from least, I would like to thank my family and friends. Without their support this journey would not have been possible.

TABLE OF CONTENTS

ACKNOWLEDGEMENTS	iv
LIST OF TABLES	ix
LIST OF FIGURES	xi
NOMENCLATURE	xix
SUMMARY	xxiii
CHAPTER 1. Introduction	1
1.1 Acid Gases	1
1.2 Activated Carbon	3
1.3 Carbide-Derived Carbon	6
1.3.1 Tunability of Carbide-Derived Carbons	7
1.3.2 Residual Metal in Carbide-Derived Carbons	11
1.4 Metal-Organic Frameworks	12
1.4.1 Traditional synthesis of metal-organic frameworks	13
1.4.2 Metal-organic frameworks from insoluble precursors	14
1.5 Thesis Overview	19
1.6 References	23
CHAPTER 2. Experimental materials and methods	31
2.1 Materials	31
2.1.1 Carbides Used for Material Synthesis	31
2.2 Experimental Methods	31
2.2.1 Horizontal Bed Reactor for Carbide-Derived Carbon Synthesis	31
2.2.2 Nitrogen Physisorption at 77 K	32
2.2.3 Surface Area Measurements	33
2.2.4 Pore-size Distribution Analysis	34
2.2.5 Sulfur Dioxide, Carbon Dioxide, and Water	35
2.2.6 Powder X-ray Diffraction (PXRD)	36
2.2.7 X-ray Photoelectron Spectroscopy (XPS)	37
2.2.8 Microscopy	38
2.3 References	39
CHAPTER 3. Synthesis and characterization of aluminum carbide-derived carbon with residual aluminum-based nanoparticles	41
3.1 Introduction	41
3.2 Materials and Methods	45
3.2.1 Materials	45
3.2.2 Methods	46
3.3 Results and Discussion	49
3.3.1 Etching temperature and time effects on residual metal in Al ₄ C ₃ -CDC	49

3.3.2	3.2. Form of metal content in Al ₄ C ₃ -CDC	55
3.3.3	²⁷ Al MAS NMR of the residual aluminum content	59
3.3.4	XPS surface analysis of samples etched at 300 and 500°C for 1h	64
3.3.5	Crystalline structure formation observed via PXRD and TEM	66
3.3.6	Dependence of Al ₄ C ₃ -CDC Porosity and Surface Area on Reaction Temperature and Time	70
3.3.7	CO ₂ and Water adsorption on Al ₄ C ₃ -CDCs	74
3.4	Conclusions	78
3.5	References	80

CHAPTER 4. Tunable nanoparticles in aluminum carbide-derived carbon for enhanced acid gas adsorption		87
4.1	Introduction	87
4.2	Materials and Methods	90
4.2.1	Materials	90
4.2.2	Methods	91
4.3	Results and Discussion	94
4.3.1	Evolution of aluminum-based nanoparticles via water vapor	94
4.3.2	Alkaline treatment of Al ₄ C ₃ -CDC materials	102
4.3.3	Sample composition from ²⁷ Al solid-state NMR	106
4.3.4	XPS analysis of surface chemistry on modified Al ₄ C ₃ -CDCs	109
4.3.5	Characterization of dry SO ₂ interaction with pre- and post-modified Al ₄ C ₃ -CDCs	111
4.4	Conclusions	118
4.5	References	120

CHAPTER 5. Partial etching of molybdenum carbide for the formation of molybdenum based nanoparticles		126
5.1	Introduction	126
5.2	Materials and Methods	127
5.2.1	Materials	127
5.2.2	Methods	128
5.3	Results and Discussion	130
5.4	Conclusions	142
5.5	References	142

CHAPTER 6. Evolution of textural and chemical properties of annealed carbide-derived carbons for acid gas adsorption		146
6.1	Introduction	146
6.2	Materials and Methods	148
6.2.1	Materials	148
6.2.2	Methods	149
6.3	Results and Discussion	152
6.3.1	Effect of annealing gas and temperature textural properties of carbide-derived carbons	152
6.3.2	Chemical alterations resulting from the annealing process	155
6.3.3	Adsorption behaviour of annealed CDCs for CO ₂ adsorption	158

6.3.4	Textural and chemical influence on water adsorption	161
6.3.5	Sulfur dioxide adsorption dependence on chemical heterogeneity and pore size	165
6.4	Conclusions	169
6.5	References	170
CHAPTER 7. Structured growth of metal-organic framework MIL-53(al) from solid aluminum carbide precursor		174
7.1	Introduction	174
7.2	Materials and Methods	176
7.2.1	Methods	176
7.3	Results and Discussion	180
7.3.1	Degradation and evolution of crystalline structures	180
7.3.2	Temporal morphology evolution	184
7.3.3	Elucidation of intermediate species	187
7.3.4	Extension of carbide synthesis to new topologies, analogues, and adsorption	192
7.3.5	Synthesis solvent effects on MIL-53(Al) from Al_4C_3	195
7.4	Conclusions	203
7.5	References	204
CHAPTER 8. Conclusions and recommendations		210
8.1	Conclusions	210
8.1.1	Metal-based nanoparticles in Al_4C_3 -CDCs and Mo_2C -CDC	210
8.1.2	Tuning textural and chemical properties of fully etched CDCs through annealing	210
8.1.3	Structured growth of metal-organic framework MIL-53(Al) from a sacrificial aluminum carbide precursor (Chapter 7)	213
8.2	Recommendations	214
8.2.1	Heat treatments on fully and partially etched carbide-derived carbons (Chapter 3 and 4 extension)	214
8.2.2	Modification and implementation of partially etched Mo_2C -CDC for catalysis	215
8.2.3	Increased understanding of the reactivity of various CDCs for oxygen and nitrogen functional groups	216
8.2.4	Expanding on MOF growth from carbide precursors	217
8.3	References	219
APPENDIX A. Supplemental Information		220
A.1	Chapter 3: Synthesis and Characterization of Aluminum Carbide-Derived Carbon with Residual Aluminum-Based Nanoparticles	220
A.1.1	Supplemental and Raw Data for Chapter 3	220
A.2	Chapter 4: Tunable Nanoparticles in Aluminum Carbide-Derived Carbon for Enhanced Acid Gas Adsorption	233
A.2.1	Supplemental and Raw Data for Chapter 4	234
A.3	Chapter 5: Evolution of Textural and Chemical Properties of Annealed Carbide-Derived Carbons for Acid Gas Adsorption	251

A.3.1	Supplemental and Raw Data for Chapter 5	251
A.4	Chapter 6: Evolution of Textural and Chemical Properties of Annealed Carbide-Derived Carbons for Acid Gas Adsorption	252
A.4.1	Supplemental and Raw Data for Chapter 6	252
A.5	Chapter 7: Structured Growth of Metal-Organic Framework MIL-53(Al) from Solid Aluminum Carbide Precursor	259
A.5.1	Supplemental and Raw Data for Chapter 7	259

LIST OF TABLES

Table 1-1	Sub-classification of Salt-like Carbide	6
Table 1-2	List of benefits seen from using solid precursors for MOF growth corresponding to the graphical representation seen in Figure 1-5	16
Table 3-1	EDS Results from points taken from Figure 3-3 images	57
Table 3-2	EDS on clustered material seen on Al ₄ C ₃ -CDC-500-1h	58
Table 3-3	²⁷ Al NMR parameters of Al ₄ C ₃ -CDCs spectra. All values correspond to lineshapes modeled in Dmfit[38]. Dmfit can accommodate different lineshape models: Gaussian is the conventional lineshape, Czjzek is a distribution of quadrupolar environments, Q MAS ½ refers to a model of the central transition only with “infinite spinning speed” assumed, Quad 1st is a model of a 1st-order quadrupolar MAS spinning sideband pattern.	60
Table 3-4	Temperature trial runs corresponding BET surface area (S _{bet}) and pore volume (V _p) calculated using QSDFT	70
Table 4-1	Changes in carbon properties observed after 5 days of water vapor exposure.	98
Table 4-2	EDS of “bubbling” feature found on Al ₄ C ₃ -CDC-300-1h after H ₂ O isotherms	100
Table 4-3	BET surface area before and after dry SO ₂ exposure for modified and unmodified materials	114
Table 6-1	Percent increase in surface area (SA) and pore volume (PV) for three CDCs with three separate annealing environments	153
Table 6-2	Changes in CO ₂ capacity at 1 bar and 25°C compared to changes in surface nitrogen and micropore volume for non-annealed samples and those annealed in NH ₃ at 500°C.	161
Table A-1	EDS of residual white powder on quartz boat for Al ₄ C ₃ -CDC-300-1h samples	220
Table A-2	EDS on Aluminum based spheres observed at 500°C by SEM	221
Table A-3	EDS of Al ₄ C ₃ -700-1h	228
Table A-4	TGA results for residual metal before and after 5 days high humidity exposure.	234

Table A-5	EDS results on “bubbling” features after 5-day exposures	234
Table A-6	N ₂ physisorption results after 5 days of water exposure for Al ₄ C ₃ -CDC-500-1h samples at 0.7 and 0.6 P/P0	235
Table A-7	High resolution C1s and O1s results before and after NaOH exposure for Al ₄ C ₃ -500-1h	242
Table A-8	Wave numbers and assignments for ATR spectra	244
Table A-9	BET surface area and pore volume (P/P0 = 0.8) of Al ₄ C ₃ -BDC-XX materials.	259
Table A-10	EDS results from points taken from Al ₄ C ₃ -BDC-72h and theoretical percentages for MIL-53(Al). ²	261
Table A-11	Elemental composition results from XPS survey scan on Al ₄ C ₃ -BDC-72h	263
Table A-12	N ₂ Physisorption data on temperature trials.	265
Table A-13	Rietveld results for post heated Al ₄ C ₃ -BDC-72h	268
Table A-14	N ₂ physisorption data before and after water exposure.	270

LIST OF FIGURES

Figure 1-1	Overview of commercial desulfurization techniques	52
Figure 1-2	Surface functionalities on a carbon basil plan a focus on: (A) Oxygen Functionalities, (B) Nitrogen Functionalities: (a) pyrrole, (b) primary amine, (c) secondary amine, (d) pyridine, (e) imine, (f) tertiary amine, (g) nitro, (h) nitroso, (i) amide, (j) pyridone, (k) pyridine-N-oxide, (l) quaternary nitrogen	
Figure 1-3	Atomic demonstration and resulting PSD for carbides etched via halogenation for (a) Ti_3SiC_2 at 1200°C and (b) 3C-SiC at 1200°C	8
Figure 1-4	Simulated structure of TiC-CDC at (a) 600°C (b) 800°C and (c) 1200°C . NLDFT PSD derived from nitrogen physisorption for (d) $\text{Ti}_3\text{SiC}_2\text{-CDC}$ and (e) SiCN PDC-CDC .	9
Figure 1-5	Adapted conceptual illustration (a) Solid-MOF precursor, (b) organic linker, (c) pseudomorphic replicated MOF, (d) controlled cation release, (e) core-shell control, (f) shape control via precursor selection, (g) patterned material on substrate, (h) patterned growth, (i) pre-allocated materials on substrate, (j) MOF film growth, (k) precursor composite, and (l) MOF composite.	15
Figure 1-6	Simulated structure of TiC-CDC at (a) 600°C (b) 800°C and (c) 1200°C . NLDFT PSD derived from nitrogen physisorption for (d) $\text{Ti}_3\text{SiC}_2\text{-CDC}$ and (e) SiCN PDC-CDC .	15
Figure 2-1	Simplified carbide-derived carbon synthesis reactor scheme	32
Figure 2-2	Experimental set-up for collecting powdered x-ray diffraction data	37
Figure 3-1	TGA data from residual metal content in $\text{Al}_4\text{C}_3\text{-CDC}$ after 1 hour of etching with Cl_2 in a temperature range of $300\text{-}900^\circ\text{C}$	52
Figure 3-2	TGA results for time trials of (a) 300°C and (b) 500°C samples in terms residual metal.	54
Figure 3-3	TEM Images of $\text{Al}_4\text{C}_3\text{-CDC}$: (a) $300\text{-}1\text{h}$, (b) $500\text{-}1\text{h}$ (c) $700\text{-}1\text{h}$ and (d) $900\text{-}1\text{h}$	56
Figure 3-4	SEM Images of (a) 500°C , and (b) 700°C	58
Figure 3-5	^{27}Al MAS NMR data of $\text{Al}_4\text{C}_3\text{-CDCs}$	61
Figure 3-6	^{27}Al MAS NMR data of $\text{Al}_4\text{C}_3\text{-CDC-}300\text{-}1\text{h}$ using a double resonance HMQC sequence.	63

Figure 3-7	²⁷ Al MAS NMR on Al ₄ C ₃ -CDC-700 spinning at 8 kHz (shown in black) including a fit (shown in red) utilizing previous parameters determined for α -Al ₂ O ₃ , CQ = 2.38 MHz and η Q = 0.0. On a smaller scale (b) we can see the hydrogen-bearing aluminum peak, at -2.7 ppm, has almost been completely removed and the emergence of a new peak centered at 14.2 ppm, which corresponds to α -Al ₂ O ₃ . * refers to spinning sidebands.	64
Figure 3-8	High resolution XPS spectra on Al ₄ C ₃ -CDC-300-1h for (a) Aluminum (b) Chlorine and (c) Oxygen	66
Figure 3-9	PXRD patterns of Al ₄ C ₃ and samples etched at 300,500,700 and 900 °C for 1 hr.	68
Figure 3-10	TEM images of Al ₄ C ₃ -CDC prepared by etching: (a) 300-1h scale bar 10 nm, (b) 500-1h, (c) 700-1h, and (d) 900-1h	69
Figure 3-11	BET surface areas via N ₂ adsorption for samples etched at times for (a) 300 °C and (b) 500 °C	71
Figure 3-12	Pore size distributions for (a) Different etching temperatures (b) Different etching times at 300 °C and (c) Different etching times at 500 °C for Al ₄ C ₃ -CDCs	73
Figure 3-13	Water adsorption isotherms at 25°C for (a) temperature trials and (b) time trials at 300 °C.	75
Figure 3-14	CO ₂ adsorption isotherms at 25 °C for Al ₄ C ₃ -CDC samples etched at (a) different temperatures 300 – 900 °C, for 1 hour and (b) at 500°C for various times (0.25 – 6 hours).	78
Figure 4-1	CO ₂ adsorption at 0°C before and after water vapor exposure for (a) water isotherms and (b) 5 days of high humidity exposure. Exposures were performed at 25°C up to 0.85 P/P ₀ .	97
Figure 4-2	SEM images of (a & b) Al ₄ C ₃ -CDC-300-1h-H ₂ O-isotherm (c) Al ₄ C ₃ -CDC-500-1h-H ₂ O-isotherm.	99
Figure 4-3	SEM images after 5-day H ₂ O exposure for (a) Al ₄ C ₃ -CDC-300-1h and (b & c) Al ₄ C ₃ -CDC-500-1h	101
Figure 4-4	(a) CO ₂ capacity at 25°C and 1 bar for post-synthetically modified Al ₄ C ₃ -CDC materials and TEM images of (b) Al ₄ C ₃ -CDC-300-1h-24h-NaOH and (c) Al ₄ C ₃ -CDC-500-1h-24h-NaOH	104
Figure 4-5	Temporal effects of NaOH treatment on CO ₂ capacity at 1 bar for (a) Al ₄ C ₃ -CDC-300-1h and (b) Al ₄ C ₃ -CDC-500-1h.	106
Figure 4-6	²⁷ Al MAS NMR spectra of (a) Al ₄ C ₃ -CDC-300-1h-24h-H ₂ O (b) Al ₄ C ₃ -CDC-300-1h-24h-NaOH (c) Al ₄ C ₃ -CDC-500-1h-24h-H ₂ O (d) Al ₄ C ₃ -CDC-500-1h-24h-NaOH	107

Figure 4-7	Elemental composition of pre- and post-modified Al ₄ C ₃ -CDC surfaces.	111
Figure 4-8	Isothermal volumetric adsorption of SO ₂ at 25°C (a) Al ₄ C ₃ -CDC-300-1h-24h-NaOH (b) Al ₄ C ₃ -CDC-500-1h-24h-NaOH & CO ₂ at 25°C pre and post SO ₂ (c) Al ₄ C ₃ -CDC-300-1h-24h-NaOH (d) Al ₄ C ₃ -CDC-500-1h-24h-NaOH	113
Figure 4-9	Pore size distribution before and after dry SO ₂ exposure for (a) Al ₄ C ₃ -300-1h and (b) Al ₄ C ₃ -500-1h (c) Modified Al ₄ C ₃ -300-1h and (d) Modified Al ₄ C ₃ -300-1h.	115
Figure 4-10	High resolution O 1S XPS spectra on (a) Al ₄ C ₃ -CDC-500-1h pre-SO ₂ (b) Al ₄ C ₃ -CDC-500-1h post-SO ₂ and (c) High resolution S 2p on Al ₄ C ₃ -CDC-500-1h post-SO ₂	118
Figure 5-1	Powdered x-ray diffraction of Mo ₂ C-CDC for (a) 1h of etching at varied temperatures and (b) samples etched at 600°C for 1 and 2 h.	131
Figure 5-2	High resolution TEM Images of (a & b) Mo ₂ C-500-1h and (c & d) Mo ₂ C-600-1h, and (e) lattice spacing of crystalline domains	133
Figure 5-3	(a) Leftover mass after etching process for Mo ₂ C-CDCs and (b) residual metal content obtained through TGA analysis for Mo ₂ C-CDCs etched for 1 h	135
Figure 5-4	Nitrogen physisorption results (a) N ₂ Isotherms, (b) BET surface area for samples etched for 1 and 2 h between 400-700°C, and (c) PSD for samples etched for 1 h.	137
Figure 5-5	XPS trends for surface functionalities between 300-700°C.	138
Figure 5-6	High resolution XPS spectra for Mo 3d: (a) Mo ₂ C-300°C-1h, (b) Mo ₂ C-400°C-1h, (c) Mo ₂ C-500°C-1h, (d) Mo ₂ C-600°C-1h, (e) Mo ₂ C-700°C-1h, and (f) Cl 2p composite spectrum of etching temperatures 300-700°C.	140
Figure 5-7	CO ₂ isotherms for Mo ₂ C-CDCs (a) 0°C and (b) 25°C	141
Figure 6-1	Change in BET surface area (SA) and pore volume (PV) for different annealing environments for: (a-b) TiC-CDC, (b-c) Al ₄ C ₃ -CDC, and (e-f) Mo ₂ C.	154
Figure 6-2	XPS analysis of surface chemistry for (a) TiC-CDC, (b) Al ₄ C ₃ -CDC and (c) Mo ₂ C-CDC and comparison of XPS (Surface concentration) and EDS (Bulk concentration) of (d) Al ₄ C ₃ -CDC, (e) TiC-CDC, and (f) Mo ₂ C-CDC	157
Figure 6-3	CO ₂ adsorption isotherms at 25°C up to 1 bar for (a) TiC-CDC, (b) Al ₄ C ₃ -CDC and (c) Mo ₂ C-CDC under different post-etching environments. Adsorption at 400 ppm CO ₂ vs (d) surface nitrogen and (e) bulk nitrogen concentration.	160

Figure 6-4	Water adsorption at 25°C for (a & b) TiC-CDC, (b & d) Al ₄ C ₃ -CDC, and (c & f) Mo ₂ C-CDC annealed under different environments	164
Figure 6-5	SO ₂ isotherms at 25°C for (a) TiC-CDCs, (b) Al ₄ C ₃ -CDCs, and (c) Mo ₂ C-CDC for four separate post-etching conditions. SO ₂ capacity vs (d-e) bulk nitrogen content, (f-g) bulk oxygen content, (h) micropore volume (≤ 2 nm), and (i) mesopore volume (>2 nm) at different pressures (P) of SO ₂	168
Figure 7-1	(a) PXRD and (b) N ₂ physisorption isotherms measurements of Al ₄ C ₃ -BDC-XXh reacted for a range of times from 0.5 to 72h. Notably early crystalline structures represent Al ₄ C ₃ reflections; later times show MIL-53 reflections.	183
Figure 7-2	SEM images of Al ₄ C ₃ -BDC-XX: (a) 2h, (b) 3h, (c) 4h, (d) 24h, and (e & f) 72h.	186
Figure 7-3	²⁷ Al MAS NMR of Al ₄ C ₃ -BDC-XXh for reaction times of (a) 0.5h, (b) 3h, (c) 4h, (d) 72h. (e) Color coded polyhedral representation from 4-coordinate Al ₄ C ₃ to 6-coordinate MIL-53(Al) serves as a legend to the spectra.	188
Figure 7-4	FIB cross section of Al ₄ C ₃ -BDC-4h focusing on (a) EDS mapping and (b) showing four distinct regions during growth: (1) Intermediate Core (Al ₂ O ₃ , Al(OH) ₃ & Al ₄ C ₃), (2) nucleation layer, (3) transitional “peeling” layer, (4) bulk MIL-53(Al)	191
Figure 7-5	Water vapor isotherm for Al ₄ C ₃ -BDC-72h taken at 25°C	193
Figure 7-6	<i>In situ</i> PXRD of Al ₄ C ₃ -BDC-72h during heating under flowing N ₂ . Three simulated crystal structure of MIL-53(Al) are included; as-synthesized (AS), high-temperature (HT), and low-temperature (LT). Room temperature (RT) scans were acquired pre and post heating.	195
Figure 7-7	PXRD patterns of MIL-53(Al) synthesized from Al ₄ C ₃ using different solvent ratios of dimethylformamide (DMF) and water (H ₂ O)	197
Figure 7-8	²⁷ Al MAS NMR of Al ₄ C ₃ -BDC-24h with various solvent ratios of DMF and H ₂ O.	199
Figure 7-9	Morphological changes as a result of different DMF/H ₂ O solvent ratios	202
Figure 8-1	Effects of post-synthetic heat treatment on Al ₄ C ₃ -CDCs regarding (a) temporal effects on N ₂ isotherms at 700°C, (b) temperature effects on N ₂ isotherms, (c) temporal effect on PSD, and (d) SEM images of oxide nanoparticles	215
Figure A-1	Aluminum based spheres observed at 500°C by SEM	221

Figure A-2	Smooth surfaces and stair like structures seen in Al_4C_3 -CDC-500-1h	222
Figure A-3	Isolated carbonaceous microspheres in Al_4C_3 -CDC-700-1h	222
Figure A-4	TEM Images of Al_4C_3 -CDC-300-1h	223
Figure A-5	TEM images of crystal lattices in Al_4C_3 -CDC-700-1h	224
Figure A-6	TEM images of crystal lattices and graphite in Al_4C_3 -CDC-900-1h	225
Figure A-7	HTEM image of an aluminum-based nanoparticle in Al_4C_3 -CDC-900-1h	226
Figure A-8	SEM Image Al_4C_3 -CDC-500-1h	227
Figure A-9	SEM Images of Al_4C_3 -CDC-700-1h	228
Figure A-10	Al 2P and O1s XPS scans on Al_4C_3 -CDC-500-1h	229
Figure A-11	N_2 isotherms for samples etched at 300, 500, 700 and 900 °C	230
Figure A-12	(left) High Angle Annular Dark Field (HAADF) of Al_4C_3 -CDC-500-1h. (right) Line profiles of elemental composition measured by EDS for Al, C, Cl species.	230
Figure A-13	(a) HAADF of Al_4C_3 -CDC-500-1h. (b) EDS on point 1 (c) EDS on point 2	231
Figure A-14	HAADF of Al_4C_3 -CDC-500-1h metal species with diffraction pattern	232
Figure A-15	Raman spectra on Al_4C_3 -CDC materials synthesized at different temperatures	233
Figure A-16	(a) CO_2 on Al_4C_3 before and after water isotherm	234
Figure A-17	Before and after CO_2 adsorption results after 5 days of water exposure for Al_4C_3 -CDC-500-1h samples at 0.7 and 0.6 P/P0.	235
Figure A-18	PAC formation after DI standard treatment on Al_4C_3 -300-1h	236
Figure A-19	XRD Patterns of Al_4C_3 -CDC-300-1h after water exposure	237
Figure A-20	PXRD on post-synthetically modified Al_4C_3 -300-1h materials	237
Figure A-21	BET surface area of materials after NaOH treatment	238
Figure A-22	Dynamic light scattering of supernatant after treatment showing polymer species in solution	239

Figure A-23	NaOH and water treatment without rinsing and direct activation after digestion period.	240
Figure A-24	Comparison of Al ₄ C ₃ -500-1h high resolution carbon Cs1 spectra (a) Pre-NaOH and (b) Post-NaOH	241
Figure A-25	ATR-IR spectra of pre and post NaOH modified samples for (a) Al ₄ C ₃ -300-1h and (b) Al ₄ C ₃ -500-1h	244
Figure A-26	1000 ppm SO ₂ breakthrough curves for (a) Al ₄ C ₃ -300-1h-24h-NaOH, and (b) Al ₄ C ₃ -500-1h-24h-NaOH	248
Figure A-27	TGA-MS results under helium flow for the decomposition of functional groups on (a) Al ₄ C ₃ -300-1h and (b) Al ₄ C ₃ -500-1h	249
Figure A-28	Al ₄ C ₃ -500-1h-48h-NaOH CO ₂ isotherms	250
Figure A-29	(a & c) HAADF of Mo ₂ C-CDC-500-1h. (b) EDS on point 1 (d) EDS on point 2	251
Figure A-30	Pore-size distribution of (a) TiC-CDCs, (b) Al ₄ C ₃ -CDCs and (b) Mo ₂ C –CDCs from 0 to 2 nm	252
Figure A-31	Powdered X-ray diffraction of (a) Al ₄ C ₃ -CDCs, (b) TiC-CDCs, and (b) Mo ₂ C -CDCs	253
Figure A-32	Raw Raman spectra for (a) TiC-CDC , (b) Al ₄ C ₃ -CDC, and (b) Mo ₂ C-CDC, (d) Integrated area ratios of the D and G band for fitted spectra.	254
Figure A-33	High resolution N 1s XPS for (a) TiC-CDC-NA, (b) TiC-CDC-H ₂ , (c) TiC-CDC-NH ₃ (500°C), (d) TiC-CDC-NH ₃ (700°C), (e) Al ₄ C ₃ -CDC-NA, (f) Al ₄ C ₃ -CDC-H ₂ , (g) Al ₄ C ₃ -CDC-NH ₃ (500°C), (h) Al ₄ C ₃ -CDC-NH ₃ (700°C) and (i) Mo ₂ C-CDC-XX.	256
Figure A-34	Comparison of surface concentrations obtained via XPS and interior elemental compositions obtained through EDS for (a) Al ₄ C ₃ -CDCs, (b) TiC-CDCs, and (b) Mo ₂ C -CDC	256
Figure A-35	CO ₂ capacity at 25°C vs (a) micropore volume, (b) mesopore volume, and (c) bulk oxygen	257
Figure A-36	Attenuated total reflectance data on all (a) Al ₄ C ₃ -CDC, (b) TiC-CDC, and (b) Mo ₂ C -CDC	258
Figure A-37	Simulated MIL-53(Al) patterns	259
Figure A-38	(a) CO ₂ adsorption isotherms at 25°C up to 1 bar and (b) CO ₂ adsorption isotherms at 0°C.	260

Figure A-39	MIL-53(Al) from $\text{Al}(\text{H}_2\text{O})_6\text{Cl}_3$ (a) N_2 physisorption isotherm, (b) CO_2 adsorption at 0°C and (c) CO_2 adsorption at 25°C on $\text{Al}_4\text{C}_3\text{-BDC-72h}$ from 0-20 bar.	261
Figure A-40	Images of $\text{Al}_4\text{C}_3\text{-BDC-72h}$ (left) and unreacted Al_4C_3 (right).	262
Figure A-41	High resolution XPS scans of (a) Al 2p (b) C 1s and (c) O 1s	263
Figure A-42	$\text{Al}_4\text{C}_3\text{-BDC-4h}$ FIB-SEM images.	264
Figure A-43	(a-c) SEM images and (d) PXRD of $\text{Al}_4\text{C}_3\text{-NH}_2\text{-BDC-72h}$	265
Figure A-44	SEM (a) and PXRD (b) on $\text{Al}_4\text{C}_3\text{-BTC-220-72h}$.	266
Figure A-45	SEM on (a) $\text{Al}_4\text{C}_3\text{-BDC-210-24h}$ (b) $\text{Al}_4\text{C}_3\text{-BDC-190-24h}$.	267
Figure A-46	Al_4C_3 in DMF from 1-72h.	267
Figure A-47	PXRD on time trials for $\text{Al}_4\text{C}_3\text{-BA-XXh}$.	268
Figure A-48	TGA of $\text{Al}_4\text{C}_3\text{-BDC-72h}$.	269
Figure A-49	TEM Images of $\text{Al}_4\text{C}_3\text{-BDC-72h}$	270
Figure A-50	Protonation and hydrolysis of DMF adapted from Cottineau et. al	271
Figure A-51	Nitrogen sorption isotherms at 77 K for $\text{Al}_4\text{C}_3\text{-MIL-53(Al)}$ samples synthesized with different DMF/ H_2O solvent ratios and (b) CO_2 adsorption at 25°C up to 20 bar for $\text{Al}_4\text{C}_3\text{-BDC-24h}$ samples with pure DMF and a 95/5 DMF to water ratio	272
Figure A-52	TGA on Al_4C_3 derived MIL-53(Al) in pure water	273

NOMENCLATURE

Abbreviations

%RH	Percent Relative Humidity
μm	micrometer
\AA	Angstrom
Al(OH)_3	Aluminum Hydroxide
Al_2O_3	Aluminum Oxide
Al_4C_3	Aluminum Carbide
AlCl_3	Aluminum Chloride
BDC	1,4-Benzenedicarboxylic Acid
BDC-COOH	1,2,4-Benzenetricarboxylic Acid
BDC-NH ₂	1,4-Benzenedicarboxylic Acid, 2-Amino
BDC-NO ₂	1,4-Benzenedicarboxylic Acid, 2-Nitro
BET	Brunauer, Emmett, and Teller
BTC	1,3,5-Benzenetricarboxylic Acid
CDC	Carbide-Derived Carbon
cm^3	Cubic Meter
CO	Carbon Monoxide
CO ₂	Carbon Dioxide
DMF	N,N'-Dimethylformamide
EDS	Energy Dispersive Spectroscopy
g	Gram
h	hours
H ₂ O	Water
H ₂ S	Hydrogen Sulfide

H ₂ SO ₄	Sulfuric Acid
I _D	Intensity of the D-Band
K	Kelvin
keV	Kiloelectron Volt
kJ	Kilojoule
m ² g ⁻¹	Square Meter per Gram
MFC	Mass Flow Controller
mg	Milligrams
MIL	Material of Institute Lavoisier
min	Minutes(s)
mL	Milliliter per min
mmol	Millimole
Mo ₂ C	Molybdenum Carbide
MOF	Metal-Organic Framework
mol	Mole
NaOH	Sodium Hydroxide
nm	Nanometer
NMR	Nuclear Magnetic Resonance
MAS	Magic Angle Spinning
P/P ₀	Relative Pressure
PSD	Pore size distribution
PSM	Post-Synthetic Modification
PXRD	Powder X-Ray Diffraction
QSDFt	Quenched Solid Density Functional Theory
s	Second(s)
SEM	Scanning Electron Microscopy
SO ₂	Sulfur Dioxide

SO ₃	Sulfur Trioxide
TEM	Transmission Electron Microscopy
TGA	Thermogravimetric Analysis
TiC	Titanium Carbide
wt%	Weight percent
XPS	X-ray Photoelectron Spectroscopy

Symbols

a_i	Theoretical Constant for Brunauer, Emmett, and Teller Theory
b_i	Theoretical Constant for Brunauer, Emmett, and Teller Theory
c	Physical Constant for Brunauer, Emmett, and Teller Theory
d	Spacing Between Crystal Planes
m_{sample}	Mass of Sample
N_{av}	Avodadro's Number
P	Pressure
R	Ideal Gas Constant
S_{BET}	Brunauer, Emmett, and Teller Theory Surface Area
T	Temperature
v	Total Volume Adsorbed
V	Volume
θ	Angle of Incidence
λ	Wavelength

SUMMARY

The implementation and utilization of adsorptive materials spans back thousands of years to the Egyptian dynasties, where activated carbons were first discovered. These primitive adsorbents were used to treat ailments, adsorb odors, and displayed a propensity for water purification, while their fundamental properties remained shrouded in mystery. In the last 100 years the adsorption phenomena and porous materials have seen significant attention in the scientific community. Activated carbon materials derived from organic precursors are now implemented industrially on large scales, while their textural and chemical properties have been well documented displaying a significant degree of tunability. However, activated carbon exhibits limitations based on their precursors and synthesis methods, and researchers began to focus on other porous materials such as zeolites, carbide-derived carbons (CDCs), and metal-organic frameworks (MOFs). Carbide-derived carbons are synthesized through halogenation, typically with chlorine, and selective etching of metal heteroatoms from a periodic carbide precursor at temperatures exceeding 300°C. The reaction of the metal center with chlorine produces a metal chloride that begins to diffuse out of the structure leaving behind a porous carbon matrix. Metal-organic frameworks are quite different than carbon-based adsorbents, with their textural and chemical properties relying on various combinations of organic linkers and metal centers. The self-assembly of the linkers and metal nodes result in a porous-periodic structure that exhibits a high degree of physical and chemical flexibility. The work within this dissertation focuses on textural and chemical tunability of CDCs for acid gas adsorption, and the extension of carbide precursors for structured MOF growth.

As populations swell, an increase in energy demands are being realized around the world, which calls for increased power production leading to an increase in overall gaseous emissions. Recent studies on the negative impact such emissions have on human health and the environment creates an urgent need to produce effective and economically viable solutions to remove and handle the increasing volume. Acid gases, a particularly nasty constituent in many power production emissions, can react with water in the atmosphere creating acid solutions leading to a series of harmful consequences such as infrastructure degradation, pollution of drinking water and irrigation, and deadly pH changes in ecosystems. Currently, adsorption with activated carbon is implemented for filtering acid gases while avoiding heavy regeneration costs seen in other removal solutions. However, as regulations begin to enforce increased emissions control, the demand for optimized adsorbents to improve capacity, durability and operations cost increases.

A major focus of this work entails controlling active sites in CDCs, pertaining to both residual metal nanoparticles and oxygen and nitrogen functionalities. Metal hydroxides, basic oxygen functionalities, and nitrogen species display increased interaction with acid gases leading to improved capacities. The improvements seen with these active sites are also highlighted in activated carbon literature but entail a series of drawbacks. The impregnation of activated carbon to integrate metal nanoparticles is notoriously plagued with poor metal dispersion and micropore blockage. The generation of nanoparticles from the ordered carbide allows for a one-step synthesis that produces well-dispersed metal sites without risking pore blockage from an impregnant. The chlorination and annealing process used to generate CDCs also provide a unique degree of control over functional groups,

allowing for an increase in chemical tunability providing a higher degree of optimization for the carbon adsorbent.

Metal-organic frameworks display highly optimized textural and chemical properties, however the traditional production via metal salts results in difficult to handle powders. Production from high-purity metal salt precursors can be expensive and reduces the available avenues for macroscale engineering of the adsorbent, creating a barrier for the industrial implementation of MOFs. Another focus of this work is to transfer the templating aspect of carbide precursors towards MOF growth. The utilization of such an “insoluble” precursor significantly increases the control over crystal growth, growth location and the feasibility of integrating MOFs into support materials. Along with these benefits there is potential for altered physical properties and economic feasibility depending on the precursor of choice. The use of carbides as a sacrificial template for MOF growth can provide a new level of engineering and synthesis control that can help overcome the barrier to entry that MOFs face for industrial use in applications such as acid gas removal.

The overall goal of this Ph.D. research is to develop a fundamental understanding of ordered and non-ordered derivatives from carbide precursors. For disordered CDCs, the goal is to develop techniques to control the residual metal and functional groups in the produced porous carbon geared towards acid gas adsorption. The major focus for ordered MOF derivatives, is to demonstrate the feasibility of using carbides as both a metal reservoir and templating agent for the controlled growth of the desired framework.

CHAPTER 1. INTRODUCTION

1.1 Acid Gases

The United States Congress passed the Clean Air Act in 1970 and had revisions to the act in 1990, ramping up political and societal awareness of gaseous emissions.¹ Concerns over the adverse effects from emissions such as acid rain, smog, and direct effects on the environment and human health highlighted the need to understand and mitigate unwanted pollutants. Pollutants such as CO₂, SO₂, NO₂, and H₂S are classified as acid gases and are a major focus of emission reductions due to their established role in deteriorating health and habitats.

Any gas that produces an acid solution when mixed with water is classified as an acid gas. Carbon dioxide produces carbonic acid (H₂CO₃), sulfur dioxide produces sulfuric (H₂SO₄)/ sulfurous acid (H₂SO₃), and nitrogen dioxide can produce nitric (HNO₃) or nitrous acid HNO₂. Before regulations these gases were able to reach high enough concentrations in the atmosphere where they were able to form acid rain. Acid rain can cause significant damage to buildings and vehicles as well as severely effect plants and animals that are sensitive to the pH of their environment. Studies also directly linked high concentrations of acid gases to chronic cardiovascular and respiratory health effects.²⁻³ Therefore, understanding how acid gases interact with materials and optimizing methods to efficiently and economically remove them are of utmost importance.

Commercially available solutions to remove acid gases such as SO₂ and H₂S can be seen in Figure 1-1. The type of process can be assessed by first determining if its reversible,

then subsequently whether or not a slurry and moisture saturated flue gas is produced.⁴ For processes that are once-through there is a heavy and continuous capital cost which can be improved upon by implementing a cyclic process. For techniques that involve regeneration, “wet” methods are effective but typically incur high energy demands for regeneration and solvent processing.⁵⁻⁶ Therefore, dry adsorption processes are attractive due to their ability to mitigate energy demands with moderate heats of adsorption while not requiring solvent during processing or regeneration. As seen in Figure 1-1, activated carbon (AC) is the most frequently used solid adsorbent in industry. The process is primarily implemented using a moving bed with granular AC, where sulfur rich gas enters, and a cleaner processed gas is produced as SO₂ is adsorbed. The carbon material can then be thermally regenerated, producing a highly concentrated stream of SO₂ that can be treated to produce sulfuric acid.⁴ Though commercially available activated carbon is cheap, it lacks sufficient tunability to offset high operation and maintenance cost incurred during desulfurization. Therefore, exploring highly tunable carbon matrices and other tunable adsorbents is of fundamental interest in order to increase the efficiency and economic viability of adsorption for acid gas removal.

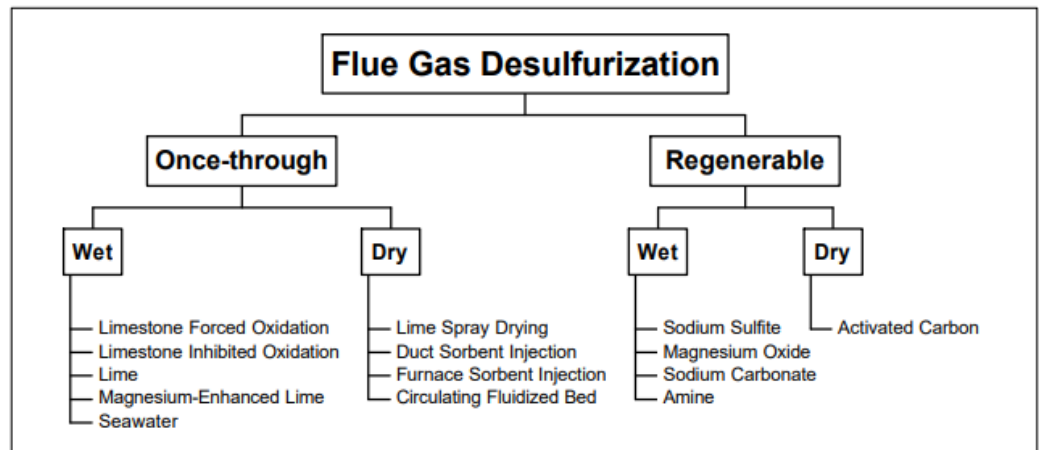


Figure 1-1: Overview of commercial desulfurization techniques⁴

1.2 Activated Carbon

Activated carbon (AC) consists of a broad, well studied, and fundamental baseline for properties of a porous carbon matrix. Activated carbon is produced from a variety of raw materials including coal, wood, and coconut shell.⁷ The production of AC can be classified into two processes, thermal or chemical. Thermal activation typically involves a two-step process of carbonization and oxidation. Carbonization involves the raw material being pyrolyzed at elevated temperatures of 600-1100°C under an inert atmosphere. Then in order to activate the material, the carbonized sample is exposed to an oxidizing agent such as steam or oxygen at temperatures from 250-1200°C depending on the desired pore-size distribution and surface functionalities.⁷ During chemical activation the raw material is first impregnated with an acid, base, or salt and then pyrolyzed between 300-900°C.⁸⁻¹⁵ This process allows for the carbon to be activated during the first step of pyrolysis giving some control over the porosity and oxygen content.

The carbon produced is classified as an (AC) and possess a range of physical and chemical properties. The main physical properties of interest are the surface area, pore volume, and pore-size distribution (PSD). The surface area of AC can range from 200-3000 m²g⁻¹ depending on the precursor and activation method.⁷ The pore volume is directly correlated with the PSD when considering the diameter of the pore, which consists of micro (<2 nm), meso- (2-50 nm), and macropores (>50 nm).¹⁶ Activated carbons notoriously suffer from wide PSD's as a result of the precursor choice and synthesis methods, making it difficult to tune the material for a desired process.¹⁶⁻¹⁷ The surface chemistry of carbon is also important when it comes to the adsorption process, especially when looking at the adsorption of polar molecules. Activated carbon can have a range of oxygen and nitrogen species decorating the surface as seen in Figure 1-2. Oxygen functionalities can act as a Lewis acid or Lewis base, while nitrogen functionalities are primarily basic in nature.¹⁸ Since the surface chemistry of AC has such a significant influence on adsorption, a multitude of methods have been utilized to tune functional groups with heat and ammonia-based treatments implemented for increasing basic functionalities.¹⁹⁻²⁰ With the ability to alter chemical and physical properties of AC, integrated with their low-cost of production and high chemical and thermal stability, carbonaceous materials are widely used in commercial applications today, such as gas separations²¹⁻²⁴, water filtration^{19, 25-27}, and catalysis²⁸⁻³⁰. This baseline of how carbon-based adsorbents can be broadly tuned and effectively implemented with respect to AC, has led to a new class of highly tunable carbon-based adsorbents.

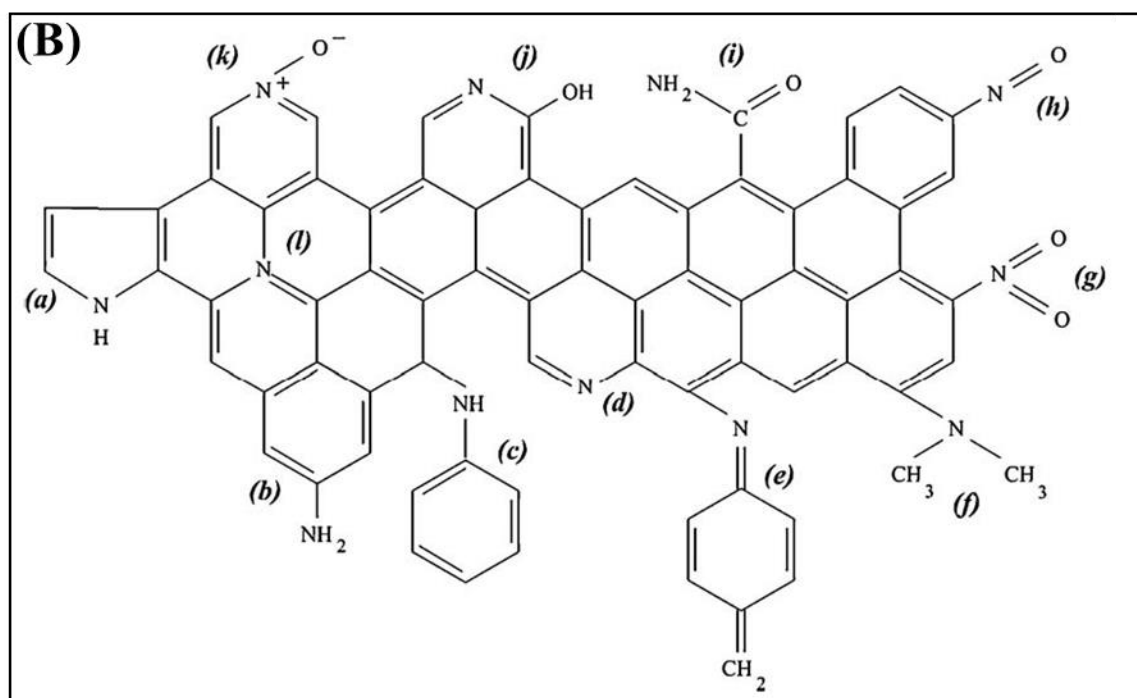
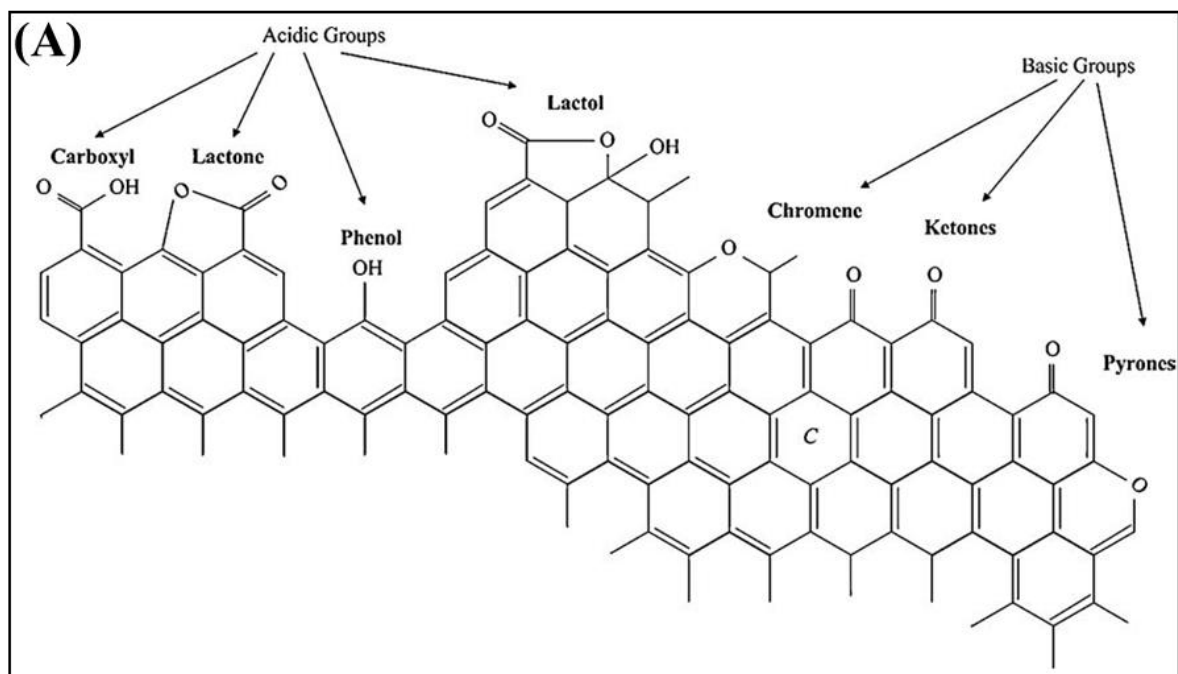


Figure 1-2: Surface functionalities on a carbon basal plane with a focus on: (A) Oxygen Functionalities^{18, 31} (B) Nitrogen Functionalities: (a) pyrrole, (b) primary amine, (c) secondary amine, (d) pyridine, (e) imine, (f) tertiary amine, (g) nitro, (h) nitroso, (i) amide, (j) pyridone, (k) pyridine-N-oxide, (l) quaternary nitrogen^{18, 32}

1.3 Carbide-Derived Carbon

The selective etching of carbide materials to produce various carbon structures has proven to be a promising technique to produce highly tunable carbon matrices. A carbide is comprised of metal or semimetal bonded to carbon, which possesses the higher electronegativity (E_N) in the matrix. This differential can be used to broadly classify different types of carbides. Salt-like carbides (e.g. Al_4C_3 , CaC_2 , and Na_2C_2) possess a high electronegativity differential (ΔE_N) and display ionic properties. Metallic carbides (e.g. Fe_3C , TiC , and LaC_2) have a moderate ΔE_N and exhibit metallic properties. Covalent carbides (e.g. B_4C , SiC) have a very small ΔE_N and therefore exhibit strong covalent bonding throughout the lattice.³³ This classification though helpful, cannot accurately cover the large range of diverse carbide structures, especially when binary and ternary carbides are considered. Literature has provided a degree of sub-classification for the three primary groups giving further criteria to categorize the structures. Salt-like carbides can be further divided into 3 categories based on the carbon anion in the matrix, as shown in Table 1.³³

Table 1-1: Sub-classification of Salt-like Carbide

Classification	Carbon Anion	Carbide Species
Methanides	C^{4-}	Al_4C_3 , Be_2C
Acetylides	C_2^{2-}	Na_2C , CaC_2
Allylenides	C_3^{4-}	Li_4C_3 , Mg_2C_3

Different methods such as (halogenation, hydrothermal treatment, vacuum decomposition, etc.) have been implemented to extract the metal cation from the carbide matrix to produce a range of carbide-derived carbons (CDCs). A multitude of carbides have been explored for their potential to create CDCs (Al_4C_3 , B_4C , CaC_2 , Cr_3C_2 , Fe_3C , Mo_2C , Nb_2 , NbC , SiC , TaC , Ta_2C , TiC , Ti_2AlC , Ti_3AlC_2 , Ti_3SiC_2 , ThC_2 , UC_2 , WC , ZrC).³⁴⁻³⁵ Depending on their precursor, etching conditions, and post-treatment, a variety of tailorable carbon-based matrices have been formed, with a range of physical and chemical properties.

1.3.1 Tunability of Carbide-Derived Carbons

The pseudomorphic replication or conformational transformation of the carbide precursor to the carbon derivative provides a high level of spatial engineering that can be transferred to CDCs via templating carbide thin films, nanorods, and nanospheres.³⁶⁻³⁸ This allows for an enhanced level of engineering outside of the physical and chemical properties of the carbon adsorbent by providing unique geometries, morphologies and macroscale templating of the carbon matrix previously unobtainable through traditional means of generating activated carbon. The reaction kinetics of CDC growth also provide control over the extent of carbon formation through a film or particle. CDC formation typically follows a linear growth rate showing kinetic control over the process, for materials 50-100 μm thick allowing for precise control over the desired thickness of a carbon coating.³⁹⁻⁴⁰ For thicker layers of CDCs, studies have shown the process becomes diffusion limited following a linear-parabolic Deal-and Grove-like growth kinetics.⁴¹⁻⁴³ Lower etching temperatures likewise exhibit a diffusion-controlled process due to activation energies for the conversion of metal carbide to the respective metal halide existing above 100 kJ mol^{-1} .⁴³ The predictable kinetics and diffusion for CDC production via halogenation allows for

optimization and control of the production process and subsequent macro properties of the carbon adsorbent.

The first degree of tunability of the internal properties of a CDC matrix is a direct result of the starting carbide precursor used during synthesis. The precursor dictates two important variables for the evolution of the carbon derivative, the starting position of carbon atoms and the metal halide formed during etching. The distance between the starting carbon atoms has a direct effect on the resulting pore structure, while the metal halide formed can affect the acceptable temperature range of synthesis due to the vaporization point of the halogenated species and in some cases catalyse graphitization.³⁵

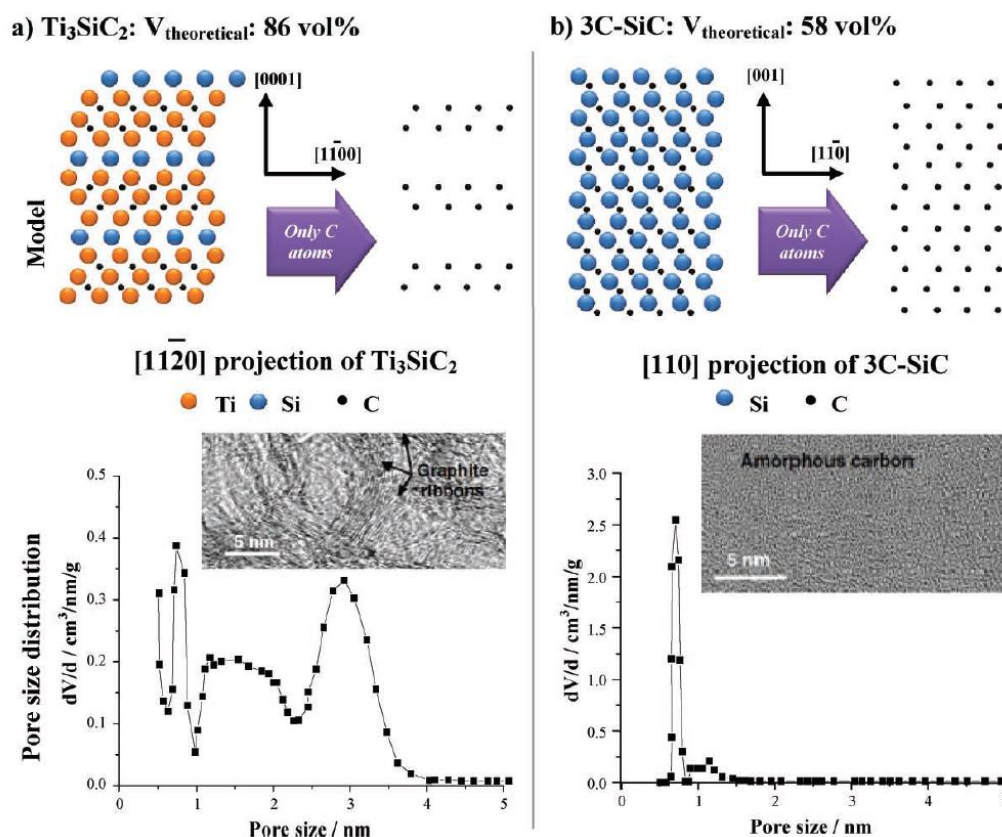


Figure 1-3: Atomic demonstration and resulting PSD for carbides etched via halogenation for (a) Ti_3SiC_2 at 1200°C and (b) 3C-SiC at 1200°C , adapted from Presser et al.³⁵

After the carbide precursor is selected, the PSD becomes a function of the etching temperature. At low temperatures, the PSD is templated by the structure of the starting crystalline lattice, which typically yields microporous carbon before significant carbon rearrangement. With an elevation in temperature, an increase in PSD is observed as the mobility of carbon increase allowing for self-rearrangement. Depicted in Figure 1-4, alterations in the etching temperature generate angstrom level changes in the PSD of the carbon matrix, allowing for an unprecedented level of tunability not seen in AC.³⁵ Carbon also crystallizes with an increase in temperatures as depicted in Figure 1-4(a-c), which computationally displays the increase in order of carbon as a direct result of the elevated etching temperature for TiC-CDC.⁴⁴

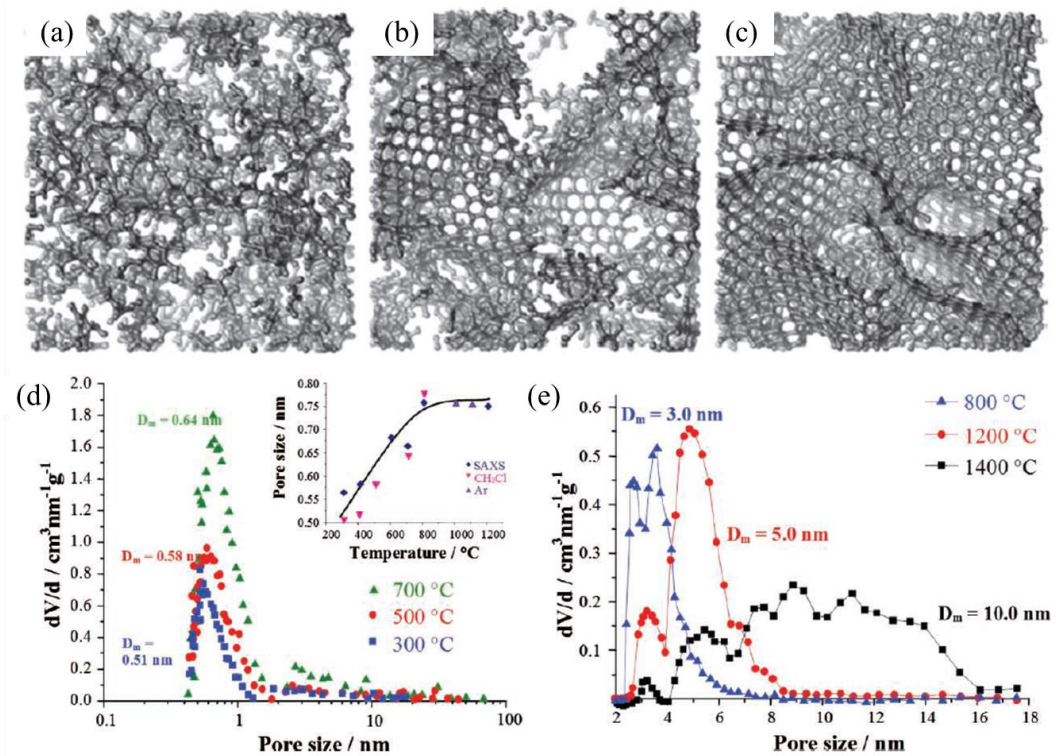


Figure 1-4: Simulated structure of TiC-CDC at (a) 600°C (b) 800°C and (c) 1200°C. NLDFT PSD derived from nitrogen physisorption for (d) Ti₃SiC₂-CDC and (e) SiCN PDC-CDC, adapted from Presser et al.³⁵

1.3.1.1 Surface chemistry of carbide-derived carbons

The functional groups on carbon materials play an important role in how they perform for a given application. Therefore, the surface chemistry of CDCs and how to manipulate said chemistry is of fundamental importance. A dearth of knowledge still exists in CDC literature relating to the mechanism by which CDCs are functionalized and how synthesis conditions can affect the quantity and identity of different functionalities. Studies have demonstrated carbide-derived carbon generated via chlorination retain chlorine species on the surface which can impart a negative effect on applications such as energy storage and biomedical device performance.⁴⁵⁻⁴⁷ Portet et al. investigated TiC-CDCs for the effect the annealing environment had on the residual chlorine and the resulting pore structure.⁴⁸ The investigation revealed annealing gases such as ammonia (NH_3) and hydrogen (H_2) are more effective at removing residual chlorine than argon (Ar) due to the reductive atmosphere. Annealing temperature also plays a dominant role in chlorine concentration with an increase in temperature resulting in a decrease in residual chlorine.⁴⁸ The presence of oxygen surface moieties, determined via EDS and TGA-MS, were verified and generalized based on the decomposition temperature and quantity of evolved CO and CO_2 . Etching temperature was determined to play a role in the type of oxygen species present throughout the CDC matrix, which can be correlated to the order of the CDC structure. Higher etching temperatures resulted in an increase in the graphitic nature of the carbon matrix, leading to reduced reactivity toward atmospheric oxygen sources and therefore a lower concentration of oxygen functionalities.⁴⁸ TiC-CDC has also been examined for post-synthetic treatment with nitric acid (HNO_3) to determine the effects oxygen content has on CO_2 uptake.⁴⁹ They found that oxygen groups on CDCs facilitate

hydrogen bonding between C-H and CO₂, challenging the idea that Lewis acid sites are not beneficial for adsorption of acid gases.⁴⁹ To date a systematic study has not been done across different CDCs to generalize how oxygen content on the carbon surface is effected by chlorination and subsequent annealing. Nitrogen functionalities, an equally important heteroatom that typically exhibits Lewis base behavior, has received even less attention in CDC literature as a result of many manuscripts focusing on super capacitors, requiring relatively pristine carbon surfaces. Therefore, a portion of this dissertation will focus on the effects that different carbide precursors and annealing environments have on surface functionalities and their respective effects on adsorption behavior.

1.3.2 Residual Metal in Carbide-Derived Carbons

Literature primarily deals with “metal free” CDCs, with few reports on controlling the amount or type of residual metal throughout the carbon matrix. There are a handful of studies that examine the core-shell behaviour of TiC-CDCs utilizing novel methods such as in-situ chlorine generation and fluidized beds to display control over the generation of the porous carbon shell.⁵⁰⁻⁵² These methods focus on controlling the amount of unreacted metal carbide left in the core of the particle, with the major focus being the carbonaceous exterior. Mangarella et. al demonstrated that partial etching of Fe₃C led to iron-based nanoparticles dispersed throughout the carbon matrix.⁵³⁻⁵⁴ They observed significant graphitization due to the catalytic properties of FeCl₃ which significantly hindered the diffusion of gaseous FeCl₂ and FeCl₃ out of the carbon structure. The retention of nanoparticles in Fe₃C-CDC demonstrated increased tunability of CDCs through controlling residual metal sites in the developing carbon matrix for catalysis or adsorption.

1.4 Metal-Organic Frameworks

Metal-organic frameworks (MOFs) are porous crystalline materials formed through linking metal nodes via polydentate organic linkers. Depending on the framework, the metal node can consist of metal ions or clusters. MOFs provide high surface areas, large pore volumes, uniform PSD, and chemical tunability.⁵⁵⁻⁵⁶ Due to the versatility of combining metal nodes and organic moieties, there are currently over 20,000 known and 120,000 hypothetical MOF structures in existence, each possessing unique properties.⁵⁷ With such diversity, MOFs show promise for a myriad of application such as gas separation^{56, 58}, drug delivery⁵⁹⁻⁶⁰, and catalysis.⁶¹

Though MOFs display potential for many applications they still possess a series of limitations that keep them from wide-spread industrial use. Stability in humid environments and cost of production have presented as the predominant limitations for these porous materials to reach large scale industrial application. With respect to humid stability, Kaskel et al. suggested the combination of hydrophobic organic linkers and hydrophilic metal nodes promotes hydrolysis of the metal-ligand bond causing irreversible degradation.⁶² Studies have taken place to improve stability through tuning metal inertness, hydrophobicity, and steric effects.⁶³ Durability of a framework in real world conditions is a critical factor for economic feasibility, therefore researching stable frameworks for large-scale production and improving general MOF stability are two rising challenges facing the MOF field today. Cost-effective production of high-quality MOFs, stable or not stable in application environments, stands as the largest barrier of entry to industry for these highly tunable frameworks. Currently, BASF produces five MOFs commercially: MIL-53(Al) (Basolite[®] A100), MOF-177 (Basolite[®] Z377), ZIF-8 (Basolite[®] Z1200), HKUST-1

(Basolite[®] C300), and FeBTC (Basolite[®] F300); however, the high cost and narrow scope of application keeps these materials from competing with other commercially available adsorbents such as activated carbon. Many MOF production variables are currently being investigated to increase commercial potential such as scale-up optimization by increasing space-time yields or implementing continuous processes that allow for large scale production of a select number of frameworks.⁶⁴⁻⁶⁶ A newer avenue towards optimizing MOFs for commercial viability is through controlling the metal source during synthesis to provide a potentially cheaper precursor, enhanced nanoscale engineering, and provide macroscopic templating.⁶⁷

1.4.1 Traditional Synthesis of Metal-Organic Frameworks

Traditionally MOFs are produced through solvothermal synthesis utilizing metal salts as the cation precursor. The self-assembling process begins with isolated metal ions coordinating with linkers or creating metal oxide clusters which proceed to connect to the organic component. In many cases, such as HKUST-1, a secondary building unit (SBU) is formed which facilitates the formation of the framework.⁶⁸ Solvothermal methods provide little control over growth kinetics or spatial templating without implementing advanced techniques. MOF growth on substrates form surface-mounted MOFs, deemed SUFMOFs, providing a degree of control over location and thickness (SAMs).⁶⁹ It was further demonstrated that noble metals and oxide surfaces functionalized with substrates such as thiol and silane self-assembled monolayer (SAMs) can facilitate growth of SURMOFs.⁷⁰ Shekhah et. al demonstrated controlled growth by functionalizing an organic surface to provide a two-dimensional nucleation site followed by a sequential process of metal and linker exposure providing monolayer control.⁷¹⁻⁷³ Layer-by-layer deposition of MOFs and

SURMOFs provide control over growth and insight into kinetics but require additional precursors, steps, and equipment that only add to the already high cost of MOF production. Therefore, providing the level of control layer-by-layer growth affords and the spatial templating SURMOFs provide while not compromising production cost is of growing interest in the field.

1.4.2 Metal-Organic Frameworks from Insoluble Precursors

In recent years, metal salt-free MOF production methods have been implemented utilizing solid materials or electrodes as the metal source.⁷⁴⁻⁷⁵ Electrochemical synthesis has proven successful for a select group of MOFs, which employs the redox method to allow for the continuous dissolution of the desired anodic metal.⁷⁶ The metal ions leach directly into an electrochemical cell that contains the organic linker promoting framework growth. Such methods have allowed BASF to commercially produce the Cu^{II} based HKUST-1 through sacrificial copper electrodes.⁶⁷ Use of solid metal precursors has garnered significant attention in the last 5 years as it proves to be a generalizable and versatile synthesis method for a variety of frameworks. Solid starting precursors include metals, metal oxides, hydroxides, carbonates, and mixed solid materials. MOF production from solid materials is realized as a result of the frameworks being more thermodynamically stable, observed through Gibbs free energy minimization, in the presence of organic ligands.⁷⁷ In contrast to traditional synthesis methods, solid precursors invoke heteronucleation of MOF crystals along with controlled cation release which provides significant control over spatiotemporal factors. Zhan et al. produced a comprehensive review covering the short history of solid precursors for MOF growth which has been summarized in Figure 1-5 and Table 1-2.⁶⁷

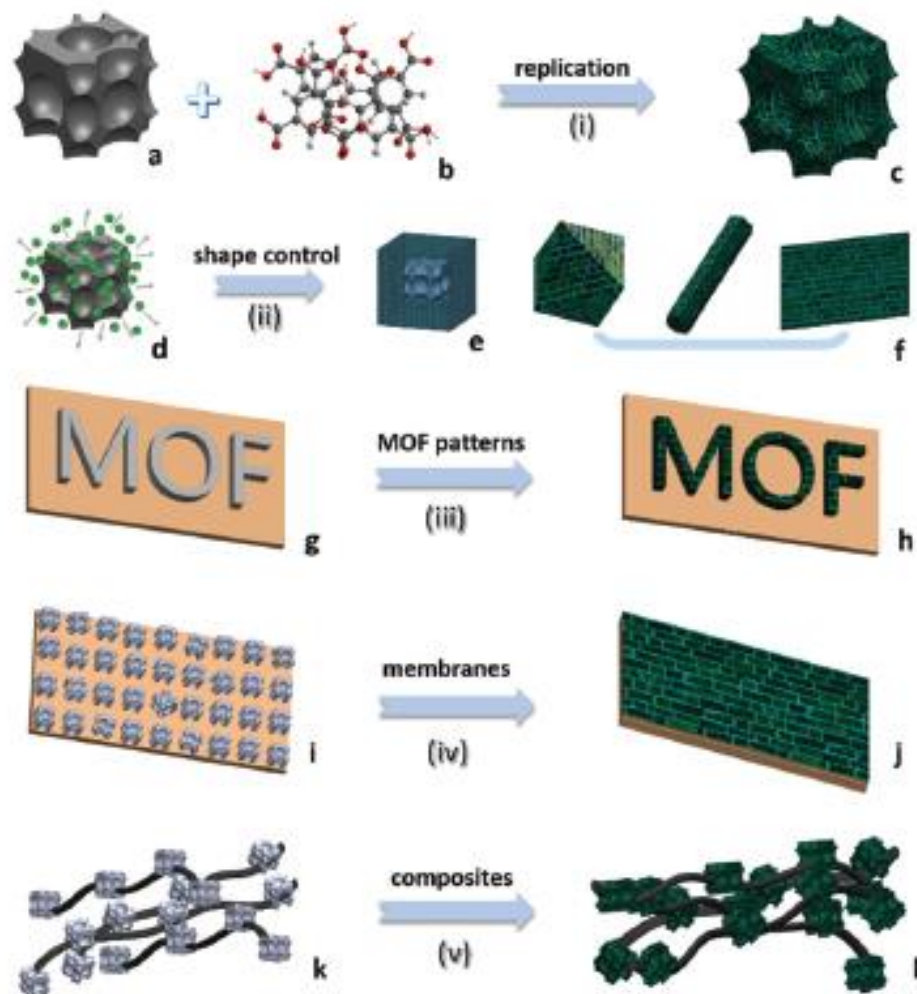


Figure 1-4: Adapted conceptual illustration (a) Solid-MOF precursor, (b) organic linker, (c) pseudomorphic replicated MOF, (d) controlled cation release, (e) core-shell control, (f) shape control via precursor selection, (g) patterned material on substrate, (h) patterned growth, (i) pre-allocated materials on substrate, (j) MOF film growth, (k) precursor composite, and (l) MOF composite. ⁶⁷

Table 1-2: List of benefits seen from using solid precursors for MOF growth corresponding to the graphical representation seen in Figure 1-5.⁶⁷

General Benefit	Details
<i>Inexpensive feedstocks</i>	Readily available feedstocks can be obtained from large-scale production, ceramics, or natural materials.
<i>Free of anion impurity</i>	Salt anions are not produced which minimises unwanted waste and eliminates risks of using potentially explosive nitrate salts and corrosive metal chlorides.
<i>Ecological advantages</i>	Rapid kinetics and the potential to be solvent free minimizes ecological issues seen for traditional methods.
<i>Morphological architectures</i>	Pseudomorphic replication of the precursor to the selected MOF derivative allows for an unprecedented level of architectural engineering of MOFs.
<i>Size and shape control of MOF</i>	The inherent control through dissolution allows for nucleation and kinetic control over MOF growth giving rise to unique properties.
<i>Pattern formation</i>	Localized growth from solid precursors allows for nanoscale engineering and control over MOF location which is essential for MOF-based devices.
<i>MOF Films</i>	Solid materials provide both a cation sink and nucleation seed site for MOF growth. Controlling the precursor thickness and implementing substrates facilitates control over the growth of MOF films or membranes.
<i>Multifunctional composites</i>	Generation of core-shell composites or integrating solid precursors in a host matrix allows for countless combinations to facilitate various potential MOF applications.

1.4.2.1 Metal-organic framework from metal sources

The oxidative dissolution of metal ions for subsequent transformation into MOFs has been successfully conducted for a handful of frameworks. Luz et. al reported a one-step method which utilizes naked copper nanocrystals to seed the growth of Cu-MOF-74 and HKUST-1 (Cu-BTC) which in turn encapsulates the metallic copper.⁷⁸ They determine that the dissolution rate of Cu^{2+} ions is key for the formation of a uniform composite, which can be tuned through reaction temperature, time, ligand concentration, and solvent. It is notable that during the earlier reaction times an amorphous copper intermediate is formed which is subsequently converted into the porous framework but further investigations were deemed out of the scope of the project.⁷⁸ Further work on solid Cu materials includes oxidative dissolution of substrates (e.g., Cu wire, meshes, and grids) to grow thin layers of HKUST-1 demonstrating the versatility of the method.⁷⁹⁻⁸⁰ Other studies demonstrated selective etching of Ni from a Pt-Ni alloy promoting the growth of Ni-MOF-74 as a result of differences in the chemical reactivity of the metal species.⁸¹

1.4.2.2 Metal oxide conversion to metal-organic frameworks

Metal oxide conversion to MOFs proceeds through an acid-base neutralization process, deemed acidic etching, involving the acidic linker and basic/amphoteric oxide. The resulting release of cations promotes controlled growth of the framework by manipulating concentrations through dissolution rates. Currently a handful of oxides (Al_2O_3 , CoO , CuO , Cu_2O , MgO , MnO , NiO , V_2O_5 , ZnO) have been used for conversion to frameworks with significant work done involving zinc for the formation of zeolitic

imidazolate frameworks (ZIFs).⁶⁷ A cumulative result of these studies revealed the size, surface roughness, and surface charge influence reactivity and conversion.⁸² Notably, metal oxides are thermodynamically stable as a result of high lattice energies in the range of 4-6 MJ mol⁻¹ which can lead to poor conversion or the absence of framework growth without optimized conditions.⁸³ Reboul et al. demonstrated the ability to generate a mesoscopic MIL-53(Al) architecture through the dissolution of an amorphous aluminum oxide architecture-directing agent. The structure demonstrated enhanced design aspects while simultaneously displaying significantly hindered properties with noticeably low surface areas and poor crystallinity.⁸⁴

1.4.2.3 Metal hydroxides for metal-organic framework growth

A variety of metal hydroxides have proven capable of being converted into porous frameworks including layered double hydroxides, hydroxyl double salts, layered simple hydroxides, oxyhydroxides, and amorphous hydroxides species.^{67, 84-86} In many of these studies an intermediate was identified as being a crucial step towards framework formation but further investigation was not pursued to elucidate information about a mechanism. A general synthesis path for hydroxide type precursors is as follows: (1) deprotonated ligands exchange with charge-balancing anions that are located throughout the layered-hydroxide matrix, (2) diffusion of the linker is promoted as a result of the positively charged layers throughout the hydroxide, and (3) linker mobility enables fast coordination to cations becoming available through dissolution allowing increased conversion.⁶⁷ Li et al. investigated alumina, an unidentified form of Al(OH)₃ which appears to be gibbsite, and

boehmite for their respective conversion to MIL-53(Al) under hydrothermal conditions.⁸⁷ The conversion from non-porous and “insoluble” precursor to MIL-53(Al) displayed slow reaction kinetics with no appreciative yield until after 18h of reaction and final surface areas ranging from 60-75% of traditional MIL-53(Al).⁸⁷⁻⁸⁸ The decreased yield and porosity can be attributed to unreacted precursor which is a result of high lattice enthalpies, diffusion-limiting particle sizes, and linker availability. The water adsorption was also altered exhibiting an increased hydrophobic nature which led to an improvement in water stability compared to traditional MIL-53(Al). A proposed mechanism for the conversion to MIL-53(Al) was put forth stating prealigned Al-O units in the precursor form the octahedral $\text{AlO}_4(\text{OH})_2$ node of the framework, which can sequentially be bridged by deprotonated terephthalic acid generating the porous structure.⁸⁷ No concrete evidence was provided for this theory and the true mechanism for conversion of insoluble Al-O precursors to a metal-organic framework has yet to be elucidated.

1.5 Thesis Overview

The application of adsorption separations to mitigate the effects of acid gases is a promising, yet challenging endeavor. The overall goal of this work is to establish fundamental knowledge of controlled synthesis techniques for increased tunability of ordered (MOFs) and disordered (CDCs) adsorbent, derived from carbide materials. This goal will be achieved through the completion of the following objectives: (1) implementation of partial etching and post-synthetic modification to control the residual metal content in CDCs, (2) tuning the surface chemistry of fully-etched CDCs for an

increase interaction with acid-gases, and (3) extension of the templating aspects of sacrificial carbide precursors towards the controlled growth of metal-organic frameworks. Objective 1 is addressed in Chapters 3-5, investigating for the first-time partial etching and post-synthetic modification of Al_4C_3 -CDC and Mo_2C -CDCs. Objective 2 is documented in chapter 6 relating to the effects annealing environments have on porous carbon derived from Al_4C_3 , Mo_2C , and TiC , while correlating physical and chemical changes to adsorption performance. Lastly Objective 3 focuses on the synthesis of MIL-53(Al) from Al_4C_3 and the effects solvent ratios have on the resulting framework, outlined in Chapter 7.

Previously, partial etching of iron carbide-derived carbon was investigated, where it was found that iron chloride nanoparticles were retained through local graphitization as a result of the catalytic properties of the metal chloride.⁵³⁻⁵⁴ Chapter 3 covers the extension of partial etching to the Al_4C_3 -CDC matrix for the retention of metal-based nanoparticles. The properties of aluminum chloride involving polymerization and irreversible hydration provided a promising candidate for the retention of aluminum-based nanoparticles. A systematic study was performed on the effects that temperature and time had on the residual metal and carbon host. The synthesis was optimized and fully characterized for the resulting properties of the Al_4C_3 -CDC matrix and their subsequent adsorption potential for CO_2 , H_2O , and SO_2 .

As a result of chlorination, residual metal nanoparticles typically exist as a metal chloride or its readily oxidized derivative, throughout the partially etched carbide-derived carbon. Such a Lewis acid site does not promote favorable adsorption of an acid gas species. Therefore, optimization of the residual metal in partially etched Al_4C_3 -CDCs is of

interest for enhanced acid gas adsorption. Chapter 4 investigates the post-synthetic conversion of residual metal nanoparticles in Al_4C_3 -CDC to polyaluminum chloride (PAC), $\text{Al}(\text{OH})_3$, and Al_2O_3 . Extensive characterization revealed the residual metal in the CDC can be manipulated through water vapor, alkaline solution, and heat treatment, all of which effect the amount and identity of aluminum-based active sites throughout the carbon host. It was found that alkaline treatment to converts the bulk of nanoparticles to amorphous $\text{Al}(\text{OH})_3$ significantly improved the adsorbents interactions with acid gases (CO_2 and SO_2).

At this point two CDC systems have demonstrated their propensity to retain metal-based nanoparticles, Fe_3C -CDC and Al_4C_3 -CDC. In each case the unique properties of the metal chloride were theorized to play a key role in the retention of the desired nanoparticles. To extend the fundamental knowledge and application of partial etching, Chapter 5 explores Mo_2C for the retention of molybdenum-based nanoparticles. Molybdenum chloride provides a promising candidate for retention due to MoCl_5 possessing a low boiling point (268°C) while also forming of a bulky dimer in the gas phase which hinders the mobility of the molybdenum species as it navigates through the evolving CDC, promoting metal retention. Molybdenum derivates are highly active for catalysis, therefore dispersed nanoparticles of molybdenum-based species in a carbon host that can facilitate diffusion of reactants and produces is also of commercial interest. A series of partially and fully etched Mo_2 -CDCs were prepared for analysis of nanoparticles, porosity, surface chemistry, and adsorption. It was discovered that low etching temperatures affords the retention of molybdenum-based nanoparticles throughout a highly amorphous carbon host while displaying minimal surface functionalities.

With many factors' contributing to CDC performance, it is difficult to deconvolute which attributes are playing a significant role. Therefore, Chapter 6 focuses on fully etched CDC materials and how various annealing environments effect the resulting surface chemistry and subsequent adsorption. Annealing techniques, typically hydrogen, have been consistently implemented in CDC literature to remove unwanted metal chlorides and residual chlorine species which usually results in higher surface areas and pore volumes. Little attention has been paid to the alteration in surface functionalities as a result of synthesis conditions. To the best of the author's knowledge a systematic study across different CDC systems to evaluate the surface chemistry of various annealing gases and temperatures has yet to published. The annealing gases of interest are, ammonia for the introduction of basic nitrogen groups, hydrogen which is commonly used in CDC production, and air exposure to explore native species formed. A combination of XPS, EDS, and various adsorption techniques revealed both annealing gas and temperature effect the resulting surface functionality composition as well as adsorption behavior for CO₂, H₂O, and SO₂.

Chapter 7 focuses on employing Al₄C₃ as a templated precursor for structured growth of aluminum terephthalate (MIL-53(Al)). Recent work on solid precursors for MOF growth is gaining traction with increased templating attributes and scale-up potential while some techniques simultaneously display decreased conversion along with pore crystallinity and porosity. Carbides are an unexplored metal source for MOF growth that demonstrate metal extraction potential during CDC formation as well as enhanced templating properties with significant work being conducted on carbide thin films, nanospheres, wires, and nanorods. For the first time the successful conversion of a metal carbide to a MOF was realized

through the conversion of Al_4C_3 to MIL-53(Al). Temporal studies revealed a 4, 5, and 6-coordinate transitional aluminum species that was a crucial component to the formation of the 6-coordinate framework. A unique needle-like morphology was observed due to planar growth of the MOF on the exfoliating carbide surface. Unique breathing behavior and stability of MIL-53(Al) is demonstrated as a direct result of growth from an insoluble precursor. The flexibility of this new synthesis method towards different topologies and functionalities was performed with the successful creation of MIL-101(Al) from trimesic acid and a series of MIL-53(Al) analogues through various functionalized terephthalic linkers. Solvent effects on synthesis success, crystal structure, porosity and morphology were performed, demonstrating the solubility of BDC, degradation of Al_4C_3 and the crystal structure of the resulting framework was heavily reliant on solvent ratios.

Chapter 8 outlines the overall conclusions of this work. Topics that are specifically discussed are extension of partial etching of carbide-derived carbons, post-synthetic modification of residual metal in CDCs, surface chemistry of fully etched CDCs and implementing carbides as metal reservoir and templates for MOF growth. In addition, recommendations for future work, based on the results of the aforementioned projects, are provided on carbide-derived adsorbents.

1.6 References

1. Clean Air Act | US EPA. <http://www.epa.gov/air/caa/>.
2. Ghorani-Azam, A.; Riahi-Zanjani, B.; Balali-Mood, M., Effects of air pollution on human health and practical measures for prevention in Iran. *Journal of Research in Medical Sciences : The Official Journal of Isfahan University of Medical Sciences* **2016**, 21, 65.
3. Skalpe, I. O., Long-term Effects of Sulphur Dioxide Exposure in Pulp Mills. *British Journal of Industrial Medicine* **1964**, 21 (1), 69-73.

4. Srivastava, R. K., *Controlling SO₂ Emissions--a Review of Technologies*. United States Environmental Protection Agency, Office of Research and Development Washington, DC: 2000.
5. Garg, B.; Verheyen, T. V.; Pearson, P.; Feron, P.; Cousins, A., A technology review for regeneration of sulfur rich amine systems. *International Journal of Greenhouse Gas Control* **2018**, 75, 243-253.
6. Camper, D.; Bara, J. E.; Gin, D. L.; Noble, R. D., Room-Temperature Ionic Liquid–Amine Solutions: Tunable Solvents for Efficient and Reversible Capture of CO₂. *Industrial & Engineering Chemistry Research* **2008**, 47 (21), 8496-8498.
7. Allen, S. J.; Whitten, L.; Mckay, G., The Production and Characterisation of Activated Carbons: A Review. *Developments in Chemical Engineering and Mineral Processing* **1998**, 6 (5), 231-261.
8. Lamine, S. M.; Ridha, C.; Mahfoud, H.-M.; Mouad, C.; Lotfi, B.; Al-Dujaili, A. H., Chemical Activation of an Activated Carbon Prepared from Coffee Residue. *Energy Procedia* **2014**, 50, 393-400.
9. Juan, Y.; Ke-qiang, Q., Preparation of Activated Carbon by Chemical Activation under Vacuum. *Environmental Science & Technology* **2009**, 43 (9), 3385-3390.
10. Acevedo, B.; Barriocanal, C.; Lupul, I.; Gryglewicz, G., Properties and performance of mesoporous activated carbons from scrap tyres, bituminous wastes and coal. *Fuel* **2015**, 151, 83-90.
11. Raymundo-Piñero, E.; Azaïs, P.; Cacciaguerra, T.; Cazorla-Amorós, D.; Linares-Solano, A.; Béguin, F., KOH and NaOH activation mechanisms of multiwalled carbon nanotubes with different structural organisation. *Carbon* **2005**, 43 (4), 786-795.
12. Lv, Y.; Zhang, F.; Dou, Y.; Zhai, Y.; Wang, J.; Liu, H.; Xia, Y.; Tu, B.; Zhao, D., A comprehensive study on KOH activation of ordered mesoporous carbons and their supercapacitor application. *Journal of Materials Chemistry* **2012**, 22 (1), 93-99.
13. Hayashi, J. i.; Kazehaya, A.; Muroyama, K.; Watkinson, A. P., Preparation of activated carbon from lignin by chemical activation. *Carbon* **2000**, 38 (13), 1873-1878.
14. Hayashi, J. i.; Horikawa, T.; Takeda, I.; Muroyama, K.; Nasir Ani, F., Preparing activated carbon from various nutshells by chemical activation with K₂CO₃. *Carbon* **2002**, 40 (13), 2381-2386.
15. Cazetta, A. L.; Vargas, A. M. M.; Nogami, E. M.; Kunita, M. H.; Guilherme, M. R.; Martins, A. C.; Silva, T. L.; Moraes, J. C. G.; Almeida, V. C., NaOH-activated carbon of high surface area produced from coconut shell: Kinetics and equilibrium studies from the methylene blue adsorption. *Chemical Engineering Journal* **2011**, 174 (1), 117-125.

16. Rouquerol, J.; Avnir, D.; Fairbridge, C.; Everett, D.; Haynes, J.; Pernicone, N.; Ramsay, J.; Sing, K.; Unger, K., Recommendations for the characterization of porous solids (Technical Report). *Pure and Applied Chemistry* **1994**, 66 (8), 1739-1758.
17. Jaroniec, M., Characterization of nanoporous materials. In *Access in nanoporous materials*, Springer: 2002; pp 255-272.
18. Shafeeyan, M. S.; Daud, W. M. A. W.; Houshmand, A.; Shamiri, A., A review on surface modification of activated carbon for carbon dioxide adsorption. *Journal of Analytical and Applied Pyrolysis* **2010**, 89 (2), 143-151.
19. Biniak, S.; Szymański, G.; Siedlewski, J.; Świątkowski, A., The characterization of activated carbons with oxygen and nitrogen surface groups. *Carbon* **1997**, 35 (12), 1799-1810.
20. Abe, M.; Kawashima, K.; Kozawa, K.; Sakai, H.; Kaneko, K., Amination of Activated Carbon and Adsorption Characteristics of Its Aminated Surface. *Langmuir* **2000**, 16 (11), 5059-5063.
21. Yang, R. T., *Gas separation by adsorption processes*. Butterworth-Heinemann: 2013.
22. Sircar, S.; Golden, T.; Rao, M., Activated carbon for gas separation and storage. *Carbon* **1996**, 34 (1), 1-12.
23. Chue, K.; Kim, J.; Yoo, Y.; Cho, S.; Yang, R., Comparison of activated carbon and zeolite 13X for CO₂ recovery from flue gas by pressure swing adsorption. *Industrial & Engineering Chemistry Research* **1995**, 34 (2), 591-598.
24. Brady, T.; Rostam-Abadi, M.; Rood, M., Applications for activated carbons from waste tires: natural gas storage and air pollution control. *Gas separation & purification* **1996**, 10 (2), 97-102.
25. Dias, J. M.; Alvim-Ferraz, M. C.; Almeida, M. F.; Rivera-Utrilla, J.; Sánchez-Polo, M., Waste materials for activated carbon preparation and its use in aqueous-phase treatment: a review. *Journal of environmental management* **2007**, 85 (4), 833-846.
26. Bhatnagar, A.; Hogland, W.; Marques, M.; Sillanpää, M., An overview of the modification methods of activated carbon for its water treatment applications. *Chemical Engineering Journal* **2013**, 219, 499-511.
27. Otowa, T.; Nojima, Y.; Miyazaki, T., Development of KOH activated high surface area carbon and its application to drinking water purification. *Carbon* **1997**, 35 (9), 1315-1319.
28. Prati, L.; Rossi, M., Gold on carbon as a new catalyst for selective liquid phase oxidation of diols. *Journal of Catalysis* **1998**, 176 (2), 552-560.

29. Peng, H.; Mo, Z.; Liao, S.; Liang, H.; Yang, L.; Luo, F.; Song, H.; Zhong, Y.; Zhang, B., High performance Fe-and N-doped carbon catalyst with graphene structure for oxygen reduction. *Scientific reports* **2013**, *3*, 1765.
30. Paulus, U.; Schmidt, T.; Gasteiger, H.; Behm, R., Oxygen reduction on a high-surface area Pt/Vulcan carbon catalyst: a thin-film rotating ring-disk electrode study. *Journal of Electroanalytical Chemistry* **2001**, *495* (2), 134-145.
31. Montes-Morán, M. A.; Suárez, D.; Menéndez, J. A.; Fuente, E., On the nature of basic sites on carbon surfaces: an overview. *Carbon* **2004**, *42* (7), 1219-1225.
32. Pietrzak, R., XPS study and physico-chemical properties of nitrogen-enriched microporous activated carbon from high volatile bituminous coal. *Fuel* **2009**, *88* (10), 1871-1877.
33. Ruschewitz, U., Binary and ternary carbides of alkali and alkaline-earth metals. *Coordination Chemistry Reviews* **2003**, *244* (1), 115-136.
34. Presser, V.; McDonough, J.; Yeon, S. H.; Gogotsi, Y., Effect of pore size on carbon dioxide sorption by carbide derived carbon. *Energy Environ Sci* **2011**, *4*.
35. Presser, V.; Heon, M.; Gogotsi, Y., Carbide-Derived Carbons-From Porous Networks to Nanotubes and Graphene. *Advanced Functional Materials* **2011**, *21* (5), 810-833.
36. Han, W.; Fan, S.; Li, Q., Continuous synthesis and characterization of silicon carbide nanorods. *Chemical Physics Letters* **1997**, *265* (3-5), 374-378.
37. He, C. N.; Zhao, N. Q.; Shi, C. S.; Song, S. Z., Fabrication of aluminum carbide nanowires by a nano-template reaction. *Carbon* **2010**, *48* (4), 931-938.
38. Gogotsi, Y., Chemical vapour deposition: Transition metal carbides go 2D. *Nat Mater* **2015**, *14* (11), 1079-1080.
39. Becker, P.; Glenk, F.; Kormann, M.; Popovska, N.; Etzold, B. J. M., Chlorination of titanium carbide for the processing of nanoporous carbon: A kinetic study. *Chemical Engineering Journal* **2010**, *159* (1-3), 236-241.
40. Chen, L.; Ye, H.; Gogotsi, Y.; McNallan, M. J., Carbothermal synthesis of boron nitride coatings on silicon carbide. *Journal of the American Ceramic Society* **2003**, *86* (11), 1830-1837.
41. Chen, L.; Behlau, G.; McNallan, M.; Gogotsi, Y., Carbide derived carbon (CDC) coatings for tyranno ZMI SiC fibers. **2003**.
42. Zelikman, A.; Leonova, L., Chlorination of carbide components of hard alloys. *Tsvetnye Metally* **1978**, 54-56.

43. Presser, V.; McDonough, J.; Yeon, S.-h.; Gogotsi, Y., Effect of pore size on carbon dioxide sorption by carbide derived carbon. *Energy & Environmental Science* **2011**, 4 (8), 3059-3066.
44. Palmer, J. C.; Llobet, A.; Yeon, S. H.; Fischer, J. E.; Shi, Y.; Gogotsi, Y.; Gubbins, K. E., Modeling the structural evolution of carbide-derived carbons using quenched molecular dynamics. *Carbon* **2010**, 48 (4), 1116-1123.
45. Darkrim, F. L.; Malbrunot, P.; Tartaglia, G. P., Review of hydrogen storage by adsorption in carbon nanotubes. *International Journal of Hydrogen Energy* **2002**, 27 (2), 193-202.
46. Frackowiak, E.; Béguin, F., Electrochemical storage of energy in carbon nanotubes and nanostructured carbons. *Carbon* **2002**, 40 (10), 1775-1787.
47. Zhu, R., Effects of residual chlorine on properties of carbide derived carbon. McNallan, M. J., Ed. ProQuest Dissertations Publishing: 2006.
48. Portet, C.; Kazachkin, D.; Osswald, S.; Gogotsi, Y.; Borguet, E., Impact of synthesis conditions on surface chemistry and structure of carbide-derived carbons. *Thermochimica Acta* **2010**, 497 (1), 137-142.
49. Xing, W.; Liu, C.; Zhou, Z.; Zhou, J.; Wang, G.; Zhuo, S.; Xue, Q.; Song, L.; Yan, Z., Oxygen-containing functional group-facilitated CO₂ capture by carbide-derived carbons. *Nanoscale Research Letters* **2014**, 9 (1), 1-8.
50. Ariyanto, T.; Zhang, G.-R.; Riyahi, F.; Gläsel, J.; Etzold, B. J. M., Controlled synthesis of core-shell carbide-derived carbons through in situ generated chlorine. *Carbon* **2017**, 115, 422-429.
51. Etzold, B. J. M.; Ariyanto, T.; Gläsel, J.; Kern, A., Synthesis and Characterization of Carbide-Derived Carbon with Core-Shell Pore Structure. *Chemie Ingenieur Technik* **2014**, 86 (9), 1558-1558.
52. Yongde, M., Synthesis and Adsorption Property of SiO₂@Co(OH)₂ Core-Shell Nanoparticles. *Nanomaterials* **2015**, 5 (2), 554-564.
53. Mangarella, M. C.; Ewbank, J. L.; Dutzer, M. R.; Alamgir, F. M.; Walton, K. S., Synthesis of embedded iron nanoparticles in Fe₃C-derived carbons. *Carbon* **2014**, 79, 74-84.
54. Mangarella, M. C.; Walton, K. S., Tailored Fe₃C-derived carbons with embedded Fe nanoparticles for ammonia adsorption. *Carbon* **2015**, 95, 208-219.
55. Férey, G., Hybrid porous solids: past, present, future. *Chemical Society Reviews* **2008**, 37 (1), 191-214.

56. Furukawa, H.; Cordova, K. E.; O’Keeffe, M.; Yaghi, O. M., The Chemistry and Applications of Metal-Organic Frameworks. *Science* **2013**, *341* (6149).
57. Wilmer, C. E.; Leaf, M.; Lee, C. Y.; Farha, O. K.; Hauser, B. G.; Hupp, J. T.; Snurr, R. Q., Large-scale screening of hypothetical metal–organic frameworks. *Nature Chemistry* **2011**, *4*, 83.
58. Li, J.-R.; Kuppler, R. J.; Zhou, H.-C., Selective gas adsorption and separation in metal–organic frameworks. *Chemical Society Reviews* **2009**, *38* (5), 1477-1504.
59. Horcajada, P.; Chalati, T.; Serre, C.; Gillet, B.; Sebrie, C.; Baati, T.; Eubank, J. F.; Heurtaux, D.; Clayette, P.; Kreuz, C.; Chang, J.-S.; Hwang, Y. K.; Marsaud, V.; Bories, P.-N.; Cynober, L.; Gil, S.; Férey, G.; Couvreur, P.; Gref, R., Porous metal–organic-framework nanoscale carriers as a potential platform for drug delivery and imaging. *Nature Materials* **2009**, *9*, 172.
60. Huxford, R. C.; Della Rocca, J.; Lin, W., Metal–organic frameworks as potential drug carriers. *Current Opinion in Chemical Biology* **2010**, *14* (2), 262-268.
61. Lee, J.; Farha, O. K.; Roberts, J.; Scheidt, K. A.; Nguyen, S. T.; Hupp, J. T., Metal–organic framework materials as catalysts. *Chemical Society Reviews* **2009**, *38* (5), 1450-1459.
62. Küsgens, P.; Rose, M.; Senkovska, I.; Fröde, H.; Henschel, A.; Siegle, S.; Kaskel, S., Characterization of metal-organic frameworks by water adsorption. *Microporous and Mesoporous Materials* **2009**, *120* (3), 325-330.
63. Burtch, N. C.; Jasuja, H.; Walton, K. S., Water Stability and Adsorption in Metal-Organic Frameworks. *Chemical Reviews* **2014**, *114*, 10575-10612.
64. Paseta, L.; Seoane, B.; Julve, D.; Sebastián, V.; Téllez, C.; Coronas, J., Accelerating the controlled synthesis of metal–organic frameworks by a microfluidic approach: a nanoliter continuous reactor. *ACS applied materials & interfaces* **2013**, *5* (19), 9405-9410.
65. Seo, Y.-K.; Yoon, J. W.; Lee, J. S.; Lee, U.-H.; Hwang, Y. K.; Jun, C.-H.; Horcajada, P.; Serre, C.; Chang, J.-S., Large scale fluorine-free synthesis of hierarchically porous iron (III) trimesate MIL-100 (Fe) with a zeolite MTN topology. *Microporous and Mesoporous Materials* **2012**, *157*, 137-145.
66. Stock, N.; Biswas, S., Synthesis of Metal-Organic Frameworks (MOFs): Routes to Various MOF Topologies, Morphologies, and Composites. *Chemical Reviews* **2012**, *112* (2), 933-969.
67. Zhan, G.; Zeng, H. C., Alternative synthetic approaches for metal-organic frameworks: transformation from solid matters. *Chemical Communications* **2017**, *53* (1), 72-81.

68. Chui, S. S. Y.; Lo, S. M. F.; Charmant, J. P. H.; Orpen, A. G.; Williams, I. D., A Chemically Functionalizable Nanoporous Material $[\text{Cu}_3(\text{TMA})_2(\text{H}_2\text{O})_3]_2$. *Science* **1999**, 283 (5405), 1148.
69. Summerfield, A.; Cebula, I.; Schröder, M.; Beton, P. H., Nucleation and Early Stages of Layer-by-Layer Growth of Metal Organic Frameworks on Surfaces. *The Journal of Physical Chemistry C* **2015**, 119 (41), 23544-23551.
70. Hermes, S.; Schröder, F.; Chelmoski, R.; Wöll, C.; Fischer, R. A., Selective Nucleation and Growth of Metal–Organic Open Framework Thin Films on Patterned COOH/CF₃-Terminated Self-Assembled Monolayers on Au(111). *Journal of the American Chemical Society* **2005**, 127 (40), 13744-13745.
71. Shekhah, O., *Layer-by-Layer Method for the Synthesis and Growth of Surface Mounted Metal-Organic Frameworks (SURMOFs)*. 2010; Vol. 3.
72. Shekhah, O.; Wang, H.; Zacher, D.; Fischer, R. A.; Wöll, C., Growth Mechanism of Metal–Organic Frameworks: Insights into the Nucleation by Employing a Step-by-Step Route. *Angewandte Chemie International Edition* **2009**, 48 (27), 5038-5041.
73. Shekhah, O.; Wang, H.; Kowarik, S.; Schreiber, F.; Paulus, M.; Tolan, M.; Sternemann, C.; Evers, F.; Zacher, D.; Fischer, R. A.; Wöll, C., Step-by-Step Route for the Synthesis of Metal–Organic Frameworks. *Journal of the American Chemical Society* **2007**, 129 (49), 15118-15119.
74. Chen, B.; Yang, Z.; Zhu, Y.; Xia, Y., Zeolitic imidazolate framework materials: recent progress in synthesis and applications. *Journal of Materials Chemistry A* **2014**, 2 (40), 16811-16831.
75. Yang, Q.; Xu, Q.; Yu, S.-H.; Jiang, H.-L., Pd Nanocubes@ZIF-8: Integration of Plasmon-Driven Photothermal Conversion with a Metal–Organic Framework for Efficient and Selective Catalysis. *Angewandte Chemie International Edition* **2016**, 55 (11), 3685-3689.
76. Martinez Joaristi, A.; Juan-Alcañiz, J.; Serra-Crespo, P.; Kapteijn, F.; Gascon, J., Electrochemical Synthesis of Some Archetypical Zn²⁺, Cu²⁺, and Al³⁺ Metal Organic Frameworks. *Crystal Growth & Design* **2012**, 12 (7), 3489-3498.
77. Altree-Williams, A.; Pring, A.; Ngothai, Y.; Brugger, J., Textural and compositional complexities resulting from coupled dissolution–reprecipitation reactions in geomaterials. *Earth-Science Reviews* **2015**, 150, 628-651.
78. Luz, I.; Loiudice, A.; Sun, D. T.; Queen, W. L.; Buonsanti, R., Understanding the Formation Mechanism of Metal Nanocrystal@MOF-74 Hybrids. *Chemistry of Materials* **2016**, 28 (11), 3839-3849.
79. Tanihara, Y.; Nozaki, A.; Kuwahara, Y.; Mori, K.; Yamashita, H., Fabrication of Densely Packed HKUST-1 Metal Organic Framework Thin Layers on a Cu Substrate

through a Controlled Dissolution of Cu. *Bulletin of the Chemical Society of Japan* **2016**, 89 (9), 1048-1053.

80. Nozaki, A.; Tanihara, Y.; Kuwahara, Y.; Mori, K.; Yamashita, H., Deposition of Metal Organic Framework Layers on Skeletal Cu Prepared from Cu-Ti Amorphous Alloy and Their Enhanced Catalytic Activities. *Chemistry Letters* **2016**, 45 (8), 976-978.

81. Li, Z.; Yu, R.; Huang, J.; Shi, Y.; Zhang, D.; Zhong, X.; Wang, D.; Wu, Y.; Li, Y., Platinum–nickel frame within metal-organic framework fabricated in situ for hydrogen enrichment and molecular sieving. *Nature Communications* **2015**, 6, 8248.

82. Guo, Y.; Mao, Y.; Hu, P.; Ying, Y.; Peng, X., Self-confined synthesis of HKUST-1 membranes from CuO nanosheets at room temperature. *ChemistrySelect* **2016**, 1 (1), 108-113.

83. Qi, F.; Stein, R. S.; Frišćić, T., Mimicking mineral neogenesis for the clean synthesis of metal–organic materials from mineral feedstocks: coordination polymers, MOFs and metal oxide separation. *Green Chemistry* **2014**, 16 (1), 121-132.

84. Reboul, J.; Furukawa, S.; Horike, N.; Tsotsalas, M.; Hirai, K.; Uehara, H.; Kondo, M.; Louvain, N.; Sakata, O.; Kitagawa, S., Mesoscopic architectures of porous coordination polymers fabricated by pseudomorphic replication. **2012**, 11, 717.

85. Zhao, J.; Nunn, W. T.; Lemaire, P. C.; Lin, Y.; Dickey, M. D.; Oldham, C. J.; Walls, H. J.; Peterson, G. W.; Losego, M. D.; Parsons, G. N., Facile Conversion of Hydroxy Double Salts to Metal–Organic Frameworks Using Metal Oxide Particles and Atomic Layer Deposition Thin-Film Templates. *Journal of the American Chemical Society* **2015**, 137 (43), 13756-13759.

86. Li, Z.; Wu, Y.-n.; Li, J.; Zhang, Y.; Zou, X.; Li, F., The Metal-Organic Framework MIL-53(Al) Constructed from Multiple Metal Sources: Alumina, Aluminum Hydroxide, and Boehmite. *Chemistry - A European Journal* **2015**, 21 (18), 6913-6920.

87. Li, Z.; Wu, Y.-n.; Li, J.; Zhang, Y.; Zou, X.; Li, F., The Metal–Organic Framework MIL-53(Al) Constructed from Multiple Metal Sources: Alumina, Aluminum Hydroxide, and Boehmite. *Chemistry – A European Journal* **2015**, 21 (18), 6913-6920.

88. Loiseau, T.; Serre, C.; Huguenard, C.; Fink, G.; Taulelle, F.; Henry, M.; Bataille, T.; Férey, G., A Rationale for the Large Breathing of the Porous Aluminum Terephthalate (MIL-53) Upon Hydration. *Chemistry – A European Journal* **2004**, 10 (6), 1373-1382.

CHAPTER 2. EXPERIMENTAL MATERIALS AND METHODS

2.1 Materials

2.1.1 Carbides Used for Material Synthesis

Three carbide precursors are implemented throughout this dissertation. Aluminum carbide (Al_4C_3) was used to produce carbide-derived carbons (CDCs) and metal-organic frameworks (MOFs) (Strem Chemicals 98% purity -325 mesh). For CDC production, 325 mesh TiC (Sigma-Aldrich, 98% purity) was purchased with no additional processing to the carbide precursor done in lab. Molybdenum carbide (Mo_2C) was purchased as granules from American Elements (99% purity). In order to maintain particle size, the granules were crushed in a ball mill and sieved to a mesh size of 325.

2.2 Experimental Methods

2.2.1 Horizontal Bed Reactor for Carbide-Derived Carbon Synthesis

A lab built horizontal bed reactor, similar to those seen in literature, was build and placed inside a fume hood for safety during the chlorination process used to produced CDCs (Figure 2-1). A lecture bottle of chlorine gas (Airgas 99.5%) was connected to a stainless-steel tee with an integrated purge line that lead to an actuator ball valve (Swagelok SS-43GS4-42AC) which enable the remote capability to disengage chlorine flow. When the valve is open the chlorine flow rate is regulated by a calibrated Alborg mass flow controller (MFC). After the MFC, a second line of Argon (Airgas 99.99%) is measured by a mass flow meter to dilute the chlorine to the desired concentration. This line was also

used for the introduction of annealing gases such as ammonia and hydrogen. The gas lines connected to a 1" OD and 20" long quartz tube reactor via a 1" Ultra Torr fittings with Viton o-rings. The tube resided in a horizontal tube furnace (Thermo Scientific Lindberg® Blue M® Mini-Mite™) which obtained a range of temperatures 200-1200°C. The effluent stream from the reaction process was sent to a scrubbing solution of NaOH to neutralize residual chlorine gas, HCl, and metal chlorides produced during the reaction.

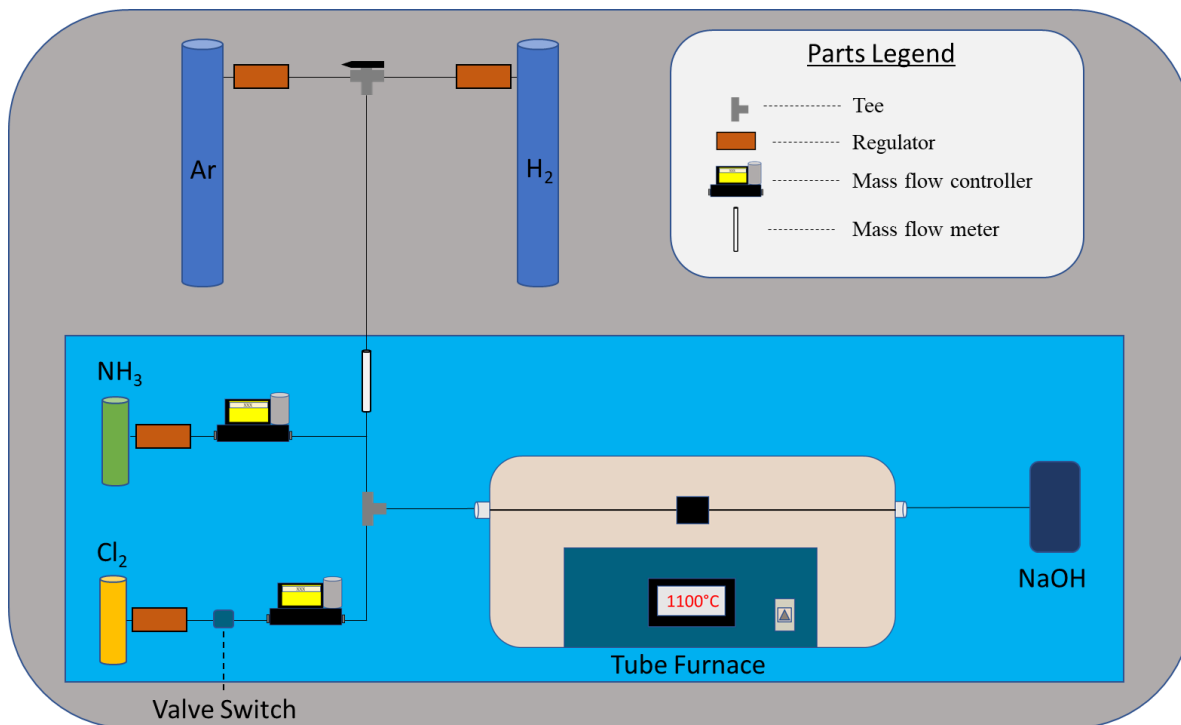


Figure 2-1: Simplified carbide-derived carbon synthesis reactor scheme

2.2.2 Nitrogen Physisorption at 77 K

Nitrogen sorption isotherms were obtained at 77 K with a Quantachrome Quadrasorb EVO volumetric analyser. Uptakes were recorded across a region of partial pressures, ranging from 3×10^{-5} to $0.990 P/P_0$. Materials were activated prior to adsorption in a Quantachrome FloVac degasser at 150°C under vacuum (~ 5 mTorr). The sample was

then backfilled with nitrogen and the activated mass was used to calculate normalized uptake.

2.2.3 Surface Area Measurements

The surface areas of all materials were modeled utilizing the Brunauer, Emmett, and Teller (BET) theory of multilayer adsorption near the condensation temperature of a given gas.¹ There are five important assumptions used during the derivation of BET that are important to note.² (1) Non-dissociative adsorption occurs only on well-defined surface sites. (2) The adsorbed species can only act as a single adsorption site for molecules in subsequent layers. (3) Equilibrium exists at the interface of the uppermost adsorbed layer and the bulk gas phase. (4) Heat is required for activation of the adsorption/desorption process. The initial heat of adsorption is the energy released from the first monolayer adhering the surface. The adsorption of subsequent layers is assumed to be equal to each other and the heat of liquefaction of the adsorbed species. (5) At saturation pressures, it can be assumed there are an infinite number of layers of adsorbate on the adsorbent surface. With these assumptions intact, the following isothermal model can be used as shown in Eq. 2.1:

$$\frac{P}{v(P_0 - P)} = \frac{1}{v_m c} + \frac{c - 1}{v_m c} \frac{P}{P_0} \quad (2.1)$$

where P is the saturation pressure, P_0 is the partial pressure of the system, v is the total volume, v_m is the volume of the adsorbed monolayer, and c is a constant. By linearizing the experimental data using $P/v(P_0 - P)$ as the y-axis and P/P_0 as the x-axis, across a range of

partial pressure from $P/P_0 = 0.03 \leq 0.3$, a slope of $(c-1)/v_m c$ and a y-intercept of $1/v_m c$ can be calculated. Using this experimentally derived information, the BET surface area can be calculated with Equation 2.2:

$$S_{BET} = \frac{v_m N_{Av} a}{v m_{sample}} \quad (2.2)$$

where N_{Av} is Avogadro's number and a is the cross-sectional area of the adsorbate.

2.2.4 Pore-size Distribution Analysis

The pore-size distribution (PSD) of carbon materials can be calculated utilizing multiple probe molecules such as Ar, N₂, and CO₂.³⁻⁵ The most common method in carbon literature is nitrogen at 77 K with the implementation of a variety of models based on density functional theory (DFT) to experimentally determine the PSD. DFT based models account for the adsorption process and the phase behaviour of fluids in micro and mesopores to obtain an accurate distribution of the pores throughout a carbon matrix.⁶ This approach is based on the solution to the adsorption integral equation:

$$a_{exp}(P/P_0) = \int_{w_{min}}^{w_{max}} a_{loc}(P/P_0, w) f(w) dw \quad (2.3)$$

where $a_{loc}(P/P_0, w)$ is the kernel function, w is the pore size, $f(w)$ is the desired PSD and $a_{exp}(P/P_0)$ is the experimental adsorption isotherm. The kernel is based on the assumption of the geometry of the pores, such as spherical, cylindrical, slit or a mixture of said geometries. Kernels can also account for pore-network connectivity as well as solid-fluid

potentials arising from the heterogeneity of the carbon surface.⁴ A product of this model is an artifact in PSD around 1 nm, produced as the model tries to interpret the layering transition between monolayer, bilayer and throughout subsequent multilayers.³ In the past decade, two advanced models have been adapted to account for the heterogeneity in the adsorbent surface which can account for the roughness of the material with quenched solid density functional theory (QSDFT) and the spatial non-uniformity of the adsorbent surface in a two dimensional manner with 2D non-local density functional theory (2D-NLDFT).³ Both models are absent of artifacts due to layering transitions and provide close agreement with each other despite using different methods to account for heterogeneity.

2.2.5 *Sulfur Dioxide, Carbon Dioxide, and Water*

Sulfur Dioxide (SO₂) adsorption isotherms were performed at 298 K up to 3 bar in a lab-built volumetric system. The system was comprised of two units, each containing a sample cell and a reference cell. During exposure the pressure was monitored in each cell and converted to moles of SO₂ through the Peng-Robinson equation of state with the use of appropriate constants.⁷ Prior to adsorption the material was activated in-situ at 150°C under vacuum.

Pure component CO₂ and H₂O isotherms were performed on a Micromeritics 3Flex device. Before exposure each sample was degassed at 150°C for 12 h under vacuum in a Micromeritics Smart VacPrep System. Water vapour exposure was performed at 298 K over a relative pressure range starting at $P/P_0 = 4 \times 10^{-6}$ up to 0.9. CO₂ isotherms were collected at 273 K and 298 K reaching relative pressures of 0.032 and 0.015 respectively.

2.2.6 Powder X-ray Diffraction (PXRD)

Crystallographic information can be obtained from powdered samples using PXRD. An X-ray source, typically copper, cobalt or chromium anode, is used to irradiate the sample across different angles and a detector is employed in-tandem to collect x-rays scatter by the sample, as depicted in Figure 2-2. Each reflection seen corresponds to the interplanar spacing between parallel crystalline planes. The interplanar spacing, also referred to as d-spacing, can be used to calculate the lattice parameter, ie size, of the unit cell through Bragg's Law (Equation 2.4). There are three main variables that contribute to a PXRD pattern that deliver important information on the crystalline system. As previously mentioned, the peak position gives information about the dimensions of the unit cell. The peak intensity corresponds to the quantity of a crystalline plane being irradiated. This information can be used to understand preferential orientation as well as give insight into crystal growth. Lastly, the width of a peak corresponds to both crystallite size and micro strain. To quantitatively analyze these features the pattern must be fit with a model such as Rietveld, which accounts for both experimental variables and crystal properties to fit a simulated pattern to experimental results. Amorphous materials do not have crystallinity

and therefore do not display sharp reflections but can be observed as broad low intensity peaks, such as the 002 peak in carbon.

$$d = \frac{\lambda}{2\sin(\frac{2\theta}{2})} \quad (2.4)$$

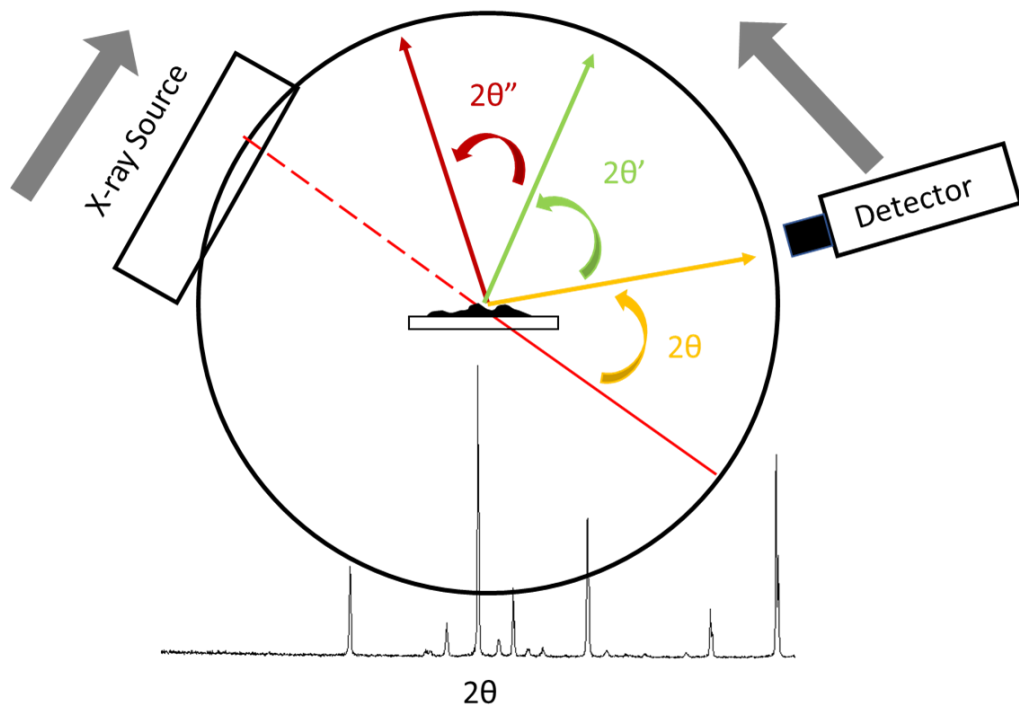


Figure 2-2: Experimental set-up for collecting powdered x-ray diffraction data

2.2.7 X-ray Photoelectron Spectroscopy (XPS)

XPS is the study of the distribution of electrons emitted from a sample that has been irradiated with X-rays. When a monoenergetic X-ray interacts with a solid sample it can cause electrons to be ejected that possess a discrete kinetic energy. The conservation of energy for the electron can be expressed by Equation 2.5:

$$E_{hv} = E_k + E_\phi + E_B(i) \quad (2.5)$$

where E_{hv} is the X-ray energy, E_k is the photoelectron kinetic energy, E_ϕ is a correction function, and $E_B(i)$ is the binding energy of the electron at the designated level i .⁸ An analyser is used to record the kinetic energy of the electron, while the X-ray energy and correction functions are known for a given system. Thus, the binding energy of the electron can be determined. This is a powerful technique since any change in the chemical environment of the atom emitting the electron corresponds to a change in the binding energy. This allows for quantitative analysis of oxidation, functional groups, bonding, and much more.

Some materials exhibit orbital splitting which gives rise to two peaks in a spectrum. This phenomena can be explained by exchange splitting, where a system with unpaired valence electrons allow for core electrons to experience a spin up and spin down interaction.⁸ This allows for a predictable separation of the binding energies that can be calculated and fit in a responsible manner.

2.2.8 *Microscopy*

Transmission electron microscopy (TEM) and scanning electron microscopy (SEM) were used to image the bulk and surface of particles respectively. TEM images can be collected in bright-field and dark-field which give different micrographic information, both image the bulk of a thin sample. Bright-field TEM images are formed by the blockage/absorbance of electrons by the sample being observed, giving areas with heavier elements or thicker regions a darker shade. Dark-field allows for the detection of electrons

by the sample which enables areas that contain elements with higher atomic numbers to show up brighter. SEM works on the principle of electrons scattering from the relative surface of a sample giving both morphological and elemental information. Secondary electrons (SE) and backscattered electrons (BSE) can be used which give different perspectives of the sample. Secondary electrons are produced when the electron beam hits the samples and valence electron are emitted. Only the electrons near the surface can escape and reach the detector, the electrons emitted deeper in the material are adsorbed by the surrounding sample. This means SE are sensitive to the surface and have a limited penetration depth of around 0.5-5 μm depending on the sample and accelerating voltage. BSE enter the sample and are scattered back to the detector, since BSE have a higher energy than SE electrons they probe deeper into the sample. BSE are sensitive to the atom number of the atoms in which they interact, with heavier atomic species providing stronger scattering, producing a brighter area in the image.

2.3 References

1. Brunauer, S.; Emmett, P. H.; Teller, E., Adsorption of Gases in Multimolecular Layers. *Journal of the American Chemical Society* **1938**, 60 (2), 309-319.
2. Walton, K. S.; Snurr, R. Q.; K.S. Walton, R. Q. S., Applicability of the BET method for determining surface areas of microporous metal-organic frameworks. *Journal of the American Chemical Society* **2007**, 129 (18), 8552-8556.
3. Landers, J.; Gor, G. Y.; Neimark, A. V., Density functional theory methods for characterization of porous materials. *Colloids and Surfaces A: Physicochemical and Engineering Aspects* **2013**, 437, 3-32.
4. Neimark, A. V.; Lin, Y.; Ravikovitch, P. I.; Thommes, M., Quenched solid density functional theory and pore size analysis of micro-mesoporous carbons. *Carbon* **2009**, 47 (7), 1617-1628.

5. Ravikovitch, P. I.; Vishnyakov, A.; Russo, R.; Neimark, A. V., Unified Approach to Pore Size Characterization of Microporous Carbonaceous Materials from N₂, Ar, and CO₂ Adsorption Isotherms. *Langmuir* **2000**, *16* (5), 2311-2320.
6. Puziy, A. M.; Poddubnaya, O. I.; Gawdzik, B.; Sobiesiak, M., Comparison of heterogeneous pore models QSDFT and 2D-NLDFT and computer programs ASiQwin and SAIEUS for calculation of pore size distribution. *Adsorption* **2016**, *22* (4), 459-464.
7. Melhem, G. A.; Saini, R.; Goodwin, B. M., A modified Peng-Robinson equation of state. *Fluid Phase Equilibria* **1989**, *47* (2), 189-237.
8. Hollander, J. M.; Jolly, W. L., X-ray photoelectron spectroscopy. *Accounts of Chemical Research* **1970**, *3* (6), 193-200.

CHAPTER 3. SYNTHESIS AND CHARACTERIZATION OF ALUMINUM CARBIDE-DERIVED CARBON WITH RESIDUAL ALUMINUM-BASED NANOPARTICLES

3.1 Introduction

The synthesis and characterization of porous solids impact a variety of applications ranging from water purification to carbon dioxide capture.¹⁻³ Carbons lack the “designable” aspect of metal-organic frameworks, for example, but exhibit very high surface areas and pore volumes and continue to be the leader in the commercial use due to low cost and good adsorption capabilities covering a wide range of adsorbate molecules.⁴ Activated carbons from traditional precursors such as wood and fruit pits or shells are known to exhibit wide pore size distributions with curved porous networks that lead to a bottle-neck effect which restricts molecule access and slows molecular diffusion.⁵ In recent years, a class of tailorable porous-carbon materials, carbide-derived carbons (CDCs), have emerged as promising materials for hydrogen and methane storage, electrochemical energy storage, protein adsorption, and pollution removal from both water and air.⁶⁻¹¹ CDCs are thermally and chemically resistant, making them applicable in a wide range of environmental conditions. These highly porous-carbon materials demonstrate a tunable, narrow pore-size distribution and surface areas exceeding $2000 \text{ m}^2 \text{ g}^{-1}$ for non-chemically activated species and over $3000 \text{ m}^2 \text{ g}^{-1}$ for chemically activated material.^{9, 12}

A multitude of binary and ternary carbides are used as precursors to CDC production, each precursor leading to a unique porous-carbon material with distinguishable

physical features and potential applications.¹³ By altering the precursor, the resulting trends seen in the physical characteristics of the CDC change, from the pore size distribution to the type of ordered carbon structures observed. Along with precursor selection, the metal extraction method plays a significant role in the resulting CDC. Multiple methods may be implemented for metal removal, such as halogenation, hydrothermal treatment, and vacuum decomposition.¹³ A large body of current literature focuses on utilizing chlorine gas to create metal chlorides as a means of halogenation treatment for metal extraction. During this process the metal heteroatom of the carbide precursor reacts with the chlorine gas forming a metal chloride that diffuses out of the developing porous-carbon structure.

Metal free porous-carbon materials have been the focus of most CDC research to date, with the exception of partially etched Fe₃C-CDC.¹⁴ Partial etching is the process of halting the chlorination reaction before complete extraction of the metal species. Mangarella et. al. demonstrated that partially etching Fe₃C-CDC produced iron chloride nanoparticles scattered throughout the Fe₃C-CDC matrix.¹⁴⁻¹⁵ The addition of such metal sites in porous-carbon materials is more typically accomplished by post-synthetic metal impregnation in activated carbon and pre-synthetic microemulsion in SiC-CDC.¹⁶⁻¹⁸ Incorporation of metal-based active sites has improved adsorption and catalytic properties for carbonaceous support materials, but these properties are often diffusion limited due to partial pore blockage by the impregnant. The generation of metal impregnated porous-carbon materials can be achieved via different methods, with wet impregnation techniques utilized in a vast majority of current literature. These procedures, specifically wet impregnation, require time consuming steps during preparation such as washing cycles,

drying and in some cases decomposition steps for nitrate impregnated materials, all of which are ancillary to the process to generate the activated carbon and the initial impregnation step.¹⁹⁻²⁵ These methods also require additional raw materials such as the metal source and solvent for impregnation. All of these additional steps and resources exponentially increase processing cost for future scale up, limiting the economic viability of the materials. The process of partially etching carbide materials has the potential to generate a porous-carbon with active metal-based sites in the form of nanoparticles, which can be synthesized in a matter of hours rather than days. Therefore, it would be advantageous to conduct an investigation into carbide precursors that can be partially etched to have tunable pore sizes and additional adsorption sites in and on the sorbent in the form of metal-based nanoparticles, without additional processing steps or reduction of the porous-carbon properties. Fe_3C -CDCs, which has demonstrated to the presence of nanoparticles, is hypothesized to retain FeCl_x nanoparticles due to the agglomeration of vaporized iron chloride in parallel with particles being trapped by carbon structures due to iron chloride's catalysis of graphitic structures.¹⁴ These results have motivated an investigation into other carbide materials that have the capacity to create active sites from the metal present in the carbide precursor via a partial etching process.

Aluminum chloride (AlCl_3), generated during the chlorination of aluminum carbide (Al_4C_3) provided the possibility for similar retention of nanoparticles due to the unique properties of the chloride. AlCl_3 sublimates at 180°C allowing access to a low range of etching temperatures. The chloride exists as both a monomer and dimer at different etching conditions, effecting how the vaporized chloride diffuses through the structure.²⁶ The equilibrium from the larger dimer to the smaller monomer will affect how the metal

chloride can diffuse out of the porous carbon structure. AlCl_3 has shown the ability to polymerize in the presence of liquid water to form polyaluminum chloride (PAC) as well as go through gas phase hydrolysis in the presence of trace amounts of water vapor. It has also been demonstrated that AlCl_3 reacts in the presence of oxygen, utilizing a chlorine catalyst at moderate temperatures to form Al_2O_3 .²⁶⁻³² These properties motivated an investigation into the potential for partially etched Al_4C_3 -CDC materials to contain nanoparticles. Studies have shown that Al_2O_3 nanoparticles display enhanced reactivity with both acid gas and volatile organic compound in terms of adsorption.³³⁻³⁴ Aluminum hydroxide particles have also demonstrated favorable adsorption properties with phosphates, as a result of the hydroxyl groups.³⁵ Therefore, it could be advantageous to incorporate aluminum based nanoparticles into a porous-carbon structure in a one pot synthesis, without reducing or hindering the carbon properties for adsorption based applications. Specifically, the various polymorphs of aluminum oxide and hydroxide have shown favorable interactions with acid gases due to their amphoteric nature.^{34, 36-37} To the best of the author's knowledge, no investigations have examined the interactions between acid gases and aluminum oxide/aluminum hydroxide nanoparticles embedded in a carbon matrix. By combining the adsorption properties of the porous-carbon and those of aluminum-based nanoparticles, a chemically and thermally resistant sorbent can be produced and tuned for adsorption as investigated with the weak acid gas, CO_2 , as part of this publication. A future application of such a material would exist in any place where a resilient adsorbent is necessary for the removal or adsorption of toxic and corrosive gases such as in a flue gas application. Therefore, a focused study on the synthesis of partially

etched Al_4C_3 -CDCs and their respective interaction with CO_2 and H_2O is of fundamental importance.

Fully etched Al_4C_3 -CDCs have been documented in literature at a variety of etching conditions, citing a range of carbon-based properties. These studies focused on electrical properties, such as capacitance, as well as observing carbon structure formation.³⁸⁻⁴³ References to aluminum-based material was briefly stated in Perkson et al., with a stated assumption of the material being aluminum chloride stuck in the pores, which is widely assumed in literature for residual metal in CDCs.³⁸ To the best of the authors' knowledge, an in-depth study on partially etched Al_4C_3 -CDCs has not been conducted. Nor has a complete study on pore size distribution and surface area as a function of etching time and temperature been completed to a degree to satisfy a full understanding of the correlation between synthesis conditions and resulting CDC properties. Herein, the effect of chlorination time and temperature on Al_4C_3 -CDC is studied to determine the effect on residual metal, material porosity, and pore size distribution. Additionally, water and CO_2 adsorption isotherms were investigated for Al_4C_3 -CDC materials etched at various temperatures and times to determine how the changes in physical properties of partially etched Al_4C_3 -CDC materials affected adsorption capacity.

3.2 Materials and Methods

3.2.1 Materials

Al_4C_3 -CDC was prepared by depositing 1 g of Al_4C_3 (Strem Chemicals 98% purity -325 mesh) in a quartz boat which is placed in a 20" long quartz tube with an outer diameter

of 1". The tube was placed in a horizontal tube furnace that was operated in the range of 300-900°C with a ramp rate for heating and cooling set at 5 °C min⁻¹. During heating and cooling a stream of argon gas (Airgas 99.999%) is flown over the bed at 150 mL min⁻¹. Once the temperature reaches the desired etching temperature, chlorine gas (Airgas 99.5%) was introduced via an Aalborg mass flow controller at a rate of 40 mL min⁻¹ while argon is still flowing at 150 mL min⁻¹. The flow continues for the duration of the run. After the argon and chlorine have passed over the bed it goes through a NaOH scrubber solution to neutralize any acidic gases. Once the etching experiment was completed, chlorine flow was discontinued and the system is cooled under argon at 150 mL min⁻¹. Note, for the sake of clarity the samples are labeled as follows Al₄C₃-CDC-T-CT. Where Al₄C₃ denotes the species of carbide, CDC refers to the general material of carbide-derived carbon, T is the temperature in degrees Centigrade at which etching occurred at, CT is the chlorination time in hours (e.g. Al₄C₃-CDC-300-1h).

3.2.2 *Methods*

3.2.2.1 Power X-ray Diffraction

Power X-ray Diffraction (PXRD) patterns were collected using an X'Pert X-ray PANalytical diffractometer with a Cu K α X-ray source (λ = 1.5418 Å). PXRD diffractograms were collected from a range of 5-90° with a step size of 0.02°. All experiments were carried out at room temperature.

3.2.2.2 Nitrogen Sorption Measurements

Nitrogen sorption measurements at 77 K were obtained using a Quantachrome Quadrasorb SI volumetric analyzer. Isotherms were collected at 77 K using a sample of 15-45 mg. Prior to each isotherm, the sample was outgassed for approximately 18 hours at 150°C and under vacuum (approximately 20 mTorr). Specific surface areas were calculated using the BET model in the relative pressure range (P/P_0) 0.005-0.03. Pore size distributions were collected for all samples using the Quenched Solid Density Functional Theory (QSDFT) model built into version 5.11 QuadraWin™ software. The QSDFT parameters were selected depending on the characteristics of the isotherm. For microporous, type I isotherms, a slit-pore model, nitrogen adsorbate, and carbon adsorbent were assumed. Whereas, for type IV isotherms that exhibit characteristic cavitation effects, an adsorption branch slit-pore/cylindrical pore model was used with an assumed nitrogen adsorbate and carbon adsorbent.

3.2.2.3 Thermogravimetric Analysis (TGA)

Thermogravimetric analysis for all samples was carried out on a NETZSCH STA 449 F1 Jupiter instrument. Measurements used 10-40 mg of material, ramped from 25-1400 °C at a ramp rate of 10 °C min⁻¹ and a flow rate of 20 mL min⁻¹ of air (Airgas 99.999%). The residual metal content was calculated by assuming total combustion of carbon, upon complete combustion, the final mass was assumed to be Al₂O₃.

2.2.4. Magic-Angle Spinning Nuclear Magnetic Resonance (MAS NMR)

No pretreatment of the sample was done before taking NMR measurements. ^{27}Al MAS NMR was carried out for all samples at a magnetic field strength of 13.9 T. A rotor synchronized (40 μs rotor period, corresponding to a spinning speed of 25 kHz) Hahn echo pulse sequence with a central transition-selective pulse was employed (CT pulse width = 1.3 μs). All spectra were referenced to a solution of 1M $\text{Al}(\text{NO}_3)_3$ at 0.0 ppm. The ^{27}Al spectra were recorded on a Redstone NMR spectrometer (TecMag) at a Larmor frequency of 153.7 MHz. For acquisition of the ^{27}Al spectra, a Bruker HX MAS probe with a 2.5 mm rotor was used. Additional measurements were recorded for select samples using a pulse-acquire experiment at a magnetic field strength of 20.0 T, spinning at 33.3 kHz, and a flip angle of $\pi/18$ (corresponding to a pulse width of 0.36 μs) to ensure quantitative 1D spectra were recorded.

3.2.2.4 Scanning electron microscopy (SEM)

Scanning electron microscopy (SEM) images were obtained using a LEO 1530 Thermally-Assisted Field Emission (TFE) Scanning Electron Microscope (SEM). All samples were deposited onto carbon tape. Images were scanned at an accelerating voltage range of 6-10 kV.

3.2.2.5 Transmission electron microscopy (TEM)

TEM and HRTEM images were obtained using a FEI Tecnai F30 at an operating voltage of 300 kV with a 1.7 \AA point resolution. Samples were prepared by suspending approximately 1 mg in methanol and deposited onto a lacy carbon copper grid.

3.2.2.6 Water Vapor Adsorption Isotherms

Water vapor adsorption experiments were performed on a volumetric Micromeritics 3-Flex device for pressures up to 1 bar at 25°C. Prior to the measurement, 10-30 mg of material were activated in situ at 150°C for 5 hours under dynamic vacuum

3.2.2.7 CO₂ Adsorption Measurements

CO₂ isotherms at 25 °C, in the pressure range of 0-20 bar, were obtained using the Hidden Isochema IGA-001 microbalance. Prior to the measurement, 10-30 mg of material was heated in-situ at 150 °C for 18 hours under vacuum.

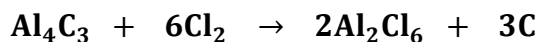
3.2.2.8 X-ray Photoelectric Spectroscopy (XPS) analysis

XPS measurements were taken on a Thermo K-alpha, monochromated Al K α source with a double-focusing hemispherical analyzer. High resolution spectra were taken of O1s, Al2p, Cl2p at a 0.1 eV step size, 50 ms dwell time, 50 eV pass energy, and a 400 μ m spot size.

3.3 Results and Discussion

3.3.1 Etching temperature and time effects on residual metal in Al₄C₃-CDC

Al_4C_3 reacts with chlorine gas to form aluminum chloride in the following manner:⁴⁴



Note that, depending on the temperature, the monomer and dimer of aluminum chloride will be present in different ratios in the vapor phase.²⁶ Near the sublimation point of aluminum chloride, 180 °C, the vaporous species is almost completely dimeric. At elevated temperatures, the equilibrium of aluminum chloride shifts to the monomeric species.²⁶ For the highest etching temperature reached in these experiments, 900°C, it has been shown that the majority of sublimed aluminum chloride species exist in the monomer phase.^{26, 45} The carbide was reacted at temperatures ranging from 300-900°C in 200 °C increments, then analyzed via TGA, NMR, XPS, TEM/SEM and PXRD to probe the physical properties of the Al_4C_3 -CDC. During chlorination, two distinct layers are formed in the bed at etching temperatures of 300 °C and 500 °C, the top layer is black with areas displaying a thin white residue, and the bottom layer is unreacted carbide. SEM-EDS (Table S2) suggests that white material on the Al_4C_3 -CDC is an amorphous aluminum oxide, based on the aluminum and oxygen content observed in EDS. Material etched at 700 and 900 °C for 1h display a homogenous sample with no distinguishable layering. These differences are likely due to changes in intermolecular diffusion in the bed with an increase in etching temperature. In order to characterize the Al_4C_3 -CDC the two layers underwent

a physical separation, if a heterogeneous sample was observed to remove the unreacted carbide portion.

TGA was performed on Al_4C_3 -CDC samples that were produced at 300, 500, 700 and 900 °C for 1 hour to observe the amount of residual aluminum that remained in the sample after chlorination. These temperatures were chosen to receive a broad overview of etching temperature effects on metal content as well as to have a comparison to fully etched samples in literature.^{38-39, 42} Figure 3-1 reports the effect of temperature on residual metal content. At 300 °C, 18% residual aluminum remains after etching. As the etching temperature is increased to 500 °C a steep drop in metal content is observed. This drastic drop in residual aluminum can be attributed to faster diffusion of gaseous species through the sample with increased temperature as well as a shift to the smaller monomeric chloride that will have fewer diffusional limitation while traveling through the porous-carbon structure. Therefore, at lower etching temperatures, where the dimer is present in larger quantities at equilibrium and where the pore size is small, which will be examined later in this paper, the amount of metal removal will be reduced for the same etching times.

Also contributing to changes in residual metal trends is the presence of carbon structures, which begin to form at an appreciable rate in the samples etched at 700 and 900 °C seen by TEM and PXRD, causing diffusion limitations and pore restructuring. This could potentially slow down the diffusion path of both the monomer and dimer species causing less of a drastic drop in metal content from etching temperatures of 500-900 °C, compared to those seen from 300-500 °C. The lowest metal content is 6% for Al_4C_3 -CDC-900-1h, showing that sample composition can be tuned to be more carbon based simply by increasing etching temperature while maintaining etching time.

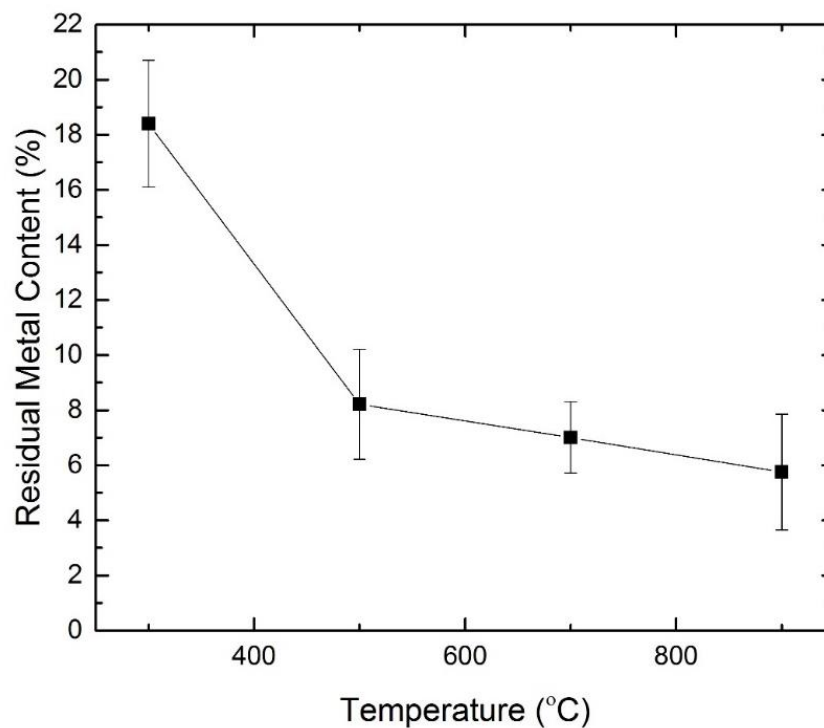


Figure 3-1: TGA data from residual metal content in Al_4C_3 -CDC after 1 hour of etching with Cl_2 in a temperature range of 300-900°C

Chlorination time also influences the residual metal content. To investigate the time dependence, two time trials were run; the chlorination times were varied from 0-6 h at 300 and 500 °C, these temperatures were chosen due to their high metal content and the significant drop in residual metal between the two, which is not as severe at other 200 °C jumps. Figure 3-2 depicts a decrease in residual metal as time increases for both etching temperatures. Unreacted Al_4C_3 is designated as 100% residual metal at an etching time of 0. At 500 °C, there is more of a significant drop off in the first hour of etching than seen at 300 °C due to more monomeric species being present at the higher temperature and more energy in the system for diffusion. The residual metal at higher etching times of 4 and 6 h is believed to be due to trapped metal species in the sample that are not easily extracted due to the formation of carbon structures or aggregation of metal-based species. Note that

4 and 6 h were arbitrary times used to show that with extended periods of etching, metal content can still be observed in the porous-carbon structure, this result is briefly touched on in literature for “fully etched” materials.³⁸ To remove this material thought to be stuck in the pores after thorough etching, annealing has been shown to be an effective method in other investigations.⁴⁶

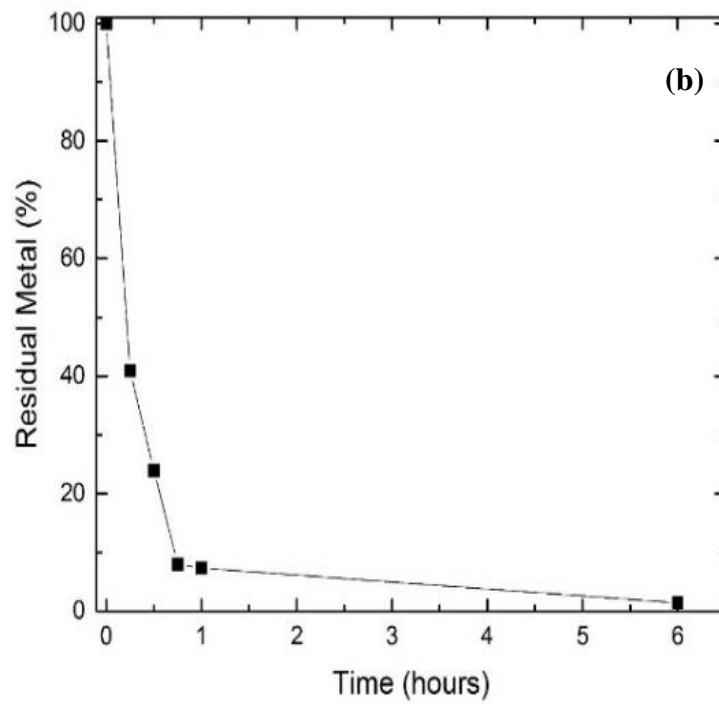
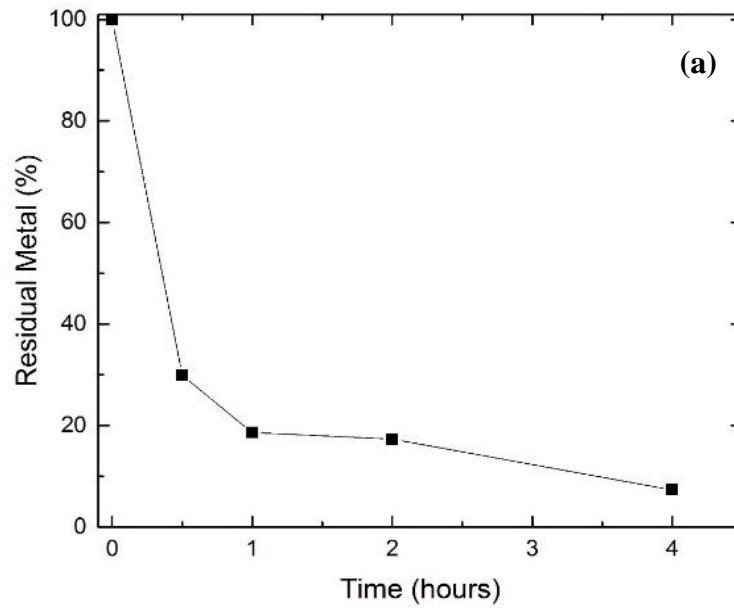


Figure 3-2: TGA results for time trials of (a) 300 °C and (b) 500 °C samples in terms residual metal.

3.3.2 3.2. Form of metal content in Al_4C_3 -CDC

The most conventional mechanism for CDC formation follows a core-shell model. This defines a mechanism where the carbide particle is etched from the outside forming a carbide core until complete etching is achieved. This is also termed layer-by-layer extraction.⁴⁷ However, Al_4C_3 -CDC appears to possess a slightly altered mechanism. This is suggested by examining the partially etched samples using TEM. Instead of a carbide core, the residual aluminum detected in Al_4C_3 -CDCs is in the form of aluminum based nanoparticles. It should be noted that at no point during this investigation were the nanoparticles determined to be elemental aluminum. Figure 3-3 depicts the TEM images for samples prepared at 300, 500, 700, and 900 °C for 1 h. As the temperature increases, the observed number of nanoparticles decreases; this observation correlates with TGA results. The form of the nanoparticles is also altered with increased temperature. At an etching temperature of 300 °C nanoparticles are 2-10 nm in size, while increasing etching temperature to 500 °C reveals aggregates a magnitude larger in size. Supporting information for these aggregates can be seen in Figures Figure A-12-Figure A-14. Once the etching temperature reaches 700 °C crystalline structures are observed in TEM, as depicted in Figure 3-3c. Table 1 shows that the materials depicted in Figure 3-3 consist of aluminum, chlorine and oxygen. EDS for Al_4C_3 -CDC-500-1h was not taken for the displayed image, other EDS indicate the same trend of Al, O, and Cl elements. Note that the high amounts of carbon content is from the grid and the sample itself while the copper content is from the grid alone. Although the reaction mechanism cannot be directly determined from this data, one theory suggests that AlCl_3 is formed during the etching process and is either trapped in the pores or by carbon structures. At the same time an

oxygen source, either from oxygen directly involved in the carbide lattice or trace amounts of water in the carbide or chlorine cylinder provides an oxidizing agent. It has been shown in literature that anhydrous aluminum chloride converts to aluminum oxide when in the presence of chlorine gas and an oxidizing agent.²⁹ This process will allow for the aluminum based nanoparticles to contain both chlorine and oxygen elements.

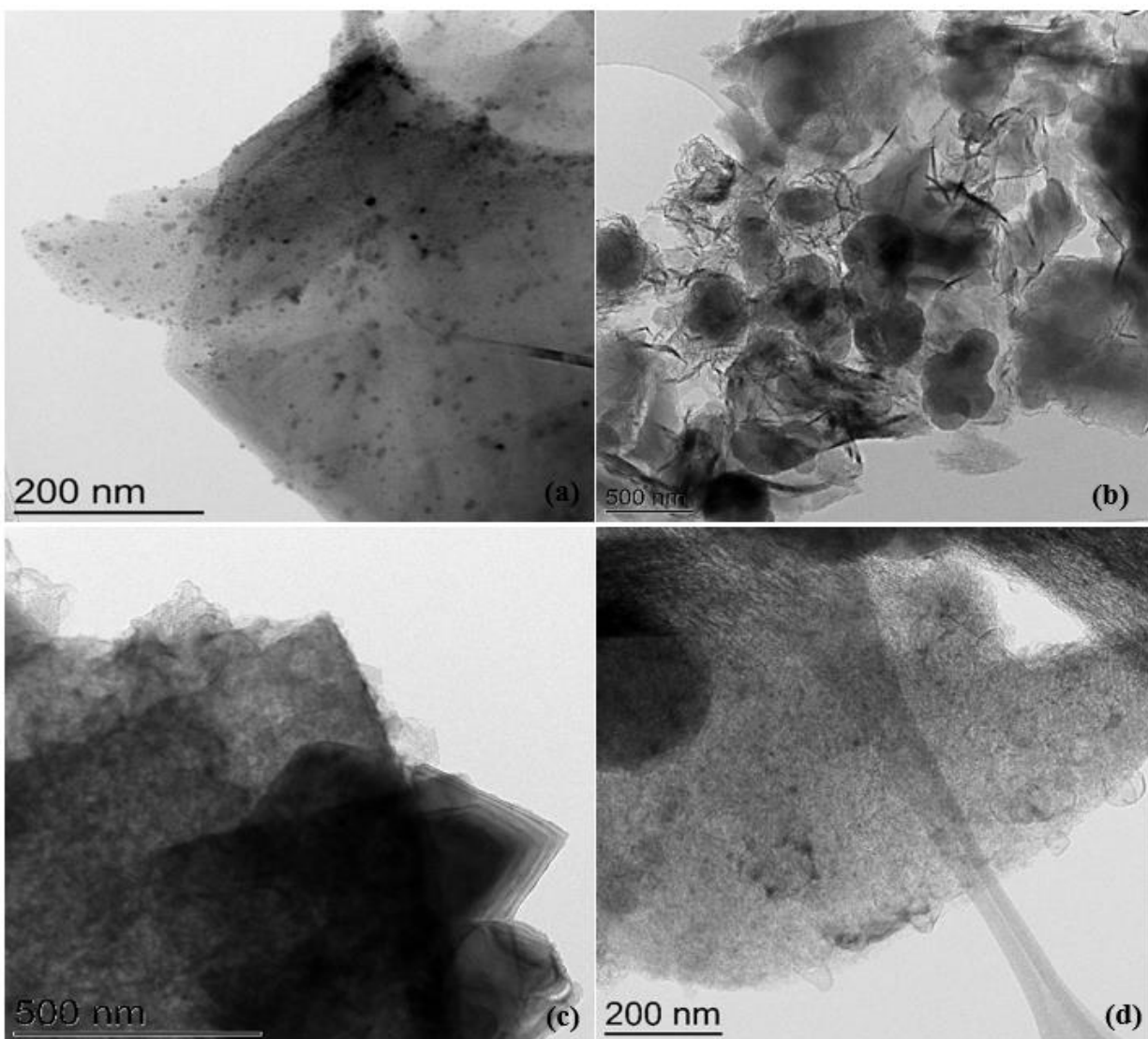


Figure 3-3: TEM Images of Al₄C₃-CDC: (a) 300-1h, (b) 500-1h (c) 700-1h and (d) 900-1h

Table 3-1: EDS Results from points taken from Figure 3-3 images

Species	Element	Weight %	Atomic %
Al₄C₃-300-1h	C	42.41	64.84
	O	8.06	9.26
	Al	16.4	11.16
	Cl	22.53	11.67
	Cu	10.58	3.05
Al₄C₃-700-1h	C	22.11	45.72
	O	13.5	20.95
	Al	14.95	13.76
	Cl	0.76	0.53
	Cu	48.66	19.01
Al₄C₃-900-1h	C	87.07	95.48
	O	2.46	2.02
	Al	0.22	0.11
	Cl	1.52	0.56
	Cu	8.7	1.8

Clusters on the surface of materials etched at 500 and 700 °C for 1h were observed in SEM. Figure 3-4 shows that there are aluminum based (Table 2) aggregates that appear on the sample surface attached to carbon artifacts emerging from the bulk. These particles are approximately 100 nm in diameter. These clusters may be forming when aluminum chloride species extracted during chlorination pass the surface and utilize the protruding carbon artifacts as nucleation centers allowing them to remain at certain etching temperatures. This evidence along with dangling particles seen in Figure 3-3 demonstrates that there are accessible particles on the surface of the partially etched Al₄C₃-CDC

samples. In theory these surface particles can be accessed and tuned for further applications of adsorption, catalysis, and altering electrical properties of the Al_4C_3 -CDC.

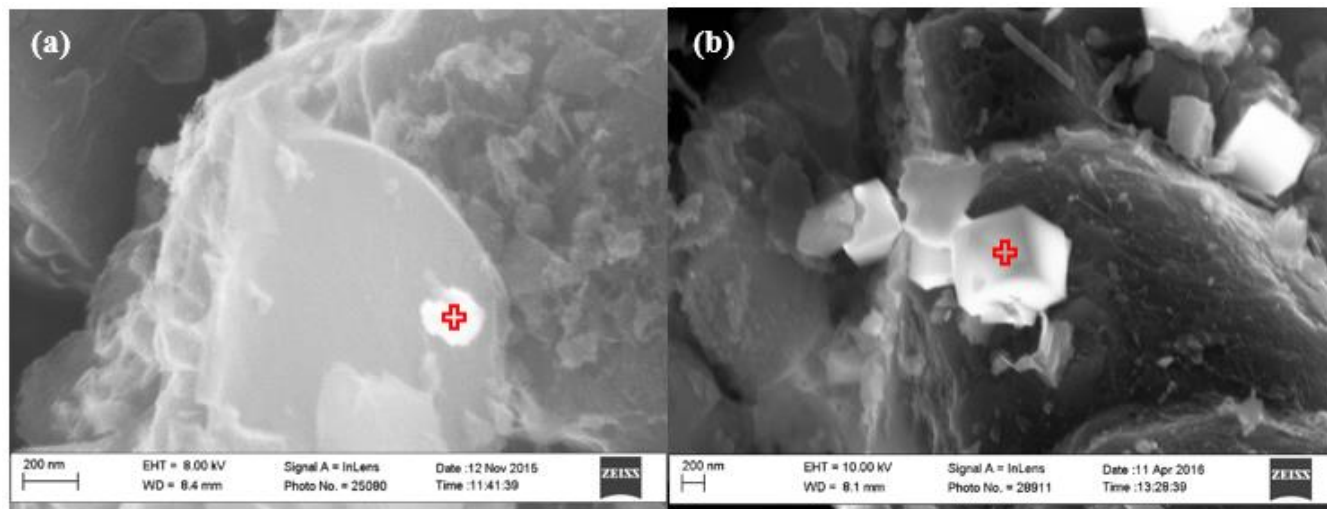


Figure 3-4: SEM Images of (a) 500 °C, and (b) 700 °C (✚) EDS analysis location

Table 3-2: EDS on clustered material seen on Al_4C_3 -CDC-500-1h

Species	Element	Weight %	Atomic %
Al_4C_3 -500-1h	C	41.33	53.94
	O	31.59	30.95
	Al	22.60	13.13
	Cl	4.48	1.98
Al_4C_3 -700-1h	C	32.36	45.82
	O	26.68	28.36
	Al	40.95	25.81

3.3.3 ^{27}Al MAS NMR of the residual aluminum content

^{27}Al solid-state NMR can monitor the chemical identity of species present after etching at various temperatures. As a quadrupolar nucleus, with nuclear spin quantum number $I = 5/2$, the local site symmetry can be observed in many instances in the lineshape for a specific quadrupolar broadened ^{27}Al resonance, depending on the local chemical environment. In fact, such lineshapes are seen in the structure of the Al_4C_3 starting material, published previously, which consists of two quadrupolar resonances corresponding to the two 4-coordinate aluminum sites in the crystal structure, both with quadrupolar asymmetry values (η_Q) of 0.0 and quadrupolar coupling (C_Q) values of 15.58 and 15.83 MHz (data not shown).⁴⁸

The ^{27}Al solid-state magic-angle spinning (MAS) NMR of the etched Al_4C_3 -CDC samples reveals significant chemical changes as the reaction proceeds, both as a function of temperature and etching time, shown in Figure 3-5 with NMR parameters given in Table 3-3. The spectrum of the Al_4C_3 -CDC sample etched at 300 °C for 1 hour (Figure 3-5a) has a quadrupolar lineshape (“Q MAS $\frac{1}{2}$ ”) centered at approximately 57 ppm that appears similar to that of the Al_4C_3 “parent” compound, and is flanked by a resonance (at low frequency) at a chemical shift with a peak near 7.6 ppm consistent with a 6-coordinate aluminum site. This 6-coordinate site has been fit to a lineshape with a Czjzek distribution, arising from a distribution of quadrupolar environments, commonly observed for amorphous aluminum oxide.⁴⁹⁻⁵¹

Table 3-3: ^{27}Al NMR parameters of Al_4C_3 -CDCs spectra. All values correspond to lineshapes modeled in Dmfit[38]. Dmfit can accommodate different lineshape models: Gaussian is the conventional lineshape, Czjzek is a distribution of quadrupolar environments, Q MAS $\frac{1}{2}$ refers to a model of the central transition only with “infinite spinning speed” assumed, Quad 1st is a model of a 1st-order quadrupolar MAS spinning sideband pattern.

Sample	Fit	δ_{iso} Isotropic Chemical Shift (ppm)	C_Q (MHz)	η_Q
300 °C-1hr	Czjzek	7.6	7.7	-
	Gaussian	94.4	-	-
	Gaussian	100.6	-	-
	“Q MAS $\frac{1}{2}$ ”	(centered ~57ppm)	14.5	0.0
500 °C-1hr	Czjzek	-0.9	3.1	-
	“Q MAS $\frac{1}{2}$ ”	74.6	10.5	0.0
500 °C-6hr	Czjzek	-1.9	1.9	-
	Gaussian	1.2	-	-
700 °C-1hr	Gaussian	-2.7	-	-
	“Quad 1 st ”	14.2	2.38	0.0

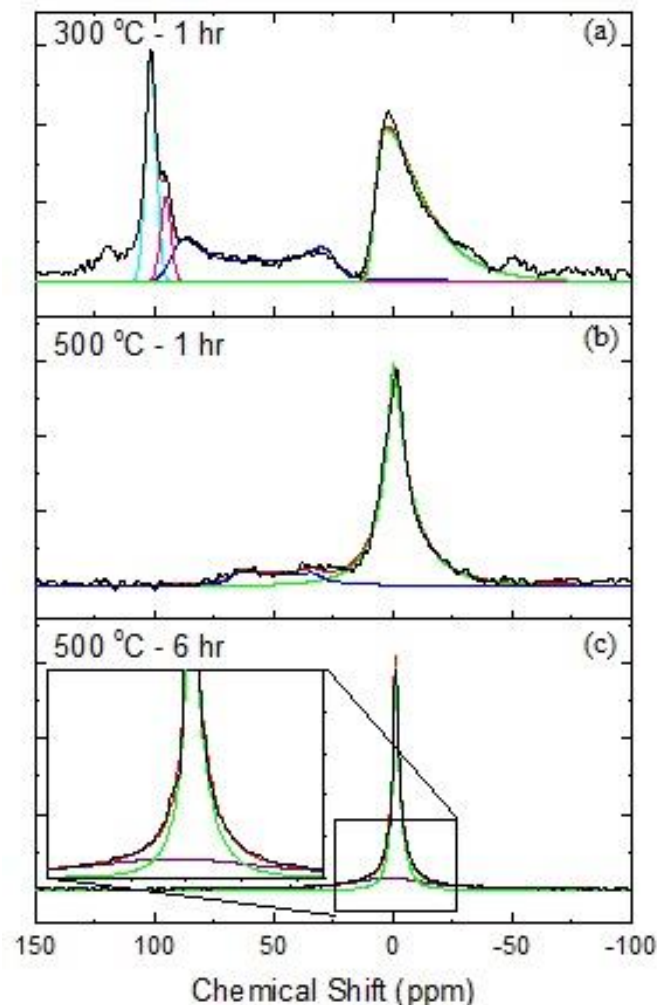


Figure 3-5: ^{27}Al MAS NMR data of $\text{Al}_4\text{C}_3\text{-CDC}$: a) 300 °C for 1 hr, b) 500 °C for 1 hr, and c) 500 °C for 6 hrs.

A separate HMQC experiment (Figure 3-6) demonstrates that this 6-coordinate site is closely coupled to protons, which allows us to assign this resonance to $\text{Al}(\text{OH})_3$. On the high frequency side of the “Q MAS $\frac{1}{2}$ ” lineshape, there are two sharp resonances in a region where 4-coordinate aluminum is typically found. These solid-state resonances are both narrow (FWHM ~ 800 Hz), and the chemical shifts at 94.4 and 100.6 ppm are consistent with different $\text{AlCl}_x(\text{OH})_y$ species, that resonate at 103 to 94 ppm.⁵², or potentially with that of Al_2Cl_6 (a “dimer” of AlCl_3). (The dimer is known to be a gaseous

or molten species, that is consistent with a narrow linewidth for these 4-coordinate sites but would not be expected to persist in a solid-state experiment, at ambient conditions, as seen here.) However, these results suggest the amorphous and porous carbon host may allow for Al_2Cl_6 to reside in the pores. The spectrum of the sample prepared at 500 °C for 1 hour of etching (Figure 3-5b) looks remarkably different from that of the 300 °C sample. It has a small residual quadrupolar-broadened lineshape (Q MAS $\frac{1}{2}$) centered at in the middle region of the spectrum (shown fit to a quadrupolar-broadened resonance, with $\eta_Q = 0.0$ and $C_Q = 10.5$ MHz), presumably sites similar to that of the remaining parent Al_4C_3 . A resonance for a 6-coordinate aluminum is present, peaked at -0.9 ppm and with a Czjzek distribution. Comparison to the 500 °C 6-hour etched sample, shows the disappearance of the resonance from the parent material, and only a more symmetric pair of resonances is found—a sharp resonance (with a relatively narrow Czjzek distribution) at -1.9ppm superimposed on a broad resonance centered at 1.2ppm. It is difficult to assign these specifically, as the porous carbon host is increasingly paramagnetic, however the sharp resonance at -1.9ppm is consistent with similar spectra of $\text{Al}(\text{H}_2\text{O})_6^{3+}$, which is formed with air exposure of the samples prior to measurement.

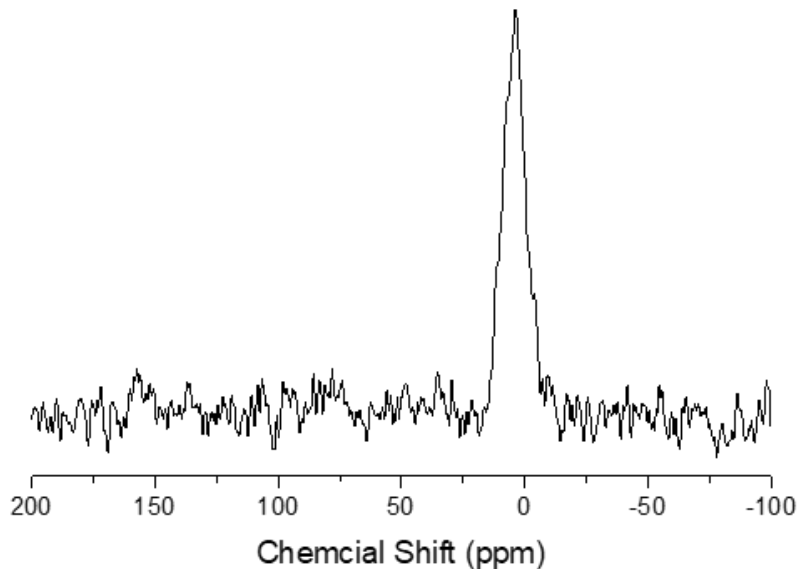


Figure 3-6: ^{27}Al MAS NMR data of $\text{Al}_4\text{C}_3\text{-CDC-300-1h}$ using a double resonance HMQC sequence. The only peak that has nearby hydrogens is the peak around 0 ppm.

Finally, in Figure 3-7 is a ^{27}Al MAS NMR spectrum of the Al-CDC materials etched at 700 °C. For the two 6-coordinate resonances observed, the one at 14.2 ppm has a large manifold of spinning sidebands, which we assign to $\alpha\text{-Al}_2\text{O}_3$.⁵³ Such a manifold of sidebands maps out the lineshape, which is consistent with a crystallographically well-defined state. Fitting of the spectrum in Figure 3-7 was done in Dmfit and is consistent with parameters previously determined for $\alpha\text{-Al}_2\text{O}_3$.^{50, 54} PXRD indicates the presence of $\alpha\text{-Al}_2\text{O}_3$, which we confirm by NMR, but there is also a small amount of residual amorphous aluminum oxide in the 700 °C sample, evidenced by the peak at -2.7 ppm (that does not possess enough long-range order to give PXRD reflections). We cannot exclude other $\text{AlCl}_x(\text{OH})_y$ or AlCl_xO_y species from some of the unassigned peaks in Figure 3-5 and Figure 3-7. For example, previous literature has assigned 4-coordinate resonances of $[\text{AlCl}_4]^-$ through $[\text{Al}(\text{OH})_4]^-$ in the chemical shift range of 103 to 79 ppm, respectively.⁵²

Further model compounds would be needed to assign such resonances with certainty in the Al_4C_3 -CDC system.

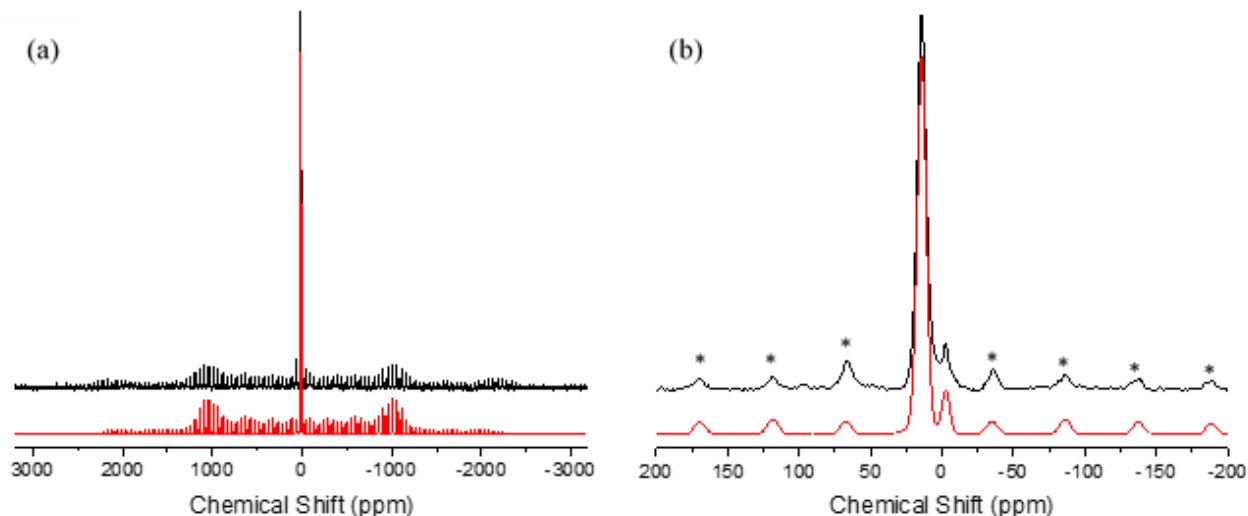


Figure 3-7: ^{27}Al MAS NMR on Al_4C_3 -CDC-700 spinning at 8 kHz (shown in black) including a fit (shown in red) utilizing previous parameters determined for $\alpha\text{-Al}_2\text{O}_3$, $C_Q = 2.38$ MHz and $\eta_Q = 0.0$. On a smaller scale (b) we can see the hydrogen-bearing aluminum peak, at -2.7 ppm, has almost been completely removed and the emergence of a new peak centered at 14.2 ppm, which corresponds to $\alpha\text{-Al}_2\text{O}_3$. * refers to spinning sidebands.

Finally, the ^{13}C spectra are wholly uninformative across this series, largely because the carbon rapidly develops paramagnetic centers with etching. It is worthwhile to note that spinning the samples at etching temperatures of 500 °C and higher was difficult, owing to the carbon becoming conductive (see section 3.5) and causing resistance to MAS from the paramagnetic sites creating “drag” or impedance to spinning in a magnetic field.

3.3.4 XPS surface analysis of samples etched at 300 and 500 °C for 1h

XPS was utilized to examine the environment of aluminum and chlorine on the surface of Al_4C_3 -CDC-300-1h and Al_4C_3 -CDC-500-1h samples. The Al_4C_3 precursor showed an $\text{Al}2p$ peak at 73.34 eV which has been assigned to the carbide in literature ⁵⁵.

As expected, samples that were etched in this investigation no longer expressed a peak at 73.34 eV, indicating aluminum content on the surface was not in its original carbide form after etching. High resolution aluminum scans reveal aluminum in two different environments, at binding energies of 74.82 and 76.58 eV on the surface of Al₄C₃-CDC-300-1h as visualized in Figure 3-8. The Al2p peak at 74.82 eV was assigned to Al(OH)₃ which agrees with NMR data, and the peak at 76.58 eV was attributed to AlCl₃ and Al-O matrix with chlorine incorporated in its structure. These assignments are supported by the Cl2p doublet at 198.48 eV seen in the high resolution chlorine spectra and O1s peaks at 531.82 in the high resolution oxygen spectra assigned to chlorine incorporated into an Al-O matrix and Al(OH)₃ respectively.⁵⁶⁻⁵⁸ Notably the Cl2p peak is represented as a 2p_{3/2} - 2p_{1/2} spin pair doublet. Recent work has shown the doublet at 198.48 and 199.98 eV is representative of surface and bulk chlorine incorporated into the Al-O matrix.^{56, 59} At a higher binding energy, the chlorine scans show chlorine chemisorbed to sp² and sp³ carbon with a Cl2p peak at 200.21 eV, with the doublet accounting for 62% of residual chlorine on the surface of Al₄C₃-CDC-300-1h.⁶⁰ This result is expected, with a majority of elemental chlorine removed when the material is put under high vacuum. A fractional amount of elemental chlorine is observed to be trapped near the surface of the sample at a binding energy of 202.68 eV.⁶⁰⁻⁶¹ Along with the oxygen incorporated into the Al-O matrix, the O1s spectra also demonstrates oxygen functional groups bound to carbon at binding energies of 532.41 and 533.25 eV representing carbonyl, hydroxyl and ether groups.⁶² Al₄C₃-CDC-500-1h displays a more uniform aluminum content on the surface centered around 74.38 eV assigned to Al(OH)₃ and Al₂O₃ with a small shoulder at a higher binding energy assigned to chlorine in the Al-O matrix supported by the Cl2p peak at 198.1 eV.

Residual chlorine content for $\text{Al}_4\text{C}_3\text{-CDC-500-1h}$ was similar to that of $\text{Al}_4\text{C}_3\text{-CDC-300-1h}$ samples with the majority of the species chemisorbed to carbon with a fraction of trapped elemental chlorine also detected (S10).

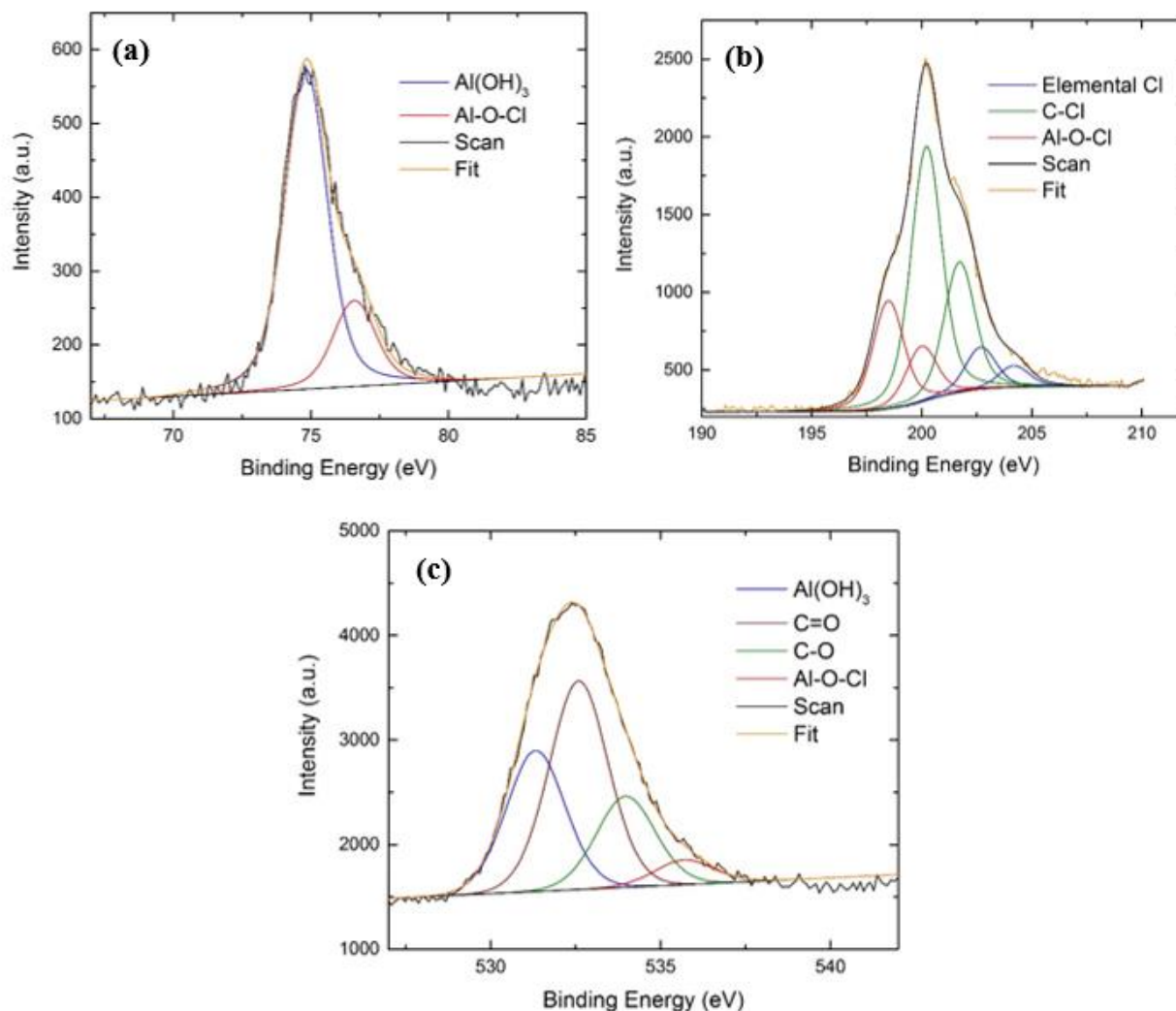


Figure 3-8: High resolution XPS spectra on $\text{Al}_4\text{C}_3\text{-CDC-300-1h}$ for (a) Aluminum (b) Chlorine and (c) Oxygen

3.3.5 Crystalline structure formation observed via PXRD and TEM

The etching temperature can also affect the carbon structure, ranging from disordered carbon to graphitic carbon polymorphs. PXRD patterns were obtained for the

samples prepared at various temperatures to determine the presence of structured carbon. As seen in Figure 3-9, samples etched at 300 °C and 500 °C exhibit a very small broad [002] peak at a 2θ value of 26.3° that is indicative of amorphous carbon. Also seen in Al_4C_3 -CDC-300-1h samples are peaks related to the carbide that was not exposed to chlorine during the chlorination. In contrast, the samples etched at 700 and 900 °C both show a sharp [002] peak at 26.3° and [100] peak at 43° representing parallel stacking of graphitic planes which both suggest highly ordered carbon structures.⁶³ The PXRD patterns also show no aluminum based crystalline species other than the original carbide for all temperatures, except for Al_4C_3 -CDC-700-1h samples. Seen in the PXRD pattern for the 700 °C samples are reflections with 2θ values of (26), (35.2), (37.7), (43), (52.5), (57.46) corresponding to $\alpha\text{-Al}_2\text{O}_3$.⁶⁴⁻⁶⁵ Samples etched for 0.25h and 2h at 700 °C also display $\alpha\text{-Al}_2\text{O}_3$ peaks. The presence of this oxide has been seen in prior work at the reaction temperature of 700 °C with aluminum chloride in the presence of oxygen and chlorine gas as a catalyst, but was found to be a polymorph of the thermodynamically stable phase, $\kappa\text{-Al}_2\text{O}_3$.^{ENREF_4_30}²⁹ The observed $\alpha\text{-Al}_2\text{O}_3$ has been shown to be repeatable with multiple runs at the same conditions. It is currently unknown as to why $\alpha\text{-Al}_2\text{O}_3$ only forms in the temperature window between 500 and 900 °C. It is speculated that for lower etching temperatures there is not adequate energy in the system for the formation of the oxide, and at the higher temperature of 900 °C any source of oxygen is more thermodynamically favorable in the gas phase and will not allow for a surface-based deposition process similar to that of atomic layer deposition of Al_2O_3 .⁶⁶⁻⁶⁷

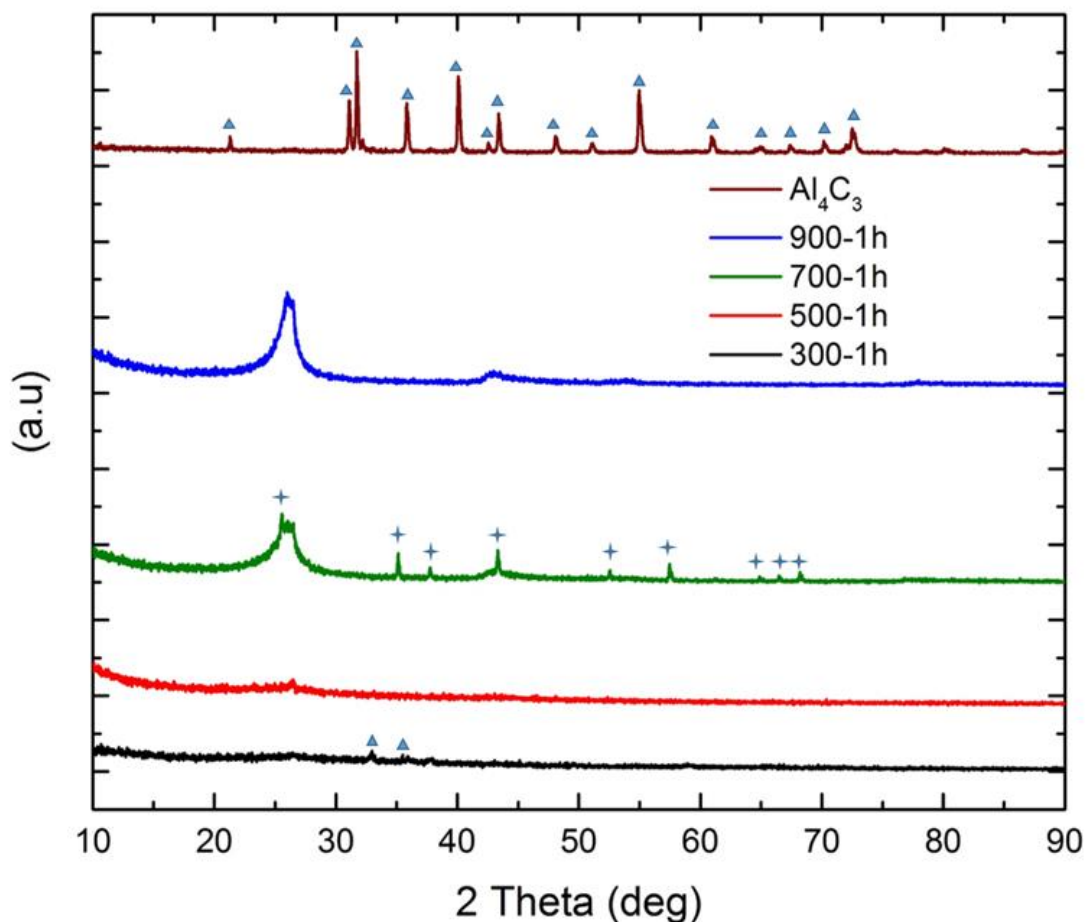


Figure 3-9: PXRD patterns of Al_4C_3 and samples etched at 300, 500, 700 and 900 °C for 1 hr. ★ = $\alpha\text{-Al}_2\text{O}_3$ ▲ = Al_4C_3

TEM/HRTEM images were taken of the samples to observe and further understand the types of carbon structures forming at different reaction conditions. At low etching temperatures, 300 °C and 500 °C, mainly amorphous carbon is seen. In select areas for $\text{Al}_4\text{C}_3\text{-CDC-500-1h}$ graphitic ribbons begin to form, as visualized in Figure 3-10b. Once the temperature reaches 700 °C graphitic structures, such as turbostratic carbon, carbon nanostructures, carbonaceous microspheres and graphene are observed. The carbon structures observed follow the trends seen in PXRD patterns, which suggest the formation of more ordered carbon structures at increased etching temperatures. The increase in the

ordering of carbon is supported by Raman (S15) with increased graphitic characteristics as etching temperature rises. The formation of these graphitic structures has also been detailed in previous studies that have evaluated the complete etching of Al_4C_3 at various temperatures.^{38-39, 42}

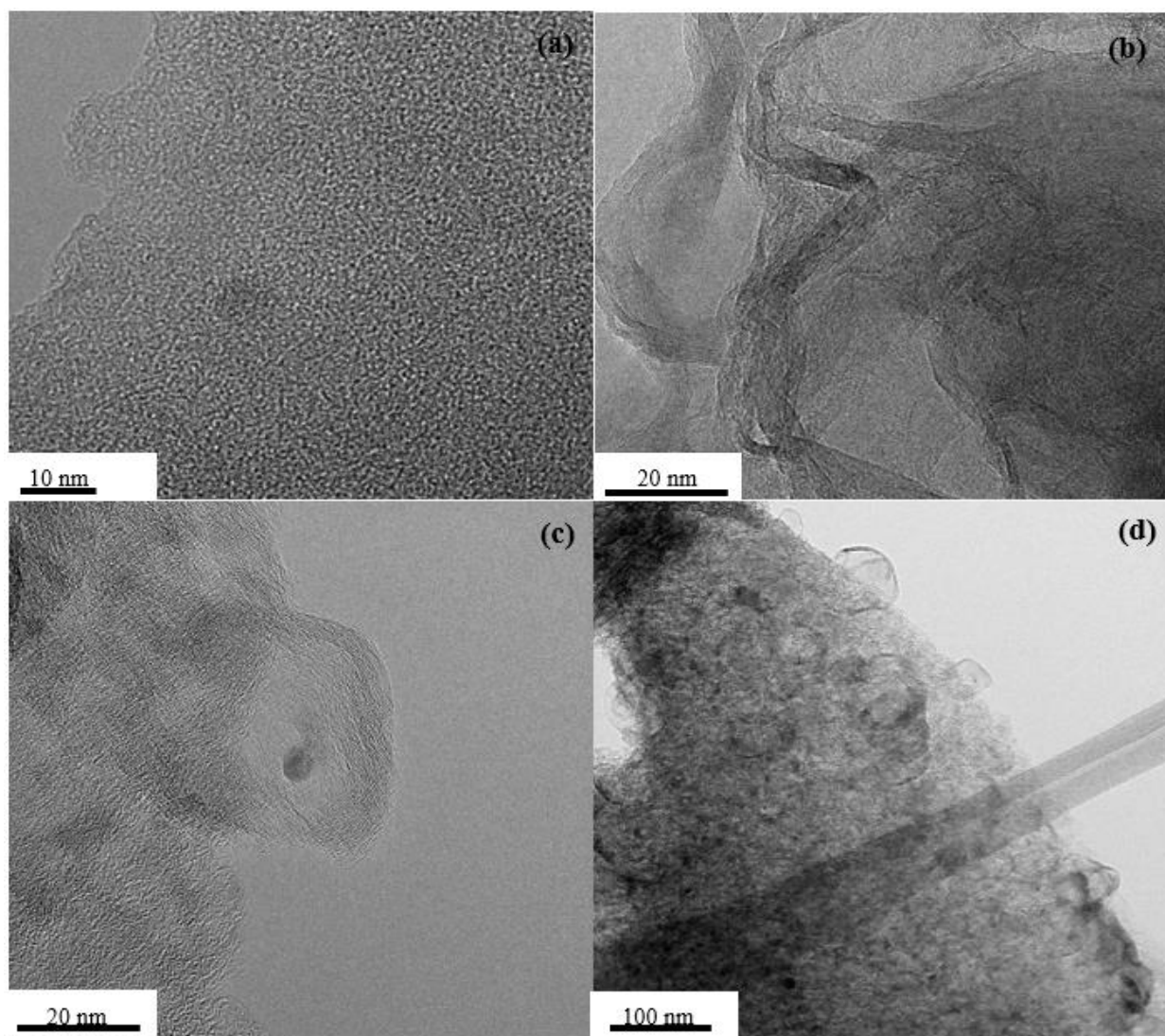


Figure 3-10: TEM images of Al_4C_3 -CDC prepared by etching: (a) 300-1h scale bar 10 nm, (b) 500-1h, (c) 700-1h, and (d) 900-1h

3.3.6 Dependence of Al_4C_3 -CDC Porosity and Surface Area on Reaction Temperature and Time

After chlorination, the Al_4C_3 -CDC samples were analyzed via nitrogen physisorption at 77K, QSDFT was used to determine the resulting effects that time and temperature had on pore size distribution and surface area. Table 3 reports the surface area and pore volume as it changes with sample preparation temperature. An increase in surface area can be seen with the increase in etching temperature from 300 to 500 °C, which can be attributed to less residual aluminum present while maintaining a primarily amorphous carbon material. At increased etching temperatures, the effects of carbon rearrangement come into play. As the etching temperature increases, carbon structure formation increases in the samples. The smaller micropores break down and become part of larger mesopores, Table 4 visualizes this trend with a decrease in microporous volume and increase in mesoporous volume as etching temperature increases. Also seen in Table 3-4, the drastic reduction in micropore volume is accompanied by a reduction in surface area. At higher etching temperatures, structures such as graphite are produced, as seen in previous work, which also results in the reduction of surface area.⁴² These trends have also been observed for materials etched at increasing times while keeping temperature constant at either 300 or 500 °C as depicted in Figure 3-11.

Table 3-4: Temperature trial runs corresponding BET surface area (S_{bet}) and pore volume (V_p) calculated using QSDFT

Sample	S_{bet} ($\text{m}^2 \text{g}^{-1}$)	V_p ($\text{cm}^3 \text{g}^{-1}$)	$V_{\text{Micropores}}$ ($\text{cm}^3 \text{g}^{-1}$)	$V_{\text{Mesopores}}$ ($\text{cm}^3 \text{g}^{-1}$)
Al_4C_3 -300-1h	643	0.20	0.20	0.00
Al_4C_3 -500-1h	1126	0.53	0.40	0.13
Al_4C_3 -700-1h	597	0.66	0.09	0.57
Al_4C_3 -900-1h	690	1.25	0.07	1.18

As etching time increases, more residual aluminum is removed from the sample, and the surface area begins to increase. After 1h of etching, the rate at which aluminum is taken from the sample is decreased, as depicted earlier via TGA analysis. This slowing, coupled with more time for carbon rearrangement in the sample, leads to a leveling off of surface area and even a slight surface area reduction, as etching time is increased for samples etched at 300 and 500 °C. This reduction is due to the allotment of more time for carbon rearrangement allowing for carbon structures and mesopores to form as previously mentioned and visualized in Figure 3-13(b and c).

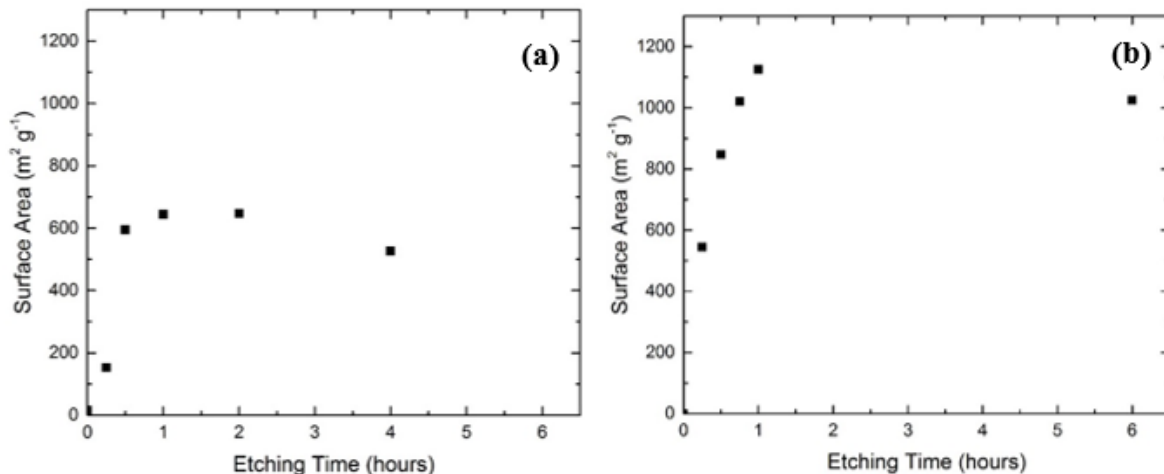


Figure 3-11: BET surface areas via N₂ adsorption for samples etched at times for (a) 300 °C and (b) 500 °C

Depending on the characteristics of the sample and the presence of hysteresis in the N₂ isotherm, different assumptions were made for the QSDFT analysis in terms of the pore geometry. The pores in samples produced at 300 °C do not show hysteresis, and pores smaller than 2 nm were assumed to be slit shaped. Pores for samples etched at 500, 700 and 900 °C for 1h, which have hysteresis and elements of both micro and mesopores, were assumed to be a mix of slit and cylindrical pores. These assumptions were heavily

influenced by the isotherms of the samples as seen in Figure A-11. Observed for Al_4C_3 -CDC-300-1h is a type I or pseudo-Langmuir isotherm where there is a sudden halt in adsorption after the knee, which is indicative of the end of micropore contribution to adsorption. Samples etched at 500 °C for 1h also exhibit a type I isotherm with a small hysteresis indicating the presence of mesopores, while 700 and 900 °C samples both exhibit type IV isotherms.⁶⁸ These samples show a large hysteresis which correlates with an appreciable amount of mesoporosity.

Following what has already been observed in the field of CDC's, Al_4C_3 -CDCs have a narrow pore-size distribution that can be affected by the etching temperature.⁹ Figure 3-12a shows that as chlorination temperature increases, the average pore size increases, and the distribution broadens. This trend can be explained by increased carbon reorganization at higher temperatures, where smaller collectives of micropores begin to form mesopores. Al_4C_3 -CDC-300-1h samples are entirely microporous with a bimodal distribution centered on 0.7 nm and 1.1 nm. This bimodal behavior can be explained due to two different types of aluminum coordination environments in the carbide precursor, which results in different Al-C bond lengths. Therefore, when the heteroatom is removed from the matrix, it will create a slightly different pore for the two types of aluminum atoms extracted.⁶⁹ Pore broadening due to carbon rearrangement may also contribute to the different pore sizes observed. It should be noted that the lower limit of nitrogen adsorption is seen at a pore size of 0.7 nm due to the limitation of pore filling and slow adsorption equilibration. Consequently, pore sizes shown at 0.7 nm for nitrogen adsorption represent pore sizes ≤ 0.7 nm. Al_4C_3 -CDC-500-1h materials display both micro and mesopores. The micropores in the sample still show a bimodal distribution

centered at slightly higher sizes of 0.9 and 1.2 nm. The mesopores being generated with carbon restructuring are distributed around 3.6 nm. Samples that have been etched at temperatures of 700 and 900 °C show a combination of micro and mesopores seen at 0.9 and 8.0 nm respectively. Figure 3-12(b and c) show that the influence of time on the etching process does not affect the pore size distribution to the degree that temperature does. It can be observed, however, with longer etching times, some carbon restructuring can occur to form slightly larger pores as observed in samples etched at 300 °C at various times.

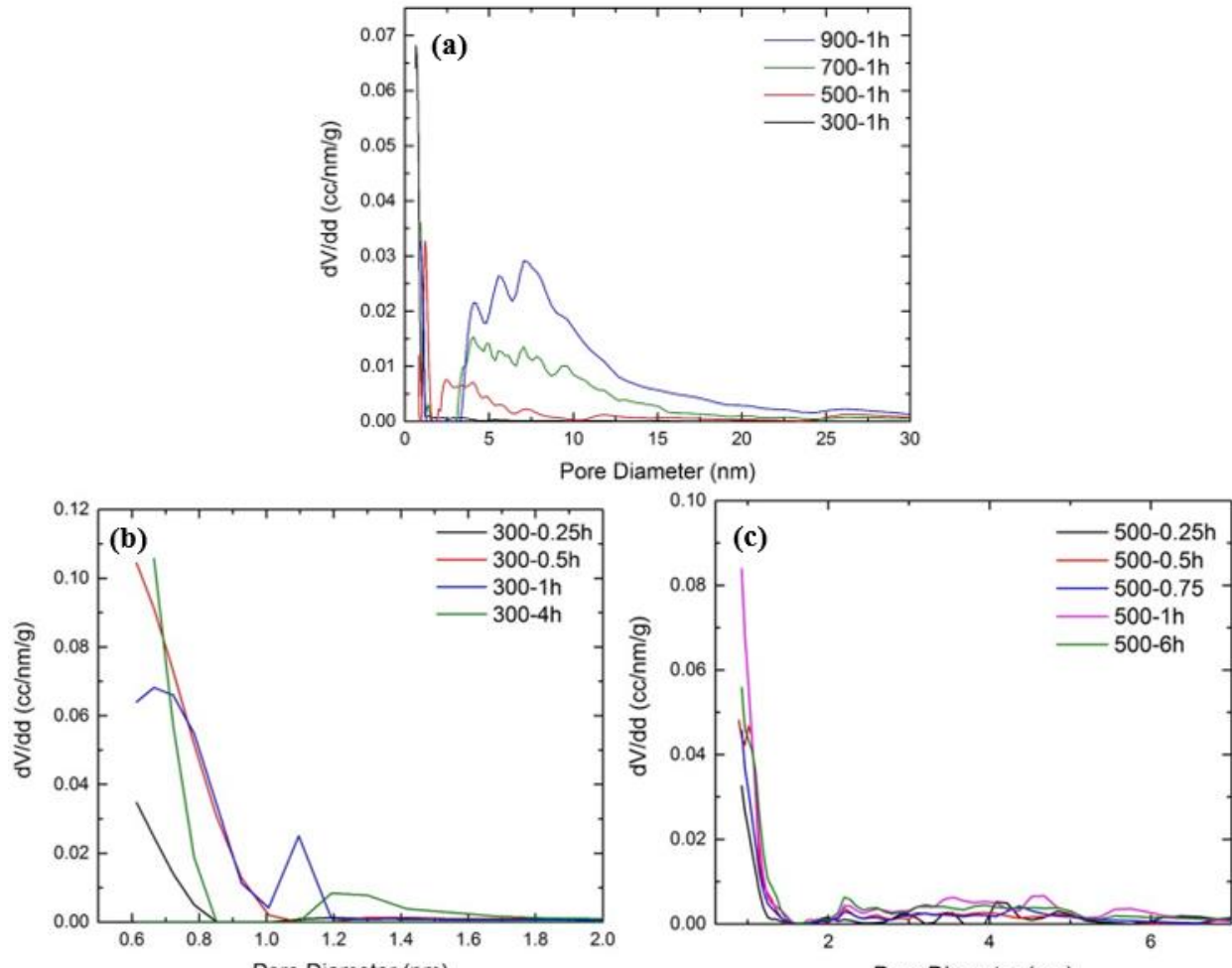


Figure 3-12: Pore size distributions for (a) Different etching temperatures (b) Different etching times at 300 °C and (c) Different etching times at 500 °C for Al_4C_3 -CDCs

3.3.7 *CO₂ and Water adsorption on Al₄C₃-CDCs*

Water adsorption and CO₂ adsorption studies were performed on the samples to probe the impact of residual aluminum species on adsorption. The water isotherm collected at 25 °C show a range of uptake from 12.5-35.0 mmol g⁻¹ as seen in Figure 3-13. The samples etched at 300-500 °C exhibit type IV isotherms and show the majority of their uptake before a relative pressure of 0.4. This region of uptake can be attributed to the mainly microporous structure of the materials.⁷⁰ After a partial pressure of 0.4, adsorption is minimal with a slight increase near 0.95 relative pressure, which can be attributed to capillary condensation. Note that an increase in pore volume from an etching temperature of 300-500 °C allows for a slightly larger adsorption saturation loading. Al₄C₃-CDC-700-1h samples also show significant uptake before relative pressures of 0.4, as well as a slight increase at higher relative pressures due to mesopores filling. The sample that significantly stands out is Al₄C₃-CDC-900-1h. This sample exhibits features of a type V isotherm with low adsorption at low partial pressures pointing towards weak gas solid affinity. The low uptake followed by a large increase can be explained by clusters of water adsorbing to the mesopores walls and reducing the pore wall radius until a critical point. At this point capillary condensation begins, and the adsorption loadings increase significantly, taking place in a region of relative pressures near 0.8 to 0.9. Also note that functional groups on the surface of the carbon material will increase the initial water uptake as they allow clusters of water to form around them before micropore filling occurs.⁷⁰ Al₄C₃-CDC materials etched for 1 hour display uptakes that correspond to a mass increase range of 23-32%, excluding materials etched at 900°C, which is significantly higher than reports of an average weight increase of 15% for other CDC materials in humid air.⁷¹ This result shows

that the type and amount of residual metal in the partially etched material affects adsorption properties. As seen in Figure 3-13b the amount of adsorbed water correlates strongly with residual metal content in the species. At low metal removal the adsorption behavior is almost identical for samples etched an hour or less, samples etched at 0.25 h are overlapped by samples etched at 0.5 h and 1 h, even though there is an increase in surface area. As etching time increases up to 2 and 4 h, the pore volume, calculated via QSDFT, in the sample increases significantly enough to allow a higher capacity for adsorption. Water stability of these samples is also of concern due to the Al_4C_3 hydrolysis reaction that produces methane.⁷² To investigate the stability of the Al_4C_3 -CDC materials PXRD and BET patterns were taken before and after water isotherms. Each sample studied displayed no reduction in surface area, pore size distribution or degradation of crystalline structures.

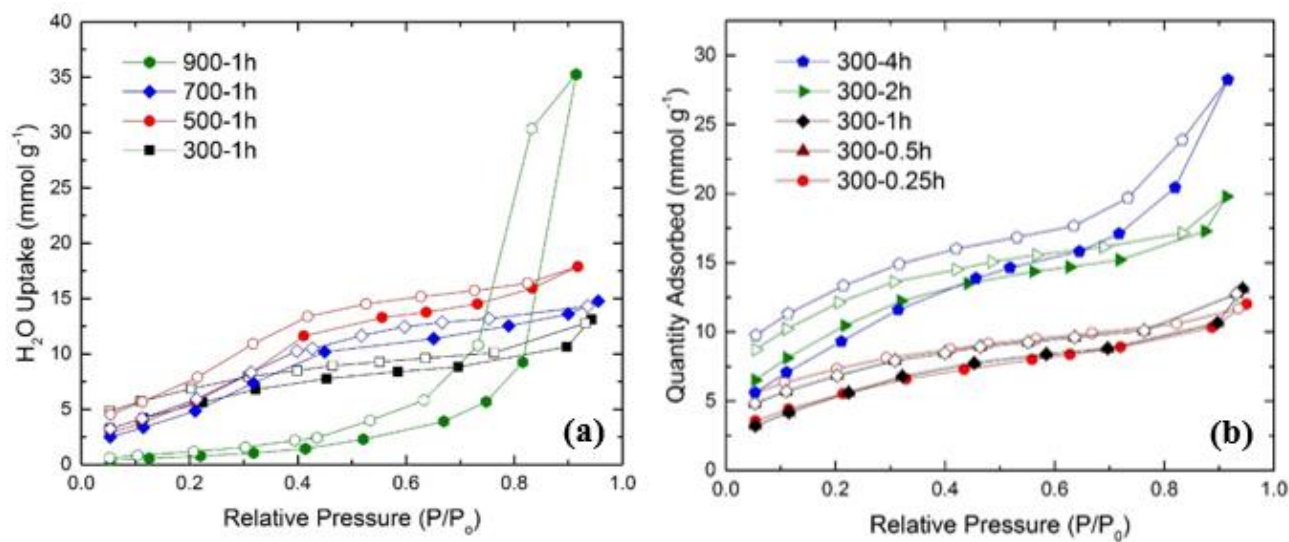


Figure 3-13: Water adsorption isotherms at 25 °C for (a) temperature trials and (b) time trials at 300 °C.

CO_2 isotherms were collected (Figure 3-14a) for the samples etched at different temperatures for 1 hour. Al_4C_3 -CDC-500-1h materials showed the highest CO_2 capture

performance from this set of samples; therefore, the 500 °C etching temperature was chosen to observe the effects that etching time will have on the materials' performance. It is important to note that none of the samples show signs of hysteresis, and sample weight before and after adsorption/desorption were the same (accuracy of 10^{-3} mg). This indicates that the adsorbed CO₂ was completely removed from the sample after desorption, lending credence to the materials' ability to be easily regenerated. The Al₄C₃-CDC samples show no deviation in uptake for 4 consecutive cycles, demonstrating stability and promising capability for repeated use. As seen in Figure 3-14a, the samples etched at 700 and 900°C for 1h show a small initial uptake in the low-pressure regions, likely due to their dominantly mesoporous structure. This same type of low relative pressure uptake is seen in ordered mesoporous carbon.⁷³ At higher pressure regions these samples show a linear increase in capacity due to mesopores being partially filled and the entire pore volume of the sample not being utilized at the recorded pressures. The Al₄C₃-CDC-300-1h samples show a high initial uptake into the micropores for pressures less than 1 bar, then drop off significantly, consistent with low pore volume at higher pressures. By increasing the etching temperature, Al₄C₃-CDC-500-1h samples show an increased capacity for CO₂ uptake for the entire 20 bar pressure range with 2.74 mmol g⁻¹ at 1 bar. CO₂ adsorption in Al₄C₃-CDC-500-1h shows improved adsorption compared to an activated carbon material, BPL, with similar carbon properties but no residual metal species. BPL has a reported BET surface area in the range of 1000-1100 m²g⁻¹ and a pore volume range of 0.49-0.7 cc g⁻¹ with a demonstrated adsorption of CO₂ around 2.1 mmol g⁻¹ at 1 bar and 25°C.⁷⁴⁻⁷⁷ Other highly activated carbon materials have shown the upper end of CO₂ adsorption onto carbon to be 2.9-4.7 mmol g⁻¹. This corresponds to 1 mmol of CO₂ adsorbed per 565-1050 m² of

carbonaceous surface at 1 bar and 25°C.⁷⁸ Al₄C₃-CDC-500-1, which receives no post-synthetic processing, demonstrates a slightly smaller adsorption compared to these highly activated materials per gram, but displays an adsorption of 1 mmol of CO₂ for every 410 m² of CDC surface, which demonstrates a higher capacity per available surface area than other highly tuned materials. This demonstrates that the interactive surface of some Al₄C₃-CDC materials is more efficient at interacting with acid gases, such as CO₂, than other highly modified carbon sorbents. The combination of micro and mesopores in Al₄C₃-CDC-500-1h allows for a high initial uptake that does not level off after micropore filling. The larger surface area leads to continuously increasing adsorption at moderate pressures after 1 bar as it continues to have its mesopores filled at higher pressures. Note that due to the samples having a variety of physical properties derived from their respective etching temperature, no straightforward correlation can be made with only residual aluminum, surface area or pore volume. The samples etched at 500°C at various times do show results that are directly correlated with surface area and pore volume. Since the pore size distribution does not deviate drastically at various etching times, the initial uptake in the micropores is almost identical for all time samples except those etched for 0.25 h. The reduced adsorption in samples etched for 0.25 h is most likely due to high residual metal content in the sample, in which PXRD shows evidence of unreacted carbide, leading to Al₄C₃-CDC-500-0.25h having the lowest pore volume and capacity. At different etching times, both the pore volume and surface area of the samples show a linear relationship with the materials' CO₂ uptake at 1bar and 25°C.

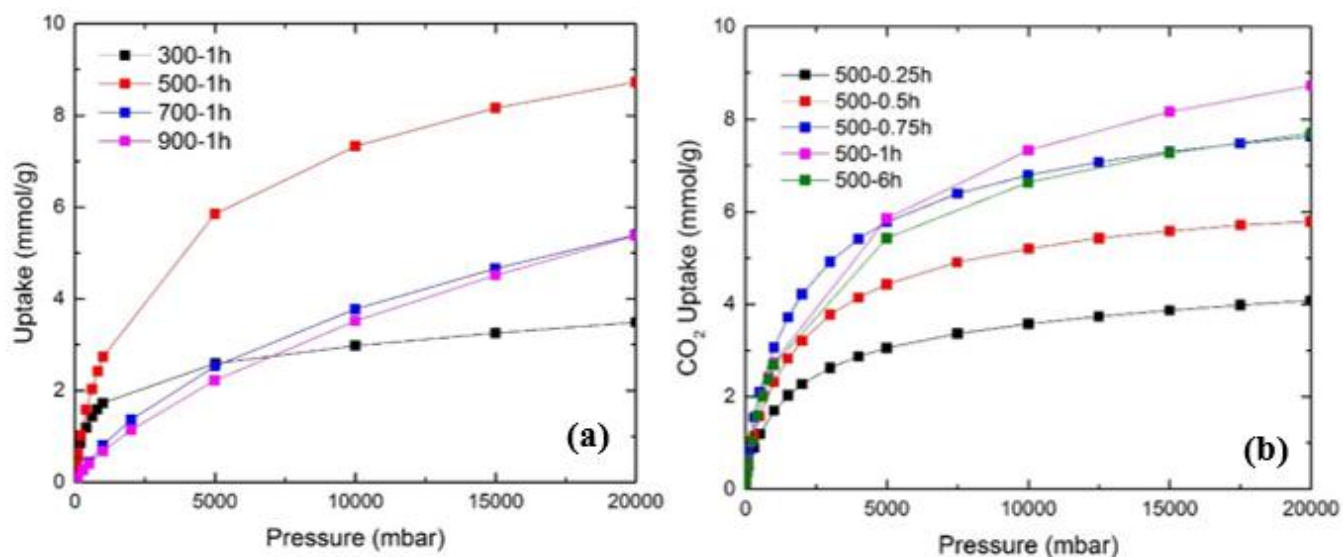


Figure 3-14: CO₂ adsorption isotherms at 25 °C for Al₄C₃-CDC samples etched at (a) different temperatures 300 – 900 °C, for 1 hour and (b) at 500°C for various times (0.25 – 6 hours).

3.4 Conclusions

After reaction of the aluminum heteroatoms from Al₄C₃ via chlorination at different temperatures and times, the physical properties of the materials were examined. The residual aluminum content of the Al₄C₃-CDC material decreases in a repeatable trend as both time and temperature increase. By varying etching temperature from 300-900°C, a range of surface areas were generated with the maximum being (1126 m² g⁻¹) when the carbide was etched at 500°C for 1h. Etching temperature enables the pore size distribution to be tuned from a material entirely microporous in Al₄C₃-CDC-300-1h, to mainly mesoporous samples at higher etching temperatures. This demonstrates the ability of Al₄C₃-CDCs to be versatile in terms of tunable pore size for a desired application. Also seen during partial etching were aluminum-based nanoparticles as well as aluminum-based clusters on the surface of certain Al₄C₃-CDC samples. These particles have been observed

to be present in larger quantities at lower etching temperatures with few observed at elevated temperatures up to 900°C. The crystalline form of the residual metal is observed to change at an elevated etching temperature of 700°C, from aluminum-based nanoparticles to crystalline α -Al₂O₃. EDS, PXRD, XPS and NMR results indicated that the form of the aluminum at etching temperatures of 300 and 500°C have a strong potential to be an amorphous composition of Al₂O₃, AlCl₃, Al(OH)₃ and BAC. Carbon structures were also observed in the samples with an increasing presence at higher temperatures, these structures varied from carbonaceous microspheres to graphene sheets. Adsorption properties were also investigated with respect to water and CO₂. Water adsorption shows a dependence on residual metal content as well as the presence of carbon structures. BET surface area and PXRD patterns after exposure have shown that the samples are stable in water vapor with no recorded loss of surface area, pore size distribution and crystal structure. CO₂ adsorption demonstrates a strong dependence on etching temperature and time. Holding etching time at 1h and increasing the temperature drastically effects the CO₂ adsorption properties. This can be attributed to changes in surface area, pore size, carbon structures, and residual aluminum content. Materials etched at 300 and 500°C show high adsorption capacity at low pressures with adsorption at 1 bar and 25°C reaching as high as 2.74 mmol g⁻¹ for Al₄C₃-500-1h, which is superior to BPL adsorption capacity, an activated carbon with comparable properties, and shows a more efficient use of surface area than highly activated carbon materials. Materials etching at 700 and 900°C show a linear increase in CO₂ adsorption throughout the pressures investigated with their pore volumes not seeing a saturation point up to 20 bar. This investigation has demonstrated that an effective one pot synthesis can be used on the Al₄C₃ precursor to generate a porous-carbon

material with aluminum-based nanoparticles that show promise for adsorption-based applications.

3.5 References

1. Saha, D.; Bao, Z.; Jia, F.; Deng, S., Adsorption of CO₂, CH₄, N₂O, and N₂ on MOF-5, MOF-177, and Zeolite 5A. *Environmental Science & Technology* **2010**, *44* (5), 1820-1826.
2. Newcombe, G.; Drikas, M.; Hayes, R., Influence of characterised natural organic material on activated carbon adsorption: II. Effect on pore volume distribution and adsorption of 2-methylisoborneol. *Water Research* **1997**, *31* (5), 1065-1073.
3. Eisenbach, D.; Gallei, E., Infrared spectroscopic investigations relating to coke formation on zeolites. *Journal of Catalysis* **1979**, *56* (3), 377-389.
4. Sevilla, M.; Fuertes, A. B., Sustainable porous carbons with a superior performance for CO₂ capture. *Energy & Environmental Science* **2011**, *4* (5), 1765-1771.
5. Kyotani, T., Control of pore structure in carbon. *Carbon* **2000**, *38* (2), 269-286.
6. Becker, P.; Glenk, F.; Kormann, M.; Popovska, N.; Etzold, B. J. M., Chlorination of titanium carbide for the processing of nanoporous carbon: A kinetic study. *Chemical Engineering Journal* **2010**, *159* (1-3), 236-241.
7. Gogotsi, Y. G.; Kofstad, P.; Yoshimura, M.; Nickel, K. G., Formation of sp³-bonded carbon upon hydrothermal treatment of SiC. *Diamond and Related Materials* **1996**, *5* (2), 151-162.
8. Yushin, G.; Hoffman, E. N.; Barsoum, M. W.; Gogotsi, Y.; Howell, C. A.; Sandeman, S. R.; Phillips, G. J.; Lloyd, A. W.; Mikhalevsky, S. V., Mesoporous carbide-derived carbon with porosity tuned for efficient adsorption of cytokines. *Biomaterials* **2006**, *27* (34), 5755-5762.
9. Osswald, S.; Portet, C.; Gogotsi, Y.; Laudisio, G.; Singer, J. P.; Fischer, J. E.; Sokolov, V. V.; Kukushkina, J. A.; Kravchik, A. E., Porosity control in nanoporous carbide-derived carbon by oxidation in air and carbon dioxide. *Journal of Solid State Chemistry* **2009**, *182* (7), 1733-1741.
10. Simon, P.; Gogotsi, Y., Materials for electrochemical capacitors. *Nat Mater* **2008**, *7* (11), 845-854.
11. Laheäär, A.; Jänes, A.; Lust, E., Electrochemical properties of carbide-derived carbon electrodes in non-aqueous electrolytes based on different Li-salts. *Electrochimica Acta* **2011**, *56* (25), 9048-9055.

12. Gogotsi, Y.; Nikitin, A.; Haihui, Y.; Wei, Z.; Fischer, J. E.; Bo, Y.; Foley, H. C.; Barsoum, M. W., Nanoporous carbide-derived carbon with tunable pore size. *Nature Materials* **2003**, 2 (9), 591-594.
13. Presser, V.; Heon, M.; Gogotsi, Y., Carbide-Derived Carbons – From Porous Networks to Nanotubes and Graphene. *Advanced Functional Materials* **2011**, 21 (5), 810-833.
14. Mangarella, M. C.; Ewbank, J. L.; Dutzer, M. R.; Alamgir, F. M.; Walton, K. S., Synthesis of embedded iron nanoparticles in Fe₃C-derived carbons. *Carbon* **2014**, 79, 74-84.
15. Mangarella, M. C.; Walton, K. S., Tailored Fe₃C-derived carbons with embedded Fe nanoparticles for ammonia adsorption. *Carbon* **2015**, 95, 208-219.
16. Borchardt, L.; Hasché, F.; Lohe, M. R.; Oschatz, M.; Schmidt, F.; Kockrick, E.; Ziegler, C.; Lescouet, T.; Bachmatiuk, A.; Büchner, B.; Farrusseng, D.; Strasser, P.; Kaskel, S., Transition metal loaded silicon carbide-derived carbons with enhanced catalytic properties. *Carbon* **2012**, 50 (5), 1861-1870.
17. Petit, C.; Karwacki, C.; Peterson, G.; Bandosz, T. J., Interactions of Ammonia with the Surface of Microporous Carbon Impregnated with Transition Metal Chlorides. *The Journal of Physical Chemistry C* **2007**, 111 (34), 12705-12714.
18. Molina-Sabio, M.; Pérez, V.; Rodríguez-Reinoso, F., Impregnation of activated carbon with chromium and copper salts: Effect of porosity and metal content. *Carbon* **1994**, 32 (7), 1259-1265.
19. Li, H.; Zhu, L.; Wang, J.; Li, L.; Shih, K., Development of Nano-Sulfide Sorbent for Efficient Removal of Elemental Mercury from Coal Combustion Fuel Gas. *Environmental Science & Technology* **2016**, 50 (17), 9551-9557.
20. Liu, W.; Vidic, R. D.; Brown, T. D., Impact of Flue Gas Conditions on Mercury Uptake by Sulfur-Impregnated Activated Carbon. *Environmental Science & Technology* **2000**, 34 (1), 154-159.
21. Henning, K. D.; Schäfer, S., Impregnated activated carbon for environmental protection. *Gas Separation & Purification* **1993**, 7 (4), 235-240.
22. Liu, W.; Vidić, R. D.; Brown, T. D., Optimization of Sulfur Impregnation Protocol for Fixed-Bed Application of Activated Carbon-Based Sorbents for Gas-Phase Mercury Removal. *Environmental Science & Technology* **1998**, 32 (4), 531-538.
23. Bhatnagar, A.; Hogland, W.; Marques, M.; Sillanpää, M., An overview of the modification methods of activated carbon for its water treatment applications. *Chemical Engineering Journal* **2013**, 219, 499-511.

24. Jiang, S. P., A review of wet impregnation—An alternative method for the fabrication of high performance and nano-structured electrodes of solid oxide fuel cells. *Materials Science and Engineering: A* **2006**, *418* (1–2), 199-210.
25. Atkinson, J. D.; Fortunato, M. E.; Dastgheib, S. A.; Rostam-Abadi, M.; Rood, M. J.; Suslick, K. S., Synthesis and characterization of iron-impregnated porous carbon spheres prepared by ultrasonic spray pyrolysis. *Carbon* **2011**, *49* (2), 587-598.
26. Aarset, K.; Shen, Q.; Thomassen, H.; Richardson, A. D.; Hedberg, K., Molecular Structure of the Aluminum Halides, Al_2Cl_6 , AlCl_3 , Al_2Br_6 , AlBr_3 , and AlI_3 , Obtained by Gas-Phase Electron-Diffraction and ab Initio Molecular Orbital Calculations. *The Journal of Physical Chemistry A* **1999**, *103* (11), 1644-1652.
27. Hartman, M.; Trnka, O.; Šolcová, O., Thermal Decomposition of Aluminum Chloride Hexahydrate. *Industrial & Engineering Chemistry Research* **2005**, *44* (17), 6591-6598.
28. Yang, Z.; Gao, B.; Wang, Y.; Wang, Q.; Yue, Q., Aluminum fractions in surface water from reservoirs by coagulation treatment with polyaluminum chloride (PAC): Influence of initial pH and $\text{OH}^-/\text{Al}^{3+}$ ratio. *Chemical Engineering Journal* **2011**, *170* (1), 107-113.
29. Bergman, L. H., Oxidation method for production of special aluminas from pure aluminum chloride. Google Patents: 1987.
30. Park, H. K.; Park, K. Y.; Jung, K. Y., Alumina-Precursor Nanoparticles Prepared by Partial Hydrolysis of AlCl_3 Vapor in Tubular Flow Reactor: Effect of Hydrolysis Conditions on Particle Size Distribution. *Industrial & Engineering Chemistry Research* **2014**, *53* (25), 10372-10379.
31. Park, K. Y.; Park, Y.-W.; Youn, S.-H.; Choi, S.-Y., Bench-Scale Decomposition of Aluminum Chloride Hexahydrate to Produce Poly(aluminum chloride). *Industrial & Engineering Chemistry Research* **2000**, *39* (11), 4173-4177.
32. Park, H. K.; Park, K. Y.; Kim, H.-J., Kinetics of Gas-Phase Hydrolysis of Aluminum Chloride for Alumina Particles. *Industrial & Engineering Chemistry Research* **2014**, *53* (39), 14956-14962.
33. Khaleel, A.; Kapoor, P. N.; Klabunde, K. J., Nanocrystalline metal oxides as new adsorbents for air purification. *Nanostructured Materials* **1999**, *11* (4), 459-468.
34. Carnes, C. L.; Kapoor, P. N.; Klabunde, K. J.; Bonevich, J., Synthesis, Characterization, and Adsorption Studies of Nanocrystalline Aluminum Oxide and a Bimetallic Nanocrystalline Aluminum Oxide/Magnesium Oxide. *Chemistry of Materials* **2002**, *14* (7), 2922-2929.

35. Tanada, S.; Kabayama, M.; Kawasaki, N.; Sakiyama, T.; Nakamura, T.; Araki, M.; Tamura, T., Removal of phosphate by aluminum oxide hydroxide. *Journal of Colloid and Interface Science* **2003**, 257 (1), 135-140.
36. Goodman, A. L.; Li, P.; Usher, C. R.; Grassian, V. H., Heterogeneous Uptake of Sulfur Dioxide On Aluminum and Magnesium Oxide Particles. *The Journal of Physical Chemistry A* **2001**, 105 (25), 6109-6120.
37. Baltrusaitis, J.; Schuttlefield, J.; Zeitler, E.; Grassian, V. H., Carbon dioxide adsorption on oxide nanoparticle surfaces. *Chemical Engineering Journal* **2011**, 170 (2–3), 471-481.
38. Perkson, A.; Leis, J.; Arulepp, M.; Kaarik, M.; Urbonaite, S.; Svensson, G., Barrel-like carbon nanoparticles from carbide by catalyst assisted chlorination. *Carbon* **2003**, 41 (9), 1729-1735.
39. Leis, J.; Perkson, A.; Arulepp, M.; Käärik, M.; Svensson, G., Carbon nanostructures produced by chlorinating aluminium carbide. *Carbon* **2001**, 39 (13), 2043-2048.
40. Bartolucci, S. F.; Paras, J.; Rafiee, M. A.; Rafiee, J.; Lee, S.; Kapoor, D.; Koratkar, N., Graphene–aluminum nanocomposites. *Materials Science and Engineering: A* **2011**, 528 (27), 7933-7937.
41. Lätt, M.; Käärik, M.; Permann, L.; Kuura, H.; Arulepp, M.; Leis, J., A structural influence on the electrical double-layer characteristics of Al₄C₃-derived carbon. *Journal of Solid State Electrochemistry* **2010**, 14 (4), 543-548.
42. Jacob, M.; Palmqvist, U.; Alberius, P. C. A.; Ekstrom, T.; Nygren, M.; Lidin, S., Synthesis of structurally controlled nanocarbons-in particular the nanobarrel carbon. *Solid State Sciences* **2003**, 5 (1), 133-137.
43. Jänes, A.; Lust, E., Electrochemical Characteristics of Nanoporous Carbide-Derived Carbon Materials in Various Nonaqueous Electrolyte Solutions. *Journal of The Electrochemical Society* **2006**, 153 (1), A113-A116.
44. Smith, D. F.; Essex, H., Process of making aluminum chlorid. Google Patents: 1918.
45. Klemperer, W., Infrared Spectrum of Gaseous Aluminum Chloride. *The Journal of Chemical Physics* **1956**, 24 (2), 353-355.
46. Thomberg, T.; Kurig, H.; Jänes, A.; Lust, E., Mesoporous carbide-derived carbons prepared from different chromium carbides. *Microporous & Mesoporous Materials* **2011**, 141 (1-3), 88-93.

47. Chen, X.; Cantrell, D. R.; Kohlhaas, K.; Stankovich, S.; Ibers, J. A.; Jaroniec, M.; Gao, H.; Li, X.; Ruoff, R. S., Carbide-Derived Nanoporous Carbon and Novel Core–Shell Nanowires. *Chemistry of Materials* **2006**, *18* (3), 753-758.
48. Bräuniger, T.; Chandran, C. V.; Wedig, U.; Jansen, M., NMR Chemical Shift and Quadrupolar Interaction Parameters of Carbon-Coordinated ^{27}Al in Aluminium Carbide, Al_4C_3 . *Zeitschrift für anorganische und allgemeine Chemie* **2011**, *637* (5), 530-535.
49. Czjzek, G.; Fink, J.; Götz, F.; Schmidt, H.; Coey, J. M. D.; Rebouillat, J. P.; Liénard, A., Atomic coordination and the distribution of electric field gradients in amorphous solids. *Physical Review B* **1981**, *23* (6), 2513-2530.
50. Massiot, D.; Fayon, F.; Capron, M.; King, I.; Le Calvé, S.; Alonso, B.; Durand, J. O.; Bujoli, B.; Gan, Z.; Hoatson, G., Modelling one-and two-dimensional solid-state NMR spectra. *Magnetic Resonance in Chemistry* **2002**, *40* (1), 70-76.
51. Sarou-Kanian, V.; Gleizes, A. N.; Florian, P.; Samélor, D.; Massiot, D.; Vahlas, C., Temperature-Dependent 4-, 5- and 6-Fold Coordination of Aluminum in MOCVD-Grown Amorphous Alumina Films: A Very High Field ^{27}Al -NMR study. *The Journal of Physical Chemistry C* **2013**, *117* (42), 21965-21971.
52. Cerny, Z.; Machacek, J.; Fusek, J.; Casensky, B.; Kriz, O.; G. Tuck, D., Aluminium-27 and ^{71}Ga NMR studies of the solution chemistry of $\text{Ga}[\text{AlCl}_4]$ and related compounds. *Journal of the Chemical Society, Dalton Transactions* **1998**, (9), 1439-1446.
53. Jakobsen, H. J.; Skibsted, J.; Bildsøe, H.; Nielsen, N. C., Magic-angle spinning NMR spectra of satellite transitions for quadrupolar nuclei in solids. *Journal of Magnetic Resonance (1969)* **1989**, *85* (1), 173-180.
54. O'Dell, L. A.; Savin, S. L. P.; Chadwick, A. V.; Smith, M. E., A ^{27}Al MAS NMR study of a sol–gel produced alumina: Identification of the NMR parameters of the θ - Al_2O_3 transition alumina phase. *Solid State Nuclear Magnetic Resonance* **2007**, *31* (4), 169-173.
55. Hauert, R.; Patscheider, J.; Tobler, M.; Zehring, R., XPS investigation of the aC: H/Al interface. *Surface science* **1993**, *292* (1-2), 121-129.
56. Natishan, P. M.; O'grady, W. E., Chloride ion interactions with oxide-covered aluminum leading to pitting corrosion: a review. *Journal of The Electrochemical Society* **2014**, *161* (9), C421-C432.
57. Augustynski, J.; Painot, J., Discussion of “On the Kinetics of the Breakdown of Passivity of Preanodized Aluminum by Chloride Ions” [Z. A. Foroulis and M. I. Thubrikar (pp. 1296–1301, Vol. 122, No. 10)]. *Journal of The Electrochemical Society* **1976**, *123* (6), 841.
58. Rotole, J. A.; Sherwood, P. M. A., Valence band x-ray photoelectron spectroscopic studies to distinguish between oxidized aluminum species. *Journal of Vacuum Science & Technology A* **1999**, *17* (4), 1091-1096.

59. McCafferty, E., Sequence of steps in the pitting of aluminum by chloride ions. *Corrosion Science* **2003**, 45 (7), 1421-1438.
60. Pérez-Cadenas, A.; amp; x, n, F.; Maldonado-Hódar, F. J.; Moreno-Castilla, C., On the nature of surface acid sites of chlorinated activated carbons. *Carbon* **2003**, 41 (3), 473-478.
61. Papirer, E.; Lacroix, R.; Donnet, J.-B.; Nansé, G.; Fioux, P., XPS study of the halogenation of carbon black—Part 2. Chlorination. *Carbon* **1995**, 33 (1), 63-72.
62. Zhou, J.-H.; Sui, Z.-J.; Zhu, J.; Li, P.; Chen, D.; Dai, Y.-C.; Yuan, W.-K., Characterization of surface oxygen complexes on carbon nanofibers by TPD, XPS and FT-IR. *Carbon* **2007**, 45 (4), 785-796.
63. Pang, H.; Wang, X.; Zhang, G.; Chen, H.; Lv, G.; Yang, S., Characterization of diamond-like carbon films by SEM, XRD and Raman spectroscopy. *Applied Surface Science* **2010**, 256 (21), 6403-6407.
64. Feng, Z.-S.; Chen, J.-J.; Zhang, R.; Zhao, N., Formation of Al₂O₃–Nb₂O₅ composite oxide films on low-voltage etched aluminum foil by complexation–precipitation and anodizing. *Ceramics International* **2012**, 38 (4), 3057-3061.
65. Santos, P. S.; Santos, H. S.; Toledo, S., Standard transition aluminas. Electron microscopy studies. *Materials Research* **2000**, 3 (4), 104-114.
66. Heyman, A.; Musgrave, C. B., A Quantum Chemical Study of the Atomic Layer Deposition of Al₂O₃ Using AlCl₃ and H₂O as Precursors. *The Journal of Physical Chemistry B* **2004**, 108 (18), 5718-5725.
67. Matero, R.; Rahtu, A.; Ritala, M.; Leskelä, M.; Sajavaara, T., Effect of water dose on the atomic layer deposition rate of oxide thin films. *Thin Solid Films* **2000**, 368 (1), 1-7.
68. Balbuena, P. B.; Gubbins, K. E., Theoretical interpretation of adsorption behavior of simple fluids in slit pores. *Langmuir* **1993**, 9 (7), 1801-1814.
69. Solozhenko, V. L.; Kurakevych, O. O., Equation of state of aluminum carbide Al₄C₃. *Solid State Communications* **2005**, 133 (6), 385-388.
70. Do, D. D.; Do, H. D., A model for water adsorption in activated carbon. *Carbon* **2000**, 38 (5), 767-773.
71. Kippeny, T. C., Chemically modified organic cdc based rapid analysis system. Google Patents: 2011.
72. Schneider, R. T.; Hauck, F. A., Method for methane production. Google Patents: 1990.

73. Yuan, B.; Wu, X.; Chen, Y.; Huang, J.; Luo, H.; Deng, S., Adsorption of CO₂, CH₄, and N₂ on Ordered Mesoporous Carbon: Approach for Greenhouse Gases Capture and Biogas Upgrading. *Environmental Science & Technology* **2013**, *47* (10), 5474-5480.
74. Kikkinides, E. S.; Yang, R. T.; Cho, S. H., Concentration and recovery of carbon dioxide from flue gas by pressure swing adsorption. *Industrial & Engineering Chemistry Research* **1993**, *32* (11), 2714-2720.
75. Sircar, S.; Golden, T.; Rao, M., Activated carbon for gas separation and storage. *Carbon* **1996**, *34* (1), 1-12.
76. Russell, B. P.; Levan, M. D., Pore size distribution of BPL activated carbon determined by different methods. *Carbon* **1994**, *32* (5), 845-855.
77. McEwen, J.; Hayman, J.-D.; Ozgur Yazaydin, A., A comparative study of CO₂, CH₄ and N₂ adsorption in ZIF-8, Zeolite-13X and BPL activated carbon. *Chemical Physics* **2013**, *412*, 72-76.
78. Wahby, A.; Ramos-Fernández, J. M.; Martínez-Escandell, M.; Sepúlveda-Escribano, A.; Silvestre-Albero, J.; Rodríguez-Reinoso, F., High-surface-area carbon molecular sieves for selective CO₂ adsorption. *ChemSusChem* **2010**, *3*.

CHAPTER 4. TUNABLE NANOPARTICLES IN ALUMINUM CARBIDE-DERIVED CARBON FOR ENHANCED ACID GAS ADSORPTION

4.1 Introduction

The emission and accumulation of SO₂ and CO₂ in the environment is a long-standing problem in the scientific community. Separation and capture of such gases via adsorption utilizing porous solids, e.g. metal organic frameworks (MOFs), zeolites, molecular sieves, and activated carbon, has proven to be a promising yet challenging endeavor.¹⁻⁹ Carbon-based adsorbents are primarily used in commercial adsorption today due to their relatively low cost, high surface areas, large micropore volumes, and tailorable surface chemistries.¹⁰⁻¹⁴ Gas adsorption onto carbon can be viewed in two general categories, nonpolar and polar gas adsorption. Physisorption capacities of nonpolar CO₂, for example, are primarily dependent on pore size and available surface area. Conversely, polar molecules like SO₂ are more strongly influenced by chemical groups and active sites which facilitate adsorbate-adsorbent binding interactions. Therefore, integrating physical and chemical tunability into next-generation porous materials would greatly enhance the acid gas removal capabilities of carbonaceous adsorbent media.

Carbide-derived carbons (CDCs) are a newer class of tailorable porous-carbon materials that are promising for many applications such as gas storage, electrochemical energy storage, protein adsorption, as well as water/air purification.¹⁵⁻²⁰ CDCs possess high thermal and chemical stability, making them an attractive adsorbent for a diverse range of conditions. These highly tunable carbon matrices demonstrate narrow pore-size

distributions (PSD) and possess BET surface areas exceeding $2000 \text{ m}^2 \text{ g}^{-1}$, making them an ideal platform for the adsorption process.^{18, 21} A significant portion of current CDC literature focuses on utilizing metal-free CDCs with annealed surfaces. These materials provide large surface areas for adsorption but are deficient of significant chemical heterogeneity that can facilitate the adsorption of polar gases. It has been demonstrated previously that partial etching of CDCs derived from Al_4C_3 and Fe_3C allows for the retention of nanoparticles, with many carbides yet to be explored for partial etching.²²⁻²³ For Al_4C_3 -CDC, aluminum hydroxide $\text{Al}(\text{OH})_3$, a naturally-occurring compound found in minerals such as bauxite, and poly(aluminum chloride) (PAC), a well-known flocculant in commercial water purification, would provide a favorable active site for acid gas interactions.^{22, 24} PAC can have a range of basicities defined as a ratio of $\text{OH}^-/\text{Al}^{3+}$ and was demonstrated to effectively remove complex organic acids such as humic acid from solution.²⁵⁻²⁷ To the best of our knowledge, PAC's interactions with acid gases has not been reported previously. However, the basic properties of PAC suggest its integration into tunable porous carbon may foster enhanced adsorption of acid gases. Aluminum hydroxide species have demonstrated favorable adsorption properties with acid gases as a result of their amphoteric nature.²⁸⁻³¹ Lewis acid sites, coordinately unsaturated aluminum atoms, in the Al-O system promote physisorption while other Lewis base sites such as anionic oxygen and surface hydroxyls provide stronger adsorption interactions.^{28, 32}

The incorporation of such metal sites in a porous-carbon matrix is typically accomplished through post-synthetic metal impregnation in activated carbons. However, these composites are notoriously diffusion-limited due to partial pore blockage by the impregnant.³³⁻³⁴ Instead, partially etched CDCs maintain high surface areas while retaining

well-dispersed nanoparticles through a one-step synthesis, making this process advantageous over traditional carbon host impregnation.

However, when nanoparticles are initially generated through partial etching, they exist in the form of a metal chloride or their readily oxidized derivatives. This is a consequence of the typical chlorination processes used for metal heteroatom extraction. Such Lewis acid sites are not favorable for the adsorption of acid gases; therefore, post-synthetic modification of the nanoparticles for targeted adsorption is desired. Modification of residual metal in partially etched CDCs would allow for the generation of a wide array of tunable carbon matrices which can be templated in the form of thin films, nanorods, nanospheres, bulk powders, etc., adding an additional degree of engineering to carbon adsorbents with embedded metal sites that is not currently available.³⁵⁻³⁶ Analyzing the effects of such modifications on the carbon host and its gas capture performance would therefore be of great technological interest.

By combining the adsorption properties of CDCs and those of tailored aluminum-based nanoparticles, a chemically and thermally-resistant adsorbent can be produced and tuned for adsorption of flue gas components such as CO₂ and SO₂. Herein, the effect of post-synthetic modification treatments with water vapor and alkaline solutions on residual-metal content, porosity, and surface chemistry of Al₄C₃-CDCs is explored. Pure component CO₂ and SO₂ adsorption isotherms were investigated both for the parent and modified materials, to observe changes in adsorption capacity as the residual metal is manipulated. Substantiation experiments were performed via SO₂ breakthrough at 1000 ppm to determine the capacity and viability of these modified adsorbents for low partial pressure applications such as flue gas scrubbing.

4.2 Materials and Methods

4.2.1 Materials

Al_4C_3 -CDC was prepared by depositing 1 g of Al_4C_3 (Strem Chemicals 98% purity, 325 mesh) in a quartz boat which is placed in a 20" long quartz tube with an outer diameter of 1". The tube was placed in a horizontal tube furnace that was operated in the range of 300-500°C with a ramp rate for heating and cooling set at 5 °C min⁻¹. During heating and cooling a stream of argon gas (Airgas 99.999%) is flown over the bed at 150 mL min⁻¹. Once the desired etching temperature is reached, chlorine gas (Airgas 99.5%) was introduced via an Aalborg mass flow controller at a rate of 40 mL min⁻¹ while argon is still flowing at 150 mL min⁻¹. The flow continues for the duration of the run. After the argon and chlorine have passed over the bed, the stream passes through a NaOH scrubber solution to neutralize any acidic gases. Once the etching experiment was completed, chlorine flow was discontinued, and the system is cooled under argon at 150 mL min⁻¹. Note, for the sake of clarity the samples are labeled as follows Al_4C_3 -CDC-T-CT-MT-Treatment. Where Al_4C_3 denotes the species of carbide, CDC refers to the general material of carbide-derived carbon, T is the temperature in °C at which etching occurred at, CT is the chlorination time in hours, and MT is the time for post-synthetic modification. (e.g. Al_4C_3 -CDC-500-1h-24h-NaOH). If no modification is performed the last three classifications are dropped for brevity.

4.2.2 *Methods*

4.2.2.1 Powder X-ray Diffraction

Powder X-ray diffraction (PXRD) patterns were collected using an X'Pert X-ray PANalytical diffractometer with a Cu K α X-ray source ($\lambda = 1.5418 \text{ \AA}$). PXRD diffractograms were collected from a range of 5-60° with a step size of 0.02°. All experiments were carried out at room temperature.

4.2.2.2 Nitrogen Sorption Measurements

Nitrogen sorption measurements at 77 K were obtained using a Quantachrome Quadrasorb SI volumetric analyzer. Isotherms were collected at 77 K using samples of 25-100 mg. Prior to each isotherm, the sample was outgassed for approximately 18 hours at 150°C and under vacuum (approximately 20 mTorr). Specific surface areas were calculated using the BET model in the relative pressure range (P/P_0) 0.005-0.03. Pore size distributions were collected for all samples using the Quenched Solid Density Functional Theory (QSDFT) model built into version 5.11 QuadraWinTM software. The QSDFT parameters were selected depending on the characteristics of the isotherm. For microporous, type I isotherms, a slit-pore model, nitrogen adsorbate, and carbon adsorbent were assumed. Whereas, for type IV isotherms that exhibit characteristic cavitation effects, an adsorption branch slit-pore/cylindrical pore model was used with an assumed nitrogen adsorbate and carbon adsorbent.

4.2.2.3 Thermogravimetric Analysis (TGA)

Thermogravimetric analysis for all samples was carried out on a NETZSCH STA 449 F1 Jupiter instrument. Measurements used 20-40 mg of material, heated from 25-1400 °C at a ramp rate of 10 °C min⁻¹ and a flow rate of 20 mL min⁻¹ of air (Airgas 99.999%). The residual metal content was calculated by assuming total combustion of carbon; upon complete combustion, the final mass was assumed to be Al₂O₃.

4.2.2.4 Magic-Angle Spinning Nuclear Magnetic Resonance (MAS NMR)

No pretreatment of the samples was done before the NMR measurements. ²⁷Al MAS NMR was carried out for all samples at a magnetic field strength of 13.9 T. All spectra were referenced to a solution of 1.0 M Al(NO₃)₃ at 0.0 ppm. The ²⁷Al spectra were recorded on a Redstone NMR spectrometer (Tecmag) at a Larmor frequency of 153.7 MHz. For acquisition of the ²⁷Al spectra, a Bruker HX MAS probe with a 2.5 mm rotor was used. Measurements were recorded using a pulse-acquire experiment, rotation frequency of 25 kHz, a recycle delay of 3s, and a flip angle of $\pi/18$ (corresponding to a pulse width of 0.36 μ s) to ensure quantitative 1D spectra.

4.2.2.5 Scanning Electron Microscopy (SEM) and Elemental dispersive spectroscopy (EDS)

Scanning electron microscopy (SEM) images were obtained using a Zeiss Ultra-60 Field Emission Scanning Electron Microscope. All samples were deposited onto carbon

tape. Images were scanned at an accelerating voltage range of 5-10 kV. EDS was employed at an accelerating voltage of 10 kV for elemental compositions.

4.2.2.6 Transmission Electron Microscopy (TEM)

Transmission electron microscopy (TEM) and HRTEM images were obtained using a FEI Tecnai F30 at an operating voltage of 300 kV with a 1.7 Å point resolution. Samples were prepared by suspending approximately 1 mg of sample in methanol and deposited onto a lacy carbon copper grid.

4.2.2.7 Water Vapor Adsorption Isotherms/Exposure

Water vapor adsorption experiments were performed on a volumetric Micromeritics 3-Flex device at 25°C. Prior to the measurement, 20-50 mg of material was activated *in situ* at 150°C for 12 hours under dynamic vacuum. For humid exposure studies, Al₄C₃-CDC materials were taken directly out of the horizontal reactor and placed under vacuum within 5 minutes to reduce ambient exposure. Pure water vapor exposure was performed from (relative pressure) $P/P_0 = 0$ to $P/P_0 = 0.9$, with total exposure time, including desorption, taking ~24h. Static exposure studies lasting 5 days were set to a desired partial pressure and equilibrated. The materials then stayed in the sealed environment for the desired time.

4.2.2.8 CO₂ Adsorption Measurements

CO₂ isotherms, in the pressure range of 0-1.2 bar, were obtained using a volumetric Micromeritics 3-Flex device at a range of temperatures. Prior to the measurement, 20-50 mg of material was heated in situ at 150 °C for 18 hours under vacuum.

4.2.2.9 X-ray Photoelectric Spectroscopy (XPS) analysis

X-ray photoelectric spectroscopy (XPS) measurements were recorded on a Thermo K-alpha, monochromated Al K α source with a double-focusing hemispherical analyzer. High resolution spectra were taken of C 1s, O 1s, Al 2p, Cl 2p, S 2p at a 0.1 eV step size, 50 ms dwell time, 50 eV pass energy, and a 400 μ m spot size.

4.3 Results and Discussion

4.3.1 *Evolution of aluminum-based nanoparticles via water vapor*

Prior studies of Al₄C₃-CDC materials have established structural and compositional changes that occur at a range of etching temperatures and times. The partial etching of Al₄C₃ allows for the retention of aluminum-containing nanoparticles when etching in the range of 300 and 500°C.²²

As previously shown in literature, Al₄C₃-CDC-300-1h is comprised of three distinct coordination environments of aluminum after brief atmospheric exposure. The three species identified were: Al₄C₃ (still present after partial etching); a range of basic aluminum chlorides (BAC), an amorphous material with the empirical formula Al_n(OH)_mCl_(3n-m) including anhydrous aluminum chloride; and the hydrated form of aluminum represented

as $[\text{Al}(\text{H}_2\text{O})_6]^{3+}$.²² During partial etching, the aluminum chloride monomer and dimer species (AlCl_3 and Al_2Cl_6) evolving from the structure can be retained in the carbon matrix. Upon brief exposure to air before characterization, the anhydrous chloride species undergo irreversible hydration to form aluminum chloride hexahydrate ($\text{Al}(\text{H}_2\text{O})_6\text{Cl}_3$), a complex rhombohedral structure in which the water molecules lie between the Al^{3+} cation and the Cl^- anion.³⁷ Notably, $\text{Al}(\text{H}_2\text{O})_6\text{Cl}_3$ does not undergo dehydration when heated; instead it decomposes into BAC at temperatures above 90°C .³⁸⁻³⁹

In contrast, when Al_4C_3 was etched at 500°C for 1h, retained metal is primarily $[\text{Al}(\text{H}_2\text{O})_6]^{3+}$ species. The same decomposition to BAC occurs during activation of the adsorption matrix which is performed at 150°C . To investigate the effects of high humidity exposure, Al_4C_3 -CDC materials were taken out of the horizontal bed reactor and activated, at which point the materials remained sealed off from atmospheric exposure during subsequent adsorption characterization. Pre- and post-humid exposure analysis utilizing CO_2 and N_2 physisorption at 273K and 77K, respectively, was performed including reactivation before each experiment. CO_2 isotherms were collected to observe any changes in how the material interacts with a relatively weak acid gas. Physisorption experiments involving N_2 were primarily used to detect changes in the porous carbon matrix as a direct result of the high humidity environment. Water vapor exposure was achieved via pure component isothermal adsorption up to a partial pressure of $P/P_0 = 0.9$ at 25°C . After isothermal exposure, a small but observable increase in interaction with CO_2 at 0°C was observed for Al_4C_3 -CDC-300-1h and Al_4C_3 -CDC-500-1h materials, as displayed in Figure 4-1a. The surface area (SA) and pore volume (PV) of the carbon displayed no significant changes which correlates with previous results.²² The increase in CO_2 interaction with no

increase in SA or PV suggests formation of favorable adsorption sites, potentially arising from the interaction of water with BAC nanoparticles formed after activation. This result correlates with water vapor isotherms collected during previous studies for materials etched at 300 and 500°C which display retention of water after desorption under high vacuum, indicating irreversible interaction with residual metal throughout the carbon host.²² It should be noted at longer etching times or higher etching temperatures where the majority of metal is removed, water exposure does not lead to changes in CO₂ adsorption. This effect can be attributed to BAC reacting with adsorbed water to form PAC. The basicity of PAC can be increased by altering the OH⁻ to Al³⁺ ratio; notably water has the capacity to provide additional hydroxyl groups for incorporation into the polymer.^{24, 26-27, 40} Literature also suggests AlCl₃ can be directly converted to Al(OH)₃ in chlorine rich environments; therefore, it is possible some of the residual material converts to an amorphous hydroxide.⁴¹

To determine if the residual metal in the Al₄C₃-CDC materials can further react, samples were exposed to a static humidity, P/P₀= 0.85, for 5 days. After prolonged exposure, a further increase in the materials' CO₂ capacity was observed, with a concomitant increase in the SA and PV, as displayed in Figure 4-1b and Table 4-1. With prolonged exposure, BAC is allotted time to migrate and convert to polymeric species promoting stronger interactions with CO₂. The ensuing increase in porosity can be attributed to the rearrangement of residual metal originally occupying the pore space. The increase in mobility of the residual metal during water vapor exposure is a result of near saturation of the carbon surface—creating films of adsorbed water and providing a new medium of transportation for the soluble aluminum-based material.

Al_4C_3 -CDC-300-1h materials display an 18% increase in surface area while Al_4C_3 -CDC-500-1h materials show a 13% increase after water vapor exposure. The increase in SA and PV after prolonged humid exposure is analogous to results achieved in other CDC materials after high temperature or vacuum annealing procedures to remove unwanted metal-based species.⁴²⁻⁴³ Characteristic of both annealing and high humidity exposure, metal is removed from the original location in the pore. But rather than being expelled from the carbon matrix, prolonged humid exposure of Al_4C_3 -CDCs promotes metal-based particle rearrangement near the surface, which is further investigated with microscopy in the following section. The retention of the metal species between pristine and water vapor-exposed samples is also supported by TGA measurements, showing the same amount of residual metal, within error, as the parent materials (Table A-4).

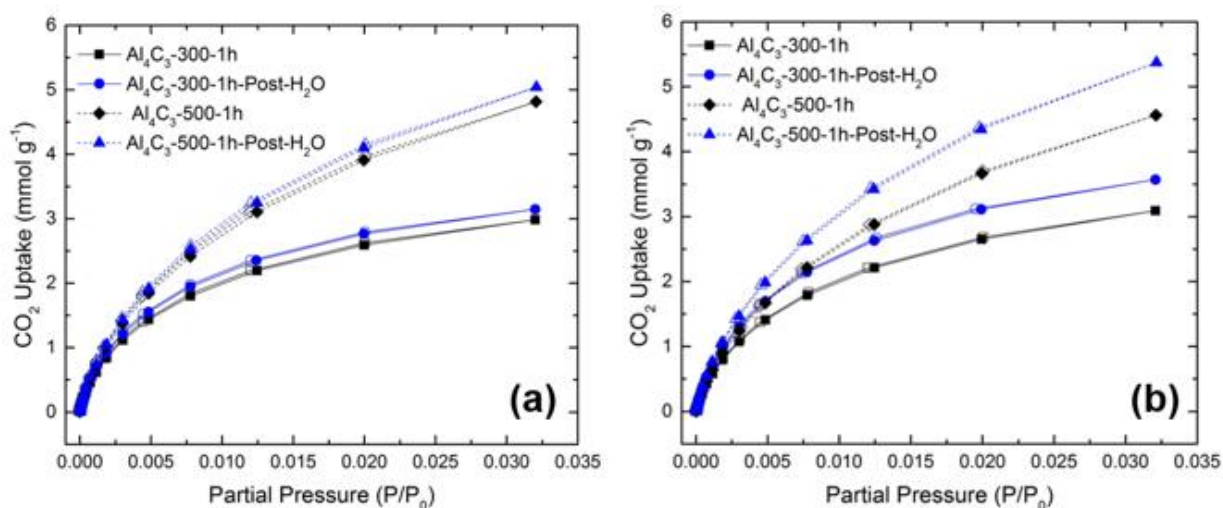


Figure 4-1: CO₂ adsorption at 0°C before and after water vapor exposure for (a) water isotherms and (b) 5 days of high humidity exposure. Exposures were performed at 25°C up to 0.85 P/P₀.

Table 4-1: Changes in carbon properties observed after 5 days of water vapor exposure.

	Al₄C₃-300-1h			Al₄C₃-500-1h		
	Before	After	Change	Before	After	Change
Surface Area (m ² g ⁻¹)	551	637	18%	1075	1159	13%
Pore Volume (cm ³ g ⁻¹)	0.21	.226	13%	0.455	0.484	6%

Further examination through SEM reveals that the morphology of the Al₄C₃-CDC particles display significant evolution during high partial pressure water vapor exposure. Al₄C₃-300-1h materials exhibit a “bubbling” feature on the surface of the carbon after short exposure times as seen in Figure 4-2. These newly evolved features are roughly 50-150nm in size, which corresponds to the aggregation of parent nanoparticles, previously observed to be 5-20nm. This resulting aggregation is consistent with literature on the formation of aluminum polymers ranging from Al₃ to Al₂₀₀.⁴⁴⁻⁴⁵ The “bubbling” feature observed on the surface can be contributed to the formation of PAC through polymerization of neighboring nanoparticles. The observation of aggregating nanoparticles with the previously observed changes in CO₂ and N₂ physisorption data point to direct manipulation of the residual aluminum-based material. Surface aggregates are less evident in Al₄C₃-500-1h samples after brief H₂O exposure, a direct consequence of an inferior quantity of aluminum-based

nanoparticles present in the carbon matrix. EDS on exposed samples reveal that the areas which display the “bubbling” morphology contain a high concentration of aluminum, oxygen and chlorine which is consistent with the formation of PAC, seen in

Table 4-2. Notably, areas with significant PAC formation such as Figure 4-2b, will be skewed to higher concentrations of polymeric materials due to the micron depth penetration of EDS and vice versa for small pockets forming on top of carbon.

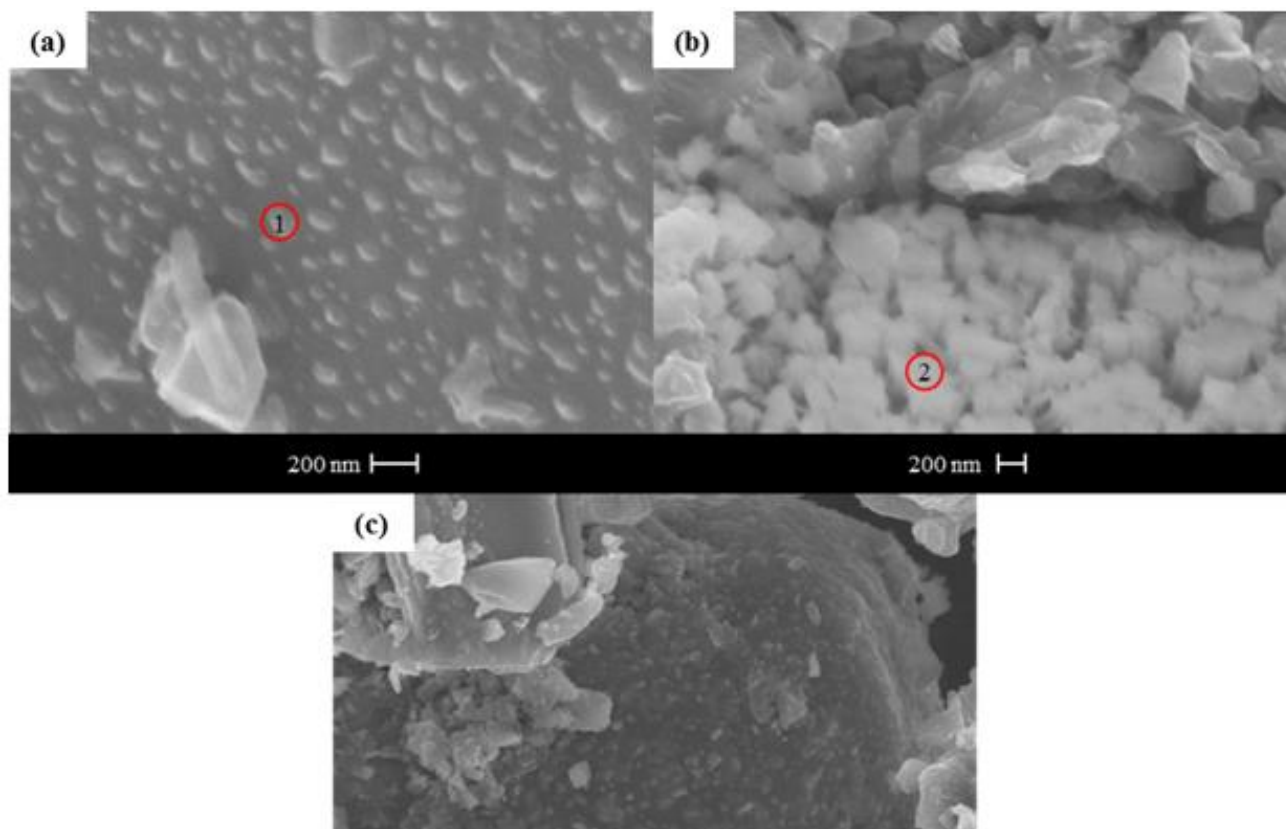


Figure 4-2: SEM images of (a & b) Al_4C_3 -CDC-300-1h- H_2O -isotherm (c) Al_4C_3 -CDC-500-1h- H_2O -isotherm. The red circle () indicates locations of EDS analysis.



Table 4-2: EDS of “bubbling” feature found on Al₄C₃-CDC-300-1h after H₂O isotherms

Element	Location 1		Location 2	
	Atomic %	Weight %	Atomic %	Weight %
C	57.36	75.36	24.88	35.32
O	8.28	8.16	43.97	46.85
Al	8.5	4.97	18.92	11.96
Cl	25.86	11.51	12.22	5.88

SEM imaging of the materials exposed to a high partial pressure of water over the period of 5 days shows further polymerization and alterations of particle morphology. With a longer gestation period, the once individual carbon particles, ranging from 10-40 μ m, aggregate together due to the flocculation properties of the evolving PAC. Seen in Figure 4-3, large clusters are formed with clearly visible fault boundaries, where the polymer has experienced a degree of thermal stress after re-activation. Surface EDS measurements in Table A-5 revealed a small increase in aluminum concentration for Al₄C₃-CDC-300-1h with a large increase in oxygen content and reduction in observable carbon composition in the first 1-2 μ m of the CDC surface. The changes in morphology, composition, and flocculation behavior provide strong evidence of the extensive formation of PAC near the surface of the Al₄C₃-CDCs. The polymerization of PAC permits the powdered carbon particles to remain in the form of the exposure container exhibiting a promising possibility for casting the porous material into a pellet or to create larger aggregates to reduce pressure drop in a packed bed, all while utilizing a cost-effective procedure. Further studies were performed to determine if PAC formation occurs at lower partial pressures for Al₄C₃-CDC-500-1h, Figure A-17. A similar increase in CO₂ capacity, surface area and pore volume was

observed with water pressures as low as $P/P_0 = 0.6$, with 5 days of exposure. These results indicate a benign modification technique to alter the adsorption capacity of carbide-derived carbons by modifying residual metal in partially etched Al_4C_3 -CDCs with the creation of polymeric species at ambient conditions. Such a procedure can be achieved by simply storing the Al_4C_3 -CDC adsorbents in high humidity storage containers, allowing parent nanoparticles to evolve before use.

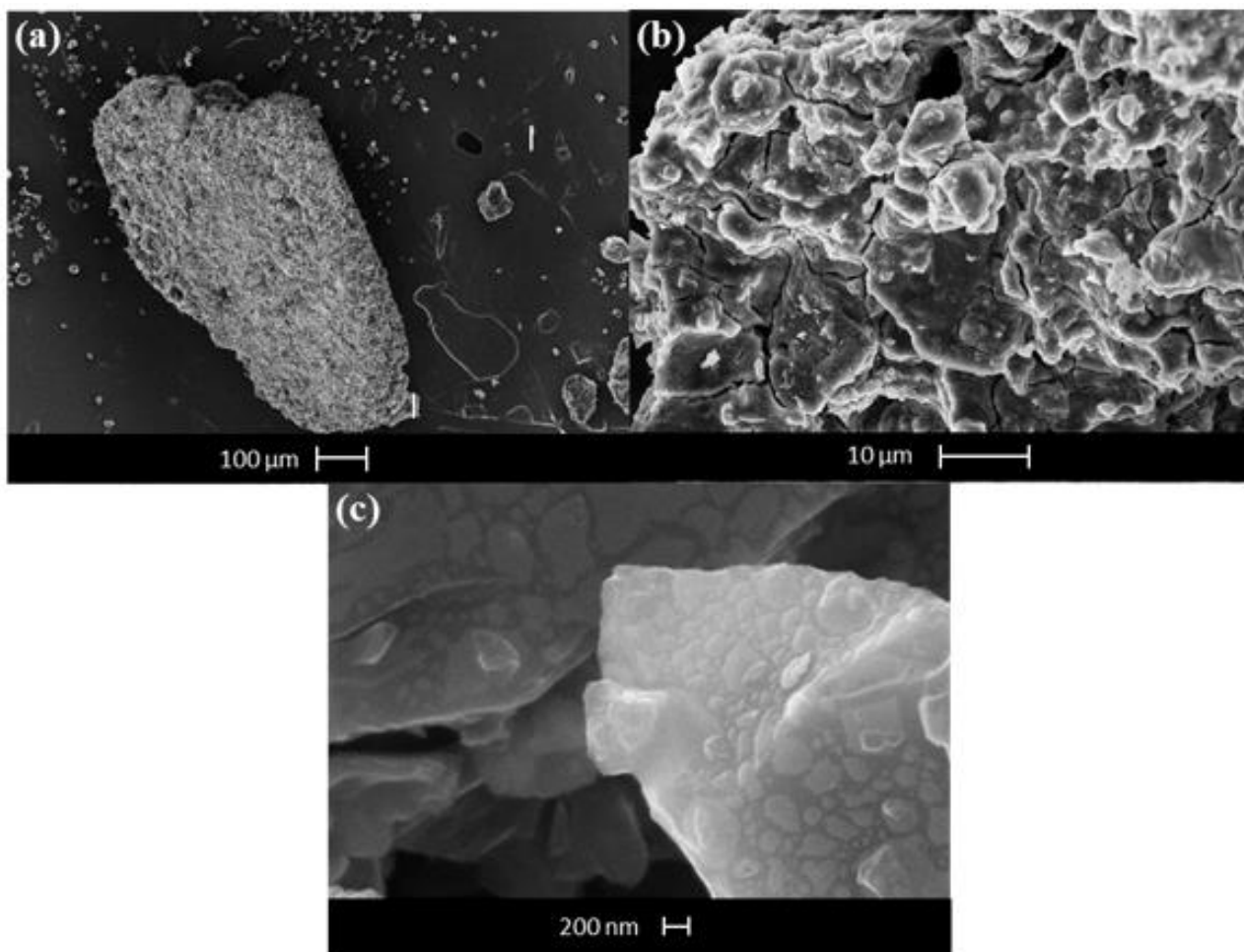


Figure 4-3: SEM images after 5-day H_2O exposure for (a) Al_4C_3 -CDC-300-1h and (b & c) Al_4C_3 -CDC-500-1h

4.3.2 Alkaline treatment of Al_4C_3 -CDC materials

Due to the capacity of water vapor to convert residual metal in Al_4C_3 -CDCs into PAC, investigations were performed to convert nanoparticles into aluminum hydroxide ($\text{Al}(\text{OH})_3$) instead. A 1M solution of NaOH was utilized due to its established ability to convert bulk $\text{Al}(\text{H}_2\text{O})_6\text{Cl}_3$ and BAC to amorphous and crystalline polymorphs of $\text{Al}(\text{OH})_3$.⁴⁶⁻⁴⁸ Al_4C_3 -CDC materials were subject to post-synthetic modification for 24h and then characterized to probe changes in adsorption, porosity and chemical functionality. As visualized in Figure 4-4a, alkaline modified derivatives of Al_4C_3 -CDC-300-1h and Al_4C_3 -CDC-500-1h both displayed large increases in CO_2 capacity, 83% and 67% respectively. Al_4C_3 -CDC-500-1h displayed a repeatable $4.2 \pm 0.2 \text{ mmol g}^{-1}$ adsorption of CO_2 at 25°C and 1 bar. Such an uptake is amongst the highest reported for carbon based sorbents, which typically entail high temperature micropore enhancement with KOH activation or incorporation of amines to reach analogous capacities.⁴⁹⁻⁵¹ Due to an observed increase in surface area after alkaline treatment, parallel studies utilizing DI water were employed to decipher the direct effects of the aqueous environment. Liquid water treatment on Al_4C_3 -CDC-500-1h provided similar increases in SA, reaching $\sim 1425 \text{ m}^2\text{g}^{-1}$. Al_4C_3 -CDC-300-1h samples likewise exhibit an increase in SA after liquid water treatment, but to a lesser degree than their alkaline counterpart. This is due to the difficulty of PAC to traverse the entirely microporous structure of Al_4C_3 -CDC-300-1h, visualized in Figure A-18, as compared to the hybrid micro/mesoporous materials etched at 500°C . As a result of the increased SA, CO_2 capacities for both Al_4C_3 -CDC-300-1h and Al_4C_3 -CDC-500-1h increased after liquid water treatment, 52% and 31%, respectively. In both cases this is at least 30% lower than the alkaline treatment. These observations suggest two phenomena

are occurring during alkaline modification. The first is an increase in capacity due to the liberation of micropore space by increasing the mobility of residual metal species in an aqueous environment. The presence of a bulk fluid for aluminum species to diffuse into allows for significant leaching of the aluminum content. This is supported by the reduction of residual metal for materials treated in an aqueous environment determined via TGA. Leaching of metal species led to residual metal concentrations of 8% and 2% for Al_4C_3 -CDC-300-1h-24h-NaOH and Al_4C_3 -CDC-500-1h-24h-NaOH, respectively. The second phenomenon is the conversion of the chloride-containing nanoparticles to a more reactive aluminum hydroxide species. With 24h of treatment no crystalline polymorph of aluminum hydroxide was formed that provided enough long-range periodicity for PXRD to detect (Figure A-19). Therefore NMR, presented later, was employed to support the identity of the amorphous residual metal. With no visual signs of PAC formation after NaOH treatment and retention of nanoparticles visualized in Figure 4-4(b and c) during TEM observation, alkaline treatment of Al-CDCs was determined to successfully deter the formation of PAC. EDS and XPS results discussed later notably do not detect residual Na^+ in the material after the washing process within their detection limits. This in tandem with an increase in SA, as opposed to a likely decrease in SA due to impregnated NaOH, supports the effective removal of Na^+ through the described rinsing procedure.

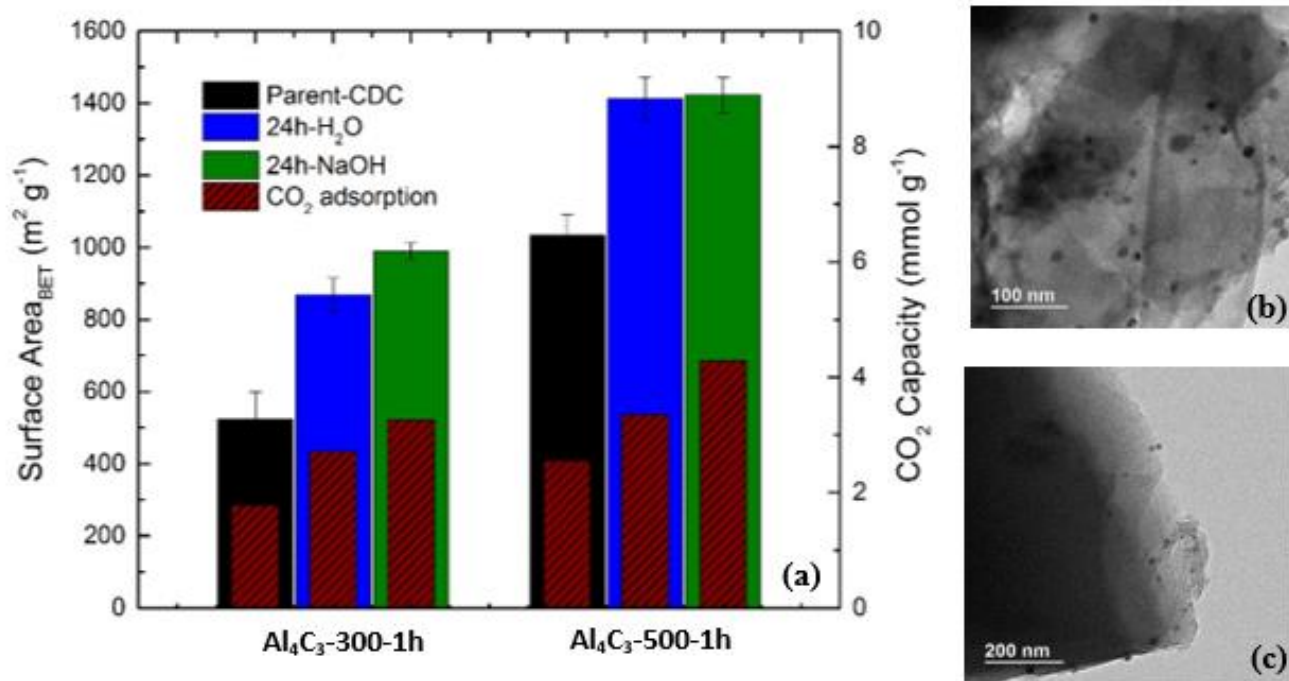


Figure 4-4: : (a) CO₂ capacity at 25°C and 1 bar for post-synthetically modified Al₄C₃-CDC materials and TEM images of (b) Al₄C₃-CDC-300-1h-24h-NaOH and (c) Al₄C₃-CDC-500-1h-24h-NaOH

The temporal effects of NaOH treatment on CO₂ adsorption were investigated and presented in Figure 4-5. Both Al₄C₃-CDC-300-1h and Al₄C₃-CDC-500-1h displayed an initial increase in CO₂ capacity at 0 and 25°C, then begin to taper off after prolonged exposure times. This behavior can be contributed to the initial conversion of residual metal to amorphous Al(OH)₃, followed by leaching of metal species into solution. Al₄C₃-CDC-500-1h samples exhibit an enhanced sensitivity to hydroxide aging/leaching compared to Al₄C₃-CDC-300-1h, which is expressed in Figure 4-5b. The large mesopores present in the Al₄C₃-CDC-500-1h carbon matrix provide a non-tortuous path for NaOH to enter the porous material to react as well as aluminum hydroxide to leach from the sorbent. Therefore, Al₄C₃-CDC samples etched at 500°C exhibit analogous CO₂ capacities for

modification durations beyond 24h. Entirely microporous Al_4C_3 -300-1h materials display larger absolute enhancement in capacity over time as a consequence of increased residual metal. The evolution of Al_4C_3 -300-1h is inherently diffusion limited and displays changes over larger temporal domains due to smaller channels, $<0.7\text{nm}$, for NaOH and $\text{Al}(\text{OH})_3$ to traverse. Prolonged NaOH exposure exhibits the ability to convert the initially amorphous $\text{Al}(\text{OH})_3$ into crystalline bayerite in Al_4C_3 -300-1h samples, detected by reflections in PXRD, after 6 days of exposure, Figure A-20. The formation of bayerite was also observed when bulk $\text{Al}(\text{H}_2\text{O})_6\text{Cl}_3$ was tested under the same conditions. A consequence of bayerite formation is a reduction in surface area of the adsorbent and subsequently the CO_2 capacity (Figure A-21 and Figure 4-5). Dynamic light scattering results (Figure A-22) reveal a homogenous distribution of large aggregates forming in solution after 11 days, corresponding to bayerite crystals, which lead to blocked pore access as crystals precipitate. Amorphous $\text{Al}(\text{OH})_3$ particles also possess a higher surface density of edge Al-OH groups compared to crystalline bayerite which can interact with acidic species leading to increased adsorption. Similar trends were observed by McBride et al. when studying catechol, an organic acid, and its respective adsorption onto gibbsite, boehmite and non-crystalline $\text{Al}(\text{OH})_3$. They observed significant increases in adsorption for amorphous hydroxides over the ordered polymorphs.⁵² These results highlight the potential capacity of post-synthetic modification to tune the active metal sites in Al_4C_3 -CDCs. Time of NaOH modification displayed an important role in both diffusion of species in and out of the CDC matrix and aging of the residual metal into crystalline hydroxide. By future manipulation of variables such as time, temperature and alkaline environment, the original chlorinated aluminum content reveals promise of being suitable to achieve a variety of $\text{Al}(\text{OH})_3$

polymorphs to be explored as adsorbents and catalyst embedded into a robust carbon matrix.

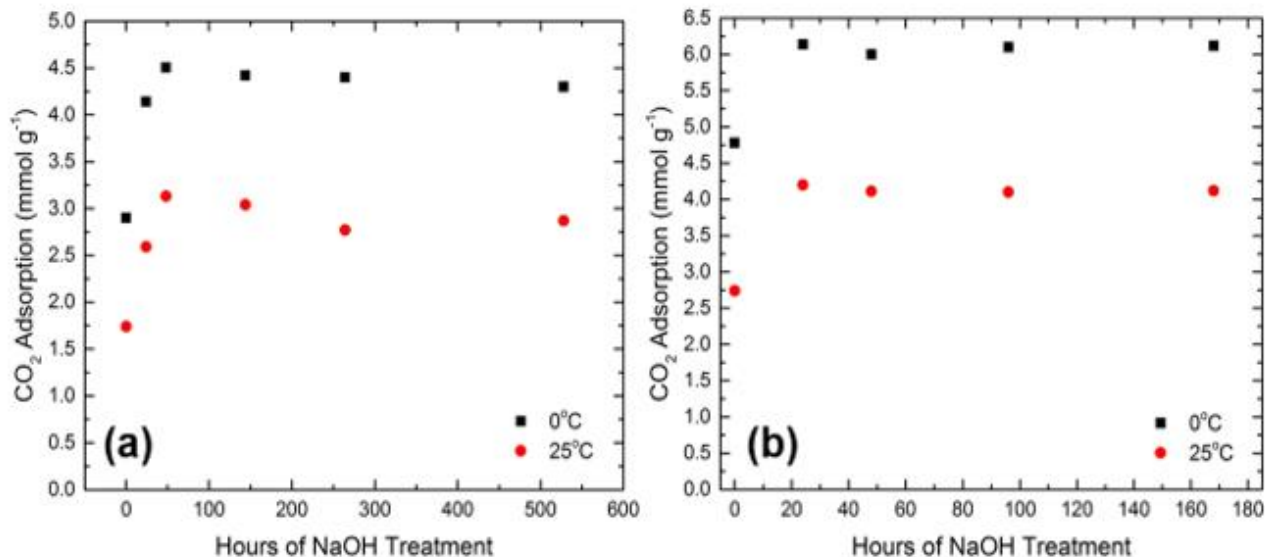


Figure 4-5: Temporal effects of NaOH treatment on CO₂ capacity at 1 bar for (a) Al₄C₃-CDC-300-1h and (b) Al₄C₃-CDC-500-1h.

4.3.3 Sample composition from ²⁷Al solid-state NMR

²⁷Al solid-state NMR can distinguish different aluminum environments present in multicomponent systems. ²⁷Al is a quadrupolar nucleus ($I = 5/2$), where information about the local site symmetry can manifest itself in the NMR spectrum. The parent material from which CDCs are derived is a nonporous crystalline material, Al₄C₃, which possesses two magnetically-inequivalent aluminum sites, each coordinated to four carbon atoms.[3–5] As shown previously, after etching for the designated time and temperature, the resulting Al₄C₃-CDC is composed of a combination of multiple polymorphs of BAC/PAC, and amorphous aluminum oxide, unreacted Al₄C₃, and a trace amount of aluminum nitride (an impurity in the starting material).²² Both methods for post-synthetic modification of Al₄C₃-

CDC involve H₂O, which reacts with Al₄C₃ to produce methane, aluminum hydroxides, and aluminum oxide. Residual Al₄C₃ should not be present since both modifications involve H₂O exposure for at least 24h.

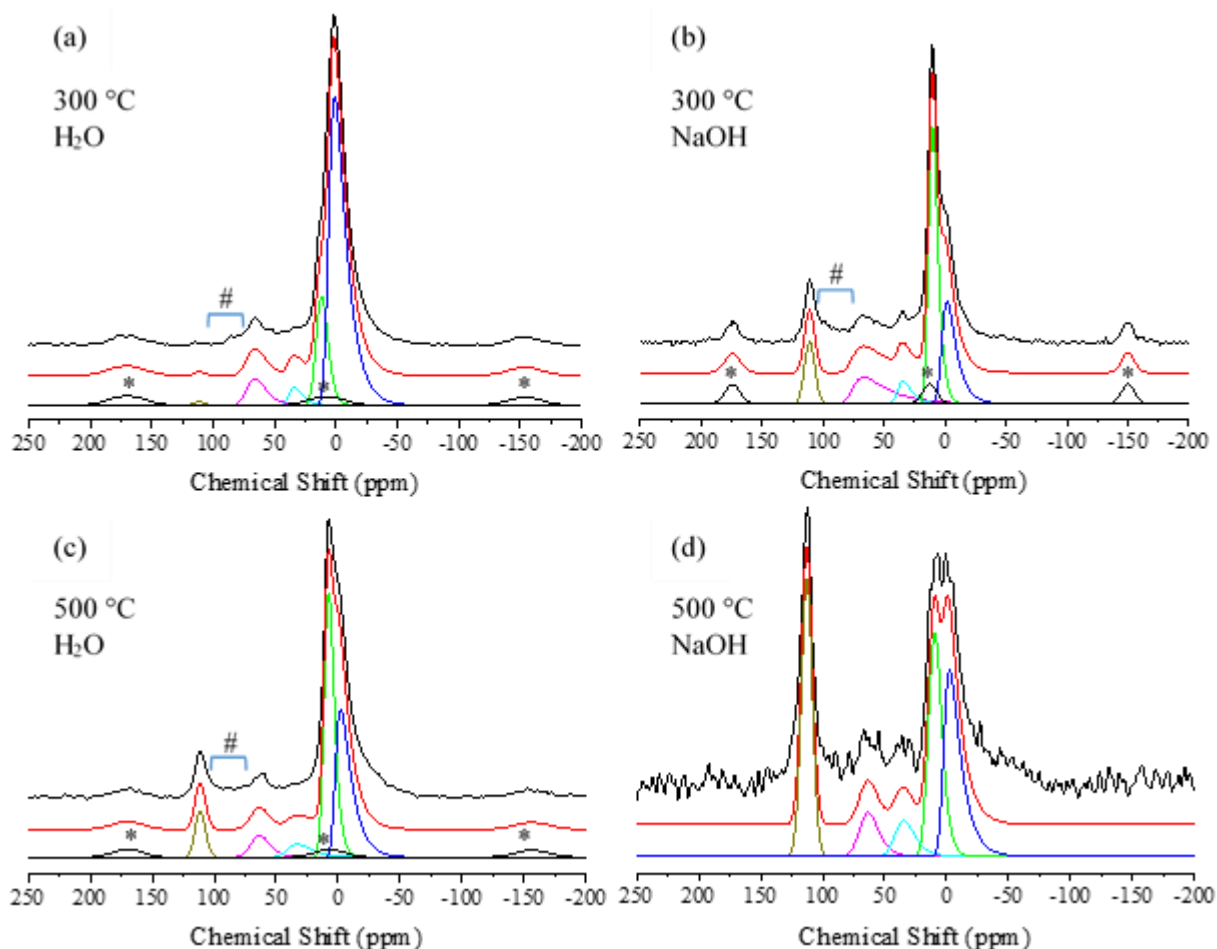


Figure 4-6: ²⁷Al MAS NMR spectra of (a) Al₄C₃-CDC-300-1h-24h-H₂O (b) Al₄C₃-CDC-300-1h-24h-NaOH (c) Al₄C₃-CDC-500-1h-24h-H₂O (d) Al₄C₃-CDC-500-1h-24h-NaOH. The asterisks (*) denote the spinning sidebands from external transitions. The external transitions were simulated with a Gaussian, and the intensities and widths were based on the $n \pm 1$ spinning sidebands.

The ²⁷Al solid-state magic-angle spinning (MAS) NMR spectra of the modified Al₄C₃-CDC materials show the existence of similar resonances for BACs (and PACs) and aluminum oxides in all of the materials, but in different proportions. All fits of the spectra

were performed with the Dmfit program. Notably, a resonance at 113ppm is found in all spectra, arising from aluminum nitride, an impurity originating in the Al_4C_3 precursor (as supplied from the manufacturer). In the range of 75 to -20 ppm, there are several resonances fitting a Czjzek distribution that are commonly associated with amorphous aluminum oxides. These resonances are attributed to 4-, 5-, and 6-coordinate aluminum oxides. There are two 6-coordinate resonances that appear in this range: we attribute the higher frequency resonance (~ 10 ppm) to 6-coordinate $\text{Al}(\text{OH})_3$, and the lower frequency resonance (~ -2 ppm) to 6-coordinate aluminum sites in BAC/PAC and aluminum oxide, that cannot be further resolved or deconvoluted. In the range of 105 – 75 ppm, there is a ^{27}Al NMR signal intensity present (above the baseline) that we attribute to a distribution of 4-coordinate sites of $[\text{AlCl}_4]^-$ through $[\text{Al}(\text{OH})_4]^-$, based on the chemical shift range. This range of 4-coordinate sites is shown in Figure 4-6. As a result of the chlorination and subsequent post-synthetic modification, it is unsurprising that a range of 4-coordinate sites would be found. Finally, at approximately 10 ppm, there is a spinning sideband from the external transitions.

All four spectra shown in Figure 4-6 display these resonances described above, but in different proportions. The comparison of one preparation (i.e., H_2O) at two different temperatures shows a dramatic change in the amount of $[\text{Al}(\text{OH})_3]$ present. Similarly, comparing a single temperature (i.e., 300°C) with two different preparations also shows a dramatic increase in the resonance corresponding to $[\text{Al}(\text{OH})_3]$. For the 500°C NaOH preparation, the signal-to-noise ratio becomes very poor, complicating the comparison between it and other spectra. It is worthwhile to note, the Al_4C_3 -CDC materials have less aluminum than the Al_4C_3 precursor as a result of the etching process. The materials etched at 300°C and 500°C are expected to have 18% and 8% of the original aluminum content,

respectively.⁵³ Due to the difference in aluminum content between the different etching temperatures, the samples prepared at 500 °C required double the number of NMR transients acquired, compared to the samples prepared at 300 °C. In addition to these differences, there is a reduction in the aluminum content due to leaching during the post-synthetic modification. In agreement with the TGA results above, it appears that the NaOH solution removes more aluminum than the H₂O modification, evident for both sets of spectra (comparing Fig. 6a versus b, and c versus d), there is poorer signal-to-noise ratios for the ²⁷Al NMR, for those samples that have gone through NaOH treatment.

4.3.4 XPS analysis of surface chemistry on modified Al₄C₃-CDCs

XPS was performed on pre- and post-modified samples to investigate the chemical environment of the surface. The parent materials represented in Figure 4-7, show significantly different surface environments, with materials etched at 300°C displaying nearly double the amount of hetero atoms than those etched at 500°C. After 24h of alkaline treatment for the Al₄C₃-CDC-300-1h materials, a small increase in surface oxygen accompanied by a reduction in aluminum and chlorine was observed. This supports the conversion of residual metal species to Al(OH)₃ as the chlorine containing nanoparticles react, and aluminum is lost to the bulk through leaching. When materials etched at 300°C were exposed to a high humidity for extended periods of time the chemical composition of the surface was drastically altered, corroborating SEM-EDS morphology observations of PAC covering the exterior of the carbonaceous material. Elemental composition variations were primarily negligible for Al₄C₃-CDC-500-1h outside a small decrease of 2% in carbon and 4% increase in oxygen for NaOH modified materials which can be contributed to the conversion of nanoparticles with a small amount of aluminum hydroxide adhering to rough

carbon surface rather than going into the bulk solution as it is leached. There is a possibility that OH⁻ groups react with the carbon matrix, with high resolution C1s and O1s XPS, Figure A-24 and Table A-7, showing ~0.5-1% increase in C-O and COOH groups. The marginal difference is well within experimental variance and literature results have indicated that NaOH does not increase oxygen containing functional groups, but rather has the capacity to change carbonyl or carboxyl groups to phenol or lactone functionalities. Therefore, the increase in oxygen due to increased hydroxyl groups on carbon is unlikely.⁵⁴⁻

⁵⁵ It is reasonable to state that the alkaline treatment has little effect on the quantity of functional species contained throughout the carbon. The contribution of additional OH⁻ groups from Al(OH)₃ and coordinated water to the hydroxides are likely the main contributor to increased oxygen content on the surface. Attenuated total reflectance infrared (ATR-IR) spectra were taken for pre- and post-modified samples, Figure A-25 , with no distinct alterations in surface functional groups outside an additional hydroxyl stretch at 3610 cm⁻¹ for modified Al₄C₃-CDC-300-1h samples. This peak can be assigned to the hydroxyl stretch in Al(OH)₃ or some form of hydrogen bonding. The presence of such a peak in samples etched at 300°C and not 500°C is reasonable due to the higher aluminum content at lower temperatures and the difficulty of analyzing groups with lower concentrations in IR for carbon. Vibrational results corroborate XPS findings, indicating no significant modification of surface chemistry during NaOH treatment. Hence the conversion of nanoparticles to Al(OH)₃ and the increase in microporosity are the main contributors to enhanced acid gas interaction.

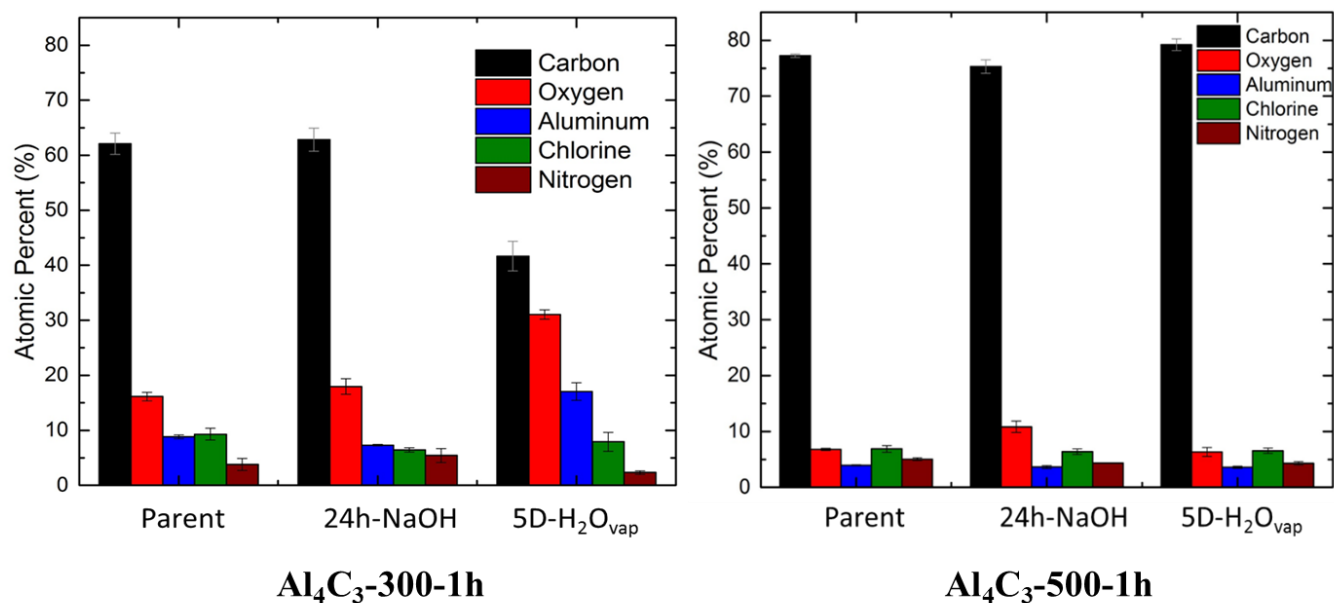


Figure 4-7: Elemental composition of pre- and post-modified Al_4C_3 -CDC surfaces.

4.3.5 Characterization of dry SO_2 interaction with pre- and post-modified Al_4C_3 -CDCs

Isothermal adsorption of dry SO_2 was performed up to $P/P_0 = 0.7$ (~ 2.1 bar) on materials that underwent aqueous modification as well as their unmodified counterparts. As seen in Figure 4-8, both parent Al_4C_3 -CDC samples display a sharp uptake at low partial pressures with saturation after $P/P_0 = 0.2$. This characteristic type 1 isotherm corresponds to filling of the micropore volume, with strong monolayer adsorption occurring in the carbon matrix. The sharp uptake also suggests active sites for adsorption throughout the porous material, which can be attributed to residual metal species and functional groups. Materials that were treated with DI water displayed an increase in capacity over all recorded pressures as a direct result of increased micropore volume and the presence of PAC. Alkaline modified materials displayed more than double the parent materials adsorption capacity at partial pressures below $P/P_0 = 0.1$ which strongly suggest enhancement of active sites and

increased microporosity. Al_4C_3 -CDC-500-1h-24h-NaOH samples displayed the highest capacities, adsorbing $\sim 12 \text{ mmol g}^{-1}$ of SO_2 at 1 bar and 25°C . Substantiation experiments were performed on Al_4C_3 -CDC-300-1h-24h-NaOH and Al_4C_3 -CDC-500-1h-24h-NaOH to verify the low-pressure adsorption region due to the sharp uptake in the isothermal curve. Breakthrough experiments, seen in Figure A-26, were performed with 1000ppm SO_2 balance nitrogen to probe the performance of SO_2 capture at flue gas concentrations. Repeatable breakthrough capacities of 2.33 and 1.98 mmol g^{-1} were observed for Al_4C_3 -CDC-300-1h-24h-NaOH and Al_4C_3 -CDC-500-1h-24h-NaOH samples respectively. This high capacity confirms strong adsorption at a partial pressure of $P/P_0 = 3 \times 10^{-3}$, falling well within the steep curve of collected SO_2 isotherms. The slightly higher capacity for samples etched at 300°C is attributed to higher quantities of $\text{Al}(\text{OH})_3$ nanoparticles and an increased density of functional groups that can contribute to low pressure adsorption. The enhanced adsorption trends after modification correlate well with previous results on CO_2 discussed in the prior section. Absolute amounts of adsorbed SO_2 is significantly higher than that of CO_2 though, mainly due to its larger kinetic size, polarizability and adsorption orientation of the gas.⁵⁶ After dry SO_2 exposure, alkaline modified material were retested for their CO_2 capacity. Materials etched at 300°C displayed the same adsorption while samples etched at 500°C exhibited lower uptakes at higher partial pressures, Figure 4-8(c and d). The loss in capacity relates to the functionalization of porous carbon walls via chemisorption of SO_2 which was further investigated.

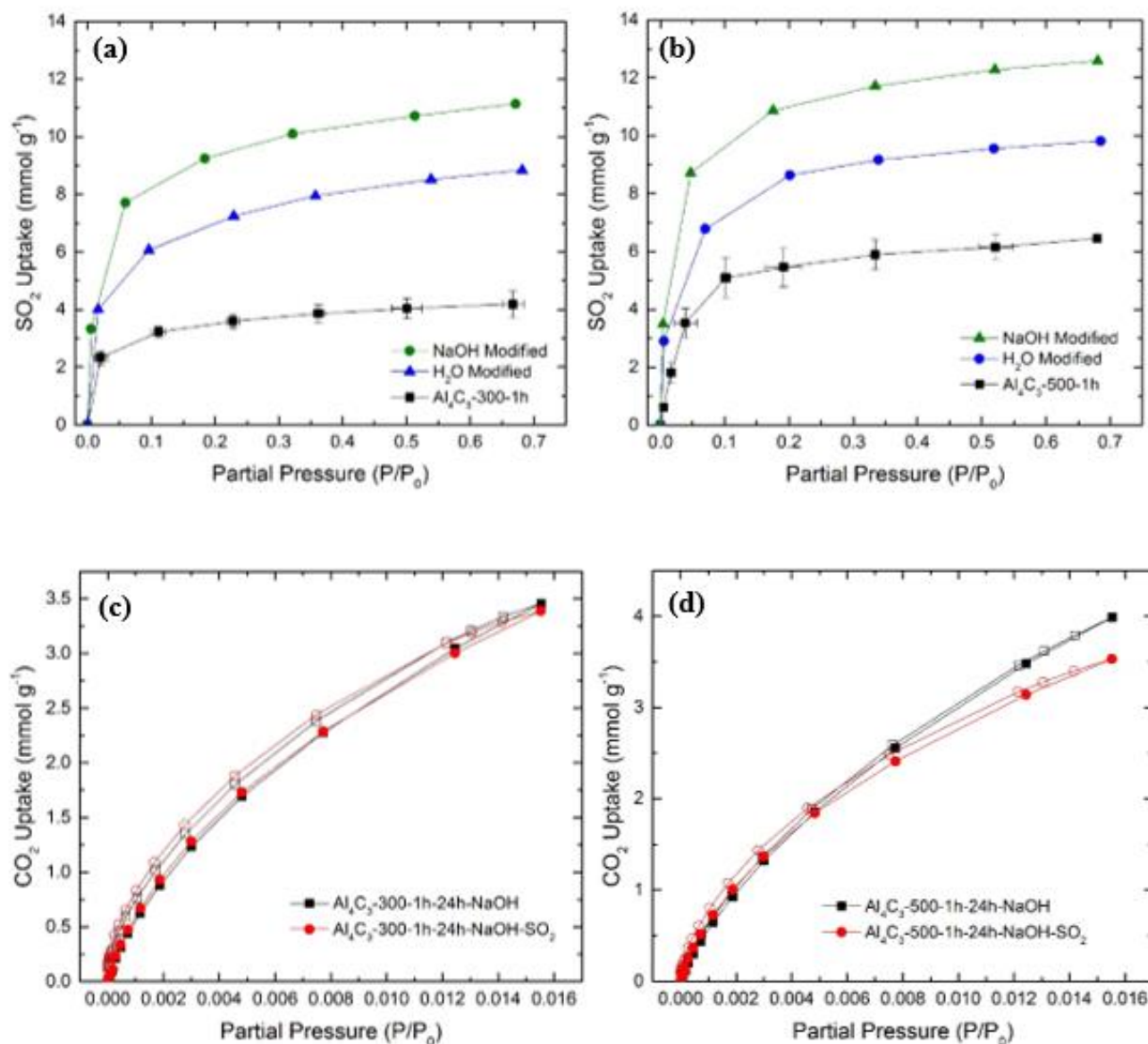


Figure 4-8: Isothermal volumetric adsorption of SO₂ at 25°C (a) Al₄C₃-CDC-300-1h-24h-NaOH (b) Al₄C₃-CDC-500-1h-24h-NaOH & CO₂ at 25°C pre and post SO₂ (c) Al₄C₃-CDC-300-1h-24h-NaOH (d) Al₄C₃-CDC-500-1h-24h-NaOH

The porosity before and after SO₂ exposure was probed with N₂ physisorption and subsequent QSDFT analysis, displayed in Figure 4-9 and Table 4-3. Al₄C₃-CDC-300-1h materials displayed no change in surface area or pore volume after dry SO₂ exposure. Water modified samples with PAC displayed reduced SA and PV which can be contributed to the

chemisorption of SO₂ on the surface of the carbon due to the generation of polymeric species. Al₄C₃-CDC-300-1h-24h-NaOH samples displayed no significant loss in microporosity after dry SO₂ exposure similar to the parent CDC. Al₄C₃-CDC-500-1h materials exhibited a consistent decrease in surface area after exposure for both parent and modified materials. The loss of porosity is a direct result of SO₂ functionalizing the carbon surface leading to partial blockage of both micro and mesopore pore volume observed through the change in pore size distribution shown in Figure 4-9.

Table 4-3: BET surface area before and after dry SO₂ exposure for modified and unmodified materials

Sample	S _{BET} (m ² g ⁻¹)		Change (%)
	Pre-Exposure	Post-Exposure	
300-1h	562	582	-
300-1h-H₂O-24h	826	544	34%
300-1h-NaOH-24h	994	925	-
500-1h	1126	887	21%
500-1h-H₂O-24h	1390	1167	16%
500-1h-NaOH-24h	1359	1183	13%

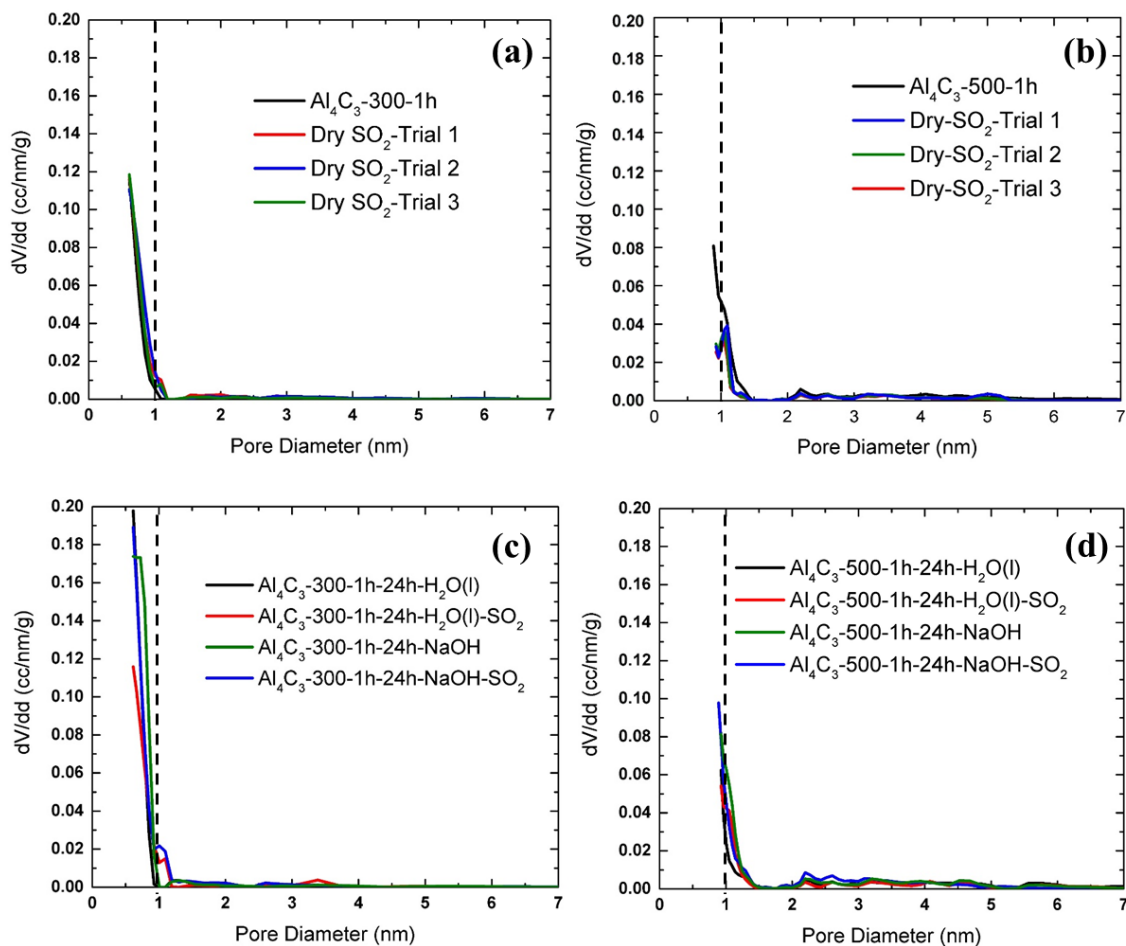


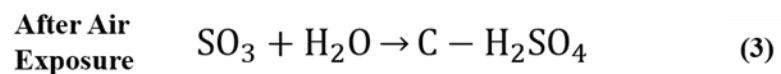
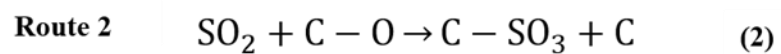
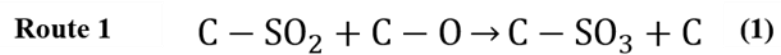
Figure 4-9: Pore size distribution before and after dry SO_2 exposure for (a) Al_4C_3 -300-1h and (b) Al_4C_3 -500-1h (c) Modified Al_4C_3 -300-1h and (d) Modified Al_4C_3 -300-1h. The dashed line (--) is used to mark a pore diameter of 1 nm.

High resolution XPS analysis was performed to probe the change in surface chemistry before and after dry SO_2 exposure. Deconvolution of the O 1s spectra, seen in Figure 4-10, reveals 5 different types of oxygen groups. The first region (531.3-531.8 eV), correlates to carbonyl oxygen possibly from quinines or Al-O species.⁵⁷⁻⁶¹ The second region (532.0-532.7 eV) represents carbonyl oxygen atoms (C=O) from anhydrides, esters and oxygen in hydroxyl groups.^{57, 62} The region from (533.1-533.8 eV) is non-carbonyl, ether-type, oxygen atoms in esters and anhydrides (COOR, C-O-C).⁶³⁻⁶⁴ The fourth region (535.82-535.72 eV) can be attributed to A-O with chlorine incorporated into the matrix or

oxygen atoms in carboxyl groups.⁵⁷ The final region (536.0-538 eV) corresponds to adsorbed water/oxygen near the surface. In the XPS spectra before and after SO₂ exposure for Al₄C₃-500-1h there is an increase in oxygen content at a binding energy of ~532 eV, the second region, and a decrease in oxygen with BE = 533-534 eV, the third region. This suggests the replacement of COOR/C-O-C surface functionalities with S=O, SO₂ or SO₄²⁻.⁶² XPS after dry SO₂ adsorption also elucidates the retention of sulfur based groups for Al₄C₃-500-1h materials after exposure and re-activation. The curves were fit using two peaks of equal full width at half max and a 2:1 area ratio to represent the 2p_{3/2} -2p_{1/2} doublet separation of 1.18eV for sulfur.⁶⁵ Two binding energies were identified, BE = 168.53 and 170.36 eV during the high resolution S 2P XPS analysis. The sulfur species at BE= 168.53 eV can be attributed to a sulfate on carbon (SO₄²⁻) which accounts for ~94% of the sulfur content remaining in the sample.⁶² This correlates well with the carbon matrix comprising the majority of the available adsorptive surface. The higher binding energy of 170.36 eV can be attributed to a sulfate species coordination to aluminum.⁶⁵⁻⁶⁷ These results strongly suggest SO₂ is chemisorbing onto Al₄C₃-CDCs via C-O sites which has been proposed in literature, shown in equations 1-4.^{6,68} Materials etched at both 300 and 500°C contain basic oxygen sites. This was elucidated in TGA-MS which show CO and CO₂ decomposition products at temperatures ranging from 700-1000°C in Figure A-27, which are the most probably chemisorption sites. The difference between the two etching temperatures is materials synthesized at 300°C exhibit smaller pores, <0.7nm, which could sterically hinder SO₂ from reacting. Oxidation restriction due to pore size is theorized in activated carbon literature as well but difficult to pin point with broad PSD.⁶⁹ The narrow PSD of Al₄C₃ samples provides compelling evidence that PSD can restrict oxidation of SO₂ which

occurs in pores $>7 \text{ \AA}$. This finding emphasizes the importance of angstrom level tunability achieved in CDCs when designing an adsorbent to be used in acid gas applications. In a one-pass application larger pores that can accommodate and chemisorb SO_2 would be desired but for a cyclic application a material that resists functionalization and allows for easy regeneration is optimal.

Equation 4-1



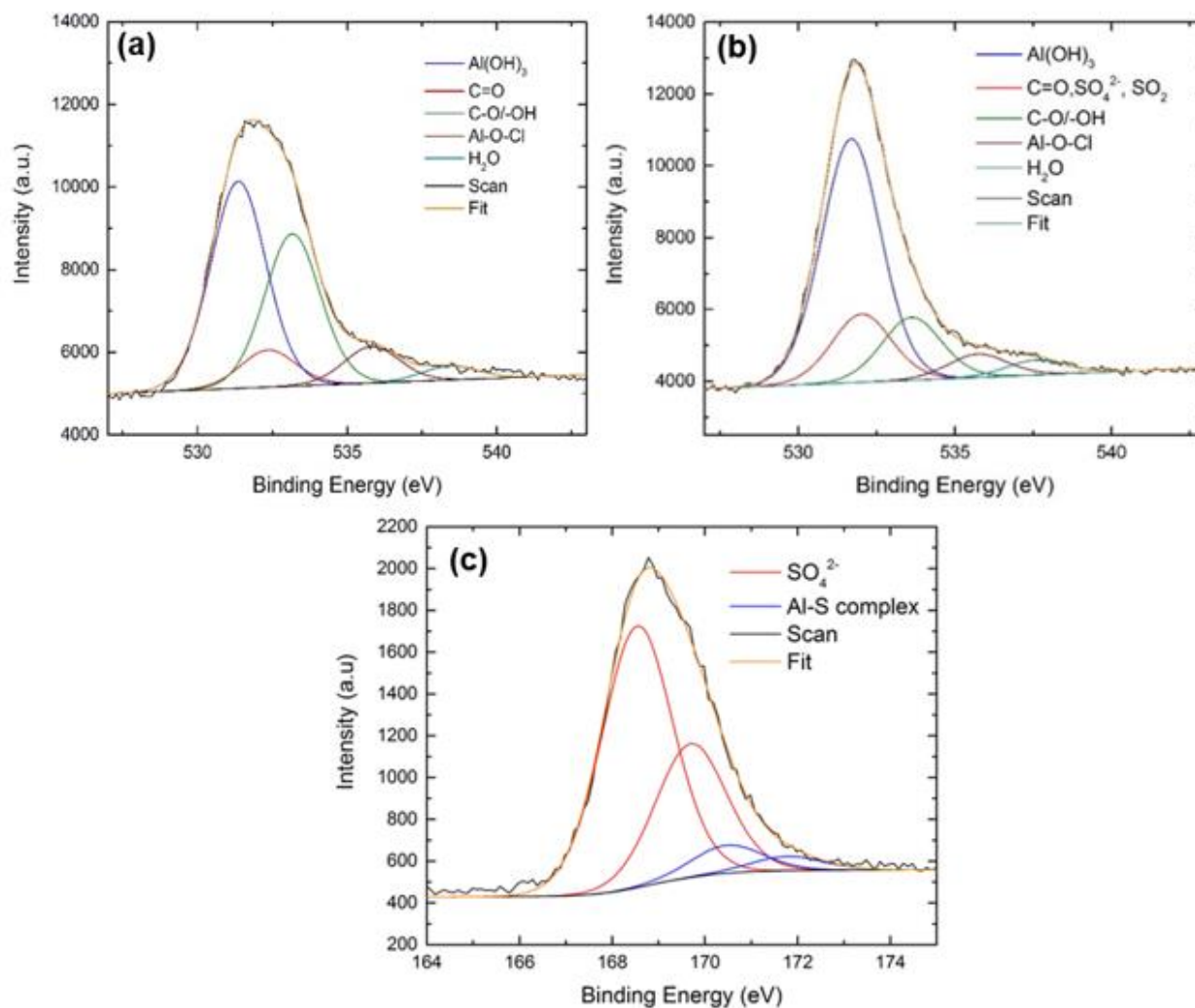


Figure 4-10: High resolution O 1s XPS spectra on (a) Al₄C₃-CDC-500-1h pre-SO₂ (b) Al₄C₃-CDC-500-1h post-SO₂ and (c) High resolution S 2p on Al₄C₃-CDC-500-1h post-SO₂

4.4 Conclusions

For the first time, post-synthetic modification has been performed to tune residual metal in partially etched carbide-derived carbons utilizing humid and alkaline treatments. An Al₄C₃ precursor was utilized to demonstrate the viability of residual metal modification

due to the presence of aluminum-based nanoparticles. High humidity exposure for short periods of time revealed the transformation of aluminum chloride species to poly(aluminum chloride), visualized after it formed via SEM. Increased durations of exposure up to 5 days allowed for further polymerization and movement of PAC towards the surface of the carbonaceous material. The formation of PAC was correlated with an increase in porosity due to the mobility of the polymer, opening up previously blocked micropores and displayed enhanced CO_2 and SO_2 interactions. Alkaline modification with aqueous NaOH was employed to steer the conversion of residual metal towards $\text{Al}(\text{OH})_3$ derivatives in order to achieve a more attractive active site. After 24-48h of treatment the nanoparticles derived from materials etched at 300 and 500°C are converted to 6-coordinate amorphous aluminum hydroxide. Upon ageing in solution, the amorphous content is converted to crystalline bayerite observed via PXRD, which causes partial pore blockage and a subsequent reduction in adsorption capacity. A significant increase in adsorption from the parent CDC was realized when post-synthetic alkaline treatment was performed for less than 48h. Al_4C_3 -CDC-500-1h-24h samples adsorbed 4.2 and 12 mmol g^{-1} CO_2 and SO_2 , respectively, which is among the highest reported in literature for either gas for a carbonaceous material. Chemisorption was detected after dry SO_2 exposure for materials with pores larger than 7 Å. XPS was used to probe the chemical state of the surface species after exposure and elucidated the retention of SO_4^{2-} species and a reduction in surface oxygen bound to carbon with a single bond. This suggest the functionalization of Al_4C_3 -CDC materials proceeds through the interaction of SO_2 with surface oxygen functional groups. Such functionalization with SO_2 led to decreased surface area and pore volume. This revelation demonstrates materials etched at 300°C and modified with NaOH

display favorable attributes for cyclic application. At low SO₂ partial pressures of 1000 ppm, the retention of Al(OH)₃ nanoparticles lead to increased interactions with SO₂ reaching upwards of 2.33 mmol g⁻¹ SO₂ at 25°C. The insights gained in this study provide a guide for future modification of residual metal in partially etched CDCs and increased understanding of how SO₂ interacts with CDCs to create a tailored adsorption matrix for enhanced acid gas interactions.

4.5 References

1. Tessmer, C. H.; Vidic, R. D.; Uranowski, L. J., Impact of Oxygen-Containing Surface Functional Groups on Activated Carbon Adsorption of Phenols. *Environmental Science & Technology* **1997**, *31* (7), 1872-1878.
2. Siriwardane, R. V.; Shen, M.-S.; Fisher, E. P.; Poston, J. A., Adsorption of CO₂ on Molecular Sieves and Activated Carbon. *Energy & Fuels* **2001**, *15* (2), 279-284.
3. Lu, C.; Bai, H.; Wu, B.; Su, F.; Hwang, J. F., Comparative study of CO₂ capture by carbon nanotubes, activated carbons, and zeolites. *Energy & Fuels* **2008**, *22* (5), 3050-3056.
4. Peng, X.; Jain, S. K.; Singh, J. K., Adsorption and Separation of N₂/CH₄/CO₂/SO₂ Gases in Disordered Carbons Obtained Using Hybrid Reverse Monte Carlo Simulations. *The Journal of Physical Chemistry C* **2017**, *121* (25), 13457-13473.
5. Mangun, C. L.; DeBarr, J. A.; Economy, J., Adsorption of sulfur dioxide on ammonia-treated activated carbon fibers. *Carbon* **2001**, *39* (11), 1689-1696.
6. Lizzio, A. A.; DeBarr, J. A., Mechanism of SO₂ Removal by Carbon. *Energy & Fuels* **1997**, *11* (2), 284-291.
7. Lee, Y.-W.; Park, J.-W.; Choung, J.-H.; Choi, D.-K., Adsorption Characteristics of SO₂ on Activated Carbon Prepared from Coconut Shell with Potassium Hydroxide Activation. *Environmental Science & Technology* **2002**, *36* (5), 1086-1092.
8. He, B.; Zheng, X.; Wen, Y.; Tong, H.; Chen, M.; Chen, C., Temperature impact on SO₂ removal efficiency by ammonia gas scrubbing. *Energy Conversion and Management* **2003**, *44* (13), 2175-2188.
9. Gaur, V.; Asthana, R.; Verma, N., Removal of SO₂ by activated carbon fibers in the presence of O₂ and H₂O. *Carbon* **2006**, *44* (1), 46-60.

10. Cheung, W. H.; Lau, S. S. Y.; Leung, S. Y.; Ip, A. W. M.; McKay, G., Characteristics of Chemical Modified Activated Carbons from Bamboo Scaffolding. *Chinese Journal of Chemical Engineering* **2012**, *20* (3), 515-523.
11. Szymański, G. S.; Karpiński, Z.; Biniak, S.; Świątkowski, A., The effect of the gradual thermal decomposition of surface oxygen species on the chemical and catalytic properties of oxidized activated carbon. *Carbon* **2002**, *40* (14), 2627-2639.
12. Shafeeyan, M. S.; Daud, W. M. A. W.; Houshmand, A.; Shamiri, A., A review on surface modification of activated carbon for carbon dioxide adsorption. *Journal of Analytical and Applied Pyrolysis* **2010**, *89* (2), 143-151.
13. Papirer, E.; Li, S.; Donnet, J.-B., Contribution to the study of basic surface groups on carbons. *Carbon* **1987**, *25* (2), 243-247.
14. Lopez-Ramon, M. V.; Stoeckli, F.; Moreno-Castilla, C.; Carrasco-Marin, F., On the characterization of acidic and basic surface sites on carbons by various techniques. *Carbon* **1999**, *37* (8), 1215-1221.
15. Becker, P.; Glenk, F.; Kormann, M.; Popovska, N.; Etzold, B. J. M., Chlorination of titanium carbide for the processing of nanoporous carbon: A kinetic study. *Chemical Engineering Journal* **2010**, *159* (1-3), 236-241.
16. Gogotsi, Y. G.; Kofstad, P.; Yoshimura, M.; Nickel, K. G., Formation of sp³-bonded carbon upon hydrothermal treatment of SiC. *Diamond and Related Materials* **1996**, *5* (2), 151-162.
17. Yushin, G.; Hoffman, E. N.; Barsoum, M. W.; Gogotsi, Y.; Howell, C. A.; Sandeman, S. R.; Phillips, G. J.; Lloyd, A. W.; Mikhlovsky, S. V., Mesoporous carbide-derived carbon with porosity tuned for efficient adsorption of cytokines. *Biomaterials* **2006**, *27* (34), 5755-5762.
18. Osswald, S.; Portet, C.; Gogotsi, Y.; Laudisio, G.; Singer, J. P.; Fischer, J. E.; Sokolov, V. V.; Kukushkina, J. A.; Kravchik, A. E., Porosity control in nanoporous carbide-derived carbon by oxidation in air and carbon dioxide. *Journal of Solid State Chemistry* **2009**, *182* (7), 1733-1741.
19. Simon, P.; Gogotsi, Y., Materials for electrochemical capacitors. *Nat Mater* **2008**, *7* (11), 845-854.
20. Laheäär, A.; Jänes, A.; Lust, E., Electrochemical properties of carbide-derived carbon electrodes in non-aqueous electrolytes based on different Li-salts. *Electrochimica Acta* **2011**, *56* (25), 9048-9055.
21. Gogotsi, Y.; Nikitin, A.; Haihui, Y.; Wei, Z.; Fischer, J. E.; Bo, Y.; Foley, H. C.; Barsoum, M. W., Nanoporous carbide-derived carbon with tunable pore size. *Nature Materials* **2003**, *2* (9), 591-594.

22. Moran, C. M.; Marti, R. M.; Hayes, S. E.; Walton, K. S., Synthesis and characterization of aluminum carbide-derived carbon with residual aluminum-based nanoparticles. *Carbon* **2017**, *114*, 482-495.
23. Mangarella, M. C.; Ewbank, J. L.; Dutzer, M. R.; Alamgir, F. M.; Walton, K. S., Synthesis of embedded iron nanoparticles in Fe₃C-derived carbons. *Carbon* **2014**, *79*, 74-84.
24. Yang, Z.; Gao, B.; Cao, B.; Xu, W.; Yue, Q., Effect of OH⁻/Al³⁺ ratio on the coagulation behavior and residual aluminum speciation of polyaluminum chloride (PAC) in surface water treatment. *Separation and Purification Technology* **2011**, *80* (1), 59-66.
25. Gao, B.-Y.; Chu, Y.-B.; Yue, Q.-Y.; Wang, B.-J.; Wang, S.-G., Characterization and coagulation of a polyaluminum chloride (PAC) coagulant with high Al13 content. *Journal of Environmental Management* **2005**, *76* (2), 143-147.
26. Pratt, W.; Stevens, J., Polyaluminum Chloride and Aluminum Chlorohydrate, Processes and Compositions: High-Basicity and Ultra High-Basicity Products. Google Patents: 2007.
27. Pratt, W. E.; Stevens, J. J.; Symons, P. G., Polyaluminum chloride and aluminum chlorohydrate, processes and compositions: high-basicity and ultra high-basicity products. Google Patents: 2010.
28. Goodman, A. L.; Li, P.; Usher, C. R.; Grassian, V. H., Heterogeneous Uptake of Sulfur Dioxide On Aluminum and Magnesium Oxide Particles. *The Journal of Physical Chemistry A* **2001**, *105* (25), 6109-6120.
29. Baltrusaitis, J.; Schuttlefield, J.; Zeitler, E.; Grassian, V. H., Carbon dioxide adsorption on oxide nanoparticle surfaces. *Chemical Engineering Journal* **2011**, *170* (2–3), 471-481.
30. Carnes, C. L.; Kapoor, P. N.; Klabunde, K. J.; Bonevich, J., Synthesis, Characterization, and Adsorption Studies of Nanocrystalline Aluminum Oxide and a Bimetallic Nanocrystalline Aluminum Oxide/Magnesium Oxide. *Chemistry of Materials* **2002**, *14* (7), 2922-2929.
31. Tanada, S.; Kabayama, M.; Kawasaki, N.; Sakiyama, T.; Nakamura, T.; Araki, M.; Tamura, T., Removal of phosphate by aluminum oxide hydroxide. *Journal of Colloid and Interface Science* **2003**, *257* (1), 135-140.
32. Datta, A.; Cavell, R. G.; Tower, R. W.; George, Z. M., Claus catalysis. 1. Adsorption of sulfur dioxide on the alumina catalyst studied by FTIR and EPR spectroscopy. *The Journal of Physical Chemistry* **1985**, *89* (3), 443-449.
33. Petit, C.; Karwacki, C.; Peterson, G.; Bandosz, T. J., Interactions of Ammonia with the Surface of Microporous Carbon Impregnated with Transition Metal Chlorides. *The Journal of Physical Chemistry C* **2007**, *111* (34), 12705-12714.

34. Molina-Sabio, M.; Pérez, V.; Rodríguez-Reinoso, F., Impregnation of activated carbon with chromium and copper salts: Effect of porosity and metal content. *Carbon* **1994**, 32 (7), 1259-1265.
35. Gogotsi, Y., Chemical vapour deposition: Transition metal carbides go 2D. *Nat Mater* **2015**, 14 (11), 1079-1080.
36. He, C. N.; Zhao, N. Q.; Shi, C. S.; Song, S. Z., Fabrication of aluminum carbide nanowires by a nano-template reaction. *Carbon* **2010**, 48 (4), 931-938.
37. Wai, C. M.; Hutchison, S. G., Evaluation of thermodynamic data for aluminum chloride hexahydrate and its dehydration. *Thermochimica Acta* **1989**, 144 (2), 241-247.
38. Hartman, M.; Trnka, O.; Šolcová, O., Thermal Decomposition of Aluminum Chloride Hexahydrate. *Industrial & Engineering Chemistry Research* **2005**, 44 (17), 6591-6598.
39. Park, K. Y.; Park, Y.-W.; Youn, S.-H.; Choi, S.-Y., Bench-Scale Decomposition of Aluminum Chloride Hexahydrate to Produce Poly(aluminum chloride). *Industrial & Engineering Chemistry Research* **2000**, 39 (11), 4173-4177.
40. Gao, B.; Yue, Q., Effect of $\text{SO}_4^{2-}/\text{Al}^{3+}$ ratio and $\text{OH}^-/\text{Al}^{3+}$ value on the characterization of coagulant poly-aluminum-chloride-sulfate (PACS) and its coagulation performance in water treatment. *Chemosphere* **2005**, 61 (4), 579-584.
41. Leygraf, C.; Wallinder, I. O.; Tidblad, J.; Graedel, T., *Atmospheric corrosion*. John Wiley & Sons: 2016.
42. Portet, C.; Kazachkin, D.; Osswald, S.; Gogotsi, Y.; Borguet, E., Impact of synthesis conditions on surface chemistry and structure of carbide-derived carbons. *Thermochimica Acta* **2010**, 497 (1-2), 137-142.
43. Presser, V.; Heon, M.; Gogotsi, Y., Carbide-Derived Carbons – From Porous Networks to Nanotubes and Graphene. *Advanced Functional Materials* **2011**, 21 (5), 810-833.
44. Pophristic, V.; Balagurusamy, V. S.; Klein, M. L., Structure and dynamics of the aluminum chlorohydrate polymer $\text{Al}_{13}\text{O}_4(\text{OH})_{24}(\text{H}_2\text{O})_{12}\text{Cl}_7$. *Physical Chemistry Chemical Physics* **2004**, 6 (5), 919-923.
45. Pophristic, V.; Klein, M. L.; Holerca, M. N., Modeling Small Aluminum Chlorohydrate Polymers. *The Journal of Physical Chemistry A* **2004**, 108 (1), 113-120.
46. Hsu, P. H., Mechanisms of gibbsite crystallization from partially neutralized aluminum chloride solutions. *Clays and Clay Minerals* **1988**, 36 (1), 25-30.
47. Violante, A.; Huang, P., Formation mechanism of aluminum hydroxide polymorphs. *Clays and Clay Minerals* **1993**, 41 (5), 590-597.

48. Bottero, J. Y.; Cases, J. M.; Fiessinger, F.; Poirier, J. E., Studies of hydrolyzed aluminum chloride solutions. 1. Nature of aluminum species and composition of aqueous solutions. *The Journal of Physical Chemistry* **1980**, *84* (22), 2933-2939.
49. Wang, J.; Lin, Y.; Yue, Q.; Tao, K.; Kong, C.; Chen, L., N-rich porous carbon with high CO₂ capture capacity derived from polyamine-incorporated metal-organic framework materials. *RSC Advances* **2016**, *6* (58), 53017-53024.
50. Lee, S.-Y.; Park, S.-J., A review on solid adsorbents for carbon dioxide capture. *Journal of Industrial and Engineering Chemistry* **2015**, *23*, 1-11.
51. Chen, T.; Deng, S.; Wang, B.; Huang, J.; Wang, Y.; Yu, G., CO₂ adsorption on crab shell derived activated carbons: contribution of micropores and nitrogen-containing groups. *RSC Advances* **2015**, *5* (60), 48323-48330.
52. McBride, M. B.; Wesselink, L. G., Chemisorption of catechol on gibbsite, boehmite, and noncrystalline alumina surfaces. *Environmental science & technology* **1988**, *22* (6), 703-708.
53. Schneider, R. T.; Hauck, F. A., Method for methane production. Google Patents: 1990.
54. Chen, J. P.; Wu, S., Acid/base-treated activated carbons: characterization of functional groups and metal adsorptive properties. *Langmuir* **2004**, *20* (6), 2233-2242.
55. Montes-Morán, M. A.; Suárez, D.; Menéndez, J. A.; Fuente, E., On the nature of basic sites on carbon surfaces: an overview. *Carbon* **2004**, *42* (7), 1219-1225.
56. Yang, S.; Sun, J.; Ramirez-Cuesta, A. J.; Callear, S. K.; DavidWilliam, I. F.; Anderson, D. P.; Newby, R.; Blake, A. J.; Parker, J. E.; Tang, C. C.; Schröder, M., Selectivity and direct visualization of carbon dioxide and sulfur dioxide in a decorated porous host. *Nat Chem* **2012**, *4* (11), 887-894.
57. Zhou, J.-H.; Sui, Z.-J.; Zhu, J.; Li, P.; Chen, D.; Dai, Y.-C.; Yuan, W.-K., Characterization of surface oxygen complexes on carbon nanofibers by TPD, XPS and FT-IR. *Carbon* **2007**, *45* (4), 785-796.
58. Natishan, P. M.; O'Grady, W. E., Chloride Ion Interactions with Oxide-Covered Aluminum Leading to Pitting Corrosion: A Review. *Journal of the Electrochemical Society* **2014**, *161* (9), C421-C432.
59. Augustynski, J.; Painot, J., Discussion of "On the Kinetics of the Breakdown of Passivity of Preanodized Aluminum by Chloride Ions" [Z. A. Foroulis and M. I. Thubrikar (pp. 1296-1301, Vol. 122, No. 10)]. *Journal of The Electrochemical Society* **1976**, *123* (6), 841.

60. Rotole, J. A.; Sherwood, P. M. A., Valence band x-ray photoelectron spectroscopic studies to distinguish between oxidized aluminum species. *Journal of Vacuum Science & Technology A* **1999**, *17* (4), 1091-1096.
61. Alexander, M. R.; Thompson, G. E.; Beamson, G., Characterization of the oxide/hydroxide surface of aluminium using x-ray photoelectron spectroscopy: a procedure for curve fitting the O 1s core level. *Surface and Interface Analysis* **2000**, *29* (7), 468-477.
62. Shi, L.; Yang, K.; Zhao, Q.; Wang, H.; Cui, Q., Characterization and Mechanisms of H₂S and SO₂ Adsorption by Activated Carbon. *Energy & Fuels* **2015**, *29* (10), 6678-6685.
63. Pérez-Cadenas, A.; amp; x; n, F.; Maldonado-Hódar, F. J.; Moreno-Castilla, C., On the nature of surface acid sites of chlorinated activated carbons. *Carbon* **2003**, *41* (3), 473-478.
64. Briggs, D.; Beamson, G., XPS studies of the oxygen 1s and 2s levels in a wide range of functional polymers. *Analytical Chemistry* **1993**, *65* (11), 1517-1523.
65. Castner, D. G.; Hinds, K.; Grainger, D. W., X-ray Photoelectron Spectroscopy Sulfur 2p Study of Organic Thiol and Disulfide Binding Interactions with Gold Surfaces. *Langmuir* **1996**, *12* (21), 5083-5086.
66. Duong, L. V.; Wood, B. J.; Klopogge, J. T., XPS study of basic aluminum sulphate and basic aluminium nitrate. *Materials Letters* **2005**, *59* (14–15), 1932-1936.
67. Guimon, C.; Gervasini, A.; Auroux, A., XPS Study of the Adsorption of SO₂ and NH₃ over Supported Tin Dioxide Catalysts Used in de-NO_x Catalytic Reaction. *The Journal of Physical Chemistry B* **2001**, *105* (42), 10316-10325.
68. Davini, P., Adsorption and desorption of SO₂ on active carbon: The effect of surface basic groups. *Carbon* **1990**, *28* (4), 565-571.
69. Bagreev, A.; Bashkova, S.; Bandosz, T. J., Adsorption of SO₂ on Activated Carbons: The Effect of Nitrogen Functionality and Pore Sizes. *Langmuir* **2002**, *18* (4), 1257-1264.

CHAPTER 5. PARTIAL ETCHING OF MOLYBDENUM CARBIDE FOR THE FORMATION OF MOLYBDENUM BASED NANOPARTICLES

5.1 Introduction

Investigations into aluminum and iron carbide precursors for the simultaneous generation of preordained nanoparticles integrated throughout a tunable carbon host generates interest into how versatile partial etching is as a synthesis technique.¹⁻³ The two aforementioned systems were generated and studied for the adsorption of toxic gases, such as ammonia and SO₂, with an emphasis on metal-based active sites. Metal sites integrated throughout a carbon matrix have a prominent history in the adsorption field which has also extended into catalysis research. To-date a systematic study on the partial etching of a carbide system for potential catalytic use has yet to be conducted.

The molybdenum metal center possess catalytic properties analogous to platinum group metals, providing a series of potential derivatives that excel in catalytic performance such as heterogeneous catalysis,⁴⁻⁵ hydrogen evolution,⁶⁻⁷ alkene metathesis,⁸ and general oxidation reactions.⁹ Therefore, integrating molybdenum-based nanoparticles into a tunable carbide-derived carbon matrix that can facilitate the diffusion of catalytic reagents and products is of interest. The molybdenum carbide precursor is a low cost and widely available reagent that demonstrates thermal stability as well as its own catalytic activity for reactions such as hydrodesulphurization, hydrodenitrogenation, water-gas shift and Fischer Tropsch reaction.¹⁰ Molybdenum carbide-derived carbon is a sparsely studied carbide

derivative, with the majority of literature focusing on fully etched carbon materials.¹¹⁻¹² The porous Mo₂C-derived carbon typically possesses a mixture of micro- and mesopores with mainly amorphous carbon below etching temperatures of 800°C.¹¹ An isolated study was conducted by Valk et. al which synthesized Mo₂C-CDCs at 750°C for different times accompanied by post-synthetic annealing at 900°C for 20 minutes in order to create a carbon-carbide composite to be used as a catalytic support and electrode material.¹³ To the authors knowledge an in-depth study on the effects partial etching has on the residual metal and carbon properties of Mo₂C-CDC has yet to be published. Adequate characterization of the surface chemistry of Mo₂C-CDC was likewise not found in literature, therefore an investigation into the effect of etching temperature on chemical functionality is of interest. Thus, the goal of this work is to develop a systematic knowledge of the role temperature and time play in the retention of residual metal content and carbon properties for partially etched Mo₂C-CDC. Adsorption experiments for CO₂ were performed to study availability of residual metal for future adsorption or catalysis applications.

5.2 Materials and Methods

5.2.1 Materials

Mo₂C-CDC was prepared by depositing 2 g of Mo₂C (American Elements 99% purity -325 mesh) held in a quartz boat inserted into a quartz tube. The tube was placed in a horizontal tube furnace that was operated in the range of 300-700°C with a ramp rate set to 5 °C min⁻¹. During the synthesis argon gas (Airgas 99.999%) is flown over the bed at 150 mL min⁻¹. Once the temperature reaches the desired etching temperature, chlorine gas (Airgas 99.5%) was introduced via an Aalborg mass flow controller at a rate of 40 mL min⁻¹.

¹. Once the etching process was completed, chlorine flow was discontinued and the system is cooled under argon at 150 mL min⁻¹. Samples are labeled as follows Mo₂C-T-CT. Where Mo₂C assigns the species of carbide, T is the etching temperature in degrees Centigrade, and CT is the chlorination time in hours (e.g. Mo₂C-500-1h).

5.2.2 *Methods*

5.2.2.1 Powder X-ray Diffraction

Powder X-ray diffraction (PXRD) patterns were collected using an X'Pert X-ray PANalytical diffractometer with a Cu K α X-ray source ($\lambda = 1.5418 \text{ \AA}$). PXRD diffractograms were collected from a range of 5-50° with a step size of 0.02°. Experiments were carried out at room temperature.

5.2.2.2 Nitrogen Sorption Measurements

Nitrogen sorption measurements were obtained at 77 K using a Quantachrome Quadrasorb SI volumetric analyzer. Prior to each isotherm, ~50 mg of sample was outgassed for approximately 18 hours at 150°C and under vacuum (approximately 20 mTorr). Specific surface areas were calculated using the BET model in the relative pressure range (P/P₀) 0.005-0.03. Pore size distributions were collected for all samples using the Quenched Solid Density Functional Theory (QSDFT) model built into version 5.11 QuadraWinTM software. The QSDFT parameters were selected assuming a nitrogen adsorbate, and carbon adsorbent. The type IV isotherms that were observed exhibit

characteristic cavitation effects, therefore an adsorption branch slit-pore/cylindrical pore model was used.

5.2.2.3 Thermogravimetric Analysis (TGA)

Thermogravimetric analysis for all samples was carried out on a NETZSCH STA 449 F1 Jupiter instrument. Measurements used 20-40 mg of material, heated from 25-1100 °C at a ramp rate of 10 °C min⁻¹ and a flow rate of 20 mL min⁻¹ of air (Airgas 99.999%). The residual metal content was calculated by assuming total combustion of carbon; upon complete combustion, the final mass was assumed to be MoO₃.

5.2.2.4 Scanning Electron Microscopy (SEM) and Elemental dispersive spectroscopy (EDS)

Scanning electron microscopy (SEM) images were obtained using a Zeiss Ultra-60 Field Emission Scanning Electron Microscope. All samples were deposited onto carbon tape. Images were scanned at an accelerating voltage range of 5-10 kV. EDS was employed at an accelerating voltage of 10 kV for elemental compositions.

5.2.2.5 Transmission Electron Microscopy (TEM)

Transmission electron microscopy (TEM) and HRTEM images were obtained using a FEI Tecnai F30 at an operating voltage of 300 kV with a 1.7 Å point resolution. Samples were prepared by suspending approximately 1 mg of sample in methanol and deposited onto a lacy carbon copper grid.

5.2.2.6 CO₂ Adsorption Measurements

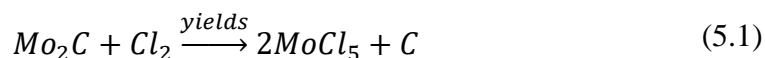
CO₂ isotherms, in the pressure range of 0-1.2 bar, were obtained using a volumetric Micromeritics 3-Flex device at a range of temperatures. Prior to the measurement, 20-50 mg of material was heated in situ at 150 °C for 18 hours under vacuum.

5.2.2.7 X-ray Photoelectric Spectroscopy (XPS) analysis

X-ray photoelectric spectroscopy (XPS) measurements were recorded on a Thermo K-alpha, monochromated Al K α source with a double-focusing hemispherical analyzer. High resolution spectra were taken of C 1s, O 1s, Mo 3d, and Cl 2p at a 0.1 eV step size, 50 ms dwell time, 50 eV pass energy, and a 400 μ m spot size.

5.3 Results and Discussion

The molybdenum carbide system is typically comprised of hexagonal β -Mo₂C with the potential to have trace amounts of poorly crystalized MoC polymorphs throughout the bulk structure.¹⁰ At elevated temperatures, assuming reaction of the bulk β -Mo₂C phase, the simplified reaction of chlorine with molybdenum carbide is depicted in equation 5-1.



β -Mo₂C remains after 1h of etching for all temperatures studied, which can be crystallographically monitored through PXRD, presented in Figure 5-1a. The intensity of the reflections belonging to β -Mo₂C diminish with increased temperature while broad reflections corresponding to γ -MoC begin to appear at 600°C, which is evident in Figure

5-1a. Further etching durations at 600°C show the complete destruction of the bulk β -Mo₂C phase while retaining the poorly crystallized γ -MoC regions. The absence, of reflections in the PXRD patterns, for all samples, of ordered carbon corroborates previous results of a mainly amorphous carbon matrix for Mo₂C-CDCs.¹² The residual β -Mo₂C seen for etching times of 1h is likely a result of diffusion limitations seen during a typical layer-by-layer etching process in a horizontal bed which can lead to unreacted precursor.

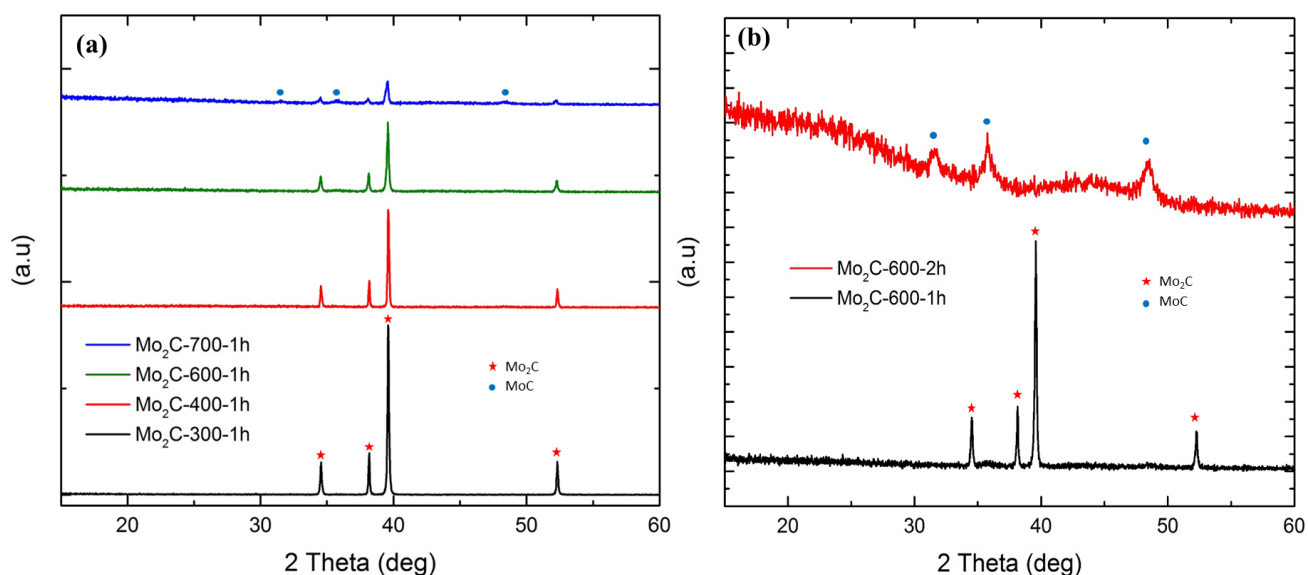


Figure 5-1: Powdered X-ray diffraction of Mo₂C-CDC for (a) 1h of etching at varied temperatures and (b) samples etched at 600°C for 1 and 2 h.

Transmission electron microscopy (TEM) revealed the presence of an abundance of nanoparticles for samples etched between 400-600°C. As presented in Figure 5-2(a and c), a portion of the newly formed nanoparticles are embedded on the surface, displaying accessibility, while other particles are surrounded by a thin amorphous shell of carbon. Both amorphous and crystalline nanoparticles are visible during TEM observations. Some nanoparticles exhibit evidence of an amorphous shell surrounding a crystalline region. Elemental analysis through EDS on the amorphous nanoparticles revealed a concentration

of molybdenum, chlorine and oxygen, as displayed in Figure A-29. The hydration of MoCl_5 to oxychlorides (MoOCl_3 and MoO_2Cl_2) upon atmospheric exposure is expected and is a likely source of the oxygen integrated into parent MoCl_5 .¹⁴ Molybdenum pentachloride presents itself as a dimer in the gas phase with each molybdenum displaying a local octahedral symmetry with two bridging chlorides between metal centers.¹⁵ The bulky dimer along with MoCl_5 's propensity to polymerize likely promotes the retention of nanoparticles as the carbon structure evolves.¹⁶ Analysis of the crystalline regions revealed two distinct lattice spacings (d-spacing) of 1.87 and 2.11 Å, displayed in Figure 5-2e. The d-spacing of 1.87 corresponds to the [1 0 1] plane of γ -MoC which correlates well with the broad peaks seen in Figure 5-1.¹⁷ The second domain may correspond to the [1 0 0] in-plane lattice spacing of graphene dots which are too small to be observed through bulk XRD methods.¹⁸ Residual β - Mo_2C seen in PXRD likely remains in the core of the partially etched sample. Many of the observed crystalline domains are surrounded by a region of amorphous MoO_yCl_x which could provide protection from further chlorination. Furthermore, γ -MoC is never absent in any synthesized material for increased chlorination temperatures or time up to 700°C and 2h. This suggests the etching conditions used in this study are not favorable for γ -MoC to react with chlorine to form molybdenum chloride or the resulting CDC.

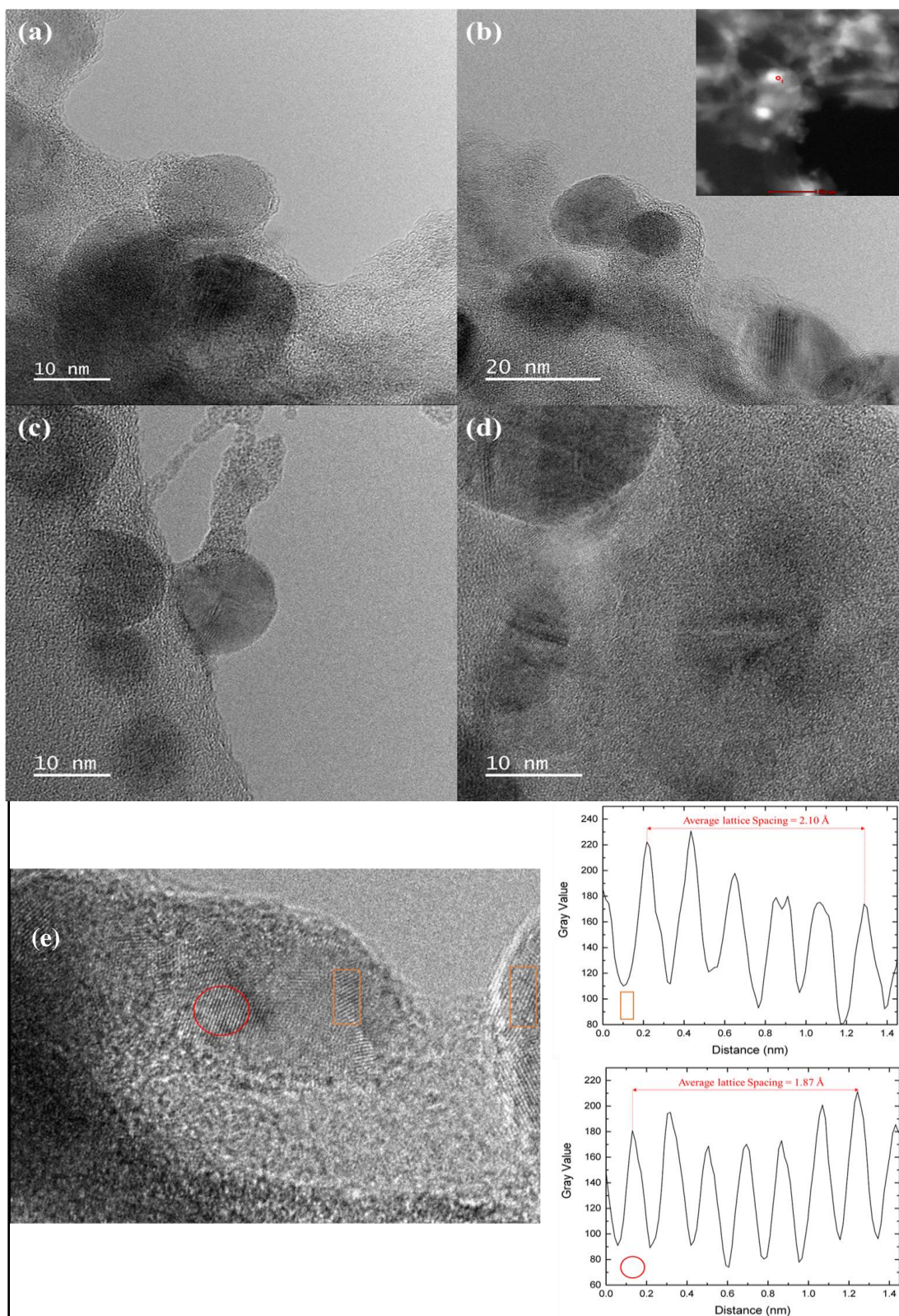


Figure 5-2: High resolution TEM Images of (a & b) Mo_2C -500-1h and (c & d) Mo_2C -600-1h, and (e) lattice spacing of crystalline domains

To gauge degree of etching, the sample mass was weighed directly before and after the etching process. For pure Mo_2C , the resulting CDC should have ~5% of the original mass of the precursor, which correlates well, within experimental error, to the 6.2% achieved through the oxidation of Mo_2C . Figure 5-3a reveals the total residual mass directly after the chlorination process. The linear trend observed with increasing etching temperature, for both times of interest, points to a traditional layer-by-layer extraction process.¹⁹ By doubling the etching time, a significant increase in metal removal is observed with lower etching conditions displaying a higher sensitivity to etching duration. The only sample made that was close to being fully etched was Mo_2C -700-2h with the remaining samples displaying a significant noncarbon residual mass. The amount of residual metal was quantified through TGA analysis as depicted in Figure 5-3b. Between etching temperatures of 300 and 400°C, significant removal of the molybdenum metal center is achieved exposing the lower limit for feasible etching of β - Mo_2C with chlorine. Residual molybdenum content ranged between 0.7-1.8% for etching temperatures between 500-700°C. Notably, molybdenum chloride has a boiling point of 268°C, Mo_2C oxidizes, in air, to molybdenum trioxide (MoO_3) above 450°C which begins to volatilize as low as 500°C with rapid oxidation and vaporization at 725°C.²⁰⁻²² Therefore, these percentages represent the lower boundary of residual metal content with some residual metal likely escaping into the vapor phase during the heating process. Inductive coupled plasma (ICP) should be employed in the future for increased accuracy of the quantity of residual molybdenum species.

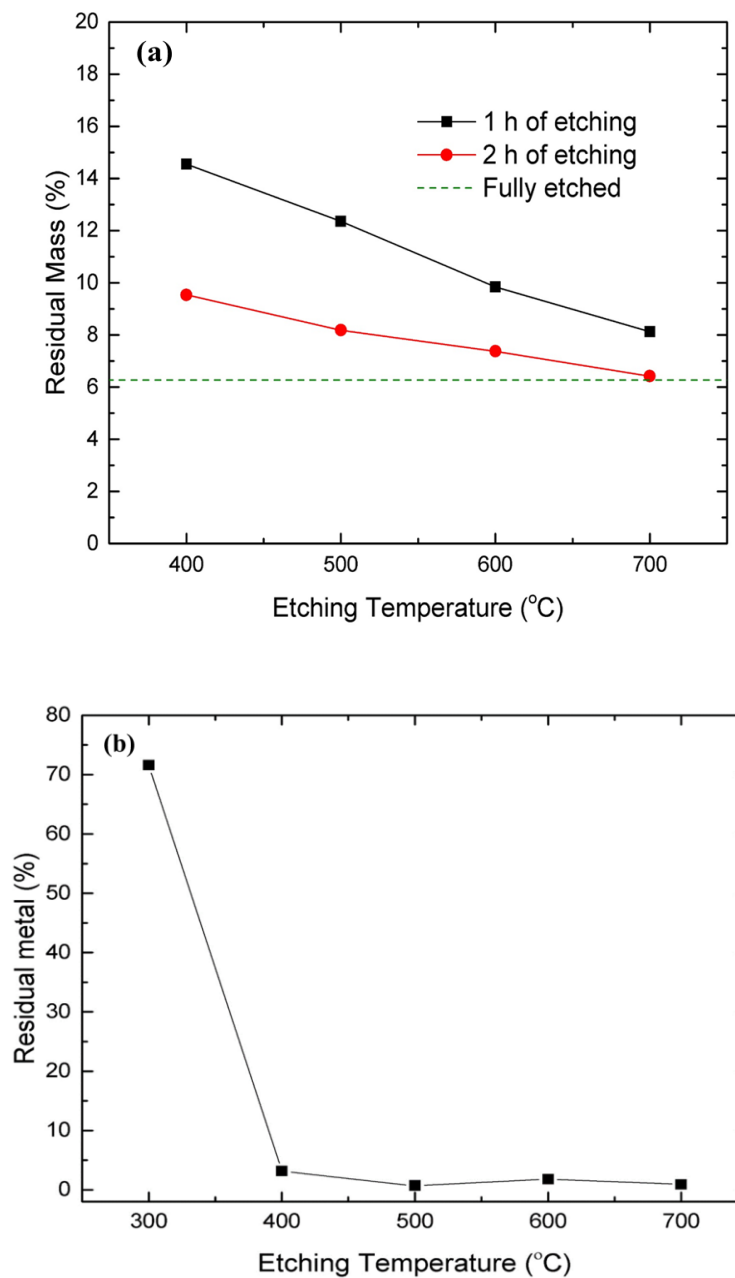
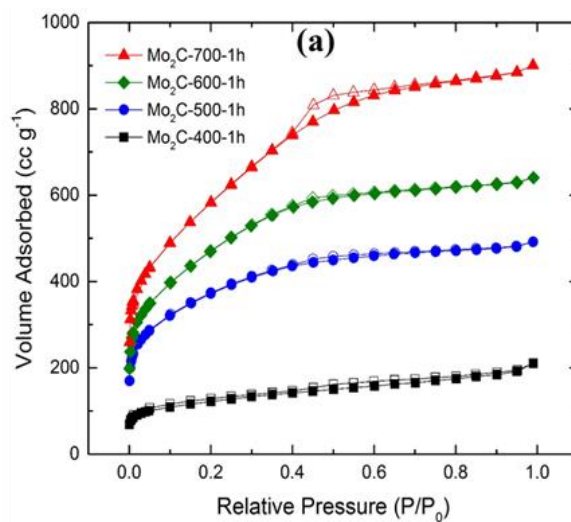


Figure 5-3: (a) Leftover mass after etching process for Mo₂C-CDCs and (b) residual metal content obtained through TGA analysis for Mo₂C-CDCs etched for 1 h

Nitrogen physisorption was employed to probe the physical properties of the carbon matrix as etching temperature was increased. Samples etched at 300°C displayed negligible porosity and were not included for clarity. Samples etched between 400-700°C displayed a Type IV isotherm, while Mo₂C-700-1h began to develop type H2 hysteresis which relates to pore network connectivity effects as the pore structure develops.²³ This can be further explained by examining the PSD evolution between samples etched at 600°C and 700°C. As the etching temperature increases to 700°C, micropore walls begin to break down to generate larger pore structures, as evident by the decrease in microporous and increase in both volume and size of mesopores for Mo₂C-700-1h. Interestingly, the size of the developing micropores do not significantly vary as temperature increases, the main effect on the porous carbon is an increase in the size of mesopores as carbon restructures. An increase in SA was observed as etching time is extended to 2h, as seen in Figure 5-4b. This result is likely caused by the continued removal of MoCl₅ from the porous structure, increasing accessibility.



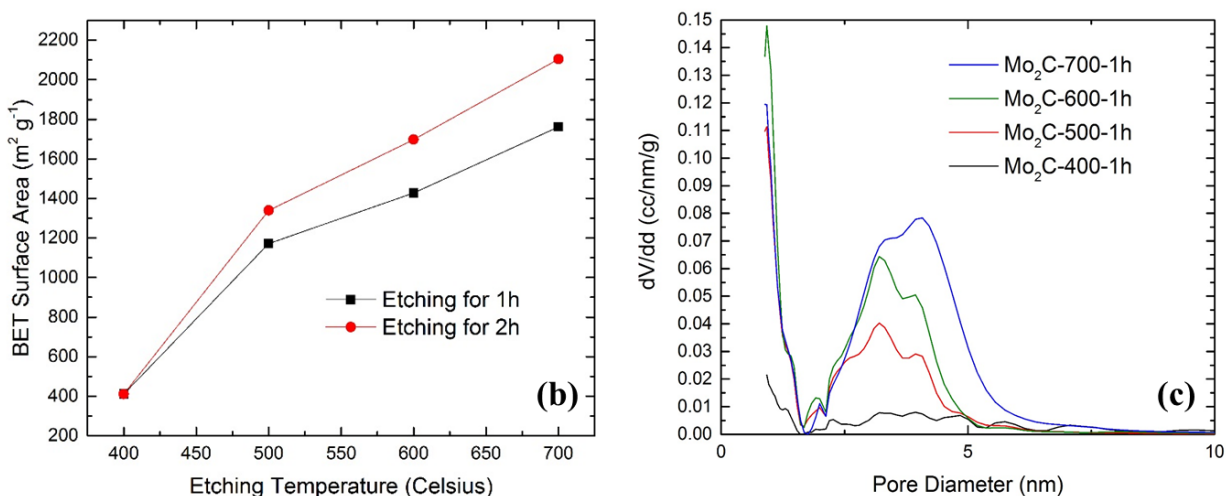


Figure 5-4: Nitrogen physisorption results (a) N₂ Isotherms, (b) BET surface area for samples etched for 1 and 2 h between 400-700°C, and (c) PSD for samples etched for 1 h.

X-ray photoelectron spectroscopy (XPS) was used to reveal the changes in surface chemistry as a function of etching temperature. As seen in Figure 5-5, the carbon matrix involves an anticipated combination of 4 heteroatoms, oxygen, chlorine, nitrogen and residual molybdenum. At an etching temperature of 300°C the CDC material is decorated mainly with chlorine as a result of slow conversion of the carbide to a CDC while lower synthesis temperatures promote the retention of adsorbed chlorine as well as metal chlorides. With increasing etching temperature each hetero atom follows a decreasing trend with atomic concentration on the surface always following $\text{Cl} > \text{O} > \text{N}$, while the surface molybdenum concentration remains relatively consistent around 1%. High quantities of chlorine are expected with the absence of an annealing procedure typical used to rid the samples of the etching agent. With the source of O₂ and N₂ being post-synthetic air exposure, concentrations of oxygen over nitrogen can be contributed to carbons tendency to adopt oxygen functionalities over nitrogen groups to pacify active sites upon atmospheric exposure. The low and consistent concentration of molybdenum in the first 5

nm of the sample is a result of high interfacial chlorine concentrations coupled with the maximum contact time with the etching agent with a near-by bulk gas phase for metal chloride to diffuse towards. This environment likely makes it difficult for nanoparticles to remain heavily decorated on the surface for the conditions used during this experiment.

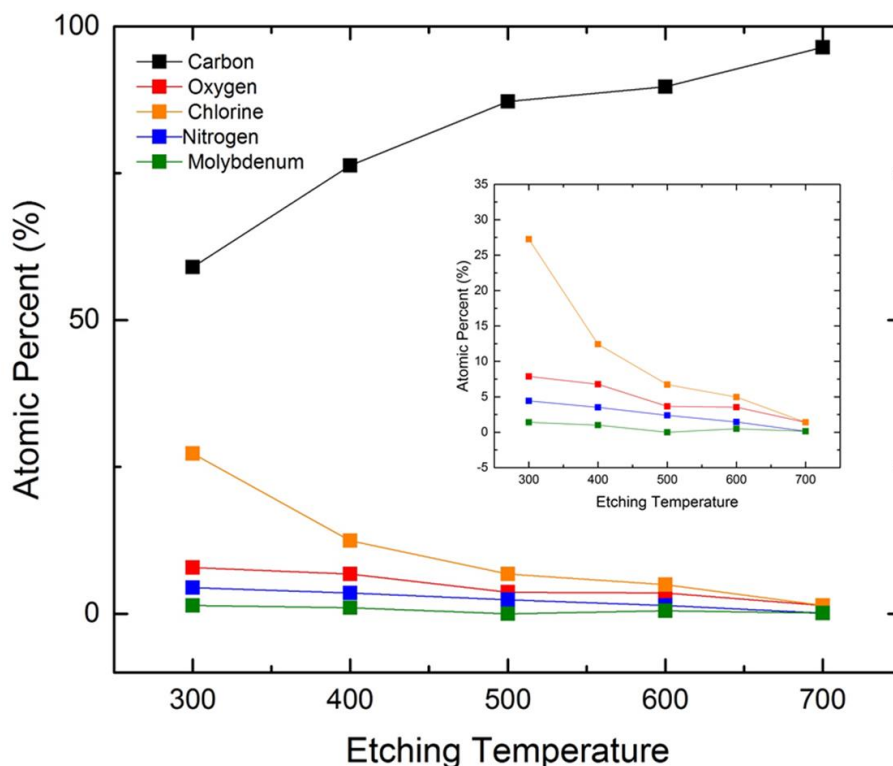


Figure 5-5: XPS trends for surface functionalities between 300-700°C.

XPS was further used to probe the changes in the oxidation state of surface molybdenum through deconvolution of the high-resolution Mo 3d envelope, as seen in Figure 5-6. Molybdenum signals display a well-defined doublet caused by spin-orbit coupling of Mo 3d_{5/2} and Mo 3d_{3/2}, therefore each species is fit with a two peak ratio of 3/2 exhibiting a ~3.13 eV split.²⁴ The binding energy of ~228.3 eV is characteristic of carbide remaining on the surface which is still present in significant quantity for nonporous Mo₂C-

300-1h samples.²⁵ The binding region of ~ 230.4 is characteristic of Mo^{4+} which can indicate the formation of MoO_2 or MoCl_4 which is observed for materials etched at or above 700°C .²⁶ The dominant species found on the surface across all samples was Mo^{6+} , which displays a binding energy of ~ 232.2 eV.^{25, 27} Peaks in this region are characteristic of MoO_3 which is likely a result of the oxidation of surface-based molybdenum nanoparticles after reaction.²⁵ The last observed binding energy of ~ 229.1 eV represents Mo^{3+} which was found in samples etched at 300 and 600°C .²⁸ It is important to note that chlorinated molybdenum complexes exhibit similar binding energies as the oxide species previously mentioned.^{26, 29} Therefore, Cl 2p spectra were collected to observe the presence of residual chlorine. As shown in Figure 5-5f, each sample displayed a prominent doublet at 200.1 eV with a shoulder around ~ 199 -198 eV, fittings removed for clarity. The dominant peak at ~ 200.1 eV is attributed to chlorine chemisorbed to sp^2 and sp^3 carbon.³⁰ The shoulder doublet can be contributed to chlorine dispersed throughout a metal oxide matrix.^{26, 31} Thus, it is likely a portion of the species corresponding to MoO_x are molybdenum oxychlorides, which corroborates previous results of amorphous nanoparticles containing Mo, O and Cl.

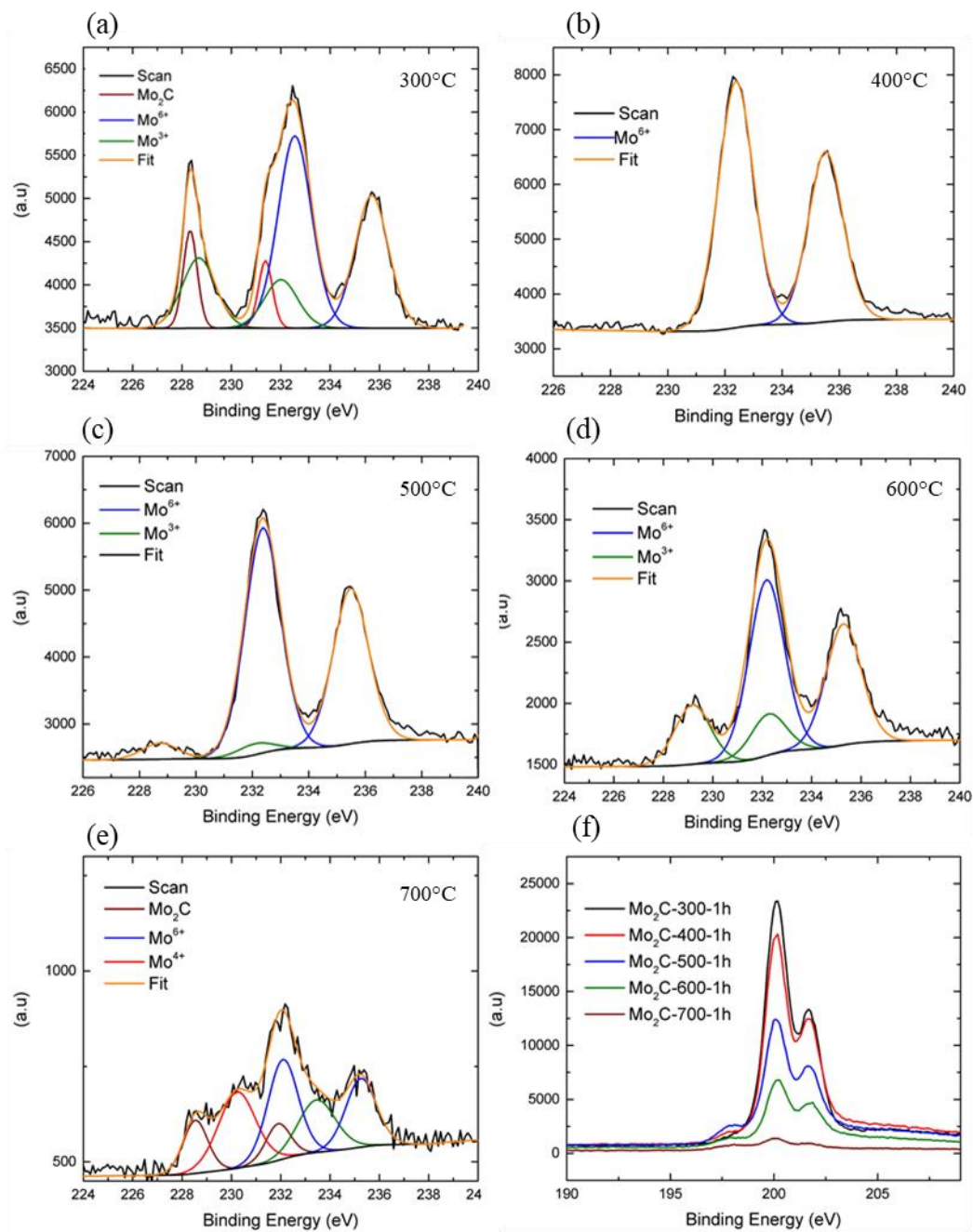


Figure 5-6: High resolution XPS spectra for Mo 3d: (a) Mo₂C-300°C-1h, (b) Mo₂C-400°C-1h, (c) Mo₂C-500°C-1h, (d) Mo₂C-600°C-1h, (e) Mo₂C-700°C-1h, and (f) Cl 2p composite spectrum of etching temperatures 300-700°C.

CO₂ isotherms were collected at 0°C and 25°C, shown in Figure 5-7, to further evaluate the evolution of porosity and determine the effect molybdenum-based nanoparticles have on adsorption. As expected, the low surface area and limited pore volume in Mo₂C-400-1h samples translated into relatively low CO₂ capacities. For CO₂ adsorption at 0°C, the CO₂ behavior correlates with the textural properties of the partially etched samples. When the adsorption temperature is increased to 25°C, analogous behavior is observed for samples etched at temperatures above 400°C. This is a product of the adsorption process becoming increasingly effected by chemical properties of the carbon adsorbent rather than the textural attributes as more energy is added to the system through heat. With each CDC exhibiting similar sized micropores and relatively low concentrations of functional groups, the change in adsorption behavior is not expected to be significant at lower partial pressures. These results indicate that though Mo₂C-CDCs have excellent textural properties and nanoparticles, they lack sufficient chemical heterogeneity for CO₂ adsorption and should be explored further in catalysis where active nanoparticles and tunable PSD will have more of an impact.

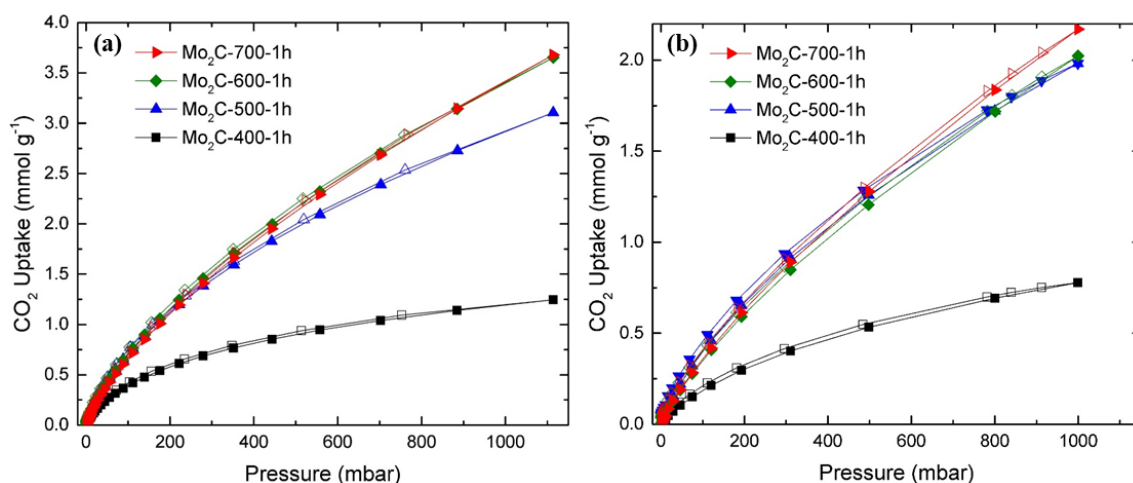


Figure 5-7: CO₂ isotherms for Mo₂C-CDCs (a) 0°C and (b) 25°C

5.4 Conclusions

After reaction of the molybdenum metal center from Mo₂C through chlorination at different temperatures and times, the physical properties of the materials were examined. The retention of bulk phase β -Mo₂C was observed for samples etched for 1 h ranging from 300-700°C. The lower limit of etching was determined to be between 300-400°C with the first porous product observable at 400°C, while lower temperatures yielded a nonporous material. Etching temperatures of 500°C and above began to show poorly crystalized γ -MoC. For temperatures which displayed reflections for the carbide polymorph an increase in etching time to 2h revealed γ -MoC as the only crystalline phase present. A mixture of crystalline and non-crystalline nanoparticles was observed for samples etched between 400-700°C. The crystalline regions exhibit lattice spacings matching γ -MoC while the amorphous regions are attributed to molybdenum oxychloride species via EDS and XPS. The properties of the carbon host display dependence on the etching temperature, with a semi-linear decrease in functional groups as etching temperature is increased and conversion of micropores to mesopores at temperatures above 600°C. This work produces a fundamental base-line for the synthesis of a molybdenum-based catalyst supported by a tunable carbon matrix via a one-pot synthesis method through the partial etching of Mo₂C.

5.5 References

1. Mangarella, M. C.; Walton, K. S., Tailored Fe₃C-derived carbons with embedded Fe nanoparticles for ammonia adsorption. *Carbon* **2015**, 95, 208-219.
2. Mangarella, M. C.; Ewbank, J. L.; Dutzer, M. R.; Alamgir, F. M.; Walton, K. S., Synthesis of embedded iron nanoparticles in Fe₃C-derived carbons. *Carbon* **2014**, 79, 74-84.

3. Moran, C. M.; Marti, R. M.; Hayes, S. E.; Walton, K. S., Synthesis and characterization of aluminum carbide-derived carbon with residual aluminum-based nanoparticles. *Carbon*.
4. Széchenyi, A.; Solymosi, F., Production of Hydrogen in the Decomposition of Ethanol and Methanol over Unsupported Mo₂C Catalysts. *The Journal of Physical Chemistry C* **2007**, *111* (26), 9509-9515.
5. Ma, Y.; Guan, G.; Phanthong, P.; Li, X.; Cao, J.; Hao, X.; Wang, Z.; Abudula, A., Steam reforming of methanol for hydrogen production over nanostructured wire-like molybdenum carbide catalyst. *International Journal of Hydrogen Energy* **2014**, *39* (33), 18803-18811.
6. Weigert, E. C.; South, J.; Rykov, S. A.; Chen, J. G., Multifunctional composites containing molybdenum carbides as potential electrocatalysts. *Catalysis Today* **2005**, *99* (3), 285-290.
7. Vrubel, H.; Hu, X., Molybdenum Boride and Carbide Catalyze Hydrogen Evolution in both Acidic and Basic Solutions. *Angewandte Chemie* **2012**, *124* (51), 12875-12878.
8. Malcolmson, S. J.; Meek, S. J.; Sattely, E. S.; Schrock, R. R.; Hoveyda, A. H., Highly efficient molybdenum-based catalysts for enantioselective alkene metathesis. *Nature* **2008**, *456*, 933.
9. Jitsukawa, K.; Kaneda, K.; Teranishi, S., Molybdenum-catalyzed oxidation of allylic alcohols using tert-butyl hydroperoxide. Regioselective cleavages of the double bond and the adjacent single bond with a hydroxyl group. *The Journal of Organic Chemistry* **1984**, *49* (1), 199-201.
10. Wan, C.; Knight, N. A.; Leonard, B. M., Crystal structure and morphology control of molybdenum carbide nanomaterials synthesized from an amine-metal oxide composite. *Chemical Communications* **2013**, *49* (88), 10409-10411.
11. Jänes, A.; Thomberg, T.; Kurig, H.; Lust, E., Nanoscale fine-tuning of porosity of carbide-derived carbon prepared from molybdenum carbide. *Carbon* **2009**, *47* (1), 23-29.
12. Kim, H. S.; Singer, J. P.; Gogotsi, Y.; Fischer, J. E., Molybdenum carbide-derived carbon for hydrogen storage. *Microporous and Mesoporous Materials* **2009**, *120* (3), 267-271.
13. Valk, P.; Nerut, J.; Tallo, I.; Tee, E.; Vaarmets, K.; Romann, T.; Kurig, H.; Palm, R.; Lust, E., Structure and stability of partially chlorinated molybdenum carbide composite materials synthesised via high temperature chlorination. *Electrochimica Acta* **2016**, *191*, 337-345.
14. Patnaik, P., *Handbook of inorganic chemicals*. 2003; Vol. 529.

15. Sands, D. E.; Zalkin, A., The crystal structure of MoCl₅. *Acta Crystallographica* **1959**, *12* (10), 723-726.
16. Beck, J.; Wolf, F., Three New Polymorphic Forms of Molybdenum Pentachloride. *Acta Crystallographica Section B* **1997**, *53* (6), 895-903.
17. KuO, K.; HÄGg, G., A New Molybdenum Carbide. *Nature* **1952**, *170*, 245.
18. Zheng, B.; Chen, Y.; Li, P.; Wang, Z.; Cao, B.; Qi, F.; Liu, J.; Qiu, Z.; Zhang, W., Ultrafast ammonia-driven, microwave-assisted synthesis of nitrogen-doped graphene quantum dots and their optical properties. *Nanophotonics* **2017**, *6* (1), 259.
19. Presser, V.; Heon, M.; Gogotsi, Y., Carbide-Derived Carbons-Frome Porous Networks to Nanotubes and Graphene. *Advanced Functional Materials* **2011**, *21* (5), 810-833.
20. Burns, R. P.; DeMaria, G.; Drowart, J.; Grimley, R. T., Mass Spectrometric Investigation of the Sublimation of Molybdenum Dioxide. *The Journal of Chemical Physics* **1960**, *32* (5), 1363-1366.
21. Gulbransen, E.; Andrew, K.; Brassart, F., Oxidation of Molybdenum 550 to 1700 C. *Journal of the Electrochemical Society* **1963**, *110* (9), 952-959.
22. Chen, Y.; Zhang, H.; Zhang, J.; Ma, J.; Ye, H.; Qian, G.; Ye, Y.; Zhong, S., Facile synthesis and thermal stability of nanocrystalline molybdenum carbide. *Materials Sciences and Applications* **2011**, *2* (09), 1313.
23. Donohue, M.; Aranovich, G., Classification of Gibbs adsorption isotherms. *Advances in Colloid and Interface Science* **1998**, *76*, 137-152.
24. Choi, J. G.; Thompson, L. T., XPS study of as-prepared and reduced molybdenum oxides. *Applied Surface Science* **1996**, *93* (2), 143-149.
25. Wei, H.; Xi, Q.; Chen, X. a.; Guo, D.; Ding, F.; Yang, Z.; Wang, S.; Li, J.; Huang, S., Molybdenum Carbide Nanoparticles Coated into the Graphene Wrapping N - Doped Porous Carbon Microspheres for Highly Efficient Electrocatalytic Hydrogen Evolution Both in Acidic and Alkaline Media. *Advanced Science* **2018**, *5* (3), 1700733.
26. Hashimoto, K.; Asami, K., An X-ray photo-electron spectroscopic study of the passivity of ferritic 19Cr stainless steels in 1 NHCl. *Corrosion Science* **1979**, *19* (4), 251-260.
27. Oshikawa, K.; Nagai, M.; Omi, S., Characterization of Molybdenum Carbides for Methane Reforming by TPR, XRD, and XPS. *The Journal of Physical Chemistry B* **2001**, *105* (38), 9124-9131.

28. Wolden, C. A.; Pickerell, A.; Gawai, T.; Parks, S.; Hensley, J.; Way, J. D., Synthesis of β -Mo₂C Thin Films. *ACS Applied Materials & Interfaces* **2011**, 3 (2), 517-521.
29. Burgmayer, S. J. N.; Kaufmann, H. L.; Fortunato, G.; Hug, P.; Fischer, B., Molybdenum–Pterin Chemistry. 3. Use of X-ray Photoelectron Spectroscopy To Assign Oxidation States in Metal Complexes of Noninnocent Ligands. *Inorganic Chemistry* **1999**, 38 (11), 2607-2613.
30. Pérez-Cadenas, A.; amp; x; n, F.; Maldonado-Hódar, F. J.; Moreno-Castilla, C., On the nature of surface acid sites of chlorinated activated carbons. *Carbon* **2003**, 41 (3), 473-478.
31. Natishan, P. M.; O’grady, W. E., Chloride ion interactions with oxide-covered aluminum leading to pitting corrosion: a review. *Journal of The Electrochemical Society* **2014**, 161 (9), C421-C432.

CHAPTER 6. EVOLUTION OF TEXTURAL AND CHEMICAL PROPERTIES OF ANNEALED CARBIDE-DERIVED CARBONS FOR ACID GAS ADSORPTION

6.1 Introduction

As global energy demands increase, a delicate balance exists between implementing cost effective energy production strategies and mitigating the effects of pollution associated with such techniques. The production of electricity from natural resources such as coal is intrinsically tied to the emission of acid gas pollutants such as CO₂ and SO₂. Currently, wet scrubbing is the most common technique used to reduce acid gas emissions. Such methods, typically involving amines, are highly efficient but suffer from the disadvantages of installation costs, corrosion, energy demands for solvent processing, and a high regeneration cost for the absorption process.¹⁻² Alternatively an adsorption bed can provide a non-corrosive, and less energy intensive option for the removal of acid gas emissions. Though many porous adsorbents are being developed in literature, such as metal-organic frameworks (MOFs) and zeolites, carbon-based adsorbents remain among the most versatile and affordable options.¹⁻³

The surface chemistry of carbon materials play a distinct and vital role in dictating their performance in applications such as catalysis,⁴ biomedical devices,⁵ electrochemical detectors,⁶ water treatment,⁷ gas sensors,⁸ and adsorption.⁹⁻¹² The adsorption field has received significant attention, with reports examining the complex nature of functional groups, both acidic and basic, in porous carbon materials and their subsequent effects on

the adsorption phenomena. The surface of carbon traditionally contains a variety of complexes where carbon atoms are bound to heteroatoms (i.e., oxygen, nitrogen, hydrogen, chlorine and sulfur).¹³⁻¹⁴ Oxygen species found decorating porous carbon contain both Lewis acid (carboxylic, phenol, carbonyl, lactol) and Lewis base (chromene, ketone, and pyrone) sites while nitrogen functional groups, such as amines, pyrroles and cyclic nitrogen species, are intrinsically basic in nature.^{12, 14-18} Enhancements in acid gas adsorption for activated carbon using Lewis base sites are well documented in literature, highlighting a multitude of techniques to improve carbons overall basicity.^{12, 19}

Carbide-derived carbons (CDCs) are a new class of carbon materials that have received significant attention for their high surface areas and tunable pore-size distributions.²⁰⁻²¹ They exhibit an excellent potential for adsorption applications with a high level of physical tunability that is afforded in the carbon matrix and achieved through the etching process. Presser et. al demonstrated control over the average pore size and total pore volume influences CO₂ adsorption, with the micropore volume of pores <0.8 nm correlating well with CO₂ uptake at low partial pressures.²² However carbide-derived carbon literature currently lacks a sufficient understanding on the effect variables such as carbide precursor, annealing gas, and annealing environment have on the chemistry of CDCs. Limited studies have investigated chlorine removal for select CDCs such as TiC-CDC while largely ignoring changes in surface chemistry.²³⁻²⁵ A majority of CDC literature assumes the annealing process removes or decrease functional groups while a comprehensive study exploring the effects of annealing across different CDCs has yet to be published. The role functional groups play in the adsorption process for CDCs has received little attention in literature, thus an increased understanding of the textural and

chemical changes occurring in CDCs, as a product of annealing environment, is an important step towards producing an optimized adsorbent for any application. Therefore, to increase the fundamental understanding of CDC materials for acid gas adsorption, the physical and chemical properties of carbon derived from TiC, Al₄C₃ and Mo₂C with different annealing environments are investigated within. Correlations between the properties of each CDC and the subsequent adsorption of H₂O, CO₂ and SO₂ are explored to further develop the relationship between synthesis variables and adsorption properties of CDCs.

6.2 Materials and Methods

6.2.1 Materials

Carbide-derived carbons were prepared using one gram of Mo₂C (American Elements 99.9% purity –325 mesh), TiC (Sigma Aldrich 99.98% purity –325 mesh), or Al₄C₃ (Strem Chemicals 98% purity –325 mesh). The carbide precursor was spread out on a quartz boat and inserted into a quartz tube inside a horizontal tube furnace. Samples were heated to 500°C at a ramp rate of 5°C min⁻¹ under 150 ml min⁻¹ of Ar flow (Airgas 99.999%). Once the desired chlorination temperature was reached, chlorine gas (Airgas 99.5%) was introduced into the reactor at a flow rate of 40 ml min⁻¹ for 2 hours, while the Ar flow was maintained.

After 2 hours of etching chlorine was turned off while Ar continued to flow. Non-annealed (NA) samples were held at 500°C for 40 minutes and then cooled to room temperature at 5°C min⁻¹ under. After chlorination, annealed samples were held at 500°C for 40 minutes to allow Cl₂ to be purged from the system to mitigate reaction with the

annealing gas. After the hold, the annealing gas was introduced for 2 hours. For H₂, a 5% H₂ in Ar (Airgas 99.999%) stream was used, flown at 150 ml min⁻¹. For ammonia, a 5% mixture of NH₃ in Ar was generated and flown at 150 ml min⁻¹. For samples annealed in ammonia at 700°C, a 5°C min⁻¹ ramp was used after etching to reach the desired annealing temperature. After the 40-minute ramp the same NH₃ annealing stream as described above was implemented for 2 hours. After each annealing process the samples were cooled under Ar at 5°C min⁻¹ to room temperature. A scrubber solution of concentrated NaOH was used to neutralize acidic gases present in the effluent stream, including HCl, Cl₂, and metal chlorides. These samples are referenced with the following designations: Carbide precursor, etching temperature, etching time, annealing temperature (if increased to 700°C), annealing time, and annealing gas (e.g TiC-500-2h-2h-NH₃).

6.2.2 *Methods*

6.2.2.1 Powder X-ray Diffraction

Powder X-ray diffraction (PXRD) patterns were collected using an X'Pert X-ray PANalytical diffractometer with a Cu K α X-ray source ($\lambda = 1.5418 \text{ \AA}$). PXRD diffractograms were collected from a range of 5-50° with a step size of 0.02°. Experiments were carried out at room temperature.

6.2.2.2 Nitrogen Sorption Measurements

Nitrogen sorption measurements were obtained at 77 K using a Quantachrome Quadrasorb SI volumetric analyzer. Prior to each isotherm, ~50 mg of sample was

outgassed for approximately 18 hours at 150°C and under vacuum (approximately 20 mTorr). Specific surface areas were calculated using the BET model in the relative pressure range (P/P_0) 0.005-0.03. Pore size distributions were collected for all samples using the Quenched Solid Density Functional Theory (QSDFT) model built into version 5.11 QuadraWinTM software. The QSDFT parameters were selected assuming a nitrogen adsorbate, and carbon adsorbent. The type IV isotherms that were observed exhibit characteristic cavitation effects, therefore an adsorption branch slit-pore/cylindrical pore model was used.

6.2.2.3 Scanning Electron Microscopy (SEM) and Elemental dispersive spectroscopy (EDS)

Scanning electron microscopy (SEM) images were obtained using a Zeiss Ultra-60 Field Emission Scanning Electron Microscope. All samples were deposited onto carbon tape. Images were scanned at an accelerating voltage range of 5-10 kV. EDS was employed at an accelerating voltage of 10 kV for elemental compositions.

6.2.2.4 CO₂ and H₂O Adsorption Measurements

CO₂ isotherms, in the pressure range of 0-1.2 bar, and H₂O isotherms ranging from $P/P_0 = 0.0$ -1.0, were obtained using a volumetric Micromeritics 3-Flex device at 25°C. Prior to the measurement, 30-50 mg of material was heated in situ at 150 °C for 18 hours under vacuum.

6.2.2.5 SO₂ Adsorption Measurements

Sulfur dioxides (SO₂) isotherms were collected at 25°C with a range of pressures from 0-3 bar in a lab-build volumetric system. The system operates based on classic pressure decay principles utilizing a sample and reference cell, both of which have their respective pressure monitored in-situ through pressure transducers. The difference in the pressuring readings are subsequently converted and normalized into mol g⁻¹ via the Peng-Robinson equation of state with the appropriate constants and the activated mass of the adsorbent.²⁶ Prior to each isotherm, the samples were activated under vacuum at 150°C for 12h.

6.2.2.6 Dynamic SO₂ adsorption breakthrough

Sulfur dioxide breakthrough experiments were performed in a homemade fixed-bed adsorption set-up utilizing a mass spectrometer: Pfeiffer GSD 320 O2C, OmniStar Gas analysis system 1-200 amu, 100-230 V, 50/60 Hz adapted for corrosive gas. Prior to adsorption, ~50 mg of sample was activated under He flow at 150°C. Breakthrough experiments were performed at 25°C with a flow rate of 20 ml min⁻¹ of 1000 ppm SO₂ balance nitrogen.

6.2.2.7 X-ray Photoelectric Spectroscopy (XPS) analysis

X-ray photoelectric spectroscopy (XPS) measurements were recorded on a Thermo K-alpha, monochromated Al K α source with a double-focusing hemispherical analyzer. High resolution spectra were taken of C 1s, O 1s, Mo 3d, and Cl 2p at a 0.1 eV step size, 50 ms dwell time, 50 eV pass energy, and a 400 μ m spot size.

6.3 Results and Discussion

6.3.1 *Effect of annealing gas and temperature textural properties of carbide-derived carbons*

Nitrogen physisorption was used to probe the changes in BET surface area, pore volume and pore-size distribution of TiC, Al₄C₃ and Mo₂C-CDCs for four different post-etching environments. An increase in surface area and total pore volume is realized when implementing different annealing procedures. The following trend for surface area (SA) and pore volume (PV) is observed across all three carbide precursors: Non-annealed (NA) < H₂ < NH₃(500°C) < NH₃(700°C), as shown in Figure 6-1. The resulting pore structure of the CDC exhibits a correlation with the effectiveness of the annealing procedure. Al₄C₃-CDC and TiC-CDC, mainly microporous materials, displayed significant increases in SA and PV across all annealing environments, Table 6-1. A smaller increase was seen for Mo₂C-CDC, which possess large mesopores (2-6 nm) and broad micropores (1-2 nm), illustrated in Figure 6-1f. The large pore structure of Mo₂C-CDC already facilitates the diffusion of gas species, particularly metal chlorides, throughout of the structure, making it less susceptible to pore blocking through metal chlorides or functional groups. The significant increase in SA and PV for CDCs dominated by narrow micropores is a product of the removal of metal chlorides and chlorine functionalities which have the propensity to block smaller pores. Across all samples, micropores <1.5 nm displayed the largest increase in volume, over all recorded post-etching environments. In each case, using ammonia as an annealing gas was the most effective at increasing porosity. When the annealing procedure was performed with NH₃ at 700°C, there is a noticeable change in PSD with increased pore-wall restructuring. A portion of the narrow micropores in TiC and Al₄C₃ begin to

broaden by 2-3Å and increase in volume, while the highly restructured broad micropores in Mo₂C display a small deviation in PSD, an enhanced image of the PSD can be seen in Figure A-30. The mesopores for Al₄C₃ and Mo₂C also display a small increase across all annealing gases and temperatures due to the increased time for carbon restructuring during the annealing process. The alterations in the pore structure were substantiated with powdered x-ray diffraction Figure A-31. An increase in the sharpness of the (002) reflection at $2\theta = 25.5^\circ$ of graphite can be seen along with the onset of a broad (100) in-plane reflections at $2\theta = 42^\circ$ for TiC and Al₄C₃-CDCs annealed in H₂(500°C) or NH₃(700°C).²⁷ The appearance of a sharp (101) in-plane reflection is also visible in Ti-CDC annealed in H₂(500°C) and NH₃(700°C) corresponding to an increase of order inside graphitic layers. Raman spectroscopy, Figure A-32, support the change in carbon order with a decrease in I(D)/I(G) ratio for all samples annealed in H₂(500°C) or NH₃(700°C). Portet et. al observed a similar increase in carbon ordering in Raman when studying annealed TiC-CDCs.²⁸

Table 6-1: Percent increase in surface area (SA) and pore volume (PV) for three CDCs with three separate annealing environments

Sample	H ₂	NH ₃ (500°C)	NH ₃ (700°C)
Mo ₂ C-CDC	SA = 9%	SA = 13%	SA = 20%
	PV= 7%	PV= 10%	PV= 31%
Al ₄ C ₃ -CDC	SA = 21%	SA = 43%	SA = 53%
	PV= 19%	PV= 40%	PV= 50%
TiC-CDC	SA = 26%	SA = 27%	SA = 46%
	PV= 23%	PV= 26%	PV= 47%

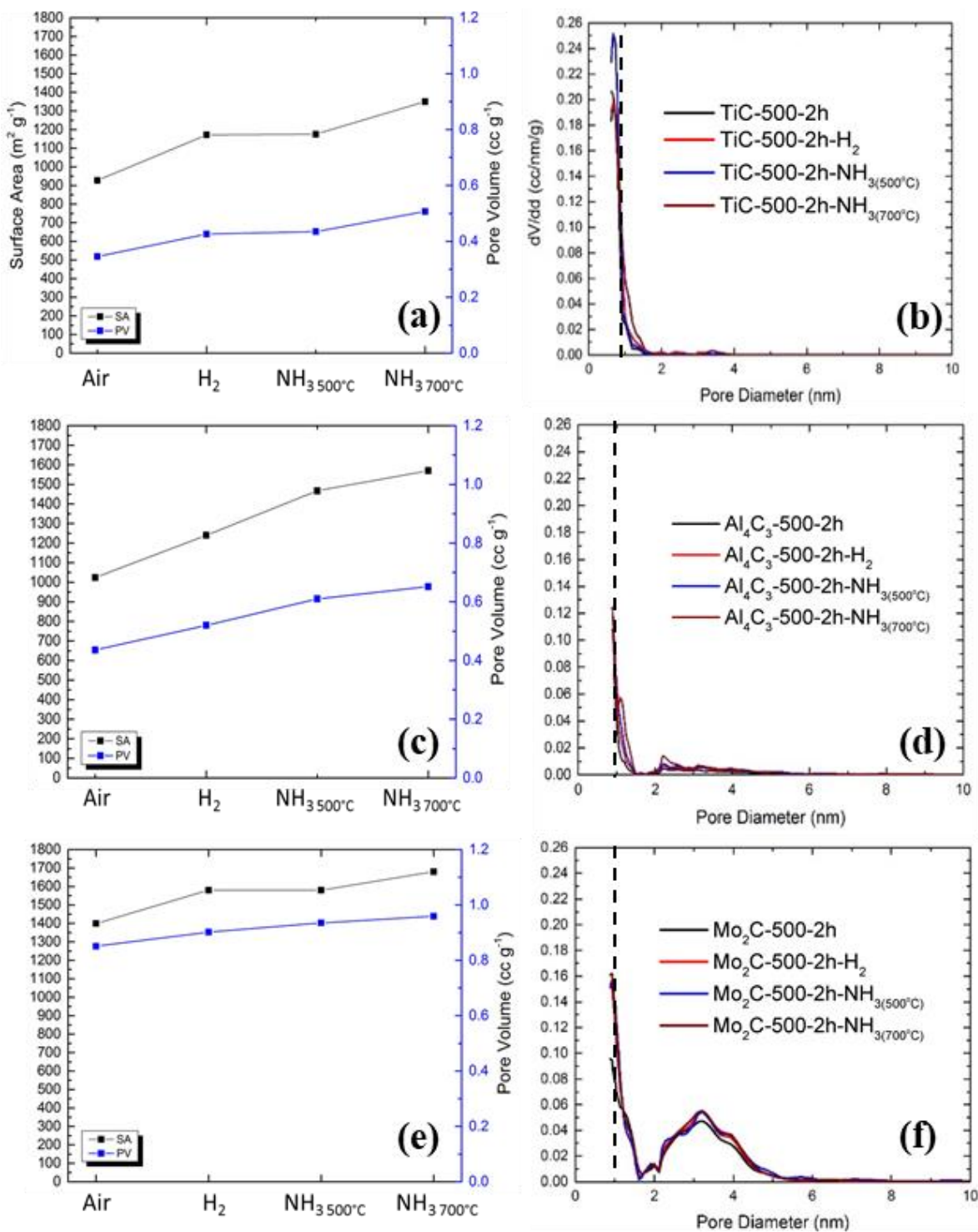


Figure 6-1: Change in BET surface area (SA) and pore volume (PV) for different annealing environments for: (a-b) TiC-CDC, (b-c) Al₄C₃-CDC, and (e-f) Mo₂C. The dashed line represents a pore diameter of 1 nm.

6.3.2 Chemical alterations resulting from the annealing process

Along with textural changes in the carbon, changes in surface chemistry resulting from the annealing environment were probed through XPS and EDS. The relative quantity of each heteroatom was observed through averaging survey scans of the bulk powder, as displayed in Figure 6-2(a-c). Each precursor, absent an annealing procedure, displayed a range of concentrations for oxygen (~3-5%), chlorine (7-8%), and nitrogen (~2.5-9%), illustrating the choice of precursor is the first factor in tuning the surface chemistry of CDCs. As expected, the implementation of any annealing process greatly reduced the chlorine concentration with ammonia treatments decreasing surface chlorine to < 1%. This corroborates the findings of Portet et al., which concluded the reductive environment of NH_3 and H_2 between 600-1100°C is effective at removing residual chlorine from TiC-CDC.²⁵ Oxygen functionalities exhibit no discernable correlation for the effects of annealing across the different carbide precursor used in the study. However, each precursor in isolation displayed significant variations in oxygen content across the different annealing environments. Comparing the lowest and highest concentration of oxygen on the surface for each sample, Al_4C_3 -CDC, TiC-CDC and Mo_2C , exhibited an increase of 96%, 70%, and 176% respectively. Therefore, the reactivity of the resulting CDC after synthesis is likely the dominant factor in the oxidation process of the carbon for the generation of oxygen functional groups once the sample is exposed to air, increasing the effect carbide precursor selection has on the resulting CDC. The effect annealing procedures have on nitrogen content follows a qualitative trend across different CDCs with $\text{NA} > \text{H}_2$ and $\text{NH}_{3(500^\circ\text{C})} > \text{NH}_{3(700^\circ\text{C})}$ with respect to quantity of nitrogen on the surface. The decrease in nitrogen content after H_2 annealing is likely due to the dissociation and subsequent reaction

of hydrogen with active carbon sites that would no longer be available for nitrogen to functionalize. Ammonia treatment at 500°C consistently exhibited the highest nitrogen content with an increase in concentration ranging from ~29-78% compared to non-annealed analogs. A reduction in nitrogen quantity is observed when ammonia annealing is performed at 700°C, a byproduct of the increased order of the carbon matrix leading to reduced reactivity for nitrogen functionalization.

Deconvolution of high-resolution N 1s spectra, Figure A-33, revealed the existence of 5 nitrogen species across all samples (N1-N5). The N1 binding region is located at BE \approx 398 eV, which is characteristic of pyridinic nitrogen while the N2 region at BE \approx 400.3 eV indicates pyrrolic species. The third region is located at BE \approx 400.8-401.5 eV and can be attributed to graphitic nitrogen located in the interior of the polycyclic system. Binding energies near 402.5 eV, classified as N4, indicate protonated pyridine and pyrrolic species while the final region, N5, corresponds to nitrogen oxides.²⁹⁻³² The changes in post-etching environment effected the relative composition of pyrrolic, pyridinic, and graphitic nitrogen surface functional groups, while there were no observable changes in protonated nitrogen species or nitrogen oxides. This demonstrates that not only does annealing CDCs effect the quantity of functional groups, but the relative concentration of species throughout the carbon matrix. Increasing the chemical tunability of the carbon matrix which already possesses a high level of textural flexibility.

Substantiation studies were performed to examine the concentration of heteroatoms in the bulk of the samples via EDS, Figure 6-2 and Figure A-34. Evaluation of the samples revealed the retention of significantly more chlorine species in bulk compared to the surface of the sample. This is likely a result of diffusional limitations during the etching

and annealing process while gases diffuse in and out of the developing structure. Ammonia treatments also provide the most efficient removal of chlorine from the bulk of the sample, analogous to the results seen on the surface via XPS. Bulk nitrogen species follow the same general trend as seen for surface functionalities, with reduced concentrations across all samples. Notably Mo₂C-CDCs displayed minimal concentration of nitrogen throughout the bulk. This observation in tandem with lower concentrations of all heteroatoms suggests a carbon matrix derived from Mo₂C has reduced reactivity with respect to functionalization. Oxygen species do not seem to follow a consistent trend across precursors, analogous to XPS results, further supporting the theory that the carbide and etching temperature provide a heavy influence on the oxidation characteristics of the carbon matrix.

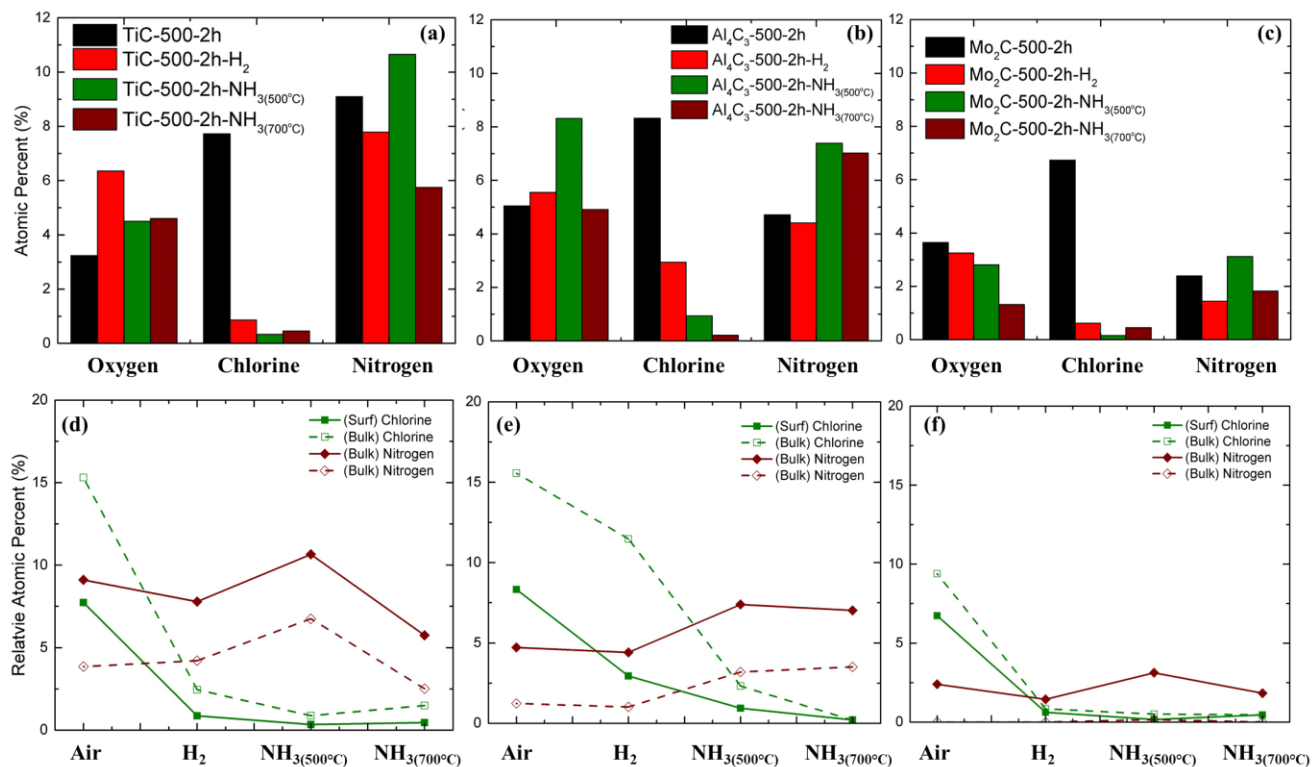


Figure 6-2: XPS analysis of surface chemistry for (a) TiC-CDC, (b) Al₄C₃-CDC and (c) Mo₂C-CDC and comparison of XPS (Surface concentration) and EDS (Bulk concentration) of (d) TiC-CDC, (e) Al₄C₃-CDC, and (f) Mo₂C-CDC

6.3.3 Adsorption behaviour of annealed CDCs for CO₂ adsorption

CO₂ is a non-polar linear molecule, classified as a weak acid gas, which is typically physisorbed by porous carbon materials. Several studies involving carbon adsorbents demonstrate an increase in micropores or basic functional groups, in particular nitrogen, correlate with increased CO₂ adsorption.^{22, 33-34} Therefore, CO₂ isotherms in Figure 6-3 were taken at 25°C to observe how the changes in porosity and surface chemistry effected CO₂ interactions. In all cases the non-annealed samples displayed the lowest capacity for CO₂. The lower adsorption is a direct consequence of reduce microporosity and functional group density compared to annealed materials. The highest CO₂ capacity, reaching ~4 mmol g⁻¹ at 1 bar for Al₄C₃-CDC and TiC-CDC, was observed for samples annealed in NH₃(500°C). Table 6-2 demonstrates the increase in adsorption for samples annealed in NH₃(500°C) correlate with both increased nitrogen and micropore volume. Interestingly, the samples annealed in NH₃(700°C) displayed lower CO₂ capacities with higher surface area and pore volume. This result indicates that the reduced nitrogen content and pore broadening that occurs offsets the increase in total micropore volume at the higher annealing temperature. Further indication of the importance of nitrogen for CO₂ adsorption can be seen in Figure 6-3. With many applications looking at CO₂ removal from air, 0.4 mbar (400 ppm) of CO₂ was chosen to observe correlations with both physical and chemical properties of the CDC adsorbents. A strong linear correlation is observed with surface and bulk nitrogen content at low pressure for CO₂ capacity. Oxygen content and micro-mesoporosity were also graphed, Figure A-35, each factor displayed weak or non-existent correlations with 400 ppm CO₂ capacity. For increasing oxygen content, a general increase in CO₂ adsorption is observed but exhibits a broad range of adsorption for similar

concentrations, which is likely a product of the simultaneous existence of basic and acidic functionalities contributing to the total oxygen concentration. Therefore, it can be concluded that total micropore volume only explains a portion of CO₂ adsorption, with CDC functionalities, particularly nitrogen, playing a significant role in the adsorption process at low pressures (≤ 1 bar). Notably, all annealed Mo₂C-CDCs display similar capacities, corresponding to low functional group density across the board similar PSDs.

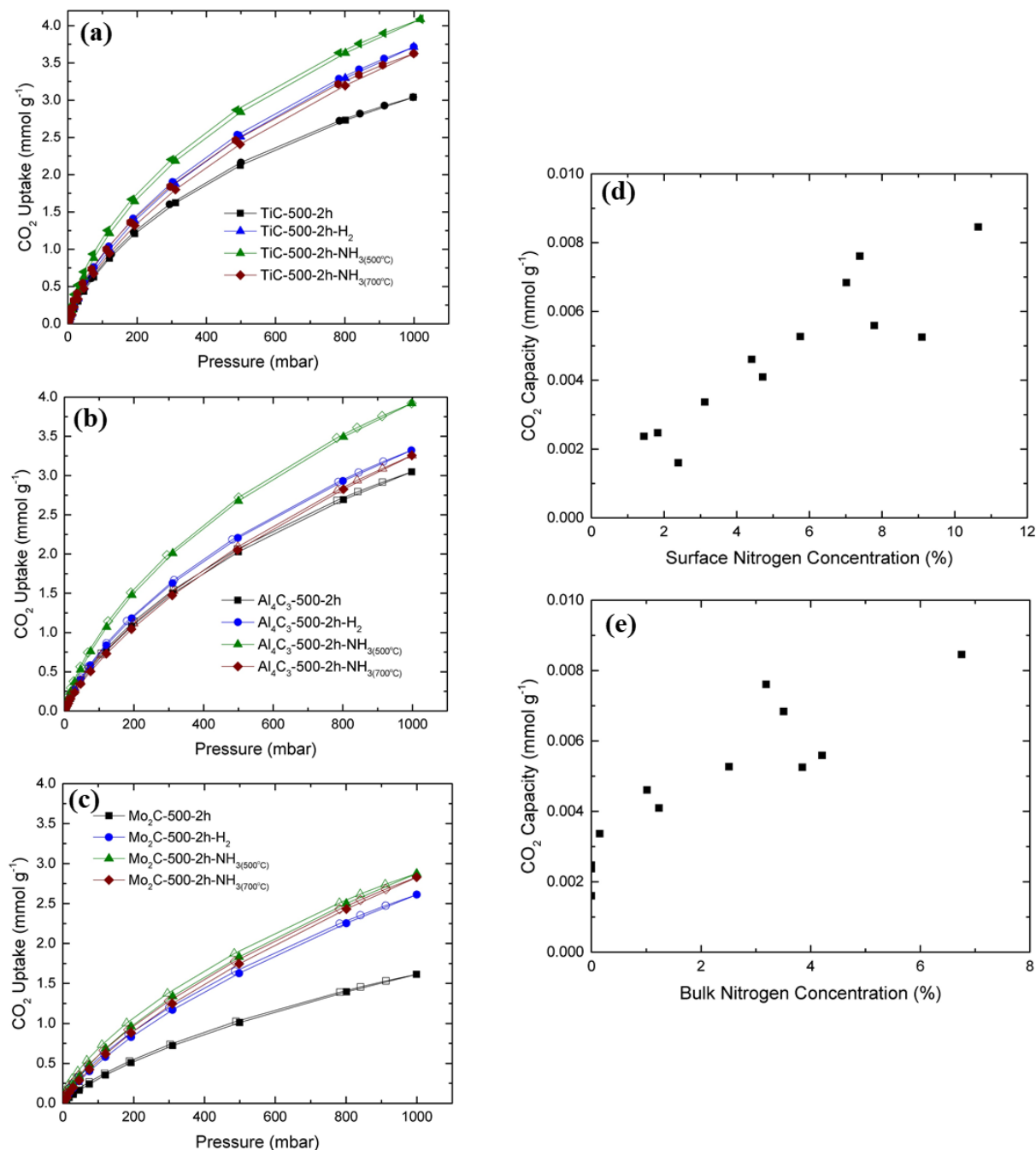


Figure 6-3: CO₂ adsorption isotherms at 25°C up to 1 bar for (a) TiC-CDC, (b) Al₄C₃-CDC and (c) Mo₂C-CDC under different post-etching environments. Adsorption at 400 ppm CO₂ vs (d) surface nitrogen and (e) bulk nitrogen concentration.

Table 6-2: Changes in CO₂ capacity at 1 bar and 25°C compared to changes in surface nitrogen and micropore volume for non-annealed samples and those annealed in NH₃ at 500°C.

Precursor	NA	NH₃(500°C)	Increase in CO₂ @ 1 bar	Increase in N	Increase in Micropores
TiC	3.039	3.08	34.3%	57%	28%
Al₄C₃	3.04	3.92	28.9	29%	30%
Mo₂C	1.61	2.87	78.3%	17%	11%

6.3.4 Textural and chemical influence on water adsorption

Water vapor is both a relevant constituent of most adsorption applications as well as a probe molecule to test the influence of functional groups and pore structure. Studies have also demonstrated the presence of water can significantly affect the co-adsorption of CO₂ and SO₂ throughout carbon adsorbents.³⁵⁻³⁷ Thus, the changes in water adsorption behavior with respect to annealing environment was investigated. A well-studied dipole exists across water molecules, placing a partial negative on the oxygen and partial positives on the hydrogen. Such polarity imparts heavy influence towards functional sites in carbon, more so than non-polar molecules, like CO₂. Figure 6-4 depicts water isotherms at 25°C across the four different post-etching environments for all three CDCs of interest. Mainly microporous TiC-CDCs display a Type III isotherm, while Al₄C₃-CDCs, a microporous adsorbent with a degree of mesopore formation, exhibits a Type IV isotherm. When Al₄C₃-CDCs are annealed in NH₃(700°C) the adsorption behavior transitions to a Type III isotherm,

a consequence of reduced overall oxygen and nitrogen content alongside noticeable pore widening. Both Al_4C_3 -CDC and TiC -CDCs show quick uptake of water at lower partial pressures leveling off after $P/P_0 = 0.4$ - 0.5 , exemplifying hydrophilic behavior. Mo_2C -CDCs display a Type V isotherm which exhibit hydrophobicity at low partial pressures followed by pore condensation at $P/P_0 = 0.4$ - 0.5 , with a large hysteresis loop observed upon desorption. The hydrophobic behavior coincides with the small number of polar heteroatoms throughout the sample, which are responsible for facilitating low pressure interaction with water molecules. At high partial pressures, each CDC displays the same trend for the four post-etching environments. Non-annealed samples exhibited the lowest capacities, H_2 and $\text{NH}_3(500^\circ\text{C})$ samples exhibited the same capacity, and $\text{NH}_3(700^\circ\text{C})$ samples reached the highest water adsorption across all carbide precursors. The high saturation capacities for $\text{NH}_3(700^\circ\text{C})$ samples are attributed to the increased pore volume and SA observed in Figure 6-1. The similar capacities for H_2 and $\text{NH}_3(500^\circ\text{C})$ are a result of analogous PSDs before the structure is fully saturated. The authors would like to point out that the adsorption process was stopped before $P/P_0 = 0.9$ to reduce the risk of water condensing in interstitial spacing throughout the adsorbent. Before reaching $P/P_0 = 1$, each sample displays various slopes in the isotherm as it approaches higher partial pressures, indicated the pores are not fully saturated. If higher saturations were reached, a small separation would likely be visible between $\text{H}_2(500^\circ\text{C})$ and $\text{NH}_3(500^\circ\text{C})$ samples. The lower partial pressure region ($P/P_0 = 0$ - 0.5) is dictated by the presence of heteroatoms and micropores across the different samples, as seen in Figure 6-4. The dipole interaction of water with additional functional groups and an increase in microporosity facilitate the increase in water adsorption for $\text{NH}_3(500^\circ\text{C})$ samples. Similar trends are highlighted in

activated carbon literature, along with adsorption models to describe water vapor adsorption onto porous carbon.³⁸ Specifically, nitrogen functionalities have shown to increase the polarity of carbons surface with pyridinic nitrogen increasing negative charge and quaternary nitrogen inducing a positive charge.³⁹ Samples annealed in $\text{NH}_3(700^\circ\text{C})$ exhibited a decreased interactions with water at low relative humidity's as a result of pore broadening and an increase in carbon ordering. These observations highlight the degree of tunability that can be achieved for CDC adsorbents through the dual effect annealing provides on both textural and chemical properties of CDCs.

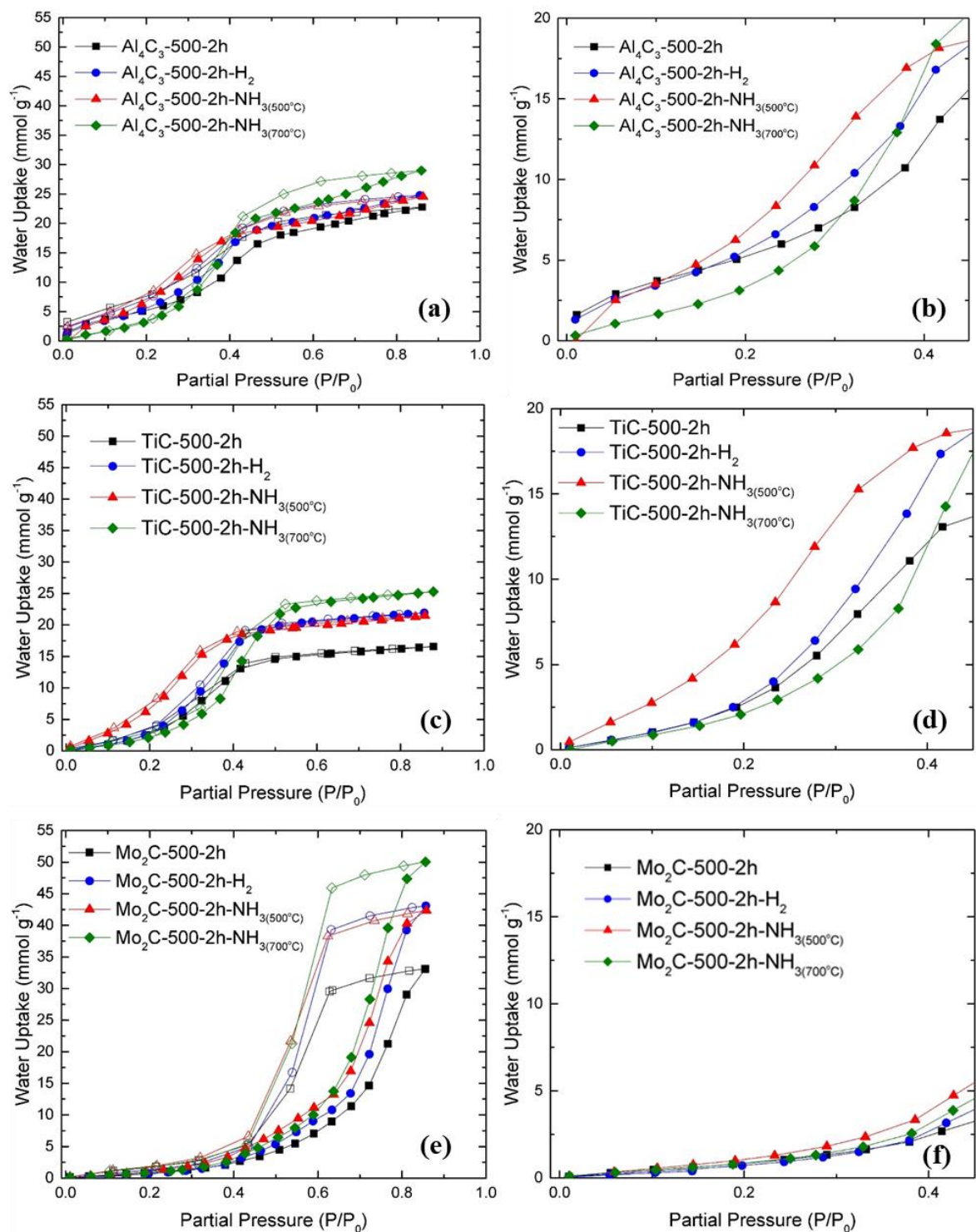


Figure 6-4: Water adsorption at 25°C for (a & b) TiC-CDC, (b & d) Al₄C₃-CDC, and (c & f) Mo₂C-CDC annealed under different environments

6.3.5 Sulfur dioxide adsorption dependence on chemical heterogeneity and pore size

The influence of physical and chemical properties for the studied CDCs were further investigated with sulfur dioxide (SO₂) isotherms at 25°C, displayed in Figure 6-5. All CDCs studied display a sharp uptake at pressures below 250 mbar, indicative of SO₂ interactions with functional groups and adsorption in micropores. There is a noticeable increase in absolute capacities of SO₂ compared to CO₂ across all samples due to the larger kinetic size, increase polarizability and adsorption orientation of the gas molecule.⁴⁰ Two trends become prevalent across the 12 samples in which SO₂ isotherms were recorded. Nitrogen content appears to have a stronger influence with pressures of SO₂ ≤ 100 mbar indicating nitrogen activity in the micropores. The second trend relates to oxygen content which depicts a correlation between increased oxygen and SO₂ adsorption up to 1 bar, illustrating reactivity of oxygen functionalities in both small and large pore structures. These trends can be seen in Figure 6-5.

For Mo₂C-CDC samples shown in Figure 6-5c, only Mo₂C-CDC treated with H₂ at 500°C had a noticeable increase beyond the first pressure point recorded. After the initial adsorption step, each isotherm displays a gradual slope that does not reach saturation by 2.75 bar, correlating with continued SO₂ interaction in the mesopores. With adsorption near the beginning of the isotherm dictated by interactions in the micropores, the significant increase of capacity at higher pressures relate to changes in larger pore structures. With similar PSD for all annealed Mo₂C-CDCs, and less overall nitrogen and oxygen functionalities for H₂ annealed samples, a change in oxygen functional group identity is likely responsible for the observed increase in uptake. With a mixture of basic and acidic oxygen moieties known to exist for carbon materials, a change towards more basic oxygen

sites would promote the oxidation of SO_2 towards SO_3 throughout pores that are large enough to facilitate the reaction.^{36, 41-42} The effect of nitrogen functional groups on the reactivity of neighboring oxygen should also be considered, which can affect the degree of oxidation of SO_2 .^{36, 43} With extremely opaque materials, vibrational techniques such as ATR (attenuated total reflectance), shown in Figure A-36, provided broad and weak peaks that cannot be responsibly deconvoluted to identify such changes, a notorious problem in carbon literature. However, it is evident that the presence of large mesopores result in Mo_2C -CDC samples obtaining the highest capacity for SO_2 at higher pressures, directly relating to the superior pore volume and surface area. The trend of increased high-pressure capacity with increase mesopore volume is depicted in Figure 6-5(i) and begins to become significant at 1 bar for all samples. In contrast, Al_4C_3 -CDC and TiC -CDC incurred significant changes in SO_2 interaction across all annealing environments, analogous to previous adsorption behavior for CO_2 and H_2O isotherms. For both Al_4C_3 -CDC and TiC -CDC, samples annealed in H_2 and $\text{NH}_3(500^\circ\text{C})$ exhibited increased capacities, when compared to non-annealed samples, for all recorded pressures. Figure 6-5(d,f,h) demonstrate the influence of microporosity, bulk nitrogen and bulk oxygen on low pressure adsorption of SO_2 . A correlation is observed for SO_2 adsorption at 0.01 bar, connecting an increase in nitrogen and oxygen content with an increase in low pressure SO_2 capacity. As pressures increase to 0.1 and 1 bar, correlations with nitrogen content begins to drop off while a general upward trend can still be made for oxygen species. A small increase in SO_2 capacity can be seen with improved microporosity at SO_2 pressures ≤ 0.1 bar. These trends indicate that SO_2 adsorption is strongly dictated by the presence of oxygen and nitrogen content throughout the microporous regions of carbide-derived carbons. It is noteworthy

to mention that annealed TiC-CDCs, Figure 6-5(a), exhibit the strongest interactions with SO₂ up to 100 mbar, reaching between 6-8 mmol g⁻¹. These materials, as shown previously, are purely microporous structures which possess the largest quantity of functional groups compared to the other CDCs studied, supporting the importance of functional group density through the microporous region for low pressure adsorption. At increased pressures, TiC-CDCs display similar SO₂ isotherms for H₂ and NH₃(500°C) samples due to the degraded influence that micropores possess at high pressures, where capacities become dictated by mesopores and saturation of pore volume, illustrated in Figure 6-5(h,i). Al₄C₃-CDC displays a combination of the behavior seen for TiC and Mo₂C derivatives. A similar low-pressure increase is seen for samples annealed in NH₃ and H₂, however, at elevated pressures, samples annealed in H₂ begin to display higher capacities. This behavior reflects the same interaction with mesopores seen for Mo₂C-CDCs. Al₄C₃-500-H₂ materials contain increased oxygen content and reduced nitrogen compared NH₃ annealed materials throughout the hybrid micro-mesoporous structure. This points towards stronger SO₂ interactions with oxygen groups in larger pores compared to nitrogen functionalities. This trend reveals similar results to finding by Joshi et. al when studying nitrogen functionalities in metal-organic frameworks for H₂S adsorption. A correlation between nitrogen groups and the textural properties of MOFs was established, where an increase in the pore size of the framework correlated with a reduced effectiveness of nitrogen groups to interact with H₂S.⁴⁴ Studies on carbon have also alluded to pore size playing an important role in SO₂ adsorption resulting in increased capacity.³⁶ The findings in this work illustrates that changes in functionalities, relating to both microporous and mesoporous regions have a

profound effect on CDC adsorption behavior. While also giving insight into the roles of oxygen and nitrogen at different partial pressures.

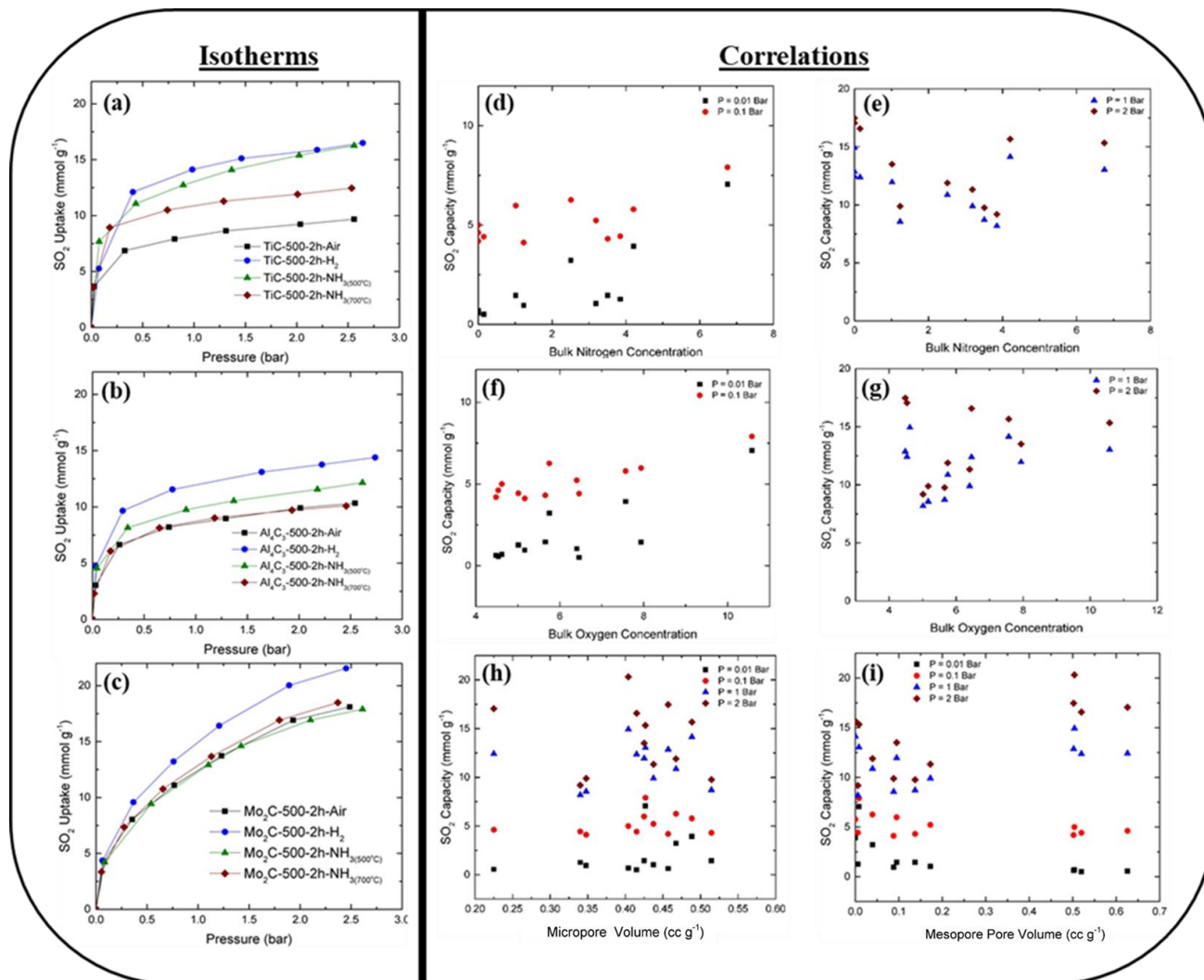


Figure 6-5: SO₂ isotherms at 25°C for (a) TiC-CDCs, (b) Al₄C₃-CDCs, and (c) Mo₂C-CDC for four separate post-etching conditions. SO₂ capacity vs (d-e) bulk nitrogen content, (f-g) bulk oxygen content, (h) micropore volume ($\leq 2\text{nm}$), and (i) mesopore volume ($>2\text{nm}$) at different pressures (P) of SO₂

6.4 Conclusions

An investigation into the effects that annealing environments have on Al_4C_3 , TiC , and Mo_2C -CDCs, with an emphasis on adsorption applications, has been performed. The surface area and pore volume of each carbide-derived carbon saw a systematic increase ranging from non-annealed, H_2 , $\text{NH}_3(500^\circ\text{C})$, and $\text{NH}_3(700^\circ\text{C})$ samples. Changes in the quantity and identity of functional groups on the surface were observed across different carbide precursors and annealing environments providing a new understanding on the effects of carbide choice and post-etching treatment. The density of oxygen on the surface and the interior of the CDC demonstrated a strong dependence on the carbide precursor with each derivative exhibiting unique variations in oxygen as the annealing environment was altered. The introduction of NH_3 allowed for control over the nitrogen content across all CDCs, with materials annealed at 500°C in NH_3 displaying the highest nitrogen densities. A higher concentration of chlorine in the interior of each sample compared to the surface points towards diffusional limitations during the annealing process. Suggesting increased time and annealing temperatures are required for complete removal of chlorine functionalities. In all cases, annealed samples possessed equal or higher capacities for the adsorption of CO_2 , H_2O , and SO_2 . A combination of micropores, oxygen, and nitrogen functionalities contributed to an overall increase in interaction of non-polar CO_2 , improving between 30-80%, and significantly affected low partial pressure adsorption of polar H_2O and SO_2 . For CO_2 and H_2O , an increase in nitrogen content is directly correlated with an increase in low pressure adsorbate interactions. Trends in SO_2 adsorption correlate with changes in functional groups in both micropores and mesopores for low and moderate pressures respectively. Nitrogen content was demonstrated to be effective for pressures at

or below 100 mbar, while oxygen content correlated with increased capacity in mesopores as a likely result of basic oxygen sites available for oxidation. TiC-CDC annealed in H₂ at 500°C reached capacities of 8 mmol g⁻¹ at 25°C and 100 mbar, which is amongst the highest reported for carbon-based adsorbents. This work for the first time highlights the profound effects annealing treatments can have on different carbide-derived carbons with respect to, porosity, chemistry, and adsorption behavior. This insight offers another degree of tunability, beyond angstrom level tuning of pores, for CDC applications that are affected by the chemistry of carbonaceous materials as exemplified by the adsorption phenomena in this study.

6.5 References

1. Vaesen, S.; Guillerm, V.; Yang, Q.; Wiersum, A. D.; Marszalek, B.; Gil, B.; Vimont, A.; Daturi, M.; Devic, T.; Llewellyn, P. L.; Serre, C.; Maurin, G.; De Weireld, G., A robust amino-functionalized titanium(IV) based MOF for improved separation of acid gases. *Chemical Communications* **2013**, 49 (86), 10082-10084.
2. Lee, Y.-W.; Park, J.-W.; Choung, J.-H.; Choi, D.-K., Adsorption Characteristics of SO₂ on Activated Carbon Prepared from Coconut Shell with Potassium Hydroxide Activation. *Environmental Science & Technology* **2002**, 36 (5), 1086-1092.
3. Ackley, M. W.; Rege, S. U.; Saxena, H., Application of natural zeolites in the purification and separation of gases. *Microporous and Mesoporous Materials* **2003**, 61 (1-3), 25-42.
4. Figueiredo, J. L., Functionalization of porous carbons for catalytic applications. *Journal of Materials Chemistry A* **2013**, 1 (33), 9351-9364.
5. Smart, S. K.; Cassady, A. I.; Lu, G. Q.; Martin, D. J., The biocompatibility of carbon nanotubes. *Carbon* **2006**, 44 (6), 1034-1047.
6. Trojanowicz, M., Analytical applications of carbon nanotubes: a review. *TrAC Trends in Analytical Chemistry* **2006**, 25 (5), 480-489.
7. Bhatnagar, A.; Hogland, W.; Marques, M.; Sillanpää, M., An overview of the modification methods of activated carbon for its water treatment applications. *Chemical Engineering Journal* **2013**, 219, 499-511.

8. Dai, L.; Soundarrajan, P.; Kim, T., Sensors and sensor arrays based on conjugated polymers and carbon nanotubes. *Pure and Applied Chemistry* **2002**, 74 (9), 1753-1772.
9. Boehm, H.-P., Chapter Thirteen - Surface Chemical Characterization of Carbons from Adsorption Studies. In *Adsorption by Carbons*, Elsevier: Amsterdam, 2008; pp 301-327.
10. Jia, Y. F.; Xiao, B.; Thomas, K. M., Adsorption of Metal Ions on Nitrogen Surface Functional Groups in Activated Carbons. *Langmuir* **2002**, 18 (2), 470-478.
11. Moreno-Castilla, C.; Carrasco-Marin, F.; Utrera-Hidalgo, E.; Rivera-Utrilla, J., Activated carbons as adsorbents of sulfur dioxide in flowing air. Effect of their pore texture and surface basicity. *Langmuir* **1993**, 9 (5), 1378-1383.
12. Shafeeyan, M. S.; Daud, W. M. A. W.; Houshmand, A.; Shamiri, A., A review on surface modification of activated carbon for carbon dioxide adsorption. *Journal of Analytical and Applied Pyrolysis* **2010**, 89 (2), 143-151.
13. Leóny León, C. A.; Radovic, L. R., *Interfacial chemistry and electrochemistry of carbon surfaces*. 2001; Vol. 24, p 225-310.
14. Montes-Morán, M. A.; Suárez, D.; Menéndez, J. A.; Fuente, E., On the nature of basic sites on carbon surfaces: an overview. *Carbon* **2004**, 42 (7), 1219-1225.
15. Barton, S. S.; Evans, M. J. B.; Halliop, E.; MacDonald, J. A. F., Acidic and basic sites on the surface of porous carbon. *Carbon* **1997**, 35 (9), 1361-1366.
16. Chen, J. P.; Wu, S., Acid/base-treated activated carbons: characterization of functional groups and metal adsorptive properties. *Langmuir* **2004**, 20 (6), 2233-2242.
17. Contescu, A.; Contescu, C.; Putyera, K.; Schwarz, J. A., Surface acidity of carbons characterized by their continuous pK distribution and Boehm titration. *Carbon* **1997**, 35 (1), 83-94.
18. Lopez-Ramon, M. V.; Stoeckli, F.; Moreno-Castilla, C.; Carrasco-Marin, F., On the characterization of acidic and basic surface sites on carbons by various techniques. *Carbon* **1999**, 37 (8), 1215-1221.
19. Boudou, J.-P.; Chehimi, M.; Broniek, E.; Siemieniewska, T.; Bimer, J., Adsorption of H₂S or SO₂ on an activated carbon cloth modified by ammonia treatment. *Carbon* **2003**, 41 (10), 1999-2007.
20. Presser, V.; Heon, M.; Gogotsi, Y., Carbide-Derived Carbons – From Porous Networks to Nanotubes and Graphene. *Advanced Functional Materials* **2011**, 21 (5), 810-833.
21. Presser, V.; McDonough, J.; Yeon, S. H.; Gogotsi, Y., Effect of pore size on carbon dioxide sorption by carbide derived carbon. *Energy Environ Sci* **2011**, 4.

22. Presser, V.; McDonough, J.; Yeon, S.-h.; Gogotsi, Y., Effect of pore size on carbon dioxide sorption by carbide derived carbon. *Energy & Environmental Science* **2011**, 4 (8), 3059-3066.
23. Adu, K. W.; Li, Q.; Desai, S. C.; Sidorov, A. N.; Sumanasekera, G. U.; Lueking, A. D., Morphological, Structural, and Chemical Effects in Response of Novel Carbide Derived Carbon Sensor to NH₃, N₂O, and Air. *Langmuir* **2009**, 25 (1), 582-588.
24. White, C., Effects of hydrogen on the physical and mechanical properties of carbide derived carbon. McNallan, M., Ed. ProQuest Dissertations Publishing: 2009.
25. Portet, C.; Kazachkin, D.; Osswald, S.; Gogotsi, Y.; Borguet, E., Impact of synthesis conditions on surface chemistry and structure of carbide-derived carbons. *Thermochimica Acta* **2010**, 497 (1-2), 137-142.
26. Smith, J.; Van Ness, H.; Abbott, M., Introduction to Chemical Engineering Thermodynamics, (2001) and 7th ed.(2005). McGraw-Hill, New York.
27. Wang, Y.; Panzik, J. E.; Kiefer, B.; Lee, K. K. M., Crystal structure of graphite under room-temperature compression and decompression. *Scientific Reports* **2012**, 2, 520.
28. Portet, C.; Kazachkin, D.; Osswald, S.; Gogotsi, Y.; Borguet, E., Impact of synthesis conditions on surface chemistry and structure of carbide-derived carbons. *Thermochimica Acta* **2010**, 497 (1), 137-142.
29. Inagaki, M.; Toyoda, M.; Soneda, Y.; Morishita, T., Nitrogen-doped carbon materials. *Carbon* **2018**, 132, 104-140.
30. Jansen, R. J. J.; van Bekkum, H., XPS of nitrogen-containing functional groups on activated carbon. *Carbon* **1995**, 33 (8), 1021-1027.
31. Faisal, S. N.; Haque, E.; Noorbehesht, N.; Zhang, W.; Harris, A. T.; Church, Tamara L.; Minett, A. I., Pyridinic and graphitic nitrogen-rich graphene for high-performance supercapacitors and metal-free bifunctional electrocatalysts for ORR and OER. *RSC Advances* **2017**, 7 (29), 17950-17958.
32. Zhang, J.; Xia, Z.; Dai, L., Carbon-based electrocatalysts for advanced energy conversion and storage. *Science Advances* **2015**, 1 (7).
33. Przepiórski, J.; Skrodziewicz, M.; Morawski, A. W., High temperature ammonia treatment of activated carbon for enhancement of CO₂ adsorption. *Applied Surface Science* **2004**, 225 (1-4), 235-242.
34. Sethia, G.; Sayari, A., Comprehensive study of ultra-microporous nitrogen-doped activated carbon for CO₂ capture. *Carbon* **2015**, 93, 68-80.

35. Cen, Q.; Fang, M.; Wang, Z.; Luo, Z. In *Effect of water on CO₂ adsorption with activated carbon*, Materials for Renewable Energy and Environment (ICMREE), 2013 International Conference on, IEEE: 2014; pp 885-888.
36. Bagreev, A.; Bashkova, S.; Bandosz, T. J., Adsorption of SO₂ on Activated Carbons: The Effect of Nitrogen Functionality and Pore Sizes. *Langmuir* **2002**, *18* (4), 1257-1264.
37. Xu, D.; Zhang, J.; Li, G.; Xiao, P.; Webley, P.; Zhai, Y.-c., Effect of water vapor from power station flue gas on CO₂ capture by vacuum swing adsorption with activated carbon. *Journal of Fuel Chemistry and Technology* **2011**, *39* (3), 169-174.
38. Do, D. D.; Do, H. D., A model for water adsorption in activated carbon. *Carbon* **2000**, *38* (5), 767-773.
39. Lahaye, J.; Nansé, G.; Bagreev, A.; Strelko, V., Porous structure and surface chemistry of nitrogen containing carbons from polymers. *Carbon* **1999**, *37* (4), 585-590.
40. Yang, S.; Sun, J.; Ramirez-Cuesta, A. J.; Callear, S. K.; DavidWilliam, I. F.; Anderson, D. P.; Newby, R.; Blake, A. J.; Parker, J. E.; Tang, C. C.; Schröder, M., Selectivity and direct visualization of carbon dioxide and sulfur dioxide in a decorated porous host. *Nat Chem* **2012**, *4* (11), 887-894.
41. Lizzio, A. A.; DeBarr, J. A., Mechanism of SO₂ Removal by Carbon. *Energy & Fuels* **1997**, *11* (2), 284-291.
42. Davini, P., Adsorption and desorption of SO₂ on active carbon: The effect of surface basic groups. *Carbon* **1990**, *28* (4), 565-571.
43. Mangun, C. L.; DeBarr, J. A.; Economy, J., Adsorption of sulfur dioxide on ammonia-treated activated carbon fibers. *Carbon* **2001**, *39* (11), 1689-1696.
44. Joshi, J. N.; Zhu, G.; Lee, J. J.; Carter, E. A.; Jones, C. W.; Lively, R. P.; Walton, K. S., Probing Metal–Organic Framework Design for Adsorptive Natural Gas Purification. *Langmuir* **2018**, *34* (29), 8443-8450.

CHAPTER 7. STRUCTURED GROWTH OF METAL-ORGANIC FRAMEWORK MIL-53(Al) FROM SOLID ALUMINUM CARBIDE PRECURSOR

7.1 Introduction

Metal-organic frameworks (MOFs) are well known for their large surface areas, ¹⁻
⁴tunable ligand moieties, ⁵⁻⁸ and reactive open metal sites. ⁹⁻¹² In general, MOFs are obtained through solution reactions between organic ligands and soluble metal salts in polar solvents (e.g., DMF). Ionic metal salts are the most common type of metal source for MOF production, but dissolution of metal salts complicates solvent recycling, and creates corrosion and oxidation issues through evolved nitrate and chloride anions. ¹³ The use of alternative metal precursors such as metal oxides and metal hydroxides would provide a more flexible and cost-effective strategy for MOF production and would also provide a potential method for direction- and shape-controlled synthesis. Elucidating information that leads toward more efficient production of this versatile nanomaterial, while extending the knowledge base of how MOFs form during reaction, is critical to advancing MOF materials into large-scale use.

Recent literature has begun to examine the growth of MOFs directly from solid precursors. For example, Majano and Pérez-Ramírez attained high yields of HKUST-1 from insoluble copper (II) hydroxide while avoiding high reaction temperatures and expensive metal precursors. ¹³ Li and coworkers ¹⁴ reported similar observations for the hydrothermal growth of the aluminum terephthalate MIL-53(Al) from insoluble aluminum oxide/hydroxide compounds. The resulting product exhibited enhanced resilience towards

humidity and high temperatures as compared to the traditionally synthesized product. In each of these studies, oxygen availability in the precursors was speculated to facilitate the reaction between pre-aligned octahedral metal centers and framework ligands. Recent work in pursuit of controlled crystal growth has also begun to develop in MOF literature, utilizing layer-by-layer growth mechanisms with self-assembled monolayers on noble metal substrates.¹⁵ Though these techniques allow for monolayer control, they entail involved synthesis procedures that rely on cyclic exposures to metal salts and linkers with intermittent rinsing steps.¹⁶⁻¹⁷ Therefore, other methods to control MOF growth are of interest.

Metal carbides are crystalline materials comprised of metal-carbon bonds, and include a large number of transition metals.¹⁸⁻¹⁹ Binary and ternary carbides provide a variety of potential mixed metal system to be explored.²⁰ MOF synthesis from metal carbides has not yet been reported, but recent developments in “green” and economical carbide production have produced high purity carbides on the time scale of seconds to minutes using elemental precursors, adding to their viability as an alternative precursor.²¹⁻²³ Nanoscale tailoring of metal carbides themselves into nanospheres, thin films, and nanorods provides an additional level of enhanced control for templated MOF growth.²⁴⁻²⁶ The transformation of metal carbides into activated carbon has previously been demonstrated through the advent of carbide-derived carbons (CDCs).²⁷⁻³⁰ CDC synthesis reports, which entail the reactive removal of metal hetero-atoms from carbide matrices through halogenation, reveal how metal carbides are unexplored metal sources that can potentially be used for MOF growth. A promising result from such a metal source can manifest as nanometer spatial control of MOF growth location. With metal access restricted

to pre-determined sites of patterned carbide, analogous to results obtained for porous carbon in CDC literature.³¹⁻³² Carbides, which can possess a range of electronegativity differentials between the metal and carbon constituents, are typically more reactive than their oxide and hydroxide counterparts which can exhibit high lattice enthalpies.^{20, 33-34} This may lead to faster reaction times and more complete conversion, which has been a noted issue with other insoluble precursors for MOF growth.^{14, 35}

In this work, we demonstrate for the first time the successful use of an insoluble metal carbide (aluminum carbide, Al_4C_3) for the growth of the aluminum terephthalate, MIL-53(Al). This highly studied framework is comprised of an interconnection (via μ_2 -OH groups) of infinite trans chains of corner-sharing octahedral metal centers [$\text{AlO}_4(\text{OH})_2$], bridged by terephthalic acid (BDC) linkers to create a one-dimensional rhombohedral channel.³⁶ The Al_4C_3 precursor generated a unique “needle-like” morphology in the resulting MOF crystals, with adsorption and stability behavior that is distinct from conventional MIL-53(Al). These results not only highlight the potential for manipulating framework properties by using an alternative metal carbide precursor, but also elucidate a new route for controlled nanoscale MOF crystal growth.

7.2 Materials and Methods

7.2.1 Methods

7.2.1.1 Synthesis procedures for Al_4C_3 -derived MIL-53(Al)

MIL-53(Al) analogues were prepared using a 3:1 organic linker to aluminum molar ratio. 50 mg of aluminum carbide (Al_4C_3 , Strem Chemicals 98% purity 325 mesh) and 693

mg of terephthalic acid ($\text{C}_6\text{H}_4(\text{COOH})_2$, Sigma Aldrich 98% purity), referred to as BDC hereafter, were placed in a 20 mL Teflon-lined stainless steel reactor. 7.5 mL of N,N-dimethylformamide ($\text{C}_3\text{H}_7\text{NO}$, Sigma Aldrich 98% purity), referred to as DMF hereafter, was added to the mixture, and the reagents were agitated via sonication for 5 minutes. The reactor was then sealed and placed in a preheated isothermal oven at 220°C , unless stated otherwise, for the entirety of the predetermined reaction time. The reactor was then removed from the oven and cooled in ambient air. The resulting liquid-solid mixture was gravity-filtered and washed three times with DMF and then methanol. In some cases the reaction mixture was decanted and the liquid portion was stored for further analysis. The naming convention used for materials involved in this publication will follow a precursor-linker-reaction time format, e.g. $\text{Al}_4\text{C}_3\text{-BDC-24h}$.

7.2.1.2 Powder X-ray Diffraction

Ex situ powder X-ray diffraction (PXRD) patterns were collected using an X'Pert X-ray PANalytical diffractometer with a $\text{Cu K}\alpha$ X-ray source ($\lambda = 1.5418 \text{ \AA}$). PXRD diffractograms were collected from a range of $5\text{-}50^\circ$ with a step size of 0.02° . All experiments were carried out at room temperature. *In situ* PXRD patterns were acquired using a PANalytical Empyrean diffractometer with $\text{Cu K}\alpha$ radiation ($\lambda = 1.5418 \text{ \AA}$). Patterns were observed as the material was heated up to 400°C at a ramp rate of $10^\circ\text{C min}^{-1}$, and held isothermally for 5 minutes before data acquisition. The material was then cooled back down to room temperature, under N_2 flow, where a final pattern was recorded.

7.2.1.3 Nitrogen Physisorption Measurements

Nitrogen adsorption measurements at 77 K were obtained using a Quantachrome Quadrasorb SI volumetric analyzer. Isotherms were collected at 77 K using a sample of 50-75 mg. Prior to each isotherm, the sample was outgassed for approximately 18 hours at 150°C and under vacuum (approximately 20 mTorr). Specific surface areas were calculated using the BET model in the relative pressure range (P/P_0) 0.005-0.03.³

7.2.1.4 Thermogravimetric Analysis (TGA)

Thermogravimetric analysis for all samples was carried out on a NETZSCH STA 449 F1 Jupiter instrument. Measurements used 10-40 mg of material, ramped from 25-1400 °C at a ramp rate of 5 °C min⁻¹ and a flow rate of 20 mL min⁻¹ of helium (Airgas 99.999%).

7.2.1.5 Magic-Angle Spinning Nuclear Magnetic Resonance (MAS NMR)

No pretreatment of the samples was done before taking NMR measurements. Samples were stored and packed in 2.5 mm MAS rotors under N₂. ²⁷Al MAS NMR measurements were carried out for all samples at a magnetic field strength of 13.9 T and an MAS rate of 25 kHz. All spectra were referenced to a 1 M solution of Al(NO₃)₃ at 0.0 ppm. The ²⁷Al spectra were recorded at a Larmor frequency of 153.7 MHz. Measurements were recorded using a pulse-acquire experiment utilizing a radio-frequency pulse with a

flip angle of $\pi/18$ (pulse width of 0.3 μ s) to ensure quantitative 1D spectra were recorded. Liquid-state ^{27}Al NMR was performed on a 4.74 T magnet, using a carrier frequency of 52.7 MHz. Measurements were recorded utilizing a home-built spectrometer and probe with an 8 mm coil. Dmfit was used for all simulated NMR spectra.³⁷

7.2.1.6 Scanning electron microscopy (SEM)/Focused Ion Beam (FIB-SEM)

Scanning electron microscopy (SEM) images were obtained using a Zeiss Ultra60 Field Emission Scanning Electron Microscope. All samples were deposited onto carbon tape. Images were scanned at an accelerating voltage range of 0.75-10 kV. Cross sections were cut using a Nova Nanolab. A precise focused Ga ion beam was employed to etch in tandem with platinum deposition for protection. Ultra-high resolution field emission scanning electron microscopy was employed after etching to image cross-sections, while samples remained under vacuum, at accelerating voltages of 2-10kV. Energy Dispersive Spectrometry (EDS) analysis was performed from 5-10kV, and notably is not sensitive enough for hydrogen.

7.2.1.7 Water Vapor Adsorption Isotherms

Water vapor adsorption experiments were performed on a volumetric Micromeritics 3-Flex device for pressures up to 1 bar at 25°C. Prior to the measurement, 30-75 mg of material were activated *in situ* at 150°C for 12 hours under dynamic vacuum.

7.2.1.8 CO₂ Adsorption Measurements

CO₂ isotherms at 25 °C, in the pressure range of 0-20 bar, were obtained using the Hiden Isochema IGA-001 microbalance. Low pressure CO₂ adsorption experiments were performed on a volumetric Micromeritics 3-Flex device for pressures up to 1 bar at 0°C and 25°C. Prior to the measurements, 30-75 mg of material was heated *in situ* at 150 °C for 18 hours under vacuum.

7.2.1.9 X-ray Photoelectric Spectroscopy (XPS) analysis

XPS measurements were taken on a Thermo K-alpha, monochromated Al K α source with a double-focusing hemispherical analyzer. High resolution spectra were taken of O1s, Al2p, and C1s at a 0.1 eV step size, 50 ms dwell time, 50 eV pass energy, and a 400 μ m spot size. Samples were activated prior to data collection, and all measurements were taken under ultra-high vacuum.

7.3 Results and Discussion

7.3.1 Degradation and Evolution of Crystalline Structures

Carbide-derived MOF syntheses were conducted for reaction times from 0.5h to 72h. As shown in Figure 7-1a, PXRD measurements were employed to monitor the degradation of the crystalline carbide as well as the formation of crystalline MIL-53(Al). Patterns for unactivated products obtained from reaction times up to 3h do not show

evidence of MOF growth or carbide degradation with respect to observed crystallinity changes. A distinct transformation occurs at 4 hours, where reflections corresponding to as-synthesized MIL-53(Al) (as-MIL-53(Al)), simulated pattern shown in Figure A-37, are clearly present alongside reflections belonging to the crystalline carbide.³⁶ Degradation of the aluminum-carbon matrix is also apparent following 4h of reaction. This is attributed to aluminum cluster coordination to BDC ligands in the emerging as-MIL-53(Al) crystals. The carbide precursor is undetected in the solvothermal reaction product after six hours, where only well crystallized as-MIL-53(Al) is detected. Evolution of the product from crystalline carbide at three hours of reaction to as-MIL-53(Al) after six hours suggests that a barrier to MOF formation exists in the early synthesis times. The naming convention used for materials hereafter will follow a precursor-linker-reaction time format, e.g. Al₄C₃-BDC-24h.

Adsorption isotherms of N₂ and CO₂ at 77 and 273 K, respectively, elucidate the evolution of porosity in the material from an ordered non-porous aluminum-carbon matrix to an ordered, highly porous framework. N₂ physisorption experiments reveal products obtained below four hours of reaction do not possess appreciable BET surface areas, listed in Table S1. This agrees with the absence of MOF observed in these materials through PXRD analyses, provided in Figure 7-1a. Greater reaction times drastically increase resulting BET surface areas and pore volumes, reaching 94% of the achievable surface area (~1200 m² g⁻¹) after 12h of reaction, delineated in Figure 7-1b and Table A-9. CO₂ isotherms at 273K in Figure A-38 display the same trend of increasing adsorption capacity for Al₄C₃-BDC materials with reaction time. Capacities at 25°C are similar to those seen in literature for MIL-53(Al) produced from conventional syntheses using ionic aluminum

salt precursors.³⁸⁻³⁹ CO₂ isotherms at 273K also display hysteresis at low partial pressures for materials reacted for 4h or longer, which can be attributed to the well-documented breathing of the MIL-53(Al) structure.^{36, 39-40} Breathing hysteresis for Al₄C₃-BDC materials was less evident than the hysteresis seen for MIL-53(Al) obtained utilizing AlCl₃•6H₂O (Figure A-39).

This could indicate the carbide-derived MIL-53(Al) structure is partially restricted from breathing, or the breathing phenomena is being hindered by unreacted material remaining from the precursor, thereby reducing the breathing effect on a per gram basis. A second breathing hysteresis transition is observed with CO₂ adsorption at 25°C ranging from 2-9 bar (Figure A-39). This Type-IV isotherm represents a further transition from an intermediate pore form towards the large pore form of MIL-53(Al).

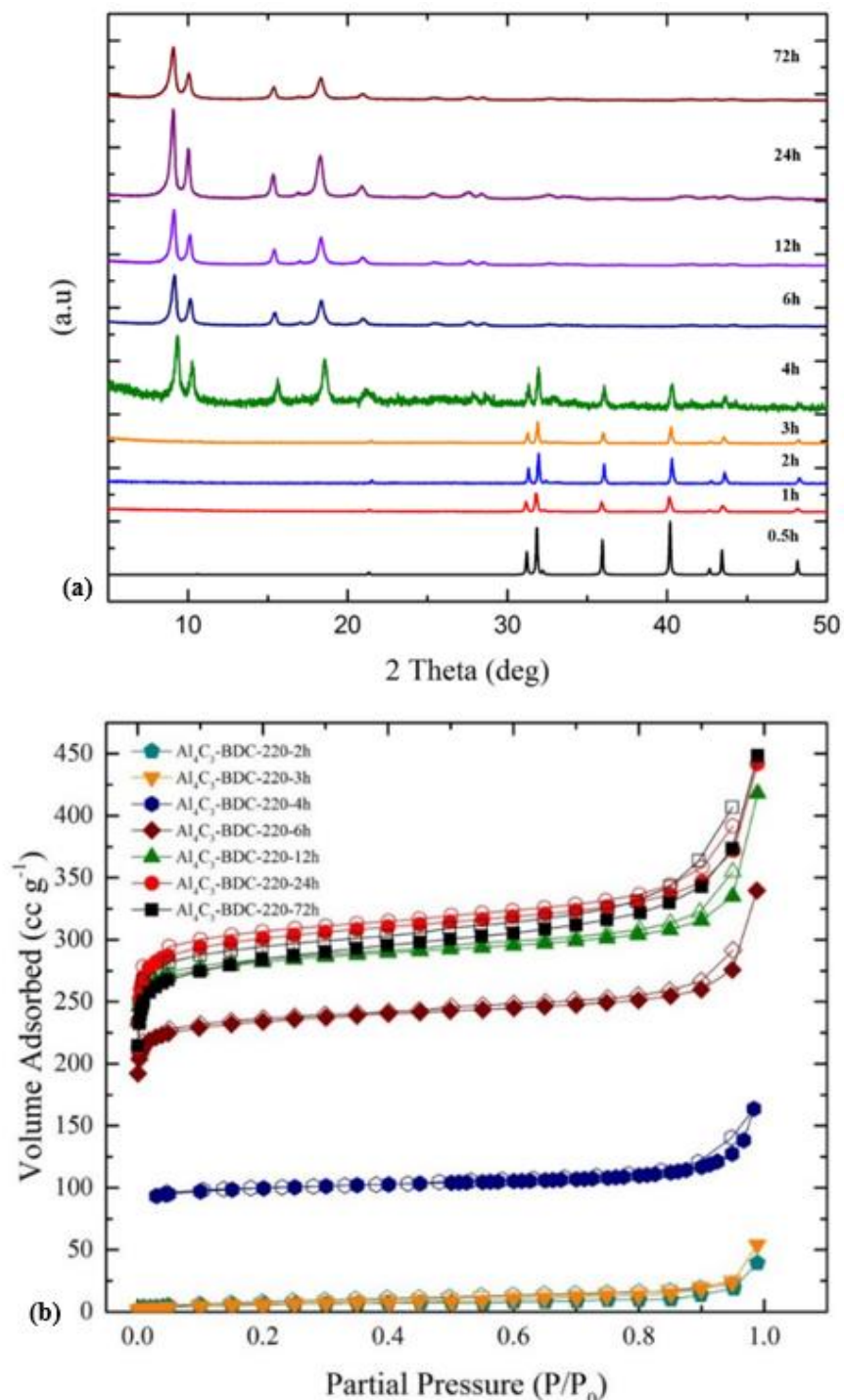


Figure 7-1: (a) PXRD and (b) N_2 physisorption isotherms measurements of $\text{Al}_4\text{C}_3\text{-BDC-XXh}$ reacted for a range of times from 0.5 to 72h. Notably early crystalline structures represent Al_4C_3 reflections; later times show MIL-53 reflections.

7.3.2 *Temporal morphology evolution*

At short reaction times, SEM images in Figure 7-2 show templating of rod-like structures on the carbide surface. Structures observed on Al_4C_3 -BDC-2h are 50-100 nm in length and run parallel to the bulk surface. The templated rods increase by a magnitude in size at three hours while continuing growth parallel to the parent surface. In agreement with the diffraction patterns presented in Figure 7-1, after 4h of reaction, the material exhibits a significant transformation, where growth in the plane of the carbide becomes distorted due to the degradation of the precursor. The needle structures continue to reside parallel to the flat plane of the parent material at 4h, but begin to extend beyond the parental plane surrounding them. At extended reaction times the precursor surface is no longer visible, with well-defined, individual needles emerging as sections of a cluster originating from the degraded precursor. A similar, needle-like morphology has also been observed for NH_2 -MIL-53(Al) (MIL-53(Al) with an NH_2 functionalized BDC linker) obtained through synthesis modulation utilizing a 30:1 acetic acid to metal precursor (aluminum nitrate nonahydrate) molar ratio.⁴¹ Analogous behavior observed for Al_4C_3 -BDC materials without the necessity of potentially corrosive and expensive acid modulators is a direct consequence of utilizing an Al_4C_3 precursor, unique from conventional syntheses involving ionic metal salts. The unique morphology is also responsible for the evident transformation from the brown 325 mesh Al_4C_3 precursor consisting of particles 10-40 μm in size, observed via SEM, to a pale blue-grey bulk material consistently aggregated into clusters on the scale of hundreds of microns to millimeters, as displayed in Figure A-40 and 2f. This behavior could allow for fixed-bed adsorption without the need to create pellets utilizing binders, which have shown to reduce breakthrough capacity as much as 32% for MIL-

53(Al), providing economic viability for commercial flow-through adsorption applications.⁴² EDS and XPS analyses, illustrated in Table A-10 and Table A-11/Figure A-41, respectively, reflect similar elemental compositions to high-temperature MIL-53(Al) for the carbide-derived MOF after activation. Two peaks were detected during high resolution Al 2p scans, one at 74.74 and 76.46 eV, as shown in Figure A-41a. The first can be attributed to the octahedral $\text{AlO}_4(\text{OH})_2$ clusters in the framework, whereas the latter is a byproduct of aluminum oxide or hydroxide produced during the synthesis.

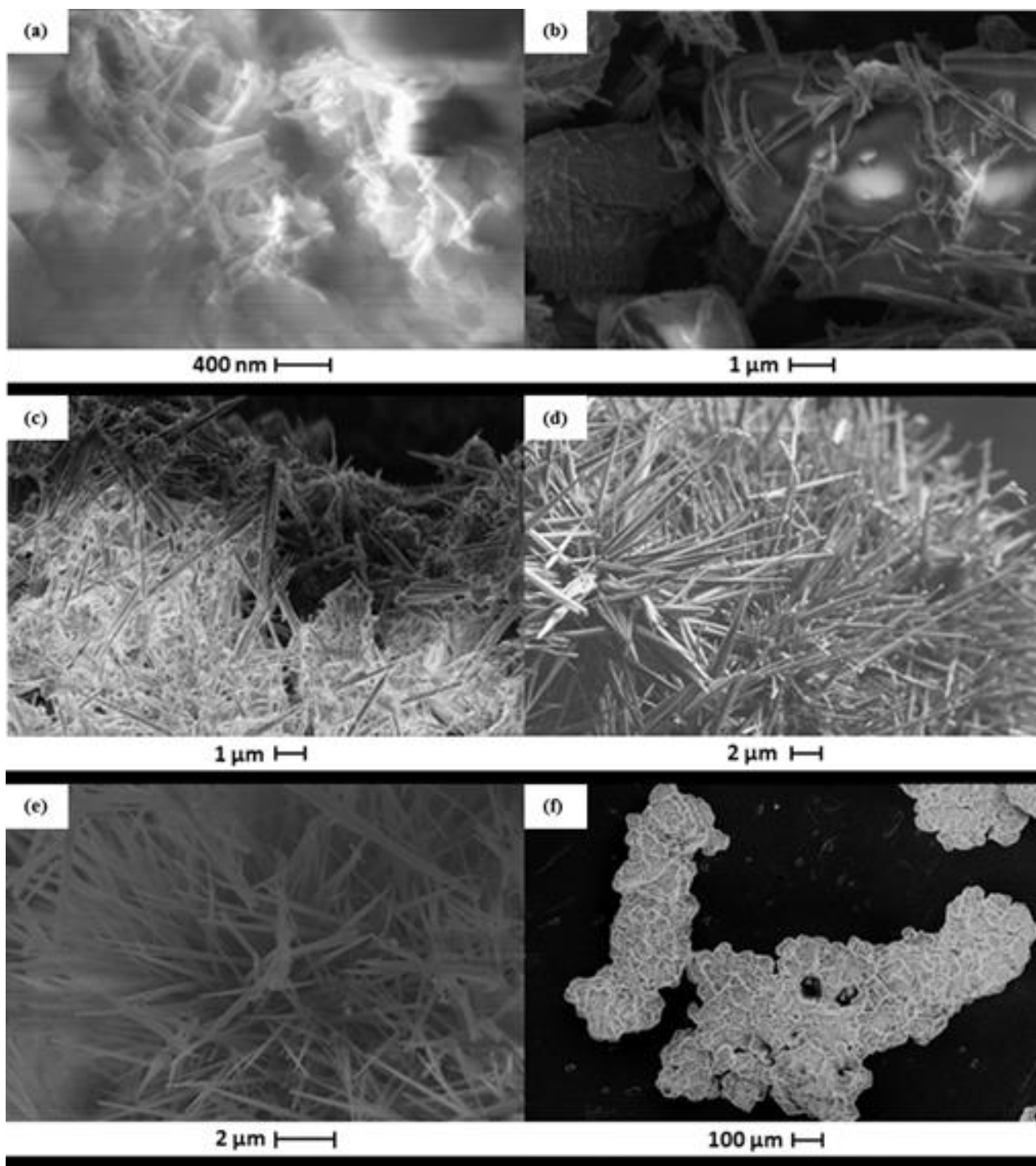


Figure 7-2: SEM images of $\text{Al}_4\text{C}_3\text{-BDC-XX}$: (a) 2h, (b) 3h, (c) 4h, (d) 24h, and (e & f) 72h.

7.3.3 Elucidation of intermediate species

^{27}Al solid-state NMR offers the opportunity to analyze structure for both crystalline and amorphous content, elucidating the coexistence of multiple species in mixtures as seen here, as a function of the reaction duration. What is shown in Figure 7-3 is a combination of resonances from Al_4C_3 ; multiple aluminum oxide sites corresponding to 4-, 5-, and 6-coordinate aluminum environments; a characteristic resonance from the MIL-53(Al) product; and an aluminum nitride impurity (at $\sim 115\text{ppm}$). The ^{27}Al solid-state MAS NMR of the Al_4C_3 -BDC-XXh materials reveals the disappearance of the Al_4C_3 over time and the emergence of as-MIL-53(Al), in agreement with PXRD patterns in Figure 7-1a.

Lineshapes for the two 4-coordinate aluminum sites of Al_4C_3 have been published previously, with quadrupolar coupling constants (C_Q) of 15.58 and 15.83 MHz.⁴³ However, from multiple-quantum magic-angle spinning (MQMAS) data, we find C_Q values for Al_4C_3 are 16.7 and 14.5 MHz, which are important parameters for the deconvolution of complex overlapping resonances shown in Figure 7-3. The MIL-53(Al) resonance has an isotropic chemical shift of 4.1 ppm and a C_Q of 10 MHz. The aluminum oxide resonances are fit with the Czek distribution with $\overline{C_Q}$ values for the 4-, 5-, and 6-coordinate Al-O sites of 8.1, 6.8, and 5.8 MHz, respectively. The C_Q values are the same for each reaction time, indicating that the amorphous aluminum oxide is structurally similar throughout the reaction, when it is present.

After 30 minutes, multiple aluminum oxide resonances are present, and these become more prominent at 3 hours. The emergence of MIL-53(Al) is not detectable until 4 hours of reaction. At 72 hours, the sample is primarily MIL-53(Al), with trace amounts of aluminum oxide present. The absence of any detectable ^{27}Al signal from liquid-state

NMR of the supernatant liquid from $\text{Al}_4\text{C}_3\text{-BDC-4h}$ provides evidence of minimal or no aluminum ions (approximately $< \mu\text{M}$ concentrations) present in the bulk solution.

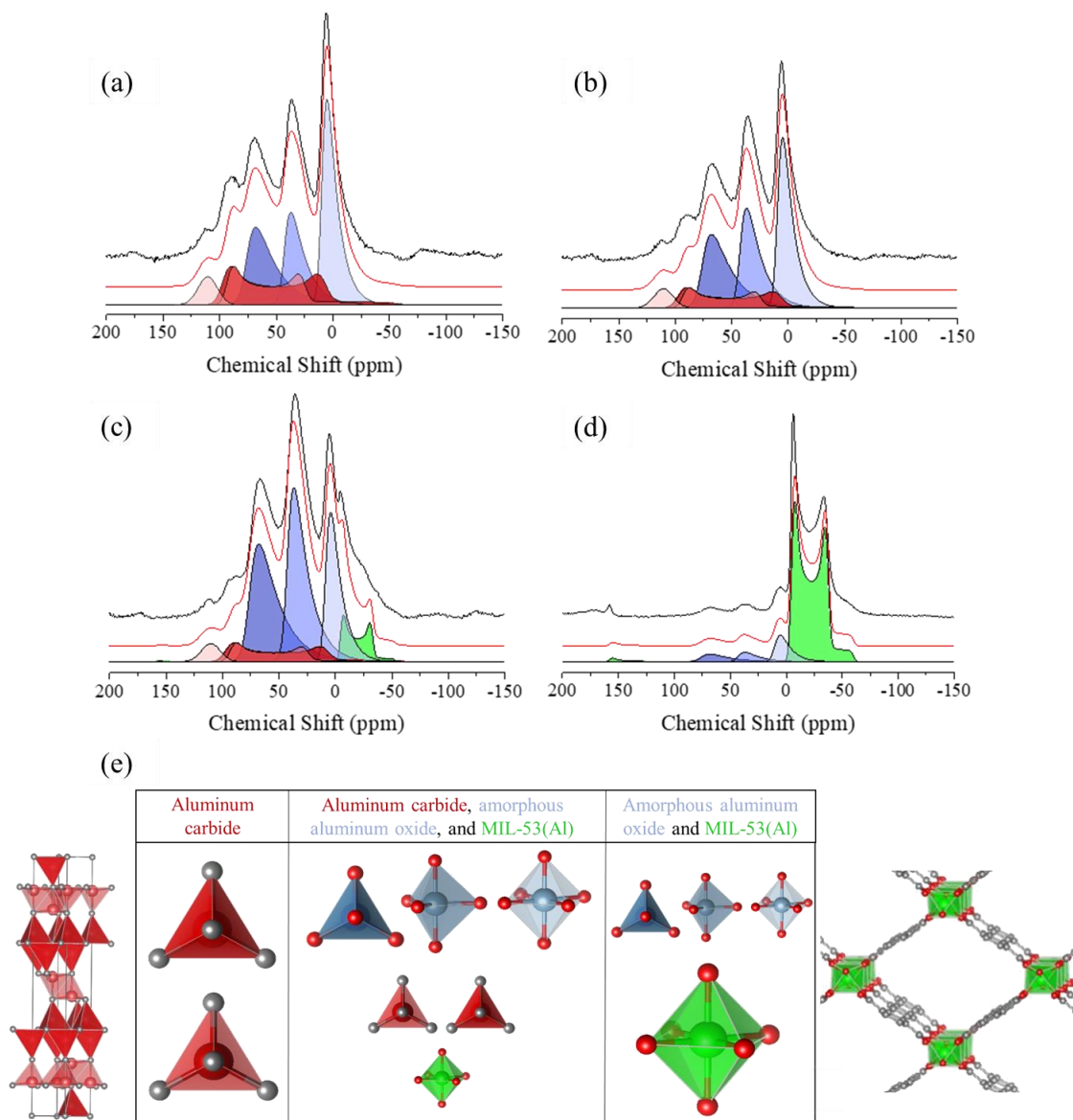


Figure 7-3: ^{27}Al MAS NMR of $\text{Al}_4\text{C}_3\text{-BDC-XXh}$ for reaction times of (a) 0.5h, (b) 3h, (c) 4h, (d) 72h. (e) Color coded polyhedral representation from 4-coordinate Al_4C_3 to 6-coordinate MIL-53(Al) serves as a legend to the spectra. The size of the polyhedra is meant to represent the major/minor components during the reaction.

The Al_4C_3 -BDC-4h sample was investigated via cross-sectional analysis, based on the presence of both crystalline carbide, as-MIL-53(Al), and amorphous alumina as shown in Figure 7-1a and Figure 7-3. Results visualized in Figure 7-4 and Figure A-42 entail two key details about the evolution of Al_4C_3 -BDC. The first observation was the presence of compact portions of unreacted material, hereby deemed nodes, with high concentrations of aluminum and oxygen, as shown in Figure 7-4a. The identity of the amorphous nodes was discussed in the previous section by NMR. Oxygen is not native to the crystalline carbide. Therefore, the high concentrations of oxygen are likely obtained during the reaction. Plausible sources of oxygen are the carboxylic acid groups of terephthalic acid and trace amounts of water in DMF. Immediately after the reaction the aliquot was collected for analysis and $\text{N,N,N}^1,\text{N}^4$ -tetramethylterephthalamide was recovered as a byproduct. This type of amidation reaction typically utilizes organic coupling agents or involves the preparation of acid chlorides and in some cases the use of a catalyst such as trimethylaluminium.⁴⁴⁻⁴⁶ The reaction involves the liberation of the hydroxyl group, which would then be able to perform a nucleophilic attack on the carbide providing a likely source for the incorporation of oxygen into the degrading carbide structure and subsequent bridging hydroxyl in MIL-53(Al).

The second observation is the transition layer from the node to the needle-like MIL-53(Al) crystals. Figure 7-4a displays the high concentration of carbon surrounding the nodes as well as the presence of gallium from the etching process. The carbon signifies the growth of MIL-53(Al) around the nodes and the presence of gallium is due to the relatively loose packing of the MIL-53(Al) nanostructures allowing dispersion of the element during etching. In Figure 7-4b and Figure A-42, imaging of the interface was obtained employing

backscattering detectors. There is a clear nucleation boundary created around the nodes that displays a different compositional identity than the core, evident by the contrast created during collection of type II secondary electrons (SE2). Also, observed in Figure 7-4b and Figure A-42 is the destructive “peeling” of layers above the nucleation region of the node, which then transfer to bulk MIL-53(Al) needles. This “peeling” behavior can be attributed to interfacial strain owing to the lattice mismatch of the evolving material as well as the availability of a bulk solution able to facilitate motion of the separating sections. These results suggest a layer-by-layer mechanism for the growth of Al_4C_3 derived MIL-53(Al). The parallel growth along the nodes seen in the cross-section leading to a transitional peeling layer and subsequently disordered needles correlates well with previously mentioned observations for morphological changes during increased reaction time in Figure 7-2. This growth pattern is likely a significant factor in the unique-needle morphology produced when utilizing an insoluble precursor such as Al_4C_3 .

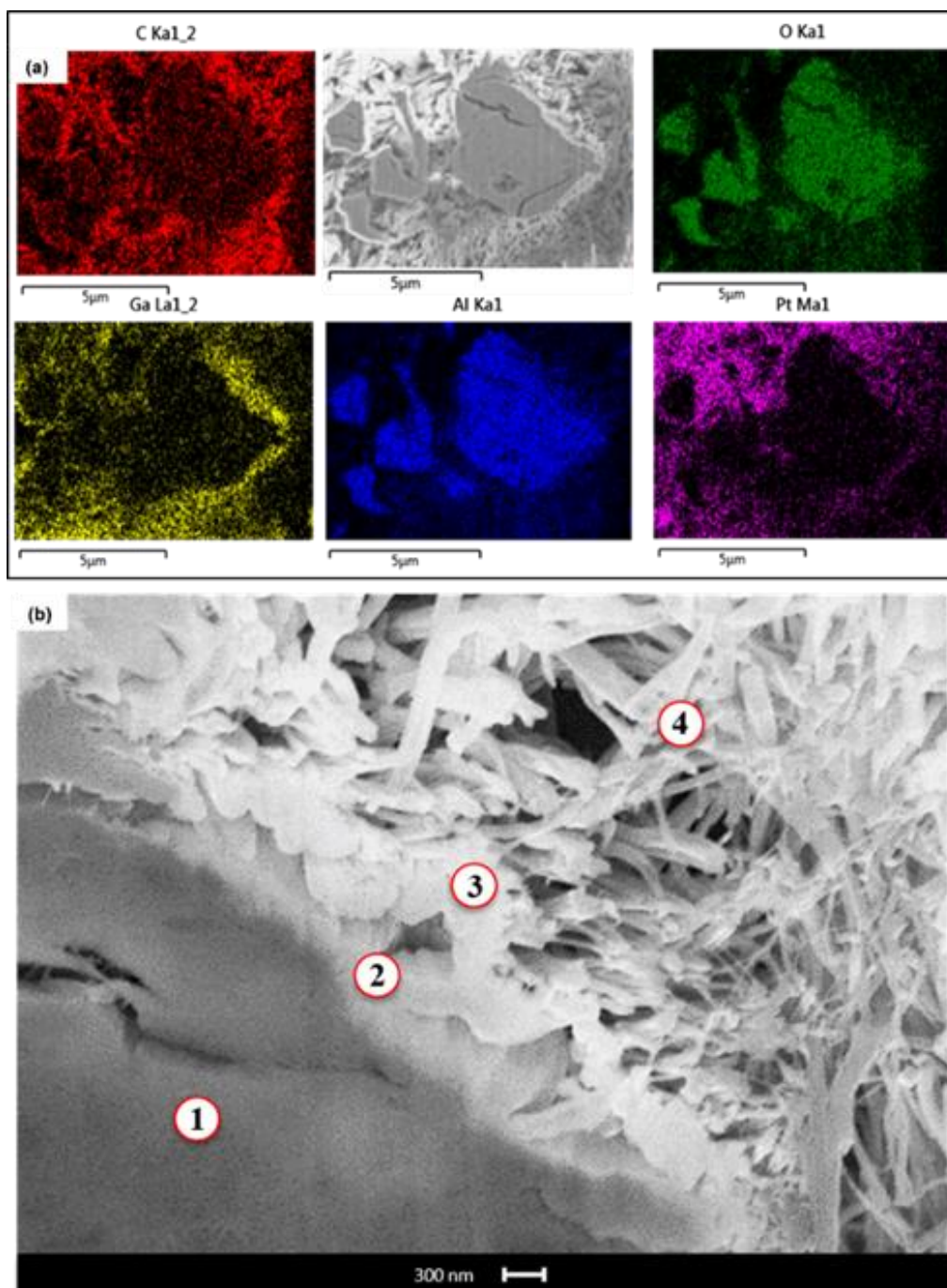


Figure 7-4: FIB cross section of $\text{Al}_4\text{C}_3\text{-BDC-4h}$ focusing on (a) EDS mapping and (b) showing four distinct regions during growth: (1) Intermediate core (Al_2O_3 , $\text{Al}(\text{OH})_3$ & Al_4C_3), (2) nucleation layer, (3) transitional “peeling” layer, (4) bulk MIL-53(Al)

7.3.4 *Extension of carbide synthesis to new topologies, analogues, and adsorption*

Additional work was pursued to probe the sensitivity of the Al_4C_3 -derived MOF synthesis. 2-amino-1,4-benzenedicarboxylic acid (NH_2 -BDC) was utilized to investigate the viability of using functionalized linkers. The successful synthesis of crystalline, needle-like nanostructures of Al_4C_3 - NH_2 -BDC-72h was achieved with reduced surface area, while maintaining the same linker to metal ratio (Figure A-43). Al_4C_3 -derived MIL-100 was also synthesized with benzene-1,3,5-tricarboxylate (BTC), Figure A-44, providing evidence of extension to different topologies. The effect of synthesis temperature on MIL-53 was investigated, and it was observed that the reaction proceeded at temperatures as low as 190°C , where lower temperatures provided a non-porous, unidentified crystalline product (Table A-12 and Figure A-45). Substantiation experiments were performed at 220°C with Al_4C_3 in DMF alone, and Al_4C_3 in DMF with benzoic acid (BA). Results indicate DMF alone does not degrade the crystalline carbide structure after three days of exposure, Figure A-46. The reaction with BA displayed slower kinetics relative to its BDC counterpart, with no change in crystallinity up to 6h. After Al_4C_3 reacted with BA at 220°C for 72h, the product was absent of PXRD reflections for Al_4C_3 and matched those of crystalline boehmite (Figure A-47), highlighting the important role the carboxylic acid plays in the degradation of the carbide and formation of a new crystalline structure with oxygen incorporated into the matrix.

Water adsorption isotherms collected on Al_4C_3 -BDC-72h materials displayed distinct behavioral patterns from those previously seen for the conventionally synthesized MOF. MIL-53(Al) exhibits a sigmoidal isothermal water vapor uptake behavior with hysteresis, displaying a single adsorption step at $P/P_0 = 0.15$ saturating around 4-5 mmol

g^{-1} .⁴⁷⁻⁴⁸ The initial step at $P/P_0 = 0.15$ is also detected for $\text{Al}_4\text{C}_3\text{-BDC-72h}$, accompanied by a secondary step after $P/P_0 = 0.58$, as seen in Figure 7-5. Hysteresis is evident for both steps suggesting a degree of flexibility in the framework. The step at $P/P_0 = 0.58$ has been observed for MIL-53(Al) synthesized from $\text{Al}(\text{NO}_3)_3 \cdot 6\text{H}_2\text{O}$, but the observed uptake was attributed to material instability in water and subsequent degradation, suggesting that the material can undergo a nucleophilic attack when in a larger pore form.⁴⁸ $\text{Al}_4\text{C}_3\text{-BDC-72h}$ exhibits framework stability following high humidity exposure and exposure to ~50% relative humidity for 3 months, with no reduction in BET surface area acquired from N_2 physisorption; results are provided in Table A-14.⁴⁹ This suggests $\text{Al}_4\text{C}_3\text{-BDC-72h}$ possesses a more robust large pore form of MIL-53(Al) as opposed to frameworks produced via conventional synthesis

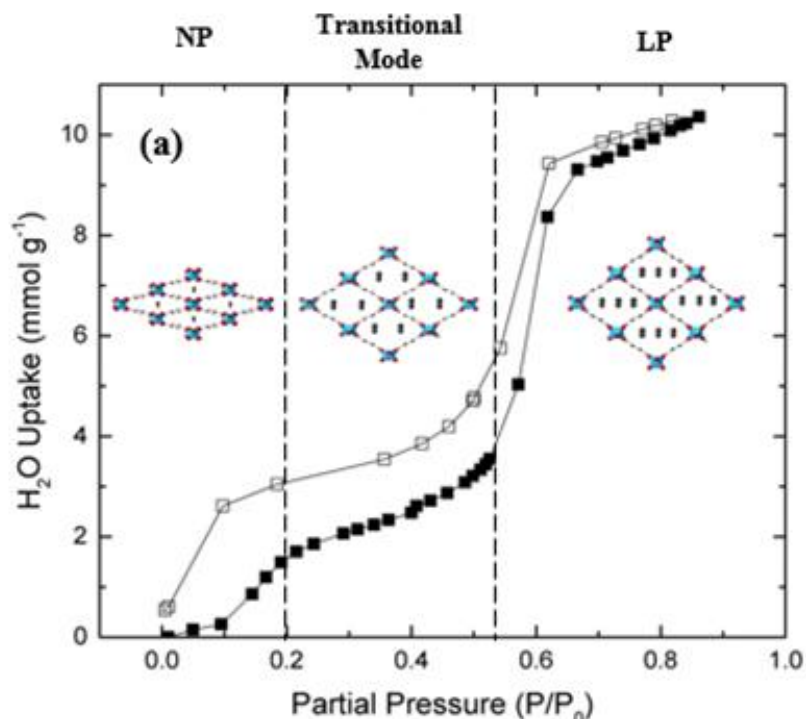


Figure 7-5: Water vapor isotherm for $\text{Al}_4\text{C}_3\text{-BDC-72h}$ taken at 25°C

Three crystal forms of MIL-53(Al) are reported in literature: high temperature/large pore (HT/LP), low temperature/narrow pore (LT/NP) forms and a generic as-synthesized material. The as-synthesized form covers a broad spectrum of transitional breathing modes which are caused by applied strains on the unit cell via guest molecules and temperature.^{36, 39, 50} Before heating, Al₄C₃-BDC-72h displays an as-MIL-53(Al) structure, as shown at the bottom right in Figure 7-6. Upon heating, the PXRD pattern begins to shift towards the HT phase of MIL-53(Al) at 100°C. This transition coincides with the evolution of the water guest molecules leaving the framework, which has been observed in literature to being a key component of the transition between the two pore phases.^{36, 50-51} After cooling under N₂ flow, the structure remained in the HT-MIL-53(Al) phase. Rietveld analysis in Table A-13 revealed an orthorhombic crystal system with an Imma (74) space group with lattice constants closely matching those reported by Loiseau et al.³⁶ After ambient air exposure, the material converted back into the as-MIL-53(Al) structure, confirming reversible breathing behavior. The material notably displayed no loss in BET surface area after being heated to 400°C under N₂ flow.

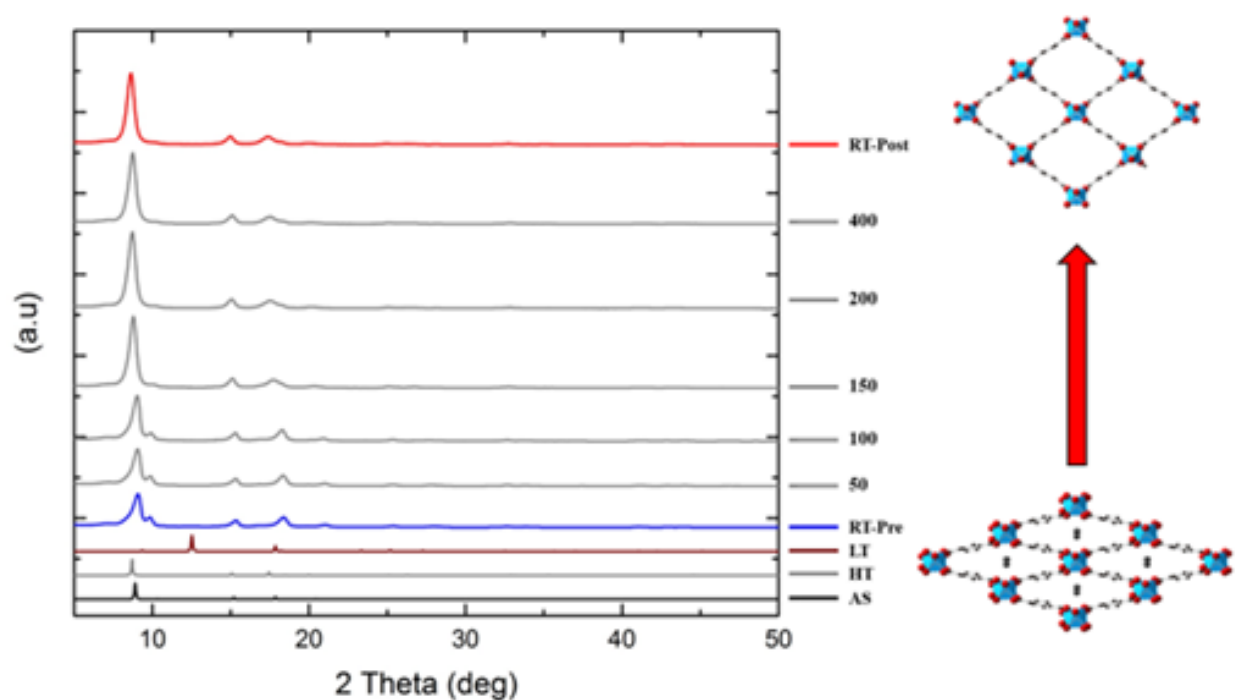


Figure 7-6: *In situ* PXRD of $\text{Al}_4\text{C}_3\text{-BDC-72h}$ during heating under flowing N_2 . Three simulated crystal structure of MIL-53(Al) are included; as-synthesized (AS), high-temperature (HT), and low-temperature (LT). Room temperature (RT) scans were acquired pre and post heating.

7.3.5 Synthesis solvent effects on MIL-53(Al) from Al_4C_3

The effect of synthesis solvent was investigated as a result of DMFs contribution towards framework oxygen for Al_4C_3 derived MIL-53(Al). Water was chosen as the second solvent to examine to determine if the reactivity of water with Al_4C_3 will outcompete the growth of MIL-53(Al), explore the effect of linker solubility on crystal growth through changes in reactant concentration, and investigate how solvent composition effects the resulting framework properties with respect to crystal structure and breathing behavior. As seen in Figure 7-7, there are significant differences between the crystal structure of $\text{Al}_4\text{C}_3\text{-MIL-53(Al)}$ synthesized in water and DMF. Both structures exhibit reflections for as-MIL-53(Al), however when pure water is used reflections that belong to np-MIL-53(Al) are

present, while a simultaneous reduction or shift in lp-MIL-(Al) reflections are observed. The presence of another crystalline structure is also noticeable in minute quantities when pure water is used which corresponds to boehmite (γ -AlO(OH)), an aluminum oxyhydroxide polymorph. This is likely formed as a byproduct through the hydrolysis of the carbide precursor before MIL-53(Al) forms. As small amounts of DMF are added to the solvent, the resulting MIL-53(Al) product exhibits signs of significant strain, represented as broad asymmetrical reflections in the pattern. As the concentration of DMF increase, each crystalline product displaying a range of pore forms with an increase in boehmite concentrations until the solvent ratios reach equal volume. When the solvent ratios reach equal volume, MIL-53(Al) is no longer produced, instead, a highly crystalline boehmite is collected from the reaction. As the ratio reaches 75% DMF, pseudo boehmite is observed, which is a distorted polymorph of the oxyhydroxide. This illustrates that a window exists, where the solvent ratio of DMF/H₂O favors the formation of boehmite over MIL-53(Al) from the carbide precursors when DMF is present. This region coincides with rapid hydrolysis of DMF and subsequent formate ion formation as illustrated in Figure A-50.⁵² Previous studies demonstrate mixtures involving 67% DMF in water consume significant amounts of hydroxyl ions in solution, which are a critical component for generating MIL-53(Al), allowing for direct hydrolysis of Al₄C₃ and boehmite formation instead.⁵³⁻⁵⁴ Once the solvent consists upwards of 90% DMF, reflections belonging to np-MIL-53(Al) and boehmite are no longer visible, as the production of lp- and as-MIL(Al) becomes favored. The change from np-MIL(53) to lp-MIL(53) as DMF become the dominant solvent results from the difference in kinetic diameter of the two solvents which saturate the pores during crystallization. The kinetic diameter of DMF is 5.5 Å while water

is significantly smaller at 2.6 Å.⁵⁵ The larger molecule requires more space during the formation of the 1-dimensional channel during synthesis which favors the formation of lp-MIL(53), while water allows for framework to crystalize in the narrow pore form.^{48, 56}

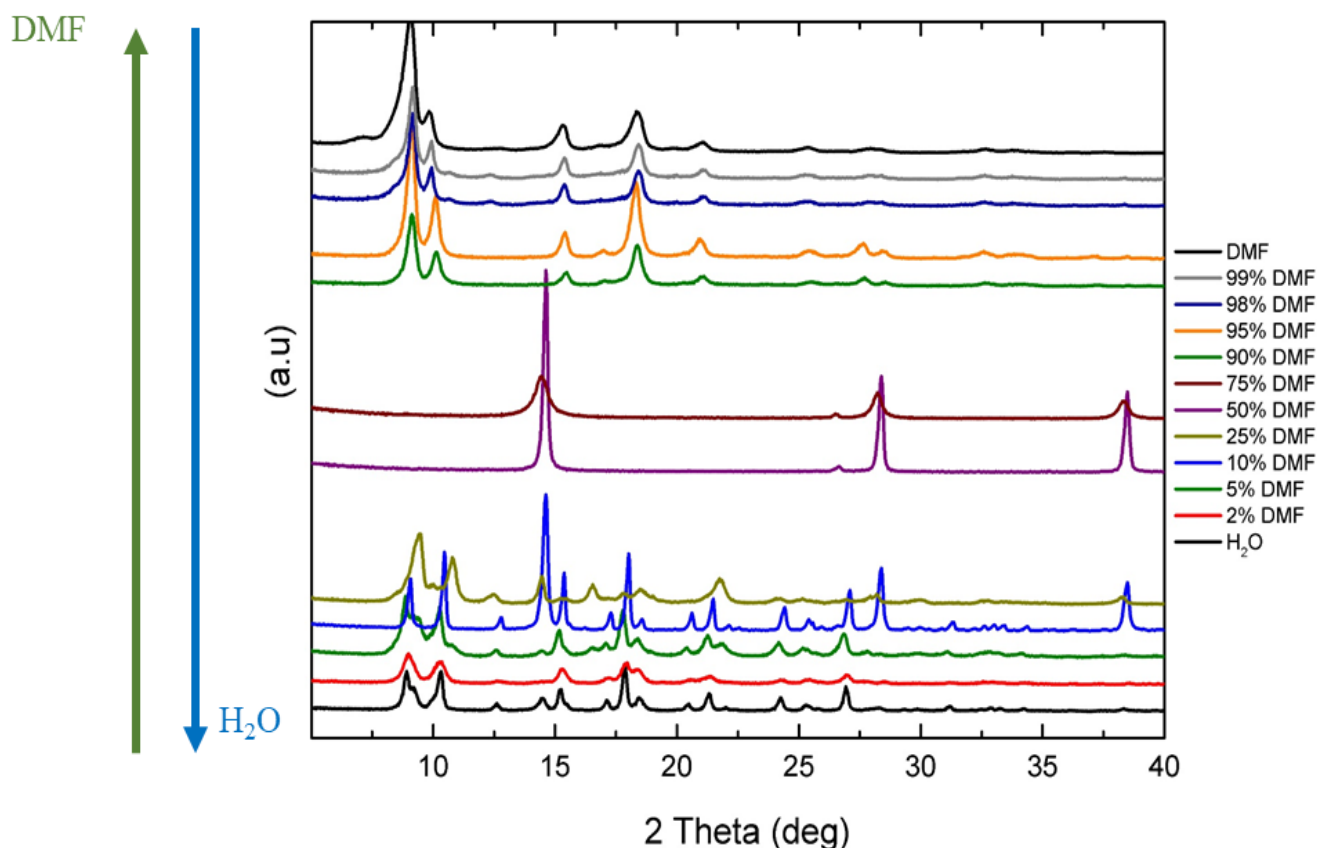


Figure 7-7: PXRD patterns of MIL-53(Al) synthesized from Al_4C_3 using different solvent ratios of dimethylformamide (DMF) and water (H_2O)

²⁷Al solid-state NMR provides an excellent complement to X-ray diffraction to further decipher between crystal structures and identify the presence of amorphous aluminum content. Figure 7-8 provides a qualitative view of the change in aluminum coordination as the solvent switches from DMF to H_2O . Analogous to PXRD, when DMF concentrations range from 75-25% a large portion, if not all of the aluminum content is present as 6-coordinate boehmite represented by a peak at ~6 ppm. As the solvent becomes

highly concentrated with DMF, the spectra match closely with observations seen in literature for lp-MIL-53(Al), consistent with PXRD.^{36, 57} When water becomes the dominant solvent, with 25% or less DMF, the spectrum becomes convoluted between -25 and -50 ppm resulting from the presence of various breathing modes of MIL-53(Al). The chemical shift and presence of features in the spectrum when water solvent concentrations are high are likely influenced by crystalline boehmite throughout the sample. The integration of the non-porous solids can induce strain on the MIL-53(Al) structure altering its coordination environment producing changes in the observable spectrum, which would also contribute to the microstrain seen through peak broadening in PXRD. ²⁷Al solid-state NMR and PXRD thoroughly demonstrate that solvent composition plays a strong role in dictating whether or not a porous material is formed and the polymorphic identity of the resulting MIL-53(Al). This information provides further fundamental understand of synthesis conditions for the formation of templated MIL-53(Al) from a sacrificial Al₄C₃ precursor. Furthermore, along with the detailed changes in pore formation observed in PXRD and NMR, the accessible surface area, pore space, and breathing behavior changes with solvent ratios, illustrated in Figure A-51. Of note, when 5% or less water was added to DMF the surface areas reached ~1400 m² g⁻¹ without post-synthetic activation in boiling DMF to remove trapped species. This is amongst the highest reported surface area for MIL-53(Al) to-date.⁴⁸ The increase in SA with small quantities of water correlates with reduced intermediate aluminum species observed as a result of the additional oxygen added to the system through water, while the growing structure is still primarily saturated with the larger DMF molecules to facilitate lp-MIL-53(Al) crystal growth. When water consists of 25% or more of the solvent, a significant restriction to pore access is observed with N₂

physisorption displaying surface areas below $100 \text{ m}^2 \text{ g}^{-1}$. This is a result of trapped disordered BDC in the 1-D channels along with non-porous boehmite present in the system, Figure A-52. Loiseau et al. observed similar retention of disordered BDC in the channels when using metal salt precursors with water as a solvent.³⁶ The change in pore form also effects the breathing behavior of MIL-53(Al) with high pressure CO_2 as seen in literature and this work (Figure A-51).^{48, 58} Therefore, it can be stated that a change in solvent composition provides a unique method of tuning the resulting adsorption properties of Al_4C_3 derived MIL-53(Al) by altering the pore form and breathing behavior allowing for further optimization of the framework.

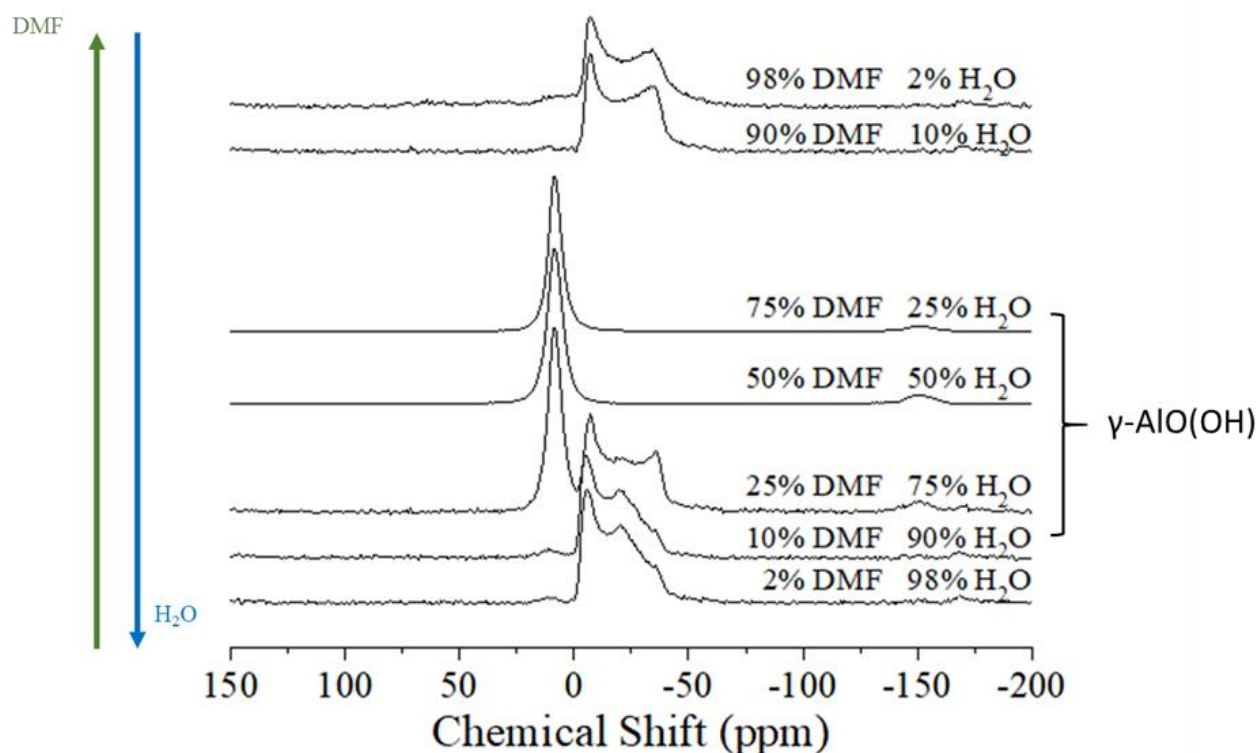


Figure 7-8: ^{27}Al MAS NMR of $\text{Al}_4\text{C}_3\text{-BDC-24h}$ with various solvent ratios of DMF and H_2O .

There is a vast difference in the solubility of terephthalic acid in water, DMF and mixtures thereof, ranging from 0.0015 to 7.2 (g BDC / g solvent) for water and DMF

respectively.⁵⁹⁻⁶⁰ Such a change in solubility will affect the local concentration at the boundary site of MOF growth and likely result in changes in growth kinetics and therefore morphology. SEM was employed to explore the changes in crystal shape and size as the solvent ratios ranged from DMF to H₂O. Figure 7-9 illustrates the general transition from short nanorods when pure water is used as a solvent, towards micron sized strips exhibiting larger aspect ratios, heading towards the needle-like structures seen when using pure DMF. Due to the heterogeneous nucleation process for MIL-53(Al) growth from Al₄C₃, the concentration of organic linker at the liquid-solid boundary will play a significant role in grain size and crystal growth. Nucleation is usually thermodynamically an “uphill” process requiring energy while growth on a crystal surface can be viewed as energetically favorable. This type of nucleation and crystal growth model was proposed by Lutsko et al. when describing zeolite formation.⁶¹ The implementation of Al₄C₃ as the metal source inherently involves heterogeneous nucleation reducing the energy cost for surface formation and total energy barrier. That leaves the effect of BDC concentration at the liquid-solid interface on crystal growth. Typically, lower concentrations of linker will facilitate slower growth allowing for larger crystals, which is the opposite of the observations in this study. Schafer et al. observed the same inhibiting effect with BTC when growing CuBTC at different linker concentrations.⁶² It was proposed that BTC partakes in a competing reversible chemical reaction that does not form CuBTC originally, similar to BDC reacting with the carbide precursor to form intermediate species. This phenomenon was previously described with NMR when using pure DMF, with the observed 4-, 5-, and 6-coordinate intermediate formation in Figure 7-3. The high concentration of BDC facilitated by the aprotic DMF solvent pushes towards the intermediate growth slowing down crystal growth

leading to the larger crystals seen in Figure 7-2d. When high concentrations of water are present, 6-coordinate alumina is the only intermediate observed which alludes to a different reaction path for MIL-53(Al) that does not proceed through multiple coordination's of alumina as water can generate 6-coordinate species through the direct hydrolysis of the carbide precursor. Therefore, the reduced concentrations of BDC with increased water ratios likely supports faster crystal growth producing the smaller nanorods seen in Figure 7-9. It is also important to point out the hexagonal plates of boehmite that are present between 25-50% water. Such hexagonal crystals of boehmite are common for both synthetic and naturally occurring species. The hydrothermal synthesis of hexagonal plates were documented by Santos et al. while demonstrating the templating effect of different precursor on boehmite morphology at 200°C, a similar temperature used in this study.⁶³ The striking resemblance of the hexagonal plates to the MIL-53(Al) rods and needles further illustrates the templating properties obtained as Al_4C_3 converts to a reactive intermediate and finally the desired MIL-53(Al) crystal.

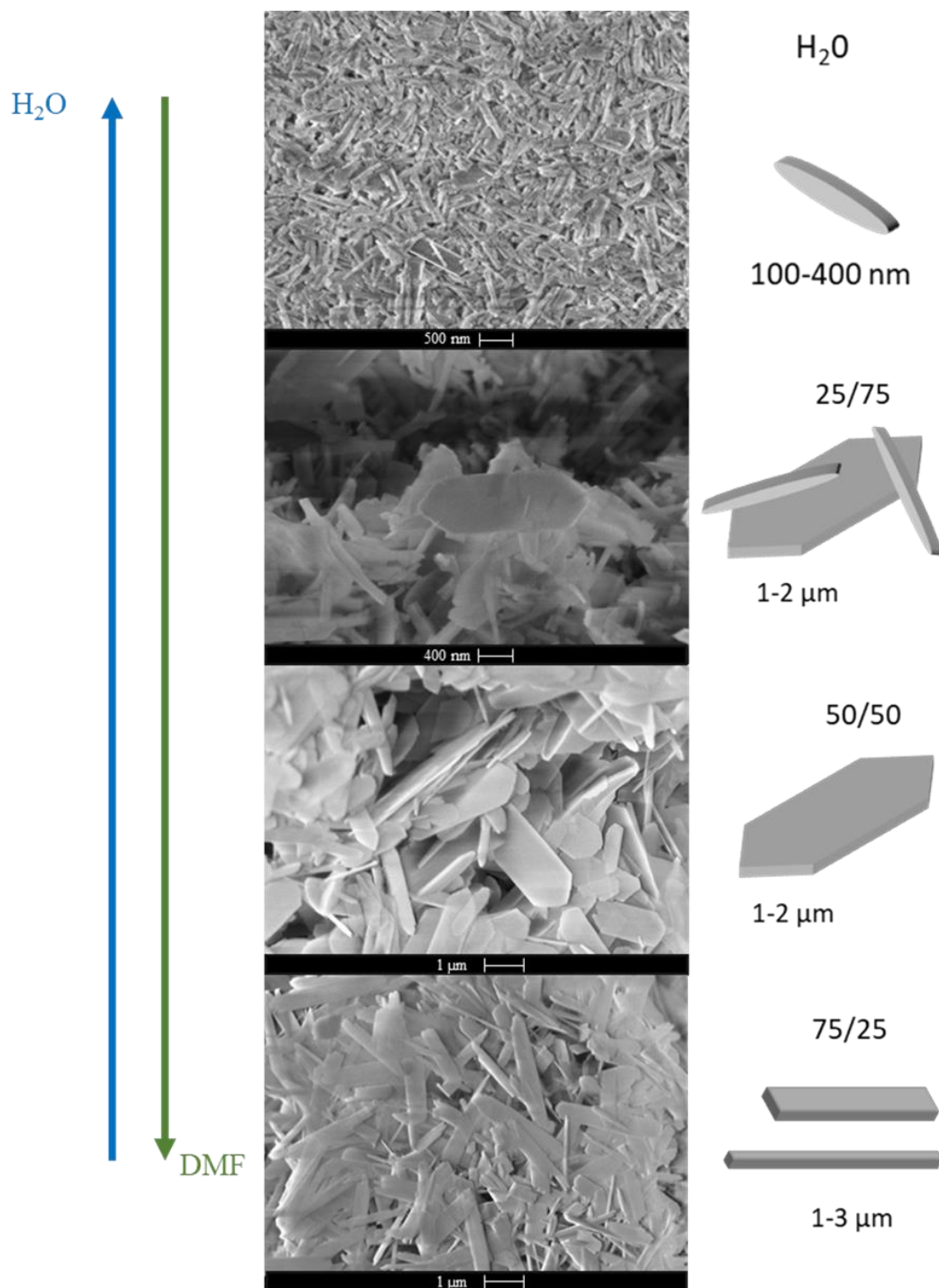


Figure 7-9: Morphological changes as a result of different DMF/H₂O solvent ratios

7.4 Conclusions

For the first time, an insoluble metal-carbon matrix was utilized as both a sacrificial metal precursor and morphological template for the growth of the metal-organic framework MIL-53(Al). The implementation of Al_4C_3 imparted a unique needle-like crystalline morphology while avoiding the use of corrosive and potentially hazardous counter-anions from ionic reagent species and acid modulating agents. Textural and chemical properties of the resulting product were found to be distinct from conventional MIL-53(Al) despite remaining topologically analogous to the parent crystal structure. Investigation of the growth mechanics indicate complete destruction of the carbide matrix and formation of new, crystalline material through solvothermal reaction in the presence of carboxylated ligands (BDC, NH_2 -BDC, BTC, and BA) in DMF. Temporal reaction studies revealed the carbide precursor yielded 94% of achievable MOF growth after 12h, formed by the evolution and conversion of 4-, 5-, and 6- coordinate aluminum oxide species, found as nodes present in the bulk material. Morphologically controlled MOF formation was observed through both surface and cross-sectional imaging, lending to the unique, needle-like morphology. Synthesized materials exhibit altered adsorption behaviors from parent MIL-53(Al), with a unique water vapor adsorption step at $P/P_0 = 0.58$ not reported to be present in traditionally synthesized MIL-53(Al). Thermodynamic stability of the materials at higher water loadings suggest a robust large pore form of MIL-53(Al) that can be implemented in high pressure adsorption applications while in the presence of water. The effect of synthesis solvent ranging from pure DMF to pure water exhibited the ability to significantly influence the resulting product with respect to crystallinity, porosity, and morphology. This report entails a previously unexplored technique towards nanoscale

tailorability of MOFs through the implementation of highly tunable precursors in the form of metal carbides. Further exploration of the extended family of metal carbides as sacrificial precursors and templates show great promise for creating unconventional MOF products that have not been previously attained. For instance, binary and tertiary carbides may be envisioned to facilitate the currently difficult task of synthesizing well-ordered mixed-metal MOFs. Furthermore, insights into the growth of MOF materials from insoluble precursors from this study can guide MOF synthesis from a variety other insoluble metal precursors to attain unique and tailorable porous nanomaterials.

7.5 References

1. Chae, H. K.; Siberio-Perez, D. Y.; Kim, J.; Go, Y. B.; Eddaoudi, M.; Matzger, A. J.; O'Keeffe, M.; Yaghi, O. M., A route to high surface area, porosity and inclusion of large molecules in crystals. *Nature (London, United Kingdom)* **2004**, 427 (6974), 523-527.
2. Sarkisov, L., Accessible Surface Area of Porous Materials: Understanding Theoretical Limits. *Advanced Materials* **2012**, 24 (23), 3130-3133.
3. Walton, K. S.; Snurr, R. Q.; K.S. Walton, R. Q. S., Applicability of the BET method for determining surface areas of microporous metal-organic frameworks. *Journal of the American Chemical Society* **2007**, 129 (18), 8552-8556.
4. Yaghi, O. M.; O'Keeffe, M.; Ockwig, N. W., Reticular synthesis and the design of new materials. *Nature* **2003**, 423, 705-714.
5. Garibay, S. J.; Cohen, S. M., Isorecticular synthesis and modification of frameworks with the UiO-66 topology. *Chemical Communications (Cambridge, England)* **2010**, 46 (41), 7700-2.
6. Jasuja, H.; Peterson, G. W.; Decoste, J. B.; Browe, M. a.; Walton, K. S., Evaluation of MOFs for air purification and air quality control applications: Ammonia removal from air. *Chemical Engineering Science* **2015**, 124, 118-124.
7. Kim, K. C.; Moghadam, P. Z.; Fairen-Jimenez, D.; Snurr, R. Q., Computational Screening of Metal Catecholates for Ammonia Capture in Metal–Organic Frameworks. *Langmuir* **2015**, 54 (13), 3257-3267.
8. Ragon, F.; Campo, B.; Yang, Q.; Martineau, C.; Wiersum, A. D.; Lago, A.; Guillerm, V.; Hemsley, C.; Eubank, J. F.; Vishnuvarthan, M.; Taulelle, F.; Horcajada, P.;

Vimont, A.; Llewellyn, P. L.; Daturi, M.; Devautour-Vinot, S.; Maurin, G.; Serre, C.; Devic, T.; Clet, G., Acid-functionalized UiO-66(Zr) MOFs and their evolution after intra-framework cross-linking: structural features and sorption properties. *J. Mater. Chem. A* **2015**, *3* (7), 3294-3309.

9. Chen, B.; Xiang, S.; Qian, G., Metal-Organic Frameworks with functional pores for recognition of small molecules. *Accounts of Chemical Research* **2010**, *43* (8), 1115-1124.

10. Kajiwar, T.; Higuchi, M.; Watanabe, D.; Higashimura, H.; Yamada, T.; Kitagawa, H., A systematic study on the stability of porous coordination polymers against ammonia. *Chem. Eur. J.* **2014**, *20* (47), 15611-15617.

11. Peterson, G. W.; Wagner, G. W.; Balboa, A.; Mahle, J.; Sewell, T.; Karwacki, C. J., Ammonia Vapor Removal by Cu₃(BTC)₂ and Its Characterization by MAS NMR. *The journal of physical chemistry. C, Nanomaterials and interfaces* **2009**, *113* (31), 13906-13917.

12. Watanabe, T.; Sholl, D. S., Molecular chemisorption on open metal sites in Cu₃(benzenetricarboxylate)₂: A spatially periodic density functional theory study. *Journal of Chemical Physics* **2010**, *133* (9).

13. Majano, G.; Pérez-Ramírez, J., Scalable Room-Temperature Conversion of Copper(II) Hydroxide into HKUST-1 (Cu₃(btc)₂). *Advanced Materials* **2013**, *25* (7), 1052-1057.

14. Li, Z.; Wu, Y.-n.; Li, J.; Zhang, Y.; Zou, X.; Li, F., The Metal-Organic Framework MIL-53(Al) Constructed from Multiple Metal Sources: Alumina, Aluminum Hydroxide, and Boehmite. *Chemistry - A European Journal* **2015**, *21* (18), 6913-6920.

15. Shekhah, O.; Wang, H.; Kowarik, S.; Schreiber, F.; Paulus, M.; Tolan, M.; Sternemann, C.; Evers, F.; Zacher, D.; Fischer, R. A.; Wöll, C., Step-by-Step Route for the Synthesis of Metal–Organic Frameworks. *Journal of the American Chemical Society* **2007**, *129* (49), 15118-15119.

16. Shekhah, O.; Liu, J.; Fischer, R. A.; Woll, C., MOF thin films: existing and future applications. *Chemical Society Reviews* **2011**, *40* (2), 1081-1106.

17. Summerfield, A.; Cebula, I.; Schröder, M.; Beton, P. H., Nucleation and Early Stages of Layer-by-Layer Growth of Metal Organic Frameworks on Surfaces. *The Journal of Physical Chemistry C* **2015**, *119* (41), 23544-23551.

18. Hoffmann R, M., Carbides. *American Scientist* **2002**, *90* (4), 318-320.

19. Presser, V.; Heon, M.; Gogotsi, Y., Carbide-Derived Carbons-Frome Porous Networks to Nanotubes and Graphene. *Advanced Functional Materials* **2011**, *21* (5), 810-833.

20. Ruschewitz, U., Binary and ternary carbides of alkali and alkaline-earth metals. *Coordination Chemistry Reviews* **2003**, *244* (1), 115-136.
21. Kennedy, J. L.; Drysdale, T. D.; Gregory, D. H., Rapid, energy-efficient synthesis of the layered carbide, Al_4C_3 . *Green Chemistry* **2015**, *17* (1), 285-290.
22. Carassiti, L.; Jones, A.; Harrison, P.; Dobson, P. S.; Kingman, S.; MacLaren, I.; Gregory, D. H., Ultra-rapid, sustainable and selective synthesis of silicon carbide powders and nanomaterials via microwave heating. *Energy & Environmental Science* **2011**, *4* (4), 1503-1510.
23. Vallance, S. R.; Kingman, S.; Gregory, D. H., Ultrarapid Materials Processing: Synthesis of Tungsten Carbide on Subminute Timescales. *Advanced Materials* **2007**, *19* (1), 138-142.
24. Han, W.; Fan, S.; Li, Q., Continuous synthesis and characterization of silicon carbide nanorods. *Chemical Physics Letters* **1997**, *265* (3-5), 374-378.
25. He, C. N.; Zhao, N. Q.; Shi, C. S.; Song, S. Z., Fabrication of aluminum carbide nanowires by a nano-template reaction. *Carbon* **2010**, *48* (4), 931-938.
26. Gogotsi, Y., Chemical vapour deposition: Transition metal carbides go 2D. *Nat Mater* **2015**, *14* (11), 1079-1080.
27. Mangarella, M. C.; Ewbank, J. L.; Dutzer, M. R.; Alamgir, F. M.; Walton, K. S., Synthesis of embedded iron nanoparticles in Fe_3C -derived carbons. *Carbon* **2014**, *79*, 74-84.
28. Moran, C. M.; Marti, R. M.; Hayes, S. E.; Walton, K. S., Synthesis and characterization of aluminum carbide-derived carbon with residual aluminum-based nanoparticles. *Carbon* **2017**, *114*, 482-495.
29. Dutzer, M. R.; Mangarella, M. C.; Schott, J. A.; Dai, S.; Walton, K. S., The effects of reactor design on the synthesis of titanium carbide-derived carbon. *Chemical Engineering Science* **2017**, *160*, 191-199.
30. Mangarella, M. C.; Walton, K. S., Tailored Fe_3C -derived carbons with embedded Fe nanoparticles for ammonia adsorption. *Carbon* **2015**, *95*, 208-219.
31. Borchardt, L.; Hoffmann, C.; Oschatz, M.; Mammitzsch, L.; Petasch, U.; Herrmann, M.; Kaskel, S., Preparation and application of cellular and nanoporous carbides. *Chemical Society Reviews* **2012**, *41* (15), 5053-5067.
32. Chmiola, J.; Largeot, C.; Taberna, P.-L.; Simon, P.; Gogotsi, Y., Monolithic carbide-derived carbon films for micro-supercapacitors. *Science* **2010**, *328* (5977), 480-483.

33. Furukawa, H.; Cordova, K. E.; O'Keeffe, M.; Yaghi, O. M., The chemistry and applications of metal-organic frameworks. *Science* **2013**, *341* (6149), 1230444-1230444.
34. Zhan, G.; Zeng, H. C., Alternative synthetic approaches for metal-organic frameworks: transformation from solid matters. *Chemical Communications* **2017**, *53* (1), 72-81.
35. Reboul, J.; Furukawa, S.; Horike, N.; Tsotsalas, M.; Hirai, K.; Uehara, H.; Kondo, M.; Louvain, N.; Sakata, O.; Kitagawa, S., Mesoscopic architectures of porous coordination polymers fabricated by pseudomorphic replication. *Nat Mater* **2012**, *11* (8), 717-723.
36. Loiseau, T.; Serre, C.; Huguenard, C.; Fink, G.; Taulelle, F.; Henry, M.; Bataille, T.; Férey, G., A Rationale for the Large Breathing of the Porous Aluminum Terephthalate (MIL-53) Upon Hydration. *Chemistry – A European Journal* **2004**, *10* (6), 1373-1382.
37. Massiot, D.; Fayon, F.; Capron, M.; King, I.; Le Calvé, S.; Alonso, B.; Durand, J.-O.; Bujoli, B.; Gan, Z.; Hoatson, G., Modelling one- and two-dimensional solid-state NMR spectra. *Magnetic Resonance in Chemistry* **2002**, *40* (1), 70-76.
38. Gomez, L. F.; Zacharia, R.; #xe9; nard, P.; Chahine, R., Simulation of Binary CO₂/CH₄ Mixture Breakthrough Profiles in MIL-53 (Al). *Journal of Nanomaterials* **2015**, *2015*, 15.
39. Boutin, A.; Coudert, F.-X.; Springuel-Huet, M.-A.; Neimark, A. V.; Férey, G.; Fuchs, A. H., The Behavior of Flexible MIL-53(Al) upon CH₄ and CO₂ Adsorption. *The Journal of Physical Chemistry C* **2010**, *114* (50), 22237-22244.
40. Férey, G.; Serre, C., Large breathing effects in three-dimensional porous hybrid matter: facts, analyses, rules and consequences. *Chem. Soc. Rev* **2009**, *38*, 1380-1399.
41. Chin, J. M.; Chen, E. Y.; Menon, A. G.; Tan, H. Y.; Hor, A. T. S.; Schreyer, M. K.; Xu, J., Tuning the aspect ratio of NH₂-MIL-53(Al) microneedles and nanorods via coordination modulation. *CrystEngComm* **2013**, *15* (4), 654-657.
42. Asadi, T.; Ehsani, M. R.; Ribeiro, A. M.; Loureiro, J. M.; Rodrigues, A. E., CO₂/CH₄ Separation by Adsorption using Nanoporous Metal organic Framework Copper-Benzene-1,3,5-tricarboxylate Tablet. *Chemical Engineering & Technology* **2013**, *36* (7), 1231-1239.
43. Bräuniger, T.; Chandran, C. V.; Wedig, U.; Jansen, M., NMR Chemical Shift and Quadrupolar Interaction Parameters of Carbon-Coordinated ²⁷Al in Aluminium Carbide, Al₄C₃. *Zeitschrift für anorganische und allgemeine Chemie* **2011**, *637* (5), 530-535.
44. Armstrong, M. W. Synthesis of stable free radicals as potential organic metals; Synthesis of oxygenated indacene derivatives; Reactions of aromaticpoly (N, N-dimethyl amides) with electrophiles. 1983.

45. Bannwart, L.; Abele, S.; Tortoioli, S., Metal-Free Amidation of Acids with Formamides and T3P. **2016**, 48 (13), 2069-2078.
46. Kumagai, T.; Anki, T.; Ebi, T.; Konishi, A.; Matsumoto, K.; Kurata, H.; Kubo, T.; Katsumoto, K.; Kitamura, C.; Kawase, T., An effective synthesis of N,N-dimethylamides from carboxylic acids and a new route from N,N-dimethylamides to 1,2-diaryl-1,2-diketones. *Tetrahedron* **2010**, 66 (46), 8968-8973.
47. Canivet, J.; Bonnefoy, J.; Daniel, C.; Legrand, A.; Coasne, B.; Farrusseng, D., Structure-property relationships of water adsorption in metal-organic frameworks. *New Journal of Chemistry* **2014**, 38 (7), 3102-3111.
48. Mounfield Iii, W. P.; Walton, K. S., Effect of synthesis solvent on the breathing behavior of MIL-53(Al). *Journal of Colloid and Interface Science* **2015**, 447, 33-39.
49. Burtch, N. C.; Jasuja, H.; Walton, K. S., Water Stability and Adsorption in Metal-Organic Frameworks. *Chemical Reviews* **2014**, 114, 10575-10612.
50. Liu, Y.; Her, J.-H.; Dailly, A.; Ramirez-Cuesta, A. J.; Neumann, D. A.; Brown, C. M., Reversible Structural Transition in MIL-53 with Large Temperature Hysteresis. *Journal of the American Chemical Society* **2008**, 130 (35), 11813-11818.
51. Serre, C.; Millange, F.; Thouvenot, C.; Noguès, M.; Marsolier, G.; Louër, D.; Férey, G., Very Large Breathing Effect in the First Nanoporous Chromium(III)-Based Solids: MIL-53 or $\text{CrIII}(\text{OH}) \cdot \{\text{O}_2\text{C}-\text{C}_6\text{H}_4-\text{CO}_2\} \cdot \{\text{HO}_2\text{C}-\text{C}_6\text{H}_4-\text{CO}_2\text{H}\}_x \cdot \text{H}_2\text{O}_y$. *Journal of the American Chemical Society* **2002**, 124 (45), 13519-13526.
52. Cottineau, T.; Richard-Plouet, M.; Mevellec, J.-Y.; Brohan, L., Hydrolysis and Complexation of N , N -Dimethylformamide in New Nanostructured Titanium Oxide Hybrid Organic–Inorganic Sols and Gel. *The Journal of Physical Chemistry C* **2011**, 115 (25), 12269-12274.
53. Buncel, E.; Kesmarky, S.; Symons, E., The inherent instability of dimethylformamide-water systems containing hydroxide ion: further observations. *Journal of the Chemical Society D: Chemical Communications* **1971**, (2), 120-120.
54. Buncel, E.; Symons, E., The inherent instability of dimethylformamide–water systems containing hydroxide ion. *Journal of the Chemical Society D: Chemical Communications* **1970**, (3), 164-165.
55. ten Elshof, J. E.; Abadal, C. R.; Sekulić, J.; Chowdhury, S. R.; Blank, D. H. A., Transport mechanisms of water and organic solvents through microporous silica in the pervaporation of binary liquids. *Microporous and Mesoporous Materials* **2003**, 65 (2), 197-208.
56. Liu, J.; Zhang, F.; Zou, X.; Yu, G.; Zhao, N.; Fan, S.; Zhu, G., Environmentally friendly synthesis of highly hydrophobic and stable MIL-53 MOF nanomaterials. *Chemical Communications* **2013**, 49 (67), 7430-7432.

57. Giovine, R.; Volkringer, C.; Trébosc, J.; Amoureux, J.-P.; Loiseau, T.; Lafon, O.; Pourpoint, F., NMR crystallography to probe the breathing effect of the MIL-53(Al) metal-organic framework using solid-state NMR measurements of ^{13}C - ^{27}Al distances. *Acta Crystallographica Section C* **2017**, *73* (3), 176-183.
58. Biswas, S.; Ahnfeldt, T.; Stock, N., New Functionalized Flexible Al-MIL-53-X (X = -Cl, -Br, -CH₃, -NO₂, -(OH)₂) Solids: Syntheses, Characterization, Sorption, and Breathing Behavior. *Inorganic Chemistry* **2011**, *50* (19), 9518-9526.
59. Harper, J. J.; Janik, P., Terephthalic acid solubility. *Journal of Chemical and Engineering Data* **1970**, *15* (3), 439-440.
60. Wang, Q.; Xu, H.; Li, X., Solubilities of Terephthalic Acid in Dimethyl Sulfoxide + Water and in N,N-Dimethylformamide + Water from (301.4 to 373.7) K. *Journal of Chemical & Engineering Data* **2005**, *50* (2), 719-721.
61. Lutsko, J. F.; Basios, V.; Nicolis, G.; Caremans, T. P.; Aerts, A.; Martens, J. A.; Kirschhock, C. E. A.; Erp, T. S. v., Kinetics of intermediate-mediated self-assembly in nanosized materials: A generic model. *The Journal of Chemical Physics* **2010**, *132* (16), 164701.
62. Schäfer, P.; Kapteijn, F.; van der Veen, M. A.; Domke, K. F., Understanding the Inhibiting Effect of BTC on CuBTC Growth through Experiment and Modeling. *Crystal Growth & Design* **2017**, *17* (11), 5603-5607.
63. Santos, P. d. S.; Coelho, A. C. V.; Santos, H. d. S.; Kiyohara, P. K., Hydrothermal synthesis of well-crystallised boehmite crystals of various shapes. *Materials Research* **2009**, *12* (4), 437-445.

CHAPTER 8. CONCLUSIONS AND RECOMMENDATIONS

8.1 Conclusions

The work within this dissertation focuses on increasing fundamental understanding of porous materials derived from carbide precursors for enhanced acid gas adsorption. Two classes of materials are explored through the effects of synthesis variables on the resulting derivative and their respective physical, chemical, and adsorption attributes. Carbide-derived carbons, disordered derivatives, were explored for active sites in the form of functional groups and retained metal-based nanoparticles. Metal-organic frameworks, an ordered carbide derivative, were for the first time synthesized using a carbide as the metal precursor to facilitate and direct framework growth.

8.1.1 Metal-based nanoparticles in Al_4C_3 -CDCs and Mo_2C -CDC (Chapter 3, 4, 5)

Chapter 3 demonstrates for the first time the retention of aluminum-based nanoparticles through an evolving CDC matrix. The residual aluminum content can be controlled through synthesis conditions, which simultaneously effect surface area, PSD, and surface chemistry. Changes in etching temperature enables the PSD to be tuned from an entirely microporous carbon to a hybrid micro-mesoporous carbon matrix. The partial etching process was shown to enable the retention of aluminum-based nanoparticles up to 800°C. The formation of α - Al_2O_3 occurs once the etching temperature reaches 600°C providing a significantly less tunable metal site. Robust characterization of the amorphous nanoparticles seen at lower etching temperatures point towards retention of a mixture of species including Al_2O_3 , $AlCl_3$, $Al(OH)_3$, and BAC.

Chapter 4 focuses on converting the aforementioned mixture to a more reactive aluminum species for increased interaction with acid gases. A conversion of BAC to PAC occurs at high humidity's demonstrating the accessibility of the parent nanoparticles for post-synthetic conversion. Treatment with an alkaline environment revealed the successful conversion of parent nanoparticles away from PAC and towards amphoteric aluminum hydroxide. After 6 days of aging, amorphous nanoparticles began to crystallize into bayerite, a crystalline $\text{Al}(\text{OH})_3$ polymorph, which lead to reduced adsorption capacity. The formation of crystalline species facilitated pore blockage throughout the carbon matrix and with reduced edge hydroxyls compared to amorphous analogs, resulted in reduced CO_2 capacities. An optimized 24h alkaline treatment provided significantly increase CO_2 and SO_2 capacity up to 1 and 3 bar respectively, as a result of nanoparticle conversion to $\text{Al}(\text{OH})_3$ and an increase in pore volume. The average pore size was also demonstrated to play a role in the oxidation of SO_2 through oxygen functionalities, with a limiting pore diameter of <0.7 nm resulting in no loss of porosity and cyclic adsorption stability.

Chapter 5 entails the extension of partial etching to Mo_2C -CDCs for the potential use of molybdenum base nanoparticles for catalysis. For etching temperatures of $300\text{--}700^\circ\text{C}$, 1 hour of reaction allowed for the retention of bulk phase $\beta\text{-Mo}_2\text{C}$ in the sample. As etching temperatures approach 500°C poorly crystalized $\gamma\text{-MoC}$ is observed. An increase of reaction time to 2h revealed $\gamma\text{-MoC}$ as the only crystalline phase present, while TEM reveals a mixture of crystalline and non-crystalline nanoparticles. The crystalline regions matched $\gamma\text{-MoC}$ while the amorphous regions are attributed to molybdenum oxychlorides. The textural properties of the carbon matrix exhibited dependence on the etching temperature, with a semi-linear decrease in functional groups as etching temperature is

increased. This work provides a fundamental understanding with respect to synthesis conditions of a molybdenum-based catalyst supported inside a highly tunable carbon matrix.

8.1.2 Tuning textural and chemical properties of fully etched CDCs through annealing (Chapter 6)

Using three carbide precursors and four separate post-etching environment, Chapter 6 explores the significant effects annealing has on textural and chemical properties of CDCs. Changes in the quantity and identity of functional groups on the surface were observed for different carbide precursors and annealing environments. The density of oxygen on the surface and the interior of the CDC was shown to rely heavily on the carbide precursor with each derivative exhibiting unique oxygen content and concentrations. Control over nitrogen species, both quantity and identity, was achieved through the introduction of NH_3 . The annealing process, which is known to remove chlorine content, displayed diffusional limitations with high chlorine concentration in the bulk of each sample, suggesting that if the removal of chlorine is required, increased time and annealing temperatures should be implemented. In each case, the annealing process produced equal or higher capacities for the adsorption of CO_2 , H_2O , and SO_2 . A combination of micropores, oxygen, and nitrogen functionalities contributed to an overall increase in interaction of non-polar CO_2 , with an increase in nitrogen content directly correlated with an increase in low pressure adsorbate interactions. For SO_2 adsorption, nitrogen content was demonstrated to be effective for low pressures regions, while oxygen content correlated with increased capacity in mesopores as a result of SO_2 oxidizing to SO_3 at basic oxygen functionalities throughout the carbon matrix. These insights offer an

increased fundamental understand of tunability, beyond angstrom level tuning of pores, for carbide-derived carbons.

8.1.3 Structured growth of metal-organic framework MIL-53(Al) from a sacrificial aluminum carbide precursor (Chapter 7)

One of the greatest attributes of carbide-derived carbon is the pseudomorphic replication from the carbide precursor to the carbon derivative. This phenomenon allows for spatial engineering on an angstrom to nanometer scale, which is unprecedented for in metal-organic framework literature. Therefore, for the first time, an insoluble metal-carbon matrix was implemented as both a sacrificial precursor and morphological template for the growth of MIL-53(Al). The implementation of the insoluble Al_4C_3 imparted a unique needle-like morphology without accessory modulating agents. Textural and chemical properties of the resulting frameworks were found to be distinct from conventional MIL-53(Al) while remaining topologically analogous. Growth mechanics indicate complete destruction of the carbide matrix and subsequent formation of a new crystalline framework through solvothermal reaction in the presence of carboxylated ligands (BDC, NH_2 -BDC, BTC, and BA) in DMF. Interestingly, the formation of 4-, 5-, and 6- coordinate aluminum oxide intermediates, found as nodes present in the bulk material were observed as a crucial step towards framework growth. Cross sections of the framework revealed a layer-by-layer process involving the conversion of Al_4C_3 to the intermediate oxide and subsequently MIL-53(Al). The process regulates growth to the surface of the precursor and led to the exfoliation of the crystalline framework into the observed needle-like morphology. Changes in stability and adsorption behavior were also realized when MIL-53(Al) was grown from the insoluble Al_4C_3 matrix, with increased water stability and altered breathing

behavior. Solvent effects were also explored, with the crystallinity and porosity of the resulting product displaying a strong dependence on the ratio of water and DMF used in the solvothermal synthesis.

8.2 Recommendations

The work presented herein provides a baseline from which the author believes further studies should be pursued. The following sections are recommendations for future work relating to each subject explored throughout this dissertation.

8.2.1 Heat treatments on fully and partially etched carbide-derived carbons (Chapter 3 and 4 extension)

The post-synthetic process of exposing a CDC to elevated temperatures possesses the ability to impart profound effects on both textural and chemical properties of the material. Preliminary studies, Figure 8-1, on heat treatment of partially etched Al_4C_3 revealed changes to the PSD, surface chemistry and residual metal content. These insights provide enough evidence to suggest that heat treatment can afford increased tunability to the already highly tuneable carbide-derived carbon with respect to angstrom level alterations on PSD and changes in surface acid/base characteristic by manipulating functional groups and the basal plane electrons of the carbon matrix. The decomposition of acidic oxygen functional groups would allow for increase basic features in the CDC while changes in the PSD have the propensity to adsorb more gas or reach a critical pore diameter for a desired separation process. Also seen in Figure 8-1d, heat treatment converts the residual metal in Al_4C_3 -CDC to Al_2O_3 polymorphs, providing a different active site for

catalysts or as a catalytic substrate. A study on heat treatment of various CDCs would provide a new and powerful technique for optimization for any desired application.

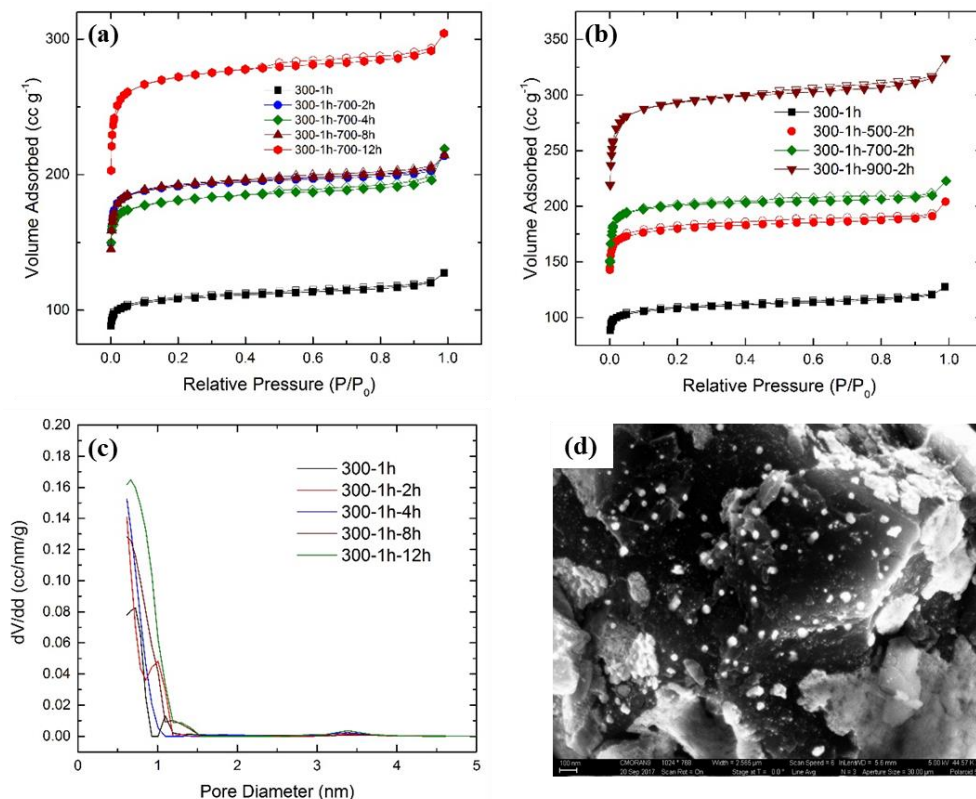


Figure 8-1: Effects of post-synthetic heat treatment on Al₄C₃-CDCs regarding (a) temporal effects on N₂ isotherms at 700°C, (b) temperature effects on N₂ isotherms, (c) temporal effect on PSD, and (d) SEM images of oxide nanoparticles

8.2.2 Modification and implementation of partially etched Mo₂C-CDC for catalysis (Chapter 5 extension)

The partial etching of Mo₂C was performed as a direct consequence of the molybdenum metal center possessing catalytic properties analogous to platinum group metals. With the demonstrated retention of molybdenum-based nanoparticles throughout the high surface area and large pore structured carbon matrix, it is recommended to implement partially etched Mo₂C-CDC for catalytic applications. As mentioned in the

introduction of Chapter 5, molybdenum derivatives excel at heterogeneous catalysis,¹⁻² hydrogen evolution,³⁻⁴ alkene metathesis,⁵ and general oxidation reactions.⁶ For optimization of such reactions, post-synthetic modification of the metal, analogous to Chapter 4, is recommended to achieve various molybdenum derivatives. As the partially etched Mo₂C-CDC stands, it should be evaluated for catalytic activity for reactions such as hydrodesulphurization, hydrodenitrogenation, water-gas shift and the Fischer Tropsch reaction.⁷ With the capacity for pseudomorphic replication, multitude of potential catalytic processes, and a porous structure large enough to facilitate diffusion of reagents and products, partially etched Mo₂C-CDC offers an excellent degree of flexibility and potential for an effective catalytic composite.

8.2.3 Increased understanding of the reactivity of various CDCs for oxygen and nitrogen functional groups (Chapter 6 extension)

A dearth of information remains around the tunability of surface chemistry of carbide-derived carbons. Therefore, it is recommended that a series of CDCs, such as (SiC, TiC, Mo₂C etc.) be studied to better understand the oxidation process of CDCs upon atmospheric exposure to understand why certain derivatives possess increased reactivity to towards oxygen and nitrogen. This is likely a complicated answer involving the spacing of the carbon in the precursor and the metal chloride formed, as well as the synthesis conditions. An XPS study of the CDCs pre- and post-atmospheric exposure along with computational work would lead to a better understanding of the chemical properties and reactivity of these unique materials. An increased understanding of why functionalities change across different precursors would lead to better predictive methods on which CDCs would be best suited for a desired application. This same understanding would elucidate

more information on the mechanism for annealing and how it alters chemical functionalities.

8.2.4 *Expanding on MOF growth from carbide precursors (Chapter 7 extension)*

With the first ever MOF grown from a carbide precursor, a significant next step is exploiting the engineering aspect of templating carbide precursors for structured MOF growth. Carbides can provide unique geometries and entail nanometer scale control over film growth. This level of engineering can be directly transferred into MOF templating, allowing for an unprecedented degree of spatial control of framework growth. The direct conversion of a film of carbide into a MOF film, in a specific design or pattern, is likely achievable through using sacrificial carbide precursors. This technique would greatly enhance the feasibility of creating MOF-based devices where spatial control of the crystal is imperative. This method could also facilitate the growth of MOF composites by generating a templated substrate with preordained carbide regions which are subsequently converted into the desired framework. The body of work relating to templating carbon materials from carbides can provide a massive leap forward in implementing templated MOFs from carbides. It is also recommended to expand work with single metal carbides to explore the potential of using different metal centers. Iron carbide (Fe_3C) displays great promise for the growth of MIL-53(Fe) in our preliminary results. By using the same synthesis conditions as outlined for MIL-53(Al), the degradation of the iron carbide structure was observed while a new distorted crystalline species began to form. Therefore, a systematic study is recommended to determine the optimal conditions for MIL-53(Fe) growth from Fe_3C .

The generation of mixed-metal MOFs has proven problematic in literature, particularly with facilitating a homogenous mixture. Binary and ternary carbides provide a well-ordered distribution of metal centers that could facilitate even growth of the mixed-metal framework which is not available through traditional methods. By controlling the synthesis environment (pH, temperature, time, and solvent) the rate of formation and resulting morphology can be manipulated. As a starting point it is suggested that Ti_2AlC and Ti_3AlC_2 be explored for framework growth. Though it would not likely produce a true mixed metal MOF, of interest would be if MIL-53(Al) and MIL-125(Ti) form independently or result in unique growth, dispersion, and morphology of the crystal system as a result of the controlled metal release from the templated carbide. An aluminum-iron based carbide would provide an interesting case study for a true mixed metal MOF with MIL-53(Al-Fe).

Lastly, of interest to this author is the combination of CDC and MOF growth. With CDC reaction kinetics well studied, there is angstrom/nanometer level of control that can be achieved when generating a carbon shell, leaving behind a desired carbide core. Future work on converting the carbide core into a framework would provide an interesting route to a carbon-MOF matrix which would likely entail unique properties. With various etching conditions available, a wide range of textural and chemical properties could be applied to the carbon shell, potentially providing environmental protection to the MOF core, promoting adsorption synergy, or creating a size selective barrier for the internal framework. The dual use of the carbide precursor is uniquely positioned to provide such a composite, with a high degree of tunability.

8.3 References

1. Széchenyi, A.; Solymosi, F., Production of Hydrogen in the Decomposition of Ethanol and Methanol over Unsupported Mo₂C Catalysts. *The Journal of Physical Chemistry C* **2007**, *111* (26), 9509-9515.
2. Ma, Y.; Guan, G.; Phanthong, P.; Li, X.; Cao, J.; Hao, X.; Wang, Z.; Abudula, A., Steam reforming of methanol for hydrogen production over nanostructured wire-like molybdenum carbide catalyst. *International Journal of Hydrogen Energy* **2014**, *39* (33), 18803-18811.
3. Weigert, E. C.; South, J.; Rykov, S. A.; Chen, J. G., Multifunctional composites containing molybdenum carbides as potential electrocatalysts. *Catalysis Today* **2005**, *99* (3), 285-290.
4. Vrubel, H.; Hu, X., Molybdenum Boride and Carbide Catalyze Hydrogen Evolution in both Acidic and Basic Solutions. *Angewandte Chemie* **2012**, *124* (51), 12875-12878.
5. Malcolmson, S. J.; Meek, S. J.; Sattely, E. S.; Schrock, R. R.; Hoveyda, A. H., Highly efficient molybdenum-based catalysts for enantioselective alkene metathesis. *Nature* **2008**, *456*, 933.
6. Jitsukawa, K.; Kaneda, K.; Teranishi, S., Molybdenum-catalyzed oxidation of allylic alcohols using tert-butyl hydroperoxide. Regioselective cleavages of the double bond and the adjacent single bond with a hydroxyl group. *The Journal of Organic Chemistry* **1984**, *49* (1), 199-201.
7. Wan, C.; Knight, N. A.; Leonard, B. M., Crystal structure and morphology control of molybdenum carbide nanomaterials synthesized from an amine-metal oxide composite. *Chemical Communications* **2013**, *49* (88), 10409-10411.

APPENDIX A. SUPPLEMENTAL INFORMATION

A.1 Chapter 3: Synthesis and Characterization of Aluminum Carbide-Derived Carbon with Residual Aluminum-Based Nanoparticles

Reproduced (adapted) from Moran C.M., et al., *Synthesis and characterization of aluminum carbide-derived carbon with residual aluminum-based nanoparticles*. Carbon (2017) 114, p.482-495.

A.1.1 Supplemental and Raw Data for Chapter 3

Table A-1: EDS of residual white powder on quartz boat for Al₄C₃-CDC-300-1h samples

Elements	Weight %	Atomic %
Carbon	5.12	8.33
Oxygen	49.64	60.69
Aluminum	34.76	25.19
Chlorine	10.48	5.78

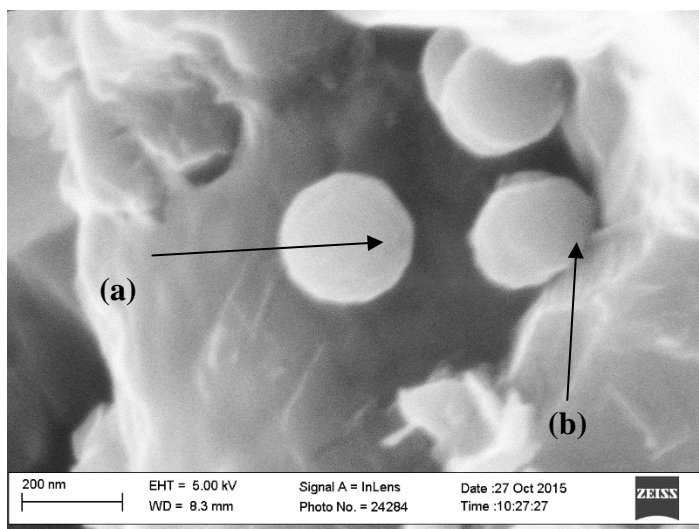


Figure A-1: Aluminum based spheres observed at 500°C by SEM

Table A-2: EDS on Aluminum based spheres observed at 500°C by SEM

Sample (a)	Elements	Weight %	Atomic %
	Carbon	69.18	79.1
	Oxygen	14.92	12.8
	Aluminum	15.9	8.09

Sample (b)	Elements	Weight %	Atomic %
	Carbon	34.36	59.27

Aluminum	13	9.98
Chlorine	52.63	30.75

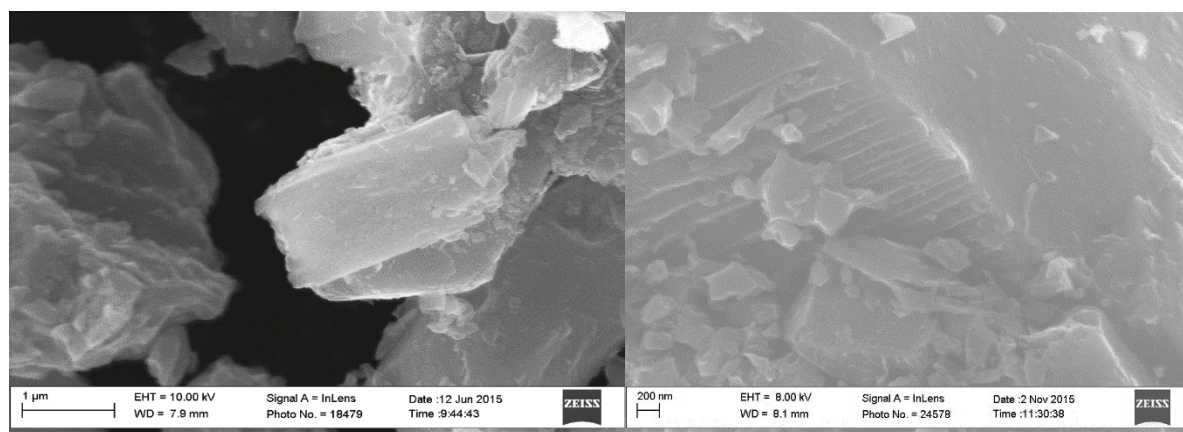


Figure A-2: Smooth surfaces and stair like structures seen in Al_4C_3 -CDC-500-1h

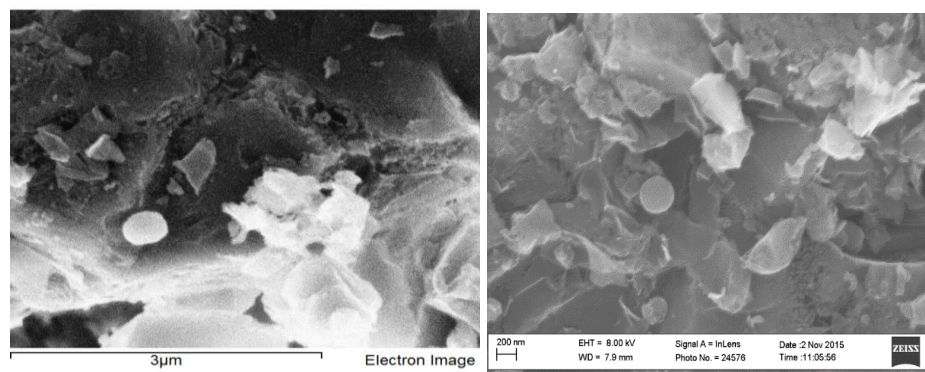


Figure A-3: Isolated carbonaceous microspheres in Al_4C_3 -CDC-700-1h

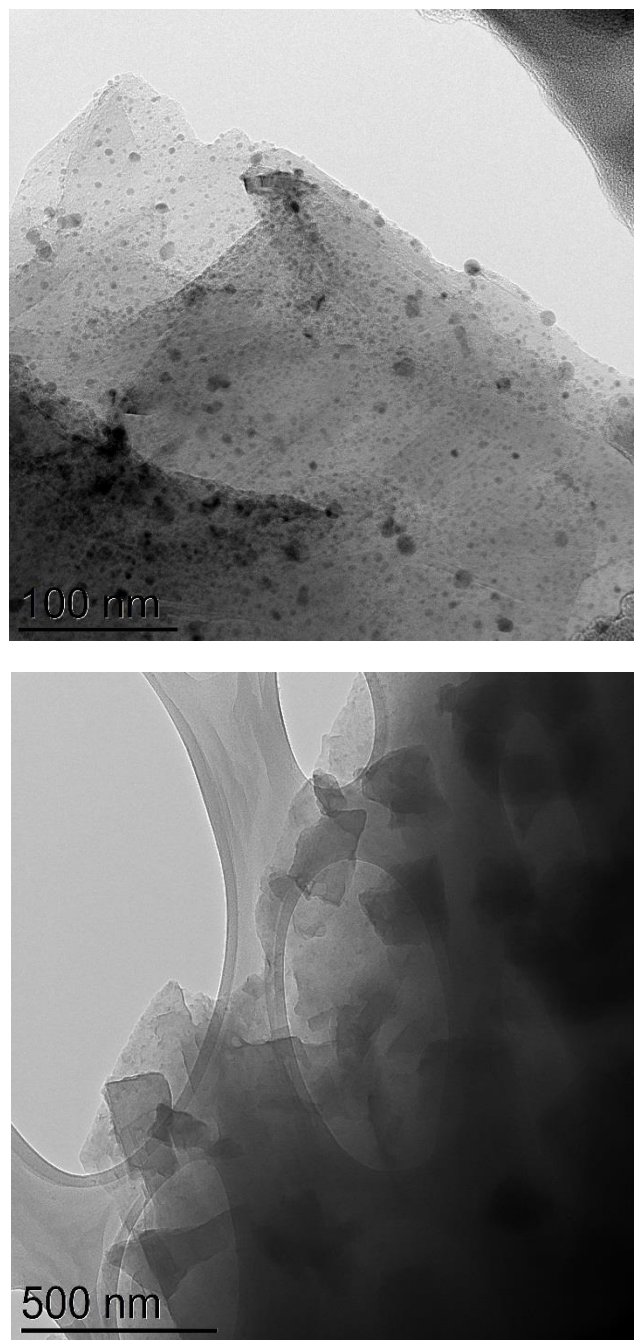


Figure A-4: TEM Images of Al_4C_3 -CDC-300-1h

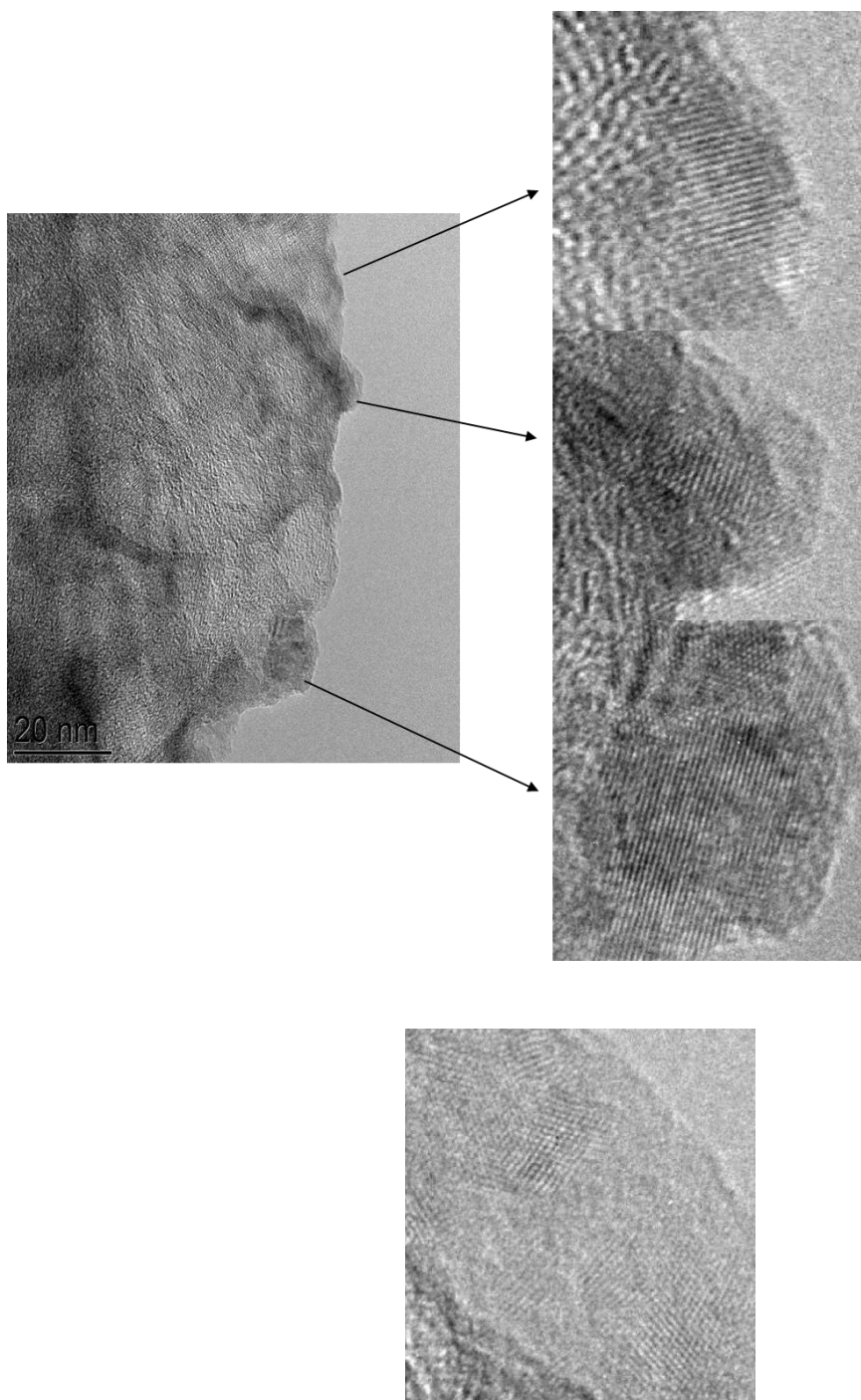


Figure A-5: TEM images of crystal lattices in Al_4C_3 -CDC-700-1h

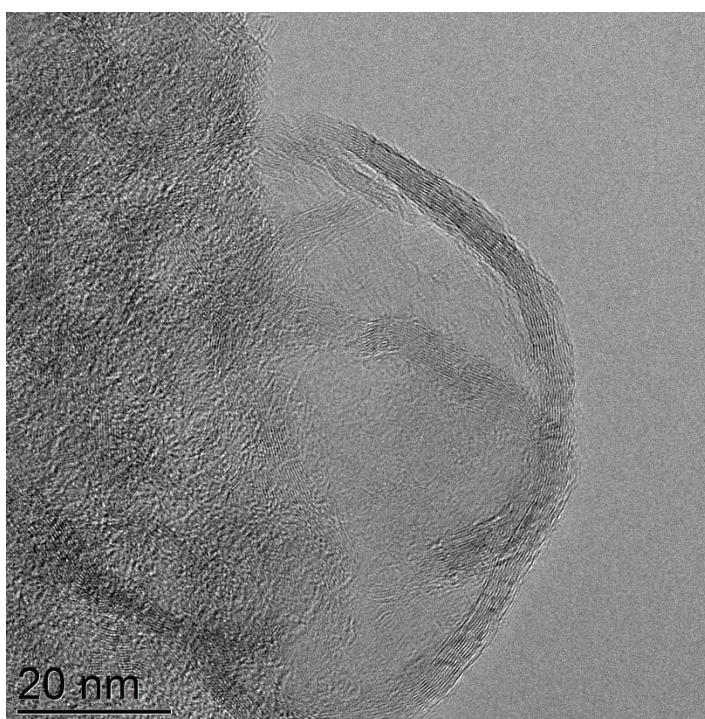
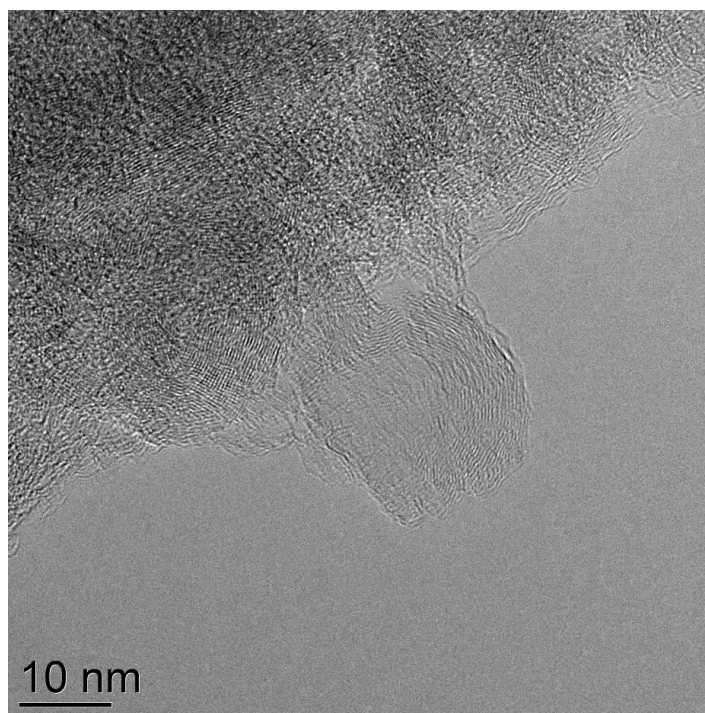


Figure A-6: TEM images of crystal lattices and graphite in Al_4C_3 -CDC-900-1h

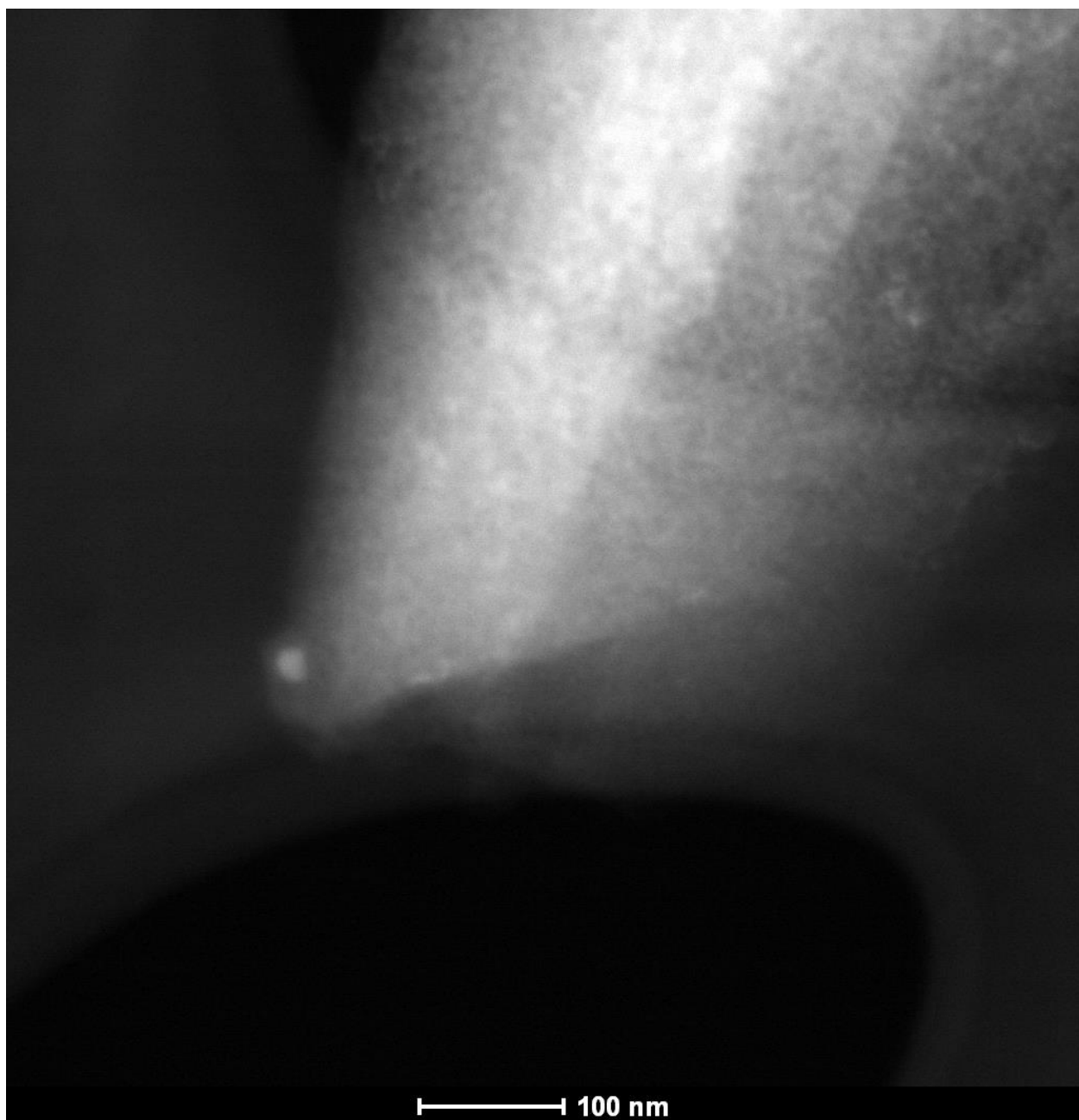


Figure A-7: HTEM image of an aluminum-based nanoparticle in Al_4C_3 -CDC-900-1h

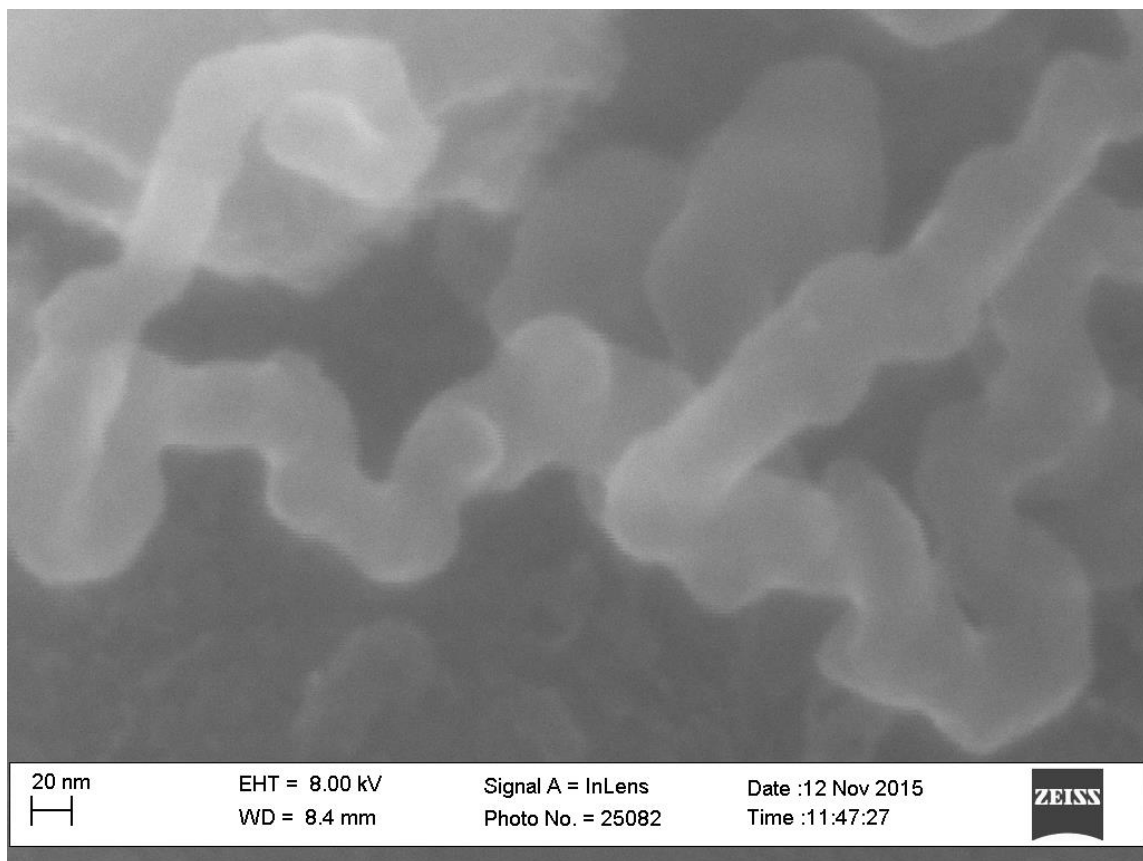


Figure A-8: SEM Image Al_4C_3 -CDC-500-1h

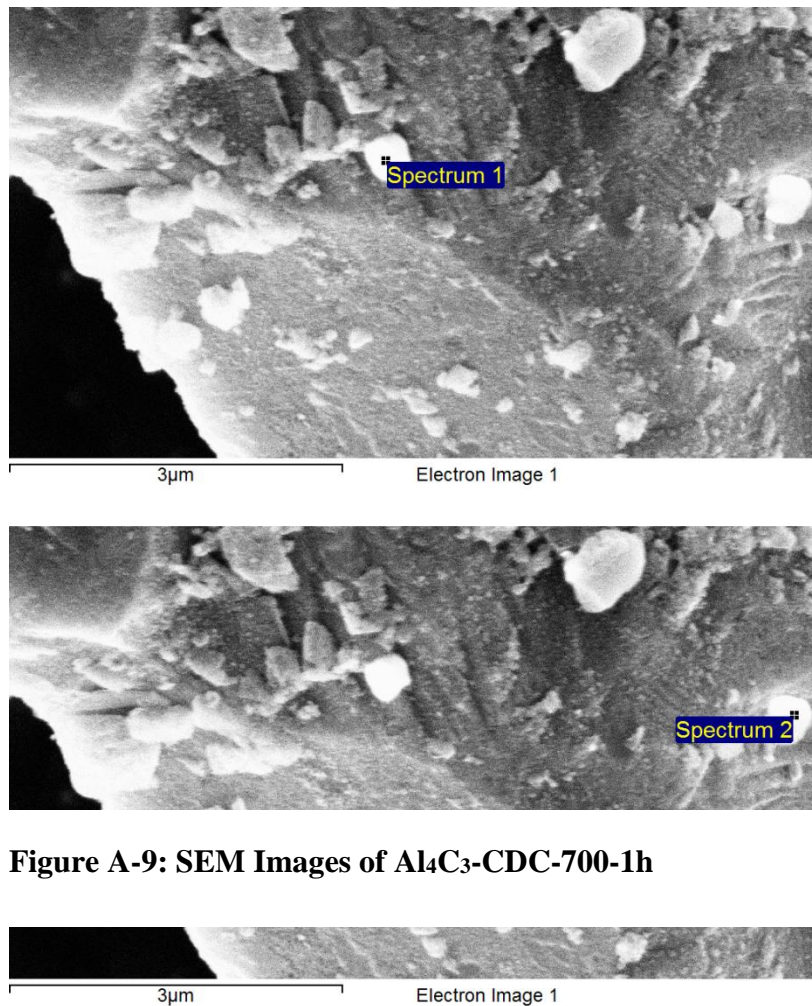


Figure A-9: SEM Images of Al₄C₃-CDC-700-1h

Table A-3: EDS of Al₄C₃-700-1h

Elements	Sample 1 Atomic %	Sample 2 Atomic %
Carbon	75.46	73.73
Oxygen	17.40	13.3
Aluminum	7.13	12.96

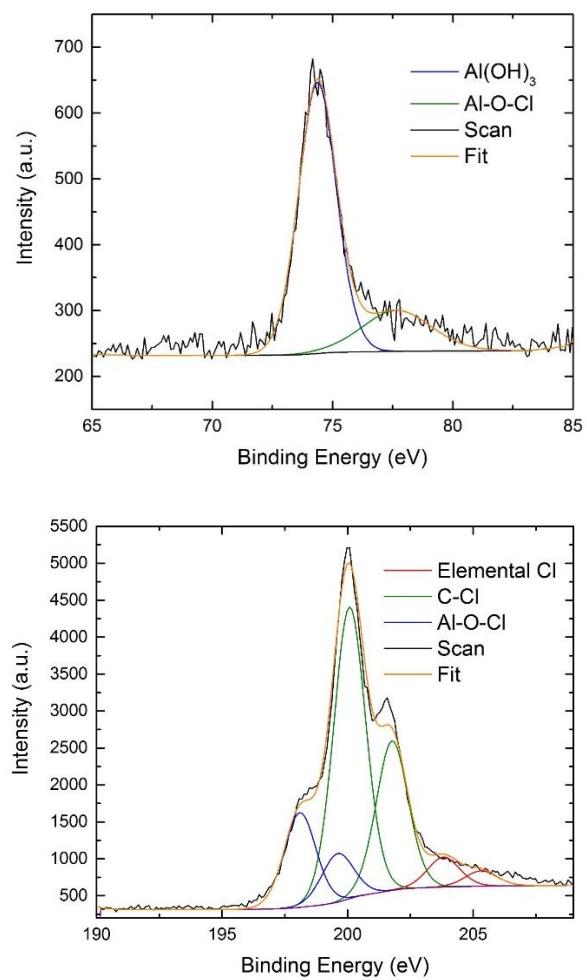


Figure A-10: Al 2P and O1s XPS scans on Al₄C₃-CDC-500-1h

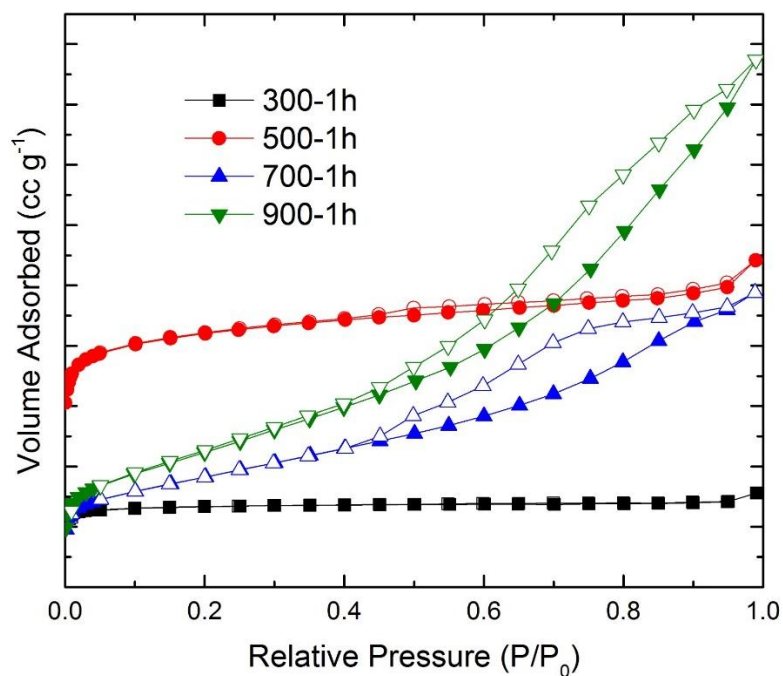


Figure A-11: N₂ isotherms for samples etched at 300, 500, 700 and 900 °C

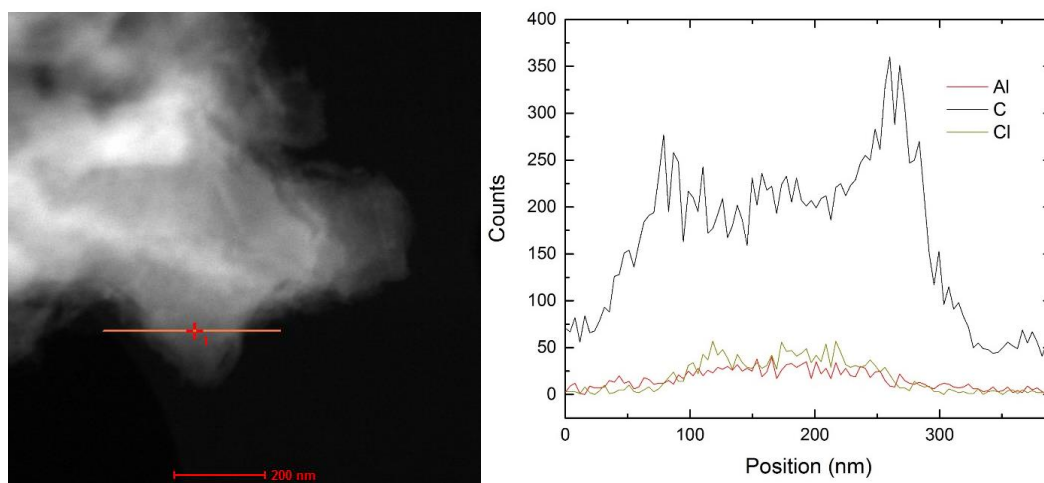


Figure A-12: (left) High Angle Annular Dark Field (HAADF) of Al₄C₃-CDC-500-1h. (right) Line profiles of elemental composition measured by EDS for Al, C, Cl species.

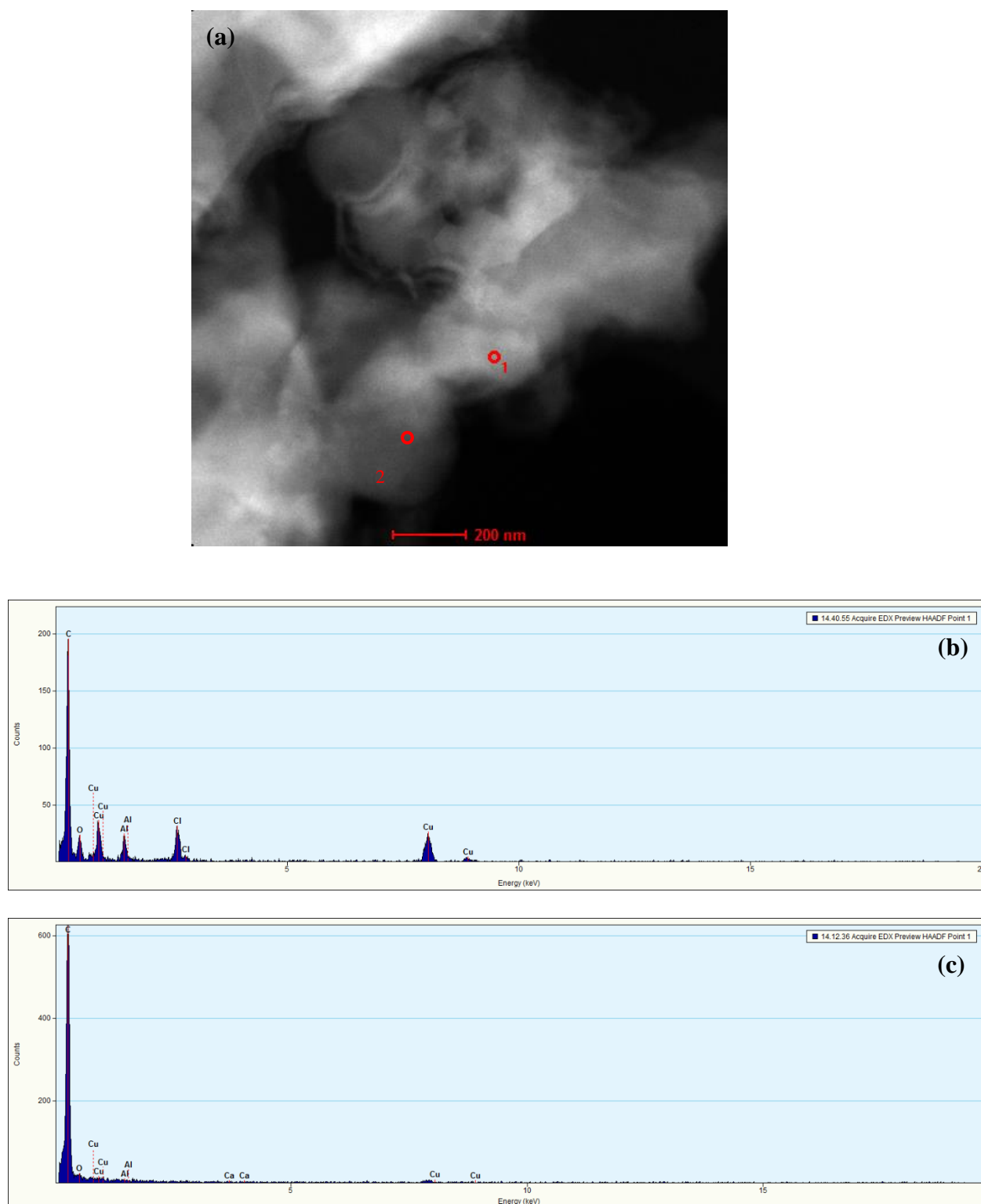


Figure A-13: (a) HAADF of Al₄C₃-CDC-500-1h. (b) EDS on point 1 (c) EDS on point 2

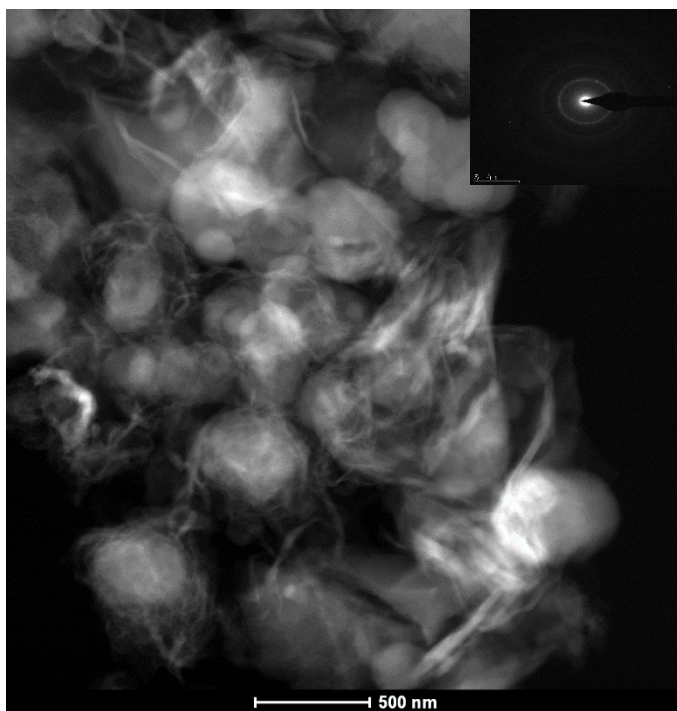


Figure A-14: HAADF of Al₄C₃-CDC-500-1h metal species with diffraction pattern

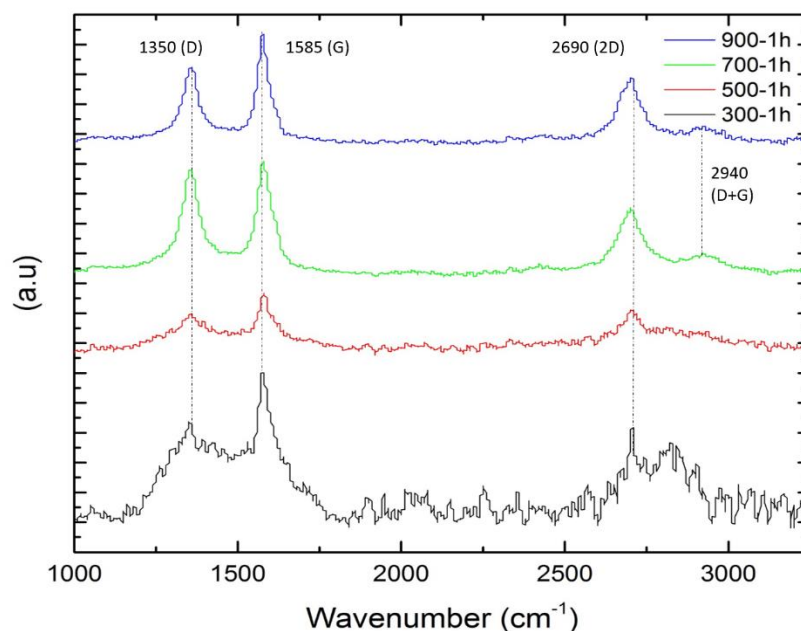


Figure A-15: Raman spectra on Al_4C_3 -CDC materials synthesized at different temperatures

Raman results follow suit with TEM observations and changes in carbon crystalline structures identified via powdered x-ray diffraction. Etching temperatures of 300°C show a mainly amorphous material with broad peaks, this is supported by only amorphous carbon characteristics visualized in TEM for Al_4C_3 -300-1h. As etching temperature increases the graphitic G band caused by the stretching of carbon-carbon bonds in graphitic carbon sharpens and at etching temperatures of 900°C the I_d/I_g ratio decreases, indicative of graphitization. These results agree with both the characterization methods used in this paper and literature on carbon formation in Al_4C_3 -CDCs.

A.2 Chapter 4: Tunable Nanoparticles in Aluminum Carbide-Derived Carbon for Enhanced Acid Gas Adsorption

A.2.1 Supplemental and Raw Data for Chapter 4

Table A-4: TGA results for residual metal before and after 5 days high humidity exposure.

Sample	Parent	5-Day-H ₂ O
300-1h	18.5%	17%
500-1h	8.5%	7%

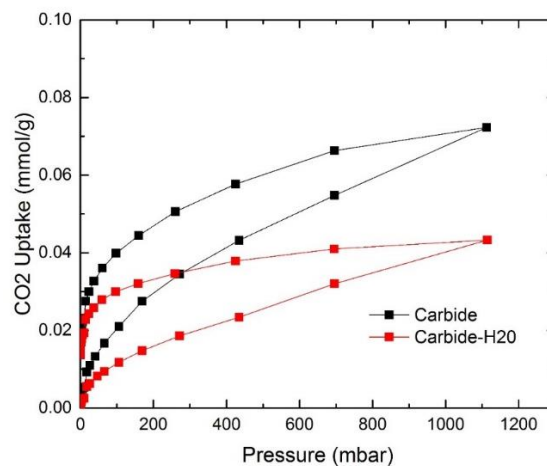
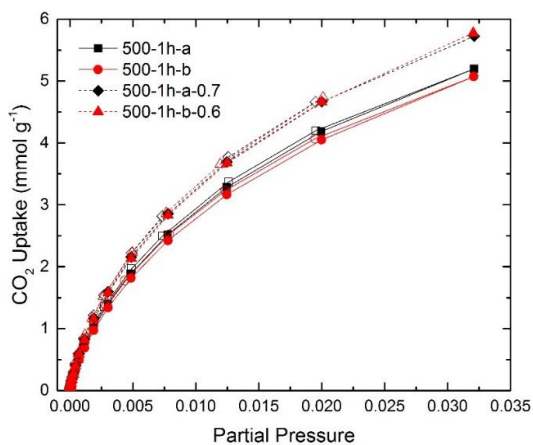


Figure A-16: (a) CO₂ on Al₄C₃ before and after water isotherm

Table A-5: EDS results on “bubbling” features after 5-day exposures

Element	300-1h-5 Day-H ₂ O		500-1h-5 Day-H ₂ O	
	Weight %	Atomic%	Weight%	Atomic%
C	50.68	65.82	75.22	86.30
O	20.76	20.24	7.81	6.73
Al	9.96	5.76	3.08	1.57
Cl	18.59	8.18	13.89	5.4

Table A-6 N₂ physisorption results after 5 days of water exposure for Al₄C₃-CDC-500-1h samples at 0.7 and 0.6 P/P₀



Sample	SA	PV
500-1h-a	1073	0.437
500-1h-0.7	1149	0.49
500-1h-b	1044	0.424
500-1h-0.6	1124	0.48

Figure A-17: Before and after CO₂ adsorption results after 5 days of water exposure for Al₄C₃-CDC-500-1h samples at 0.7 and 0.6 P/P₀.

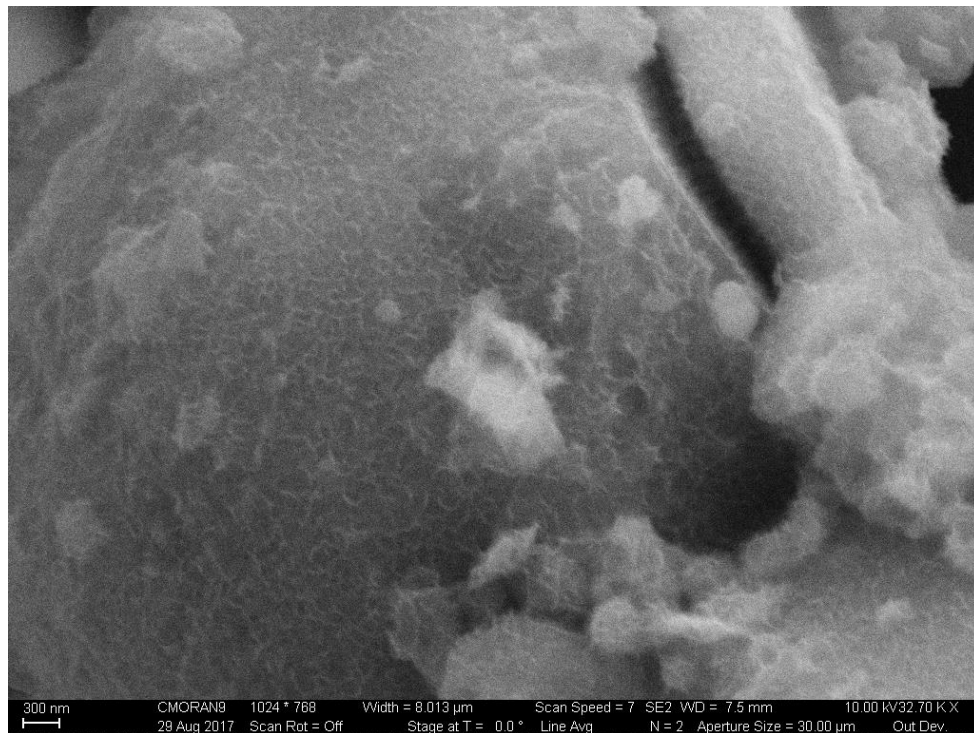
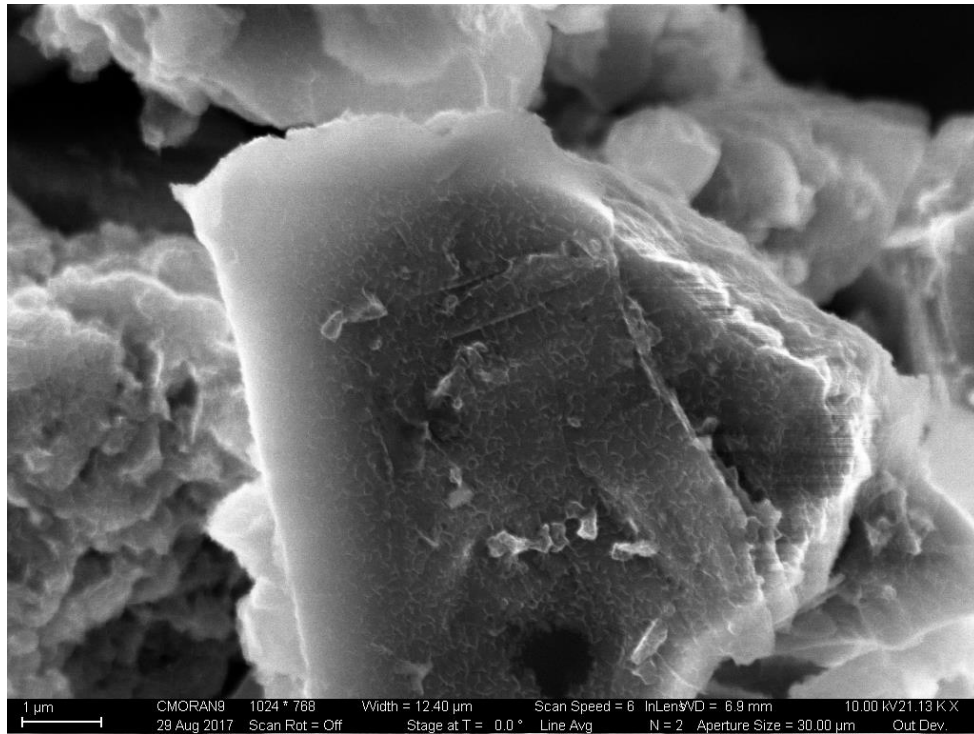


Figure A-18: PAC formation after DI standard treatment on Al_4C_3 -300-1h

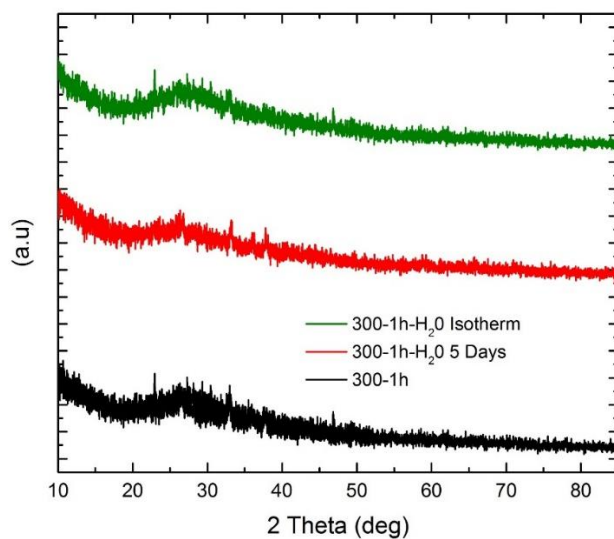


Figure A-19: XRD Patterns of $\text{Al}_4\text{C}_3\text{-CDC-300-1h}$ after water exposure

Note the peak at 26° 2θ is from the 002 plane of carbon and the emergence of peaks between $30\text{-}40^\circ$ 2θ are from a small AlN impurity in the precursor.

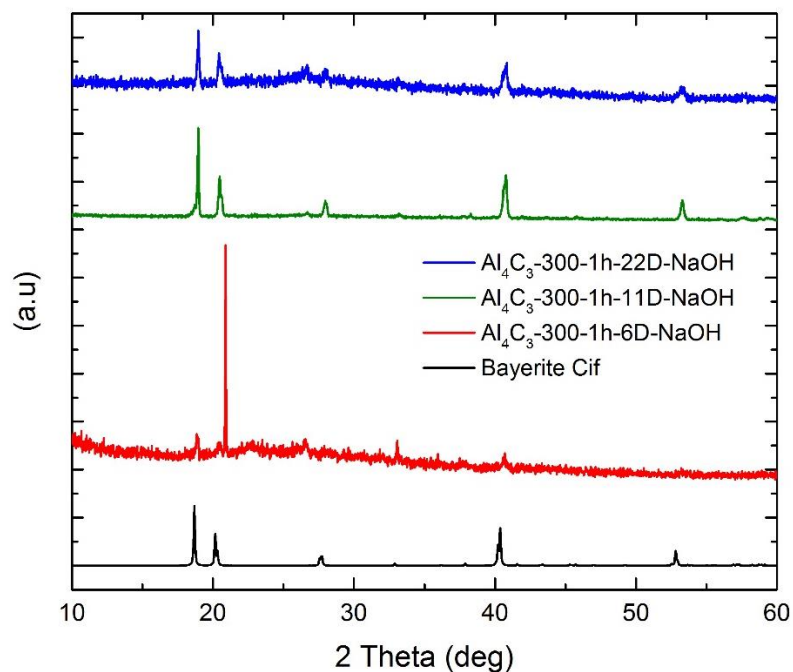


Figure A-20: PXRD on post-synthetically modified $\text{Al}_4\text{C}_3\text{-300-1h}$ materials

*Note that a strong reflection at $2\theta = 21$ is observed in Al_4C_3 -300-1h-6D-NaOH that is unique from Bayerite.¹

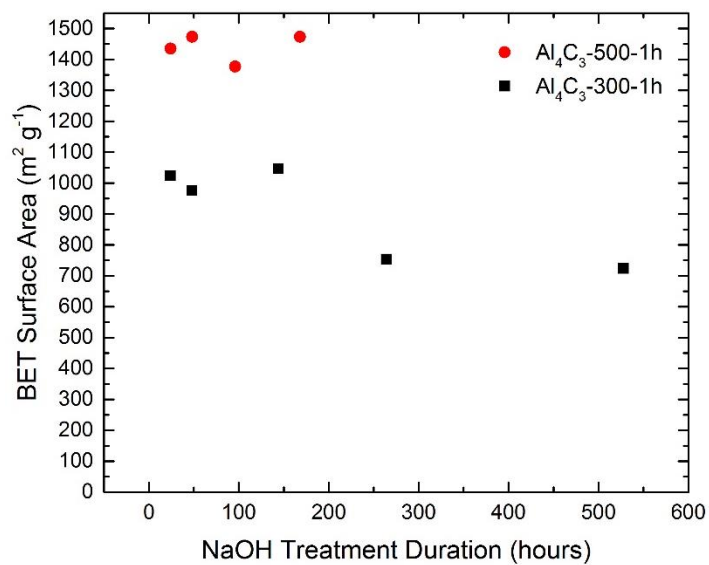


Figure A-21: BET surface area of materials after NaOH treatment

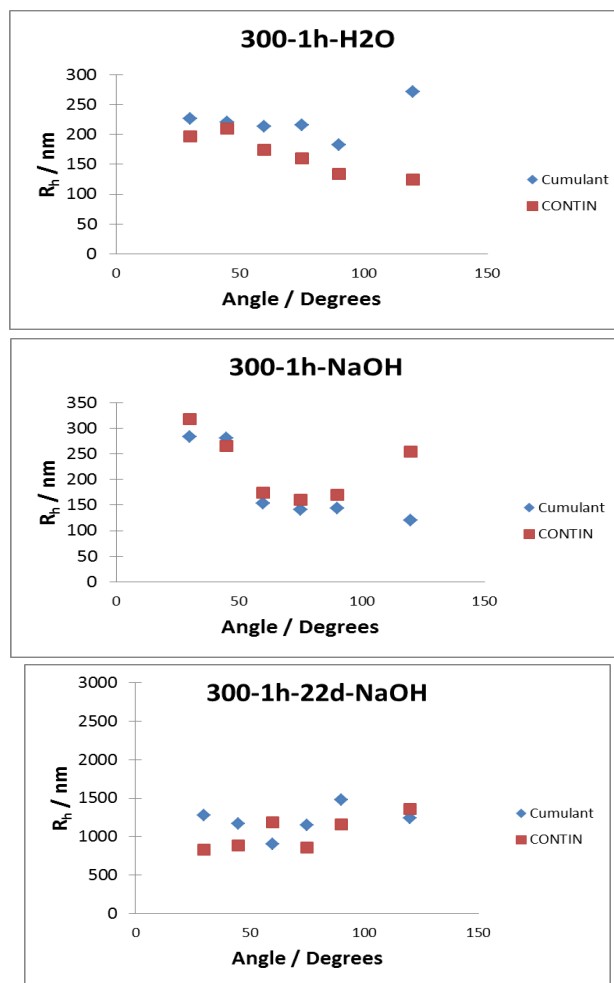


Figure A-22: Dynamic light scattering of supernatant after treatment showing polymer species in solution

Note* Large crystalline species appear once bayerite forms

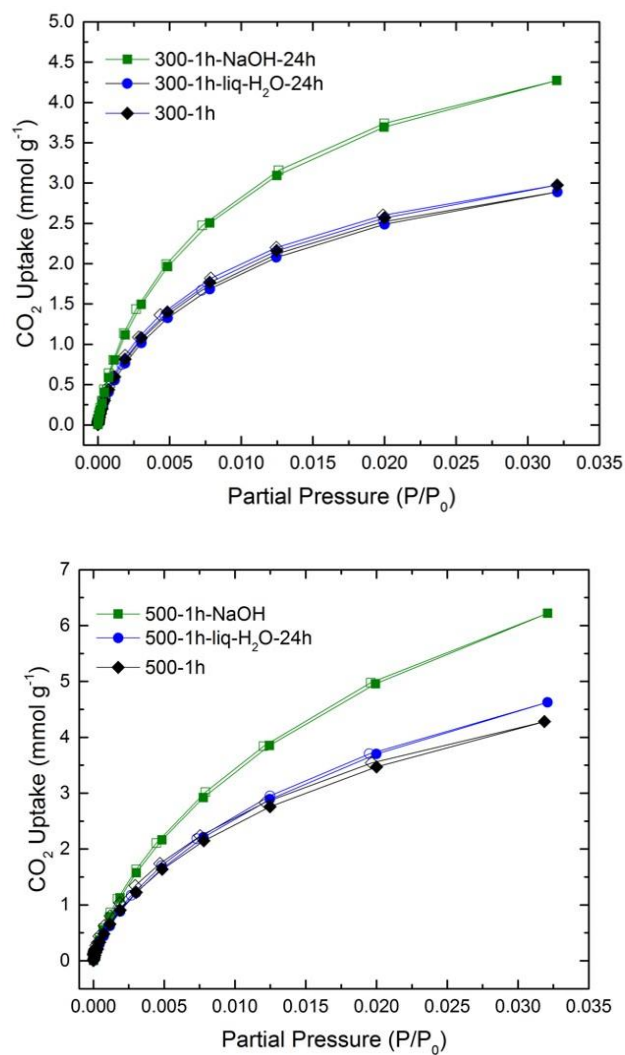


Figure A-23: NaOH and water treatment without rinsing and direct activation after digestion period.

*Note: Metal leaching to open pore space is negated with water treatment if the water is not filtered or decanted multiple times.

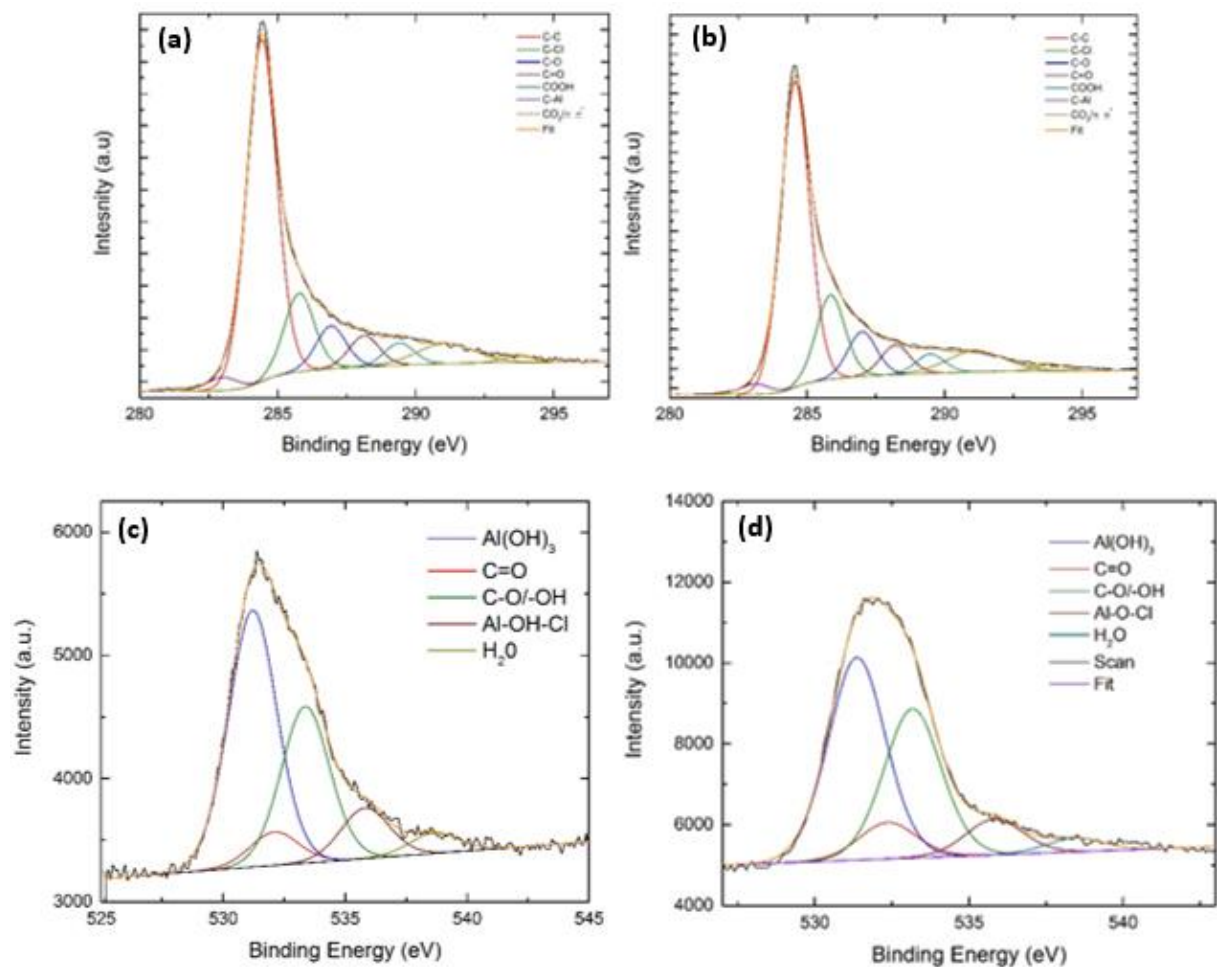
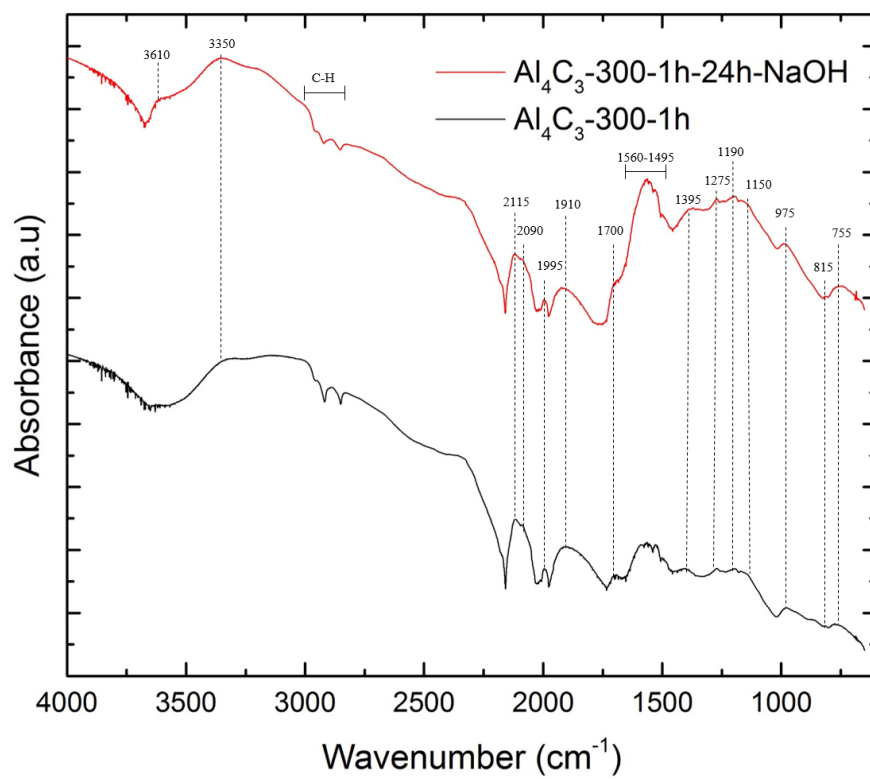


Figure A-24: Comparison of Al_4C_3 -500-1h high resolution carbon Cs1 spectra (a) Pre-NaOH and (b) Post-NaOH

Table A-7: High resolution C1s and O1s results before and after NaOH exposure for Al₄C₃-500-1h

Binding Energy (eV)	500-1h-Pre NaOH Relative %	500-1h-24h NaOH Relative %	Binding Energy (eV)
282.735	2.16	1.99	283.1
284.525	59.57	56.31	284.56
285.84	14.9	15.53	285.85
287	7.3	8.22	286.99
288.28	4.8	5.47	288.21
289.635	3.25	3.55	289.47
291.155	6.83	7.78	291.13
293.655	1.41	1.15	293.85
531.21	50.84	49.86	531.4
532.10	6.61	5.1	532.58
533.37	31.07	35.58	533.15
535.82	10.07	8.37	535.84
538.64	1.41	1.09	538.48



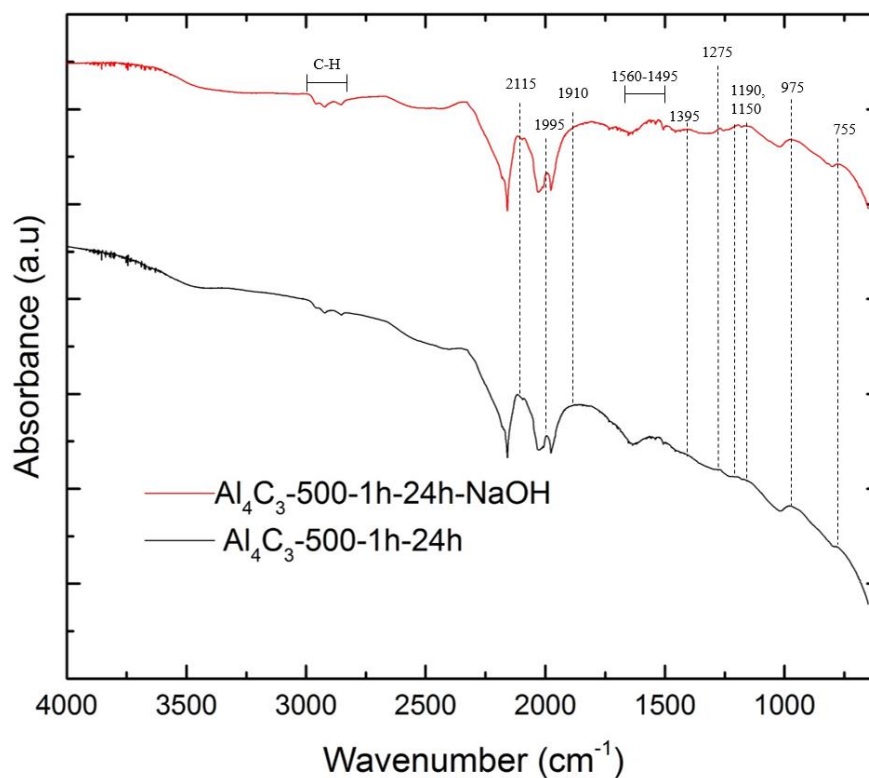


Figure A-25 ATR-IR spectra of pre and post NaOH modified samples for (a) Al_4C_3 -300-1h and (b) Al_4C_3 -500-1h

Table A-8: Wave numbers and assignments for ATR spectra

Wavenumber/Region	Possible Assignments	Citation
755	C-Cl	2-4
	o-disubstitued benzene ring	
	m-substitued benzene rings	
815	$\gamma(\text{C-H})$	

	m-disubstitued benzene ring	
870	$\gamma(\text{C-H})$ Tri or higher substituted benzene ring	2, 5
975	Acid chloride/aliphatic carbon $\text{CH}_2\text{CO-Cl}$, $=\text{CH}_2$ Wag C-O-C asymmetric $=\text{CH}$ out-of-plane deformation	4
1150	$\nu_{\text{as}} (= \text{C-O-C})$	2, 5-6
1190	$\nu_{\text{s}} (= \text{C-O-C})$ Aromatic ether	7
1249	Ether bridges between rings $\nu_{\text{as}} (= \text{C-O-C})$ 2H-chromene 2-pyrone	2, 6-8
1275	Ethers (due to 1150 stretch) Chromene and pyrone Lactones C-O-C	2, 9

	$\delta(\text{O-H})$ - $\nu(\text{C-O})$	
1395	$\delta(\text{O-H})$ Phenol Carboylic acid	2
1495	$\nu(\text{C=C})$ Aromatic Ring	2
1525-1560	Carbonaceous band aromatic structure and Unconjugated chelated carbonyl groups $\nu(\text{C=C})$ skeletal $\nu(\text{C=C})$	2, 5, 8
1700	Carbonyl C=O Carboxylic C=O $\nu(\text{C=C})$ 2-pyrone structures COCl	7-8
1910	Pyrone carboxylic acid Lactone	8

1995	Substituted benzene ring	4
2090	unassigned	
2115	Water in micropores	10
2830-2982	ν(C-H) Aliphatic ν(C-H) Aromatic	2, 4, 6-7
3350-3610	ν(O-H) region	2, 4, 7

*Abbreviations: ν, stretching; δ, bending (in-plane); γ, bending (out-of-plane); s, symmetric; as, asymmetric.

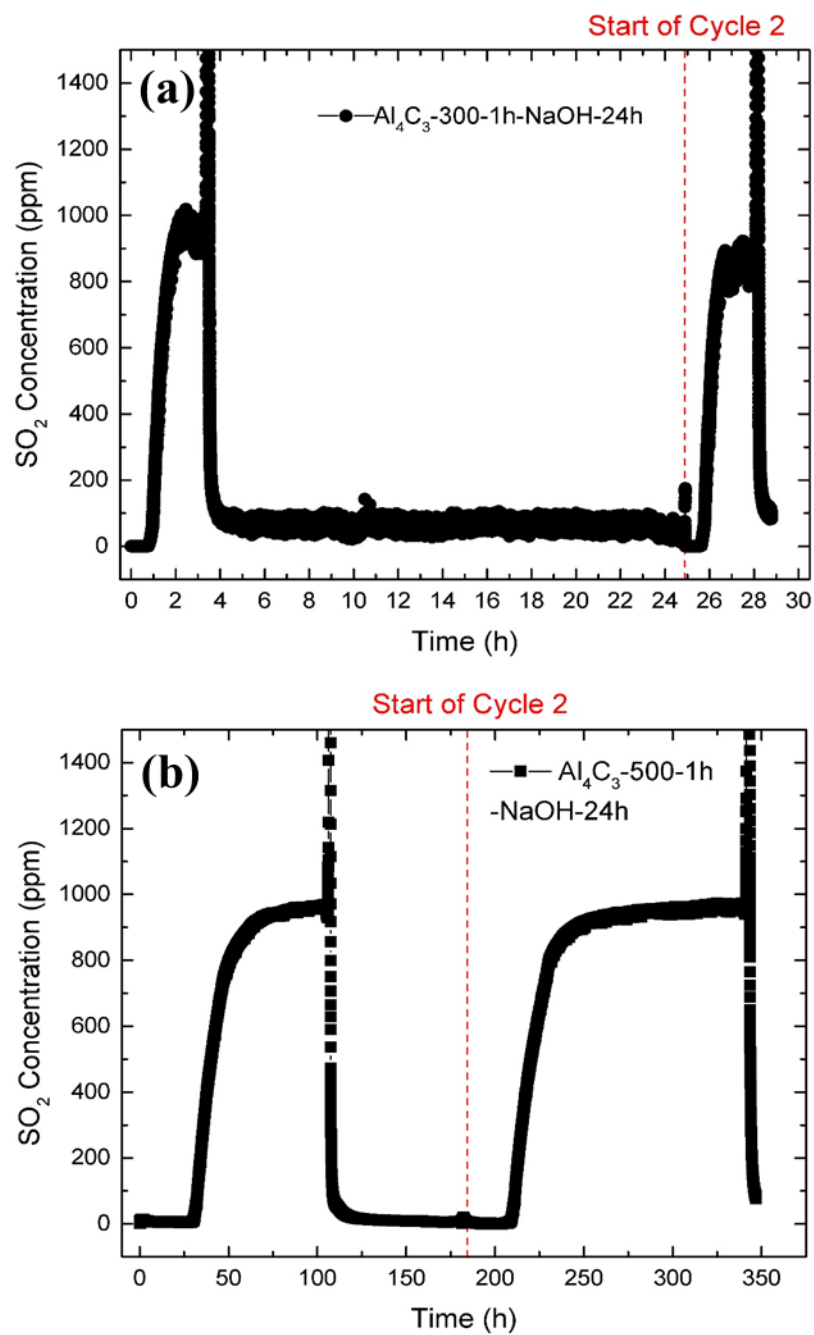


Figure A-26: 1000 ppm SO₂ breakthrough curves for (a) $\text{Al}_4\text{C}_3\text{-300-1h-24h-NaOH}$, and (b) $\text{Al}_4\text{C}_3\text{-500-1h-24h-NaOH}$

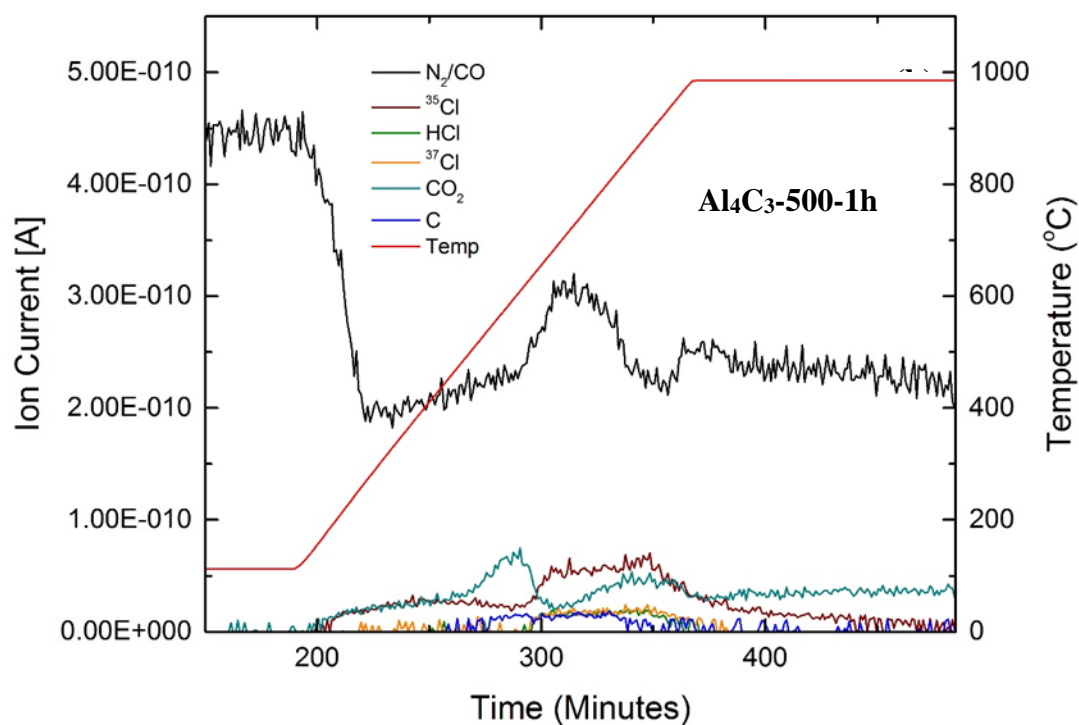
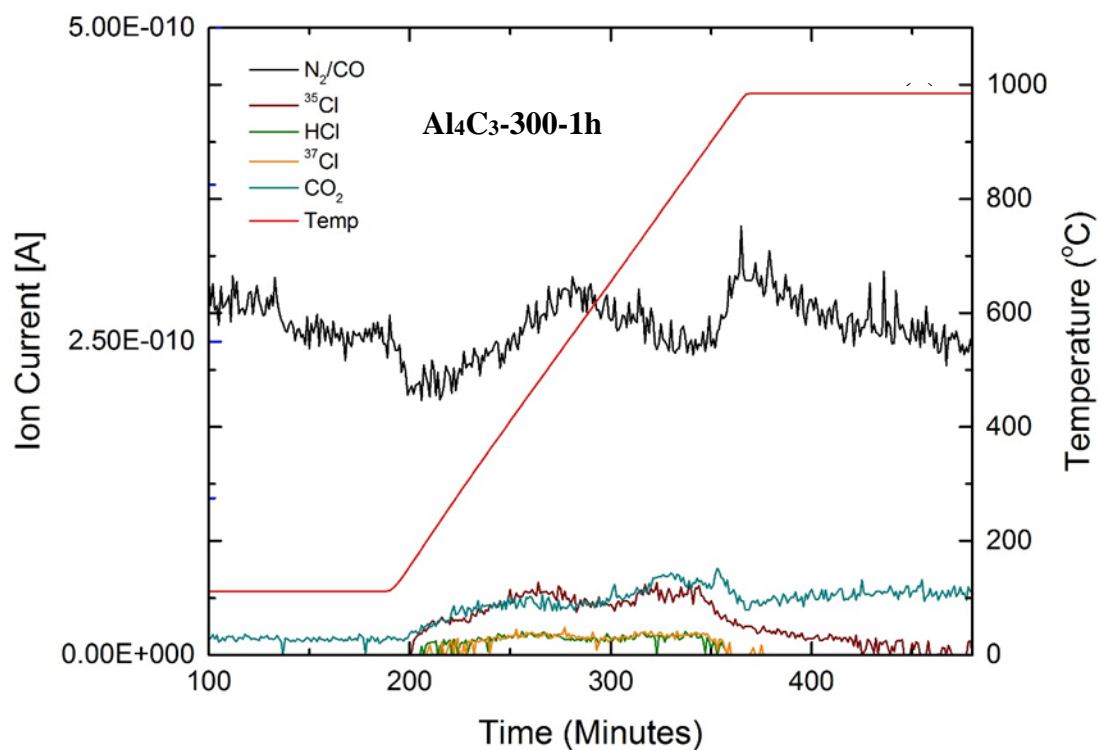


Figure A-27: TGA-MS results under helium flow for the decomposition of functional groups on (a) $\text{Al}_4\text{C}_3\text{-300-1h}$ and (b) $\text{Al}_4\text{C}_3\text{-500-1h}$

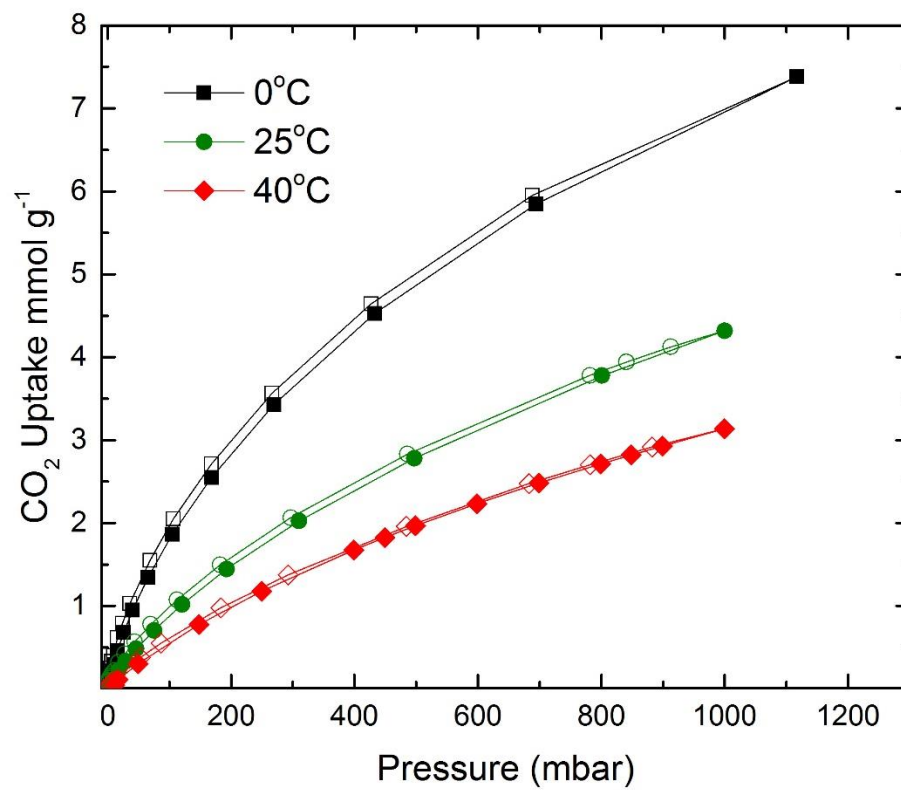


Figure A-28: Al₄C₃-500-1h-48h-NaOH CO₂ isotherms

A.3 Chapter 5: Evolution of Textural and Chemical Properties of Annealed Carbide-Derived Carbons for Acid Gas Adsorption

A.3.1 Supplemental and Raw Data for Chapter 5

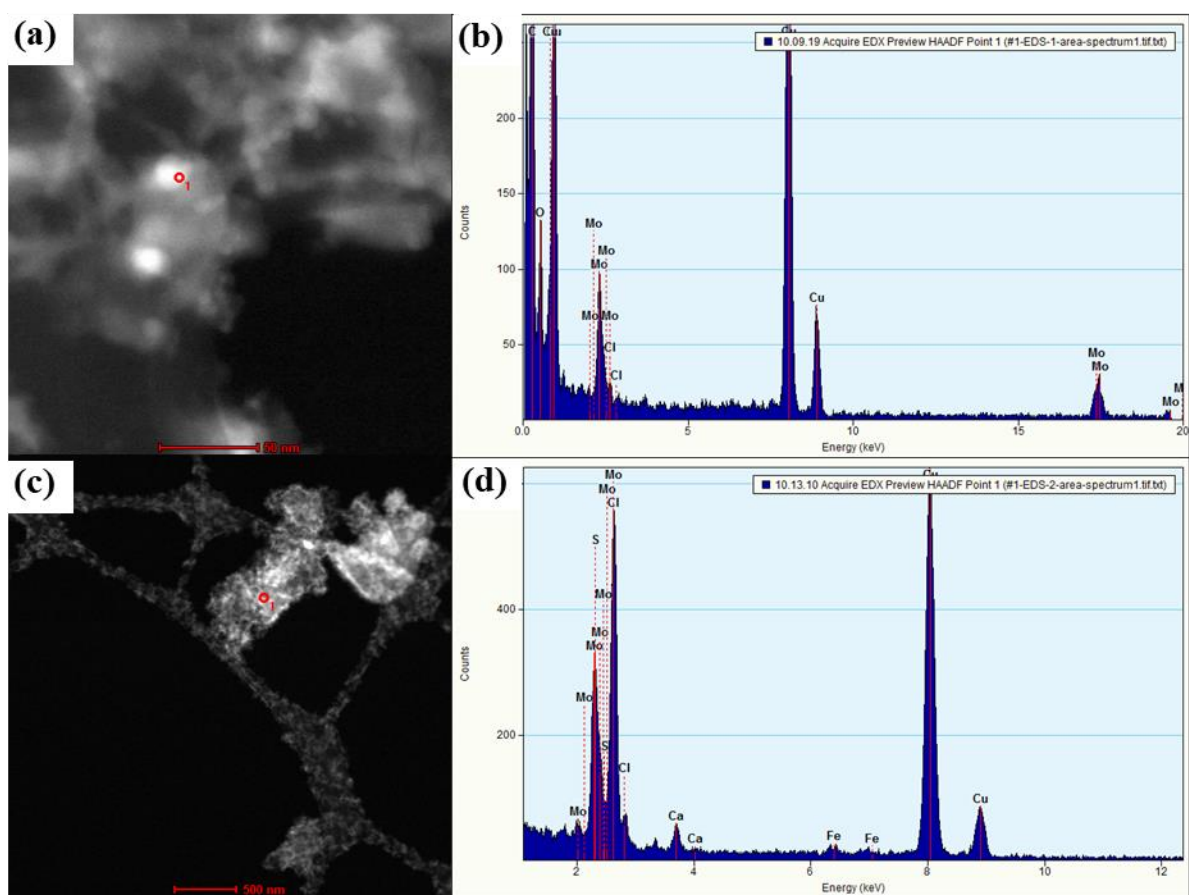


Figure A-29: (a & c) HAADF of Mo₂C-CDC-500-1h. (b) EDS on point 1 (d) EDS on point 2

A.4 Chapter 6: Evolution of Textural and Chemical Properties of Annealed Carbide-Derived Carbons for Acid Gas Adsorption

A.4.1 Supplemental and Raw Data for Chapter 6

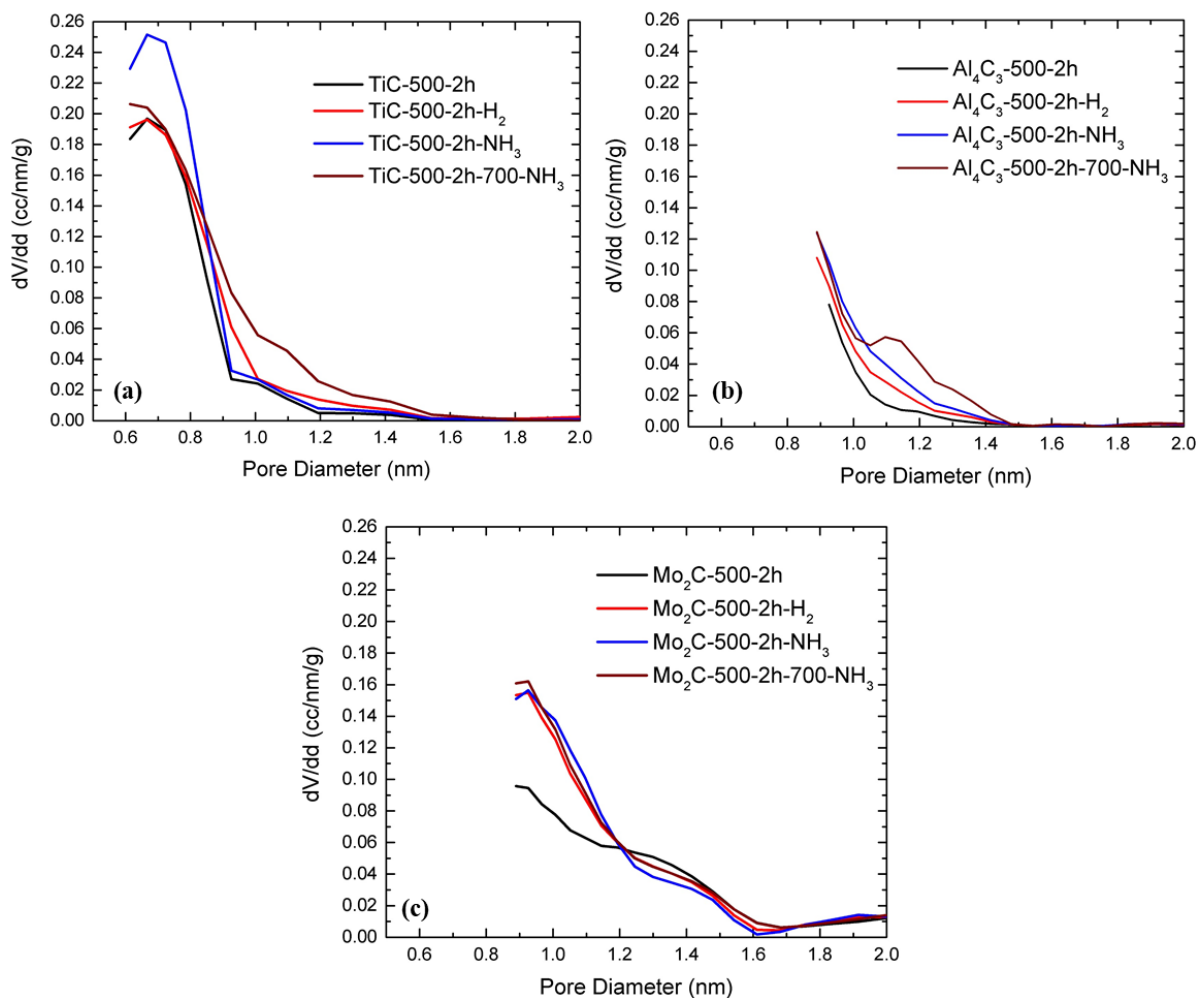


Figure A-30: Pore-size distribution of (a) TiC-CDCs, (b) Al₄C₃-CDCs and (b) Mo₂C-CDCs from 0 to 2 nm

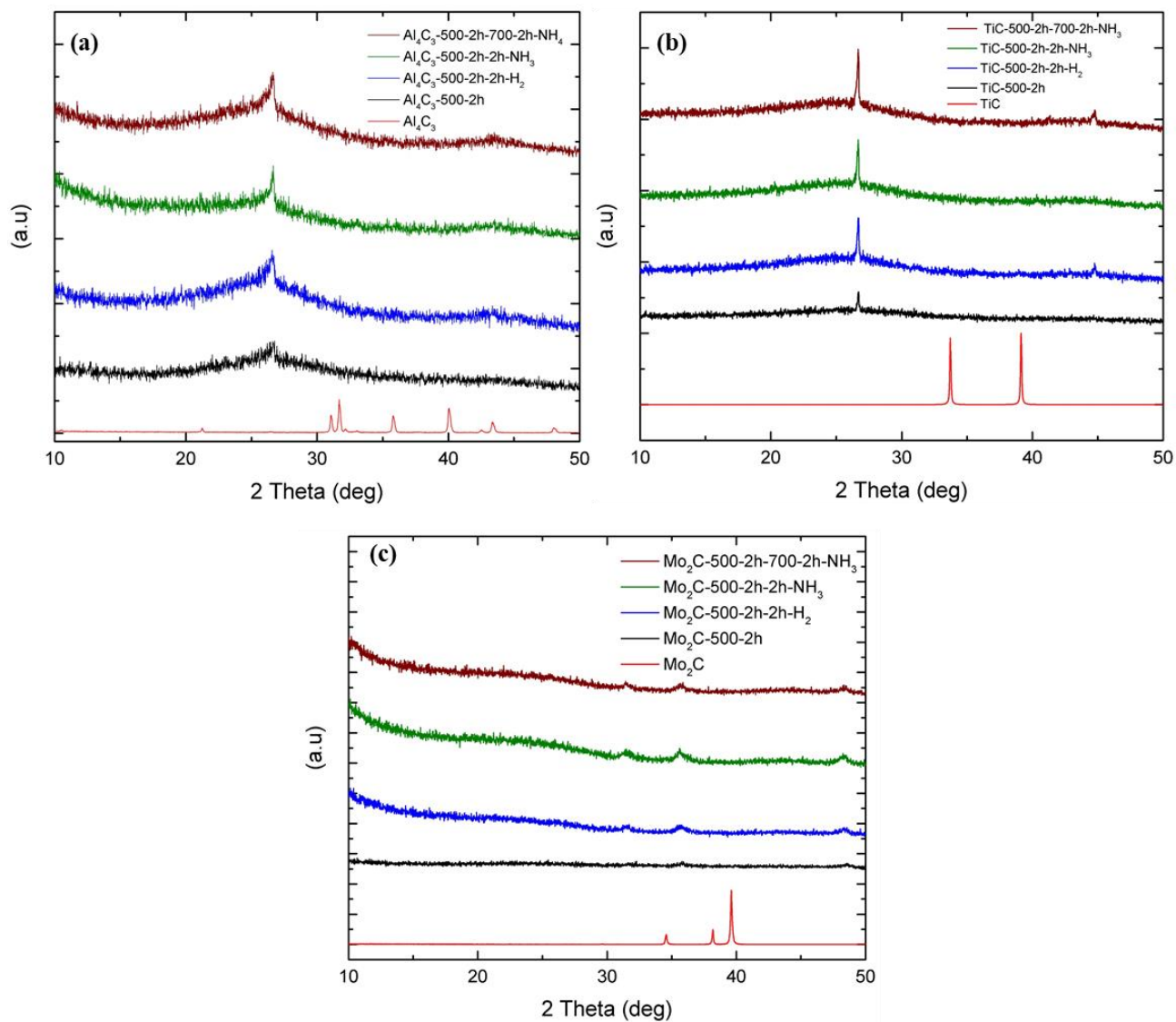


Figure A-31: Powdered X-ray diffraction of (a) Al_4C_3 -CDCs, (b) TiC-CDCs, and (b) Mo_2C -CDCs

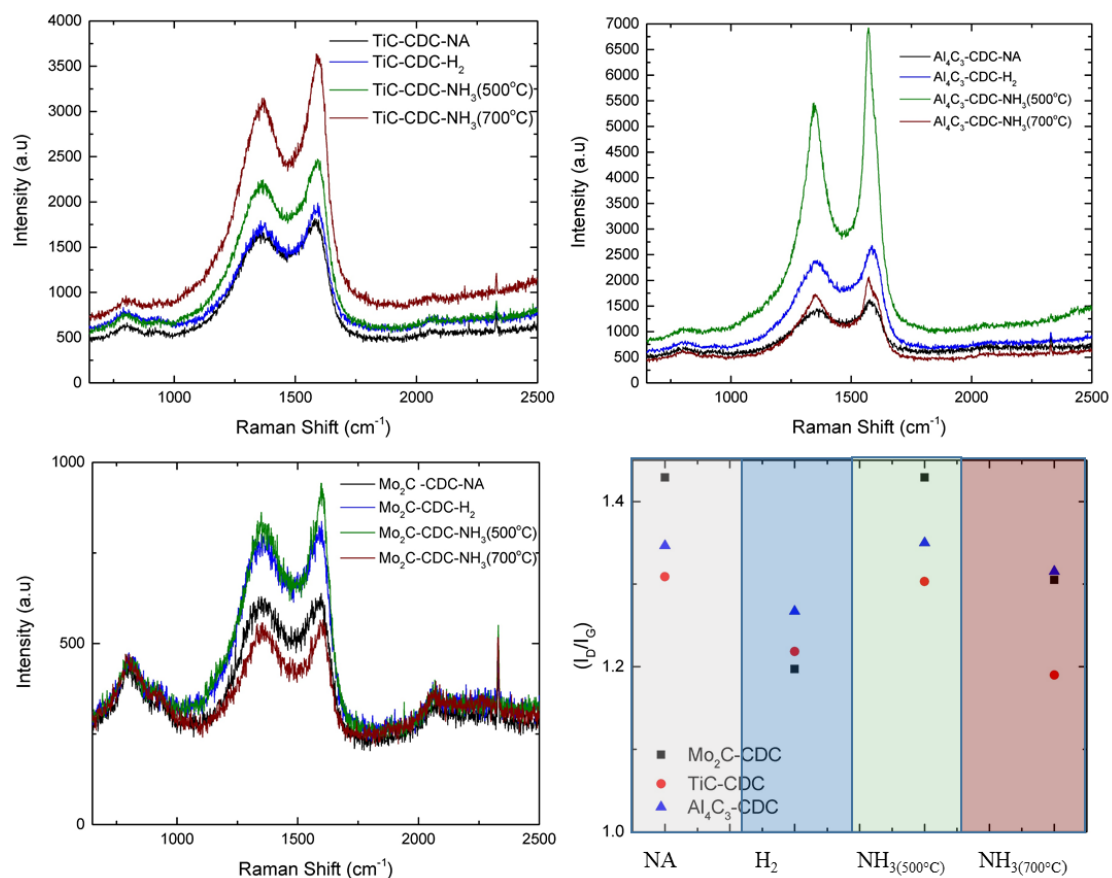
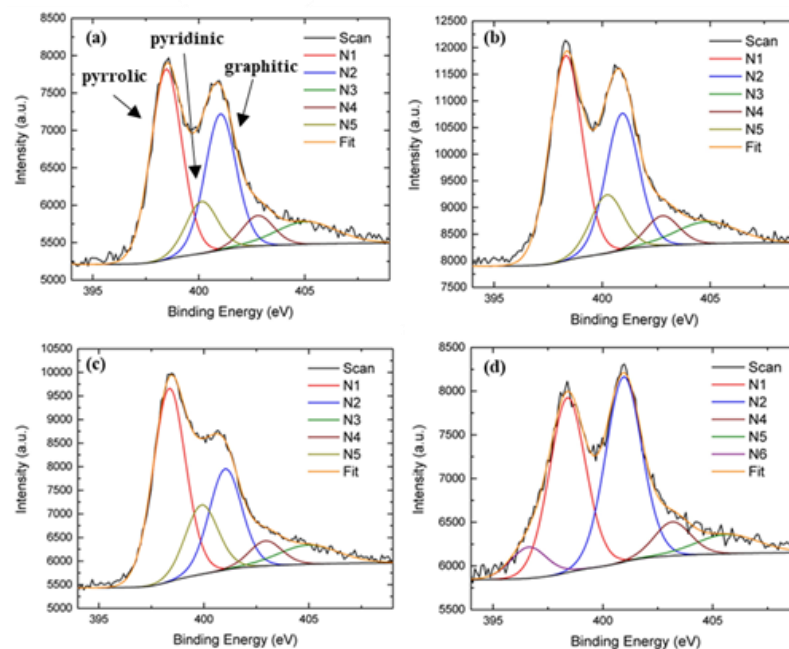
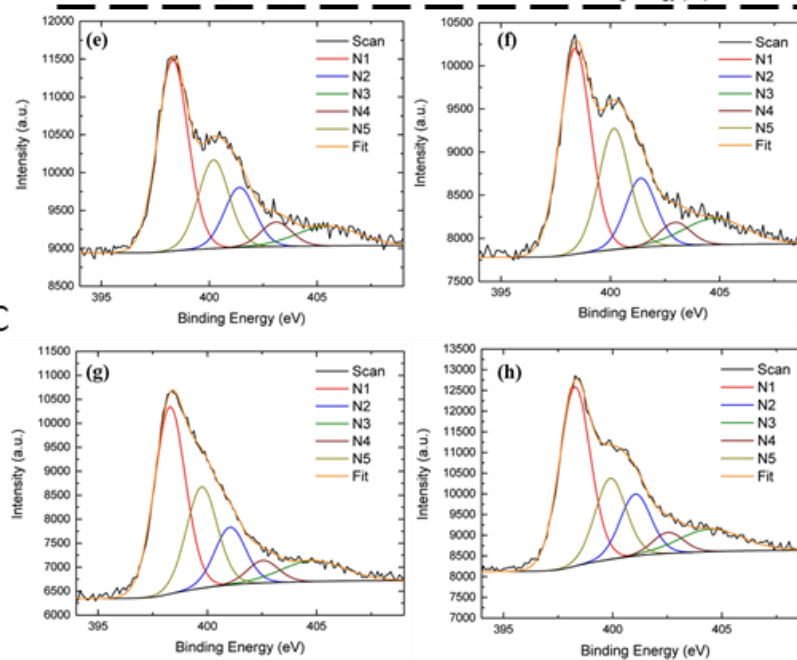


Figure A-32: Raw Raman spectra for (a) TiC-CDC , (b) Al_4C_3 -CDC, and (c) Mo_2C - CDC, (d) Integrated area ratios of the D and G band for fitted spectra.

TiC-CDC



Al₄C₃-CDC



Mo₂C-CDC

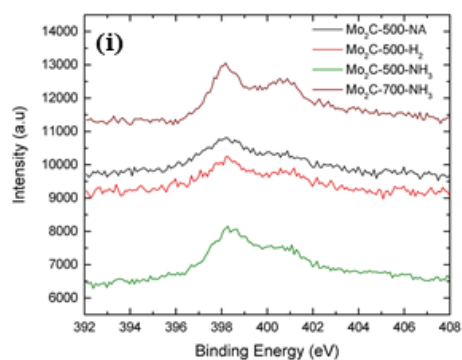


Figure A-33: High resolution N 1s XPS for (a) TiC-CDC-NA, (b) TiC-CDC-H₂, (c) TiC-CDC-NH₃ (500°C), (d) TiC-CDC-NH₃ (700°C), (e) Al₄C₃-CDC-NA, (f) Al₄C₃-CDC-H₂, (g) Al₄C₃-CDC-NH₃ (500°C), (h) Al₄C₃-CDC-NH₃ (700°C) and (i) Mo₂C-CDC-XX.

*Note the raw data is presented rather than fitted spectra for Mo₂C-CDCs due to the low signal to noise ratio.

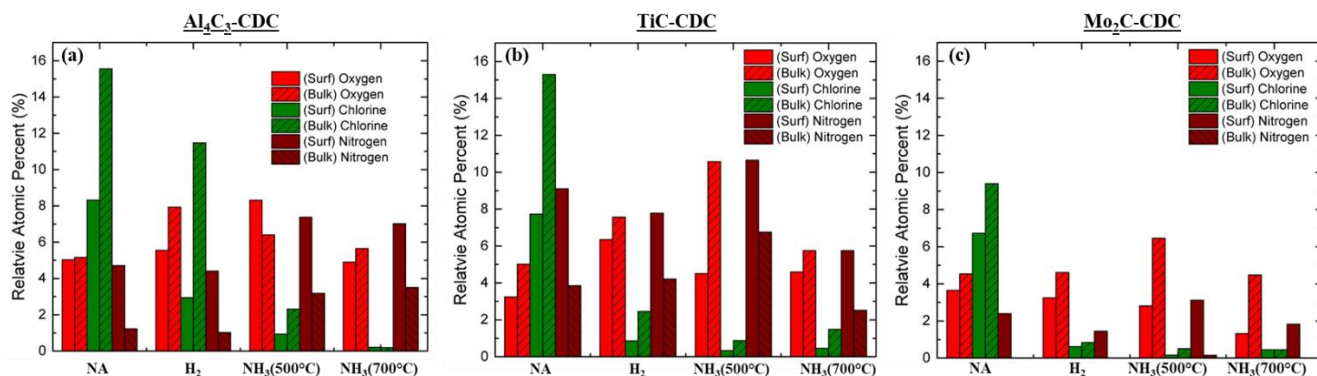


Figure A-34: Comparison of surface concentrations obtained via XPS and interior elemental compositions obtained through EDS for (a) Al₄C₃-CDCs, (b) TiC-CDCs, and (b) Mo₂C -CDC

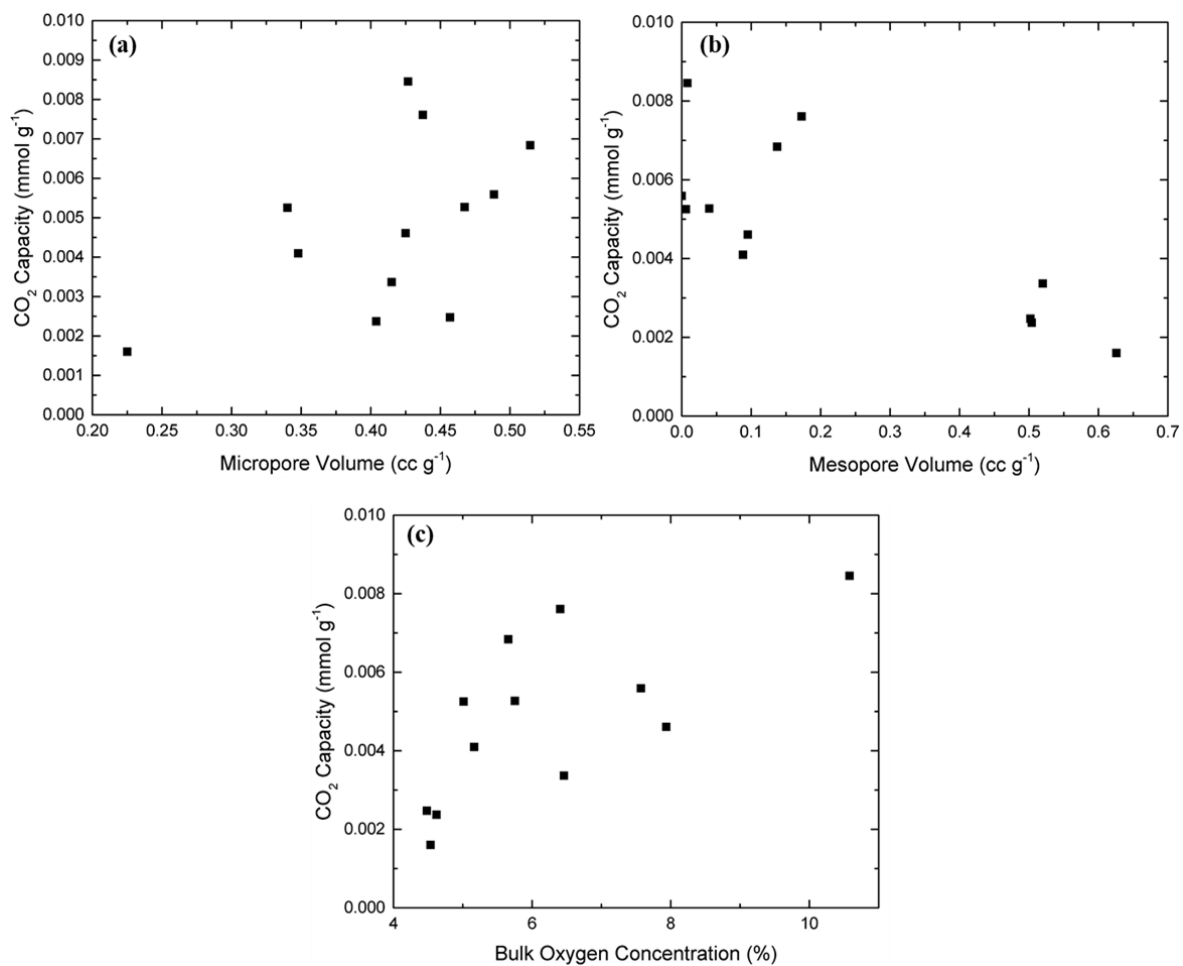


Figure A-35: CO₂ capacity at 25°C vs (a) micropore volume, (b) mesopore volume, and (c) bulk oxygen

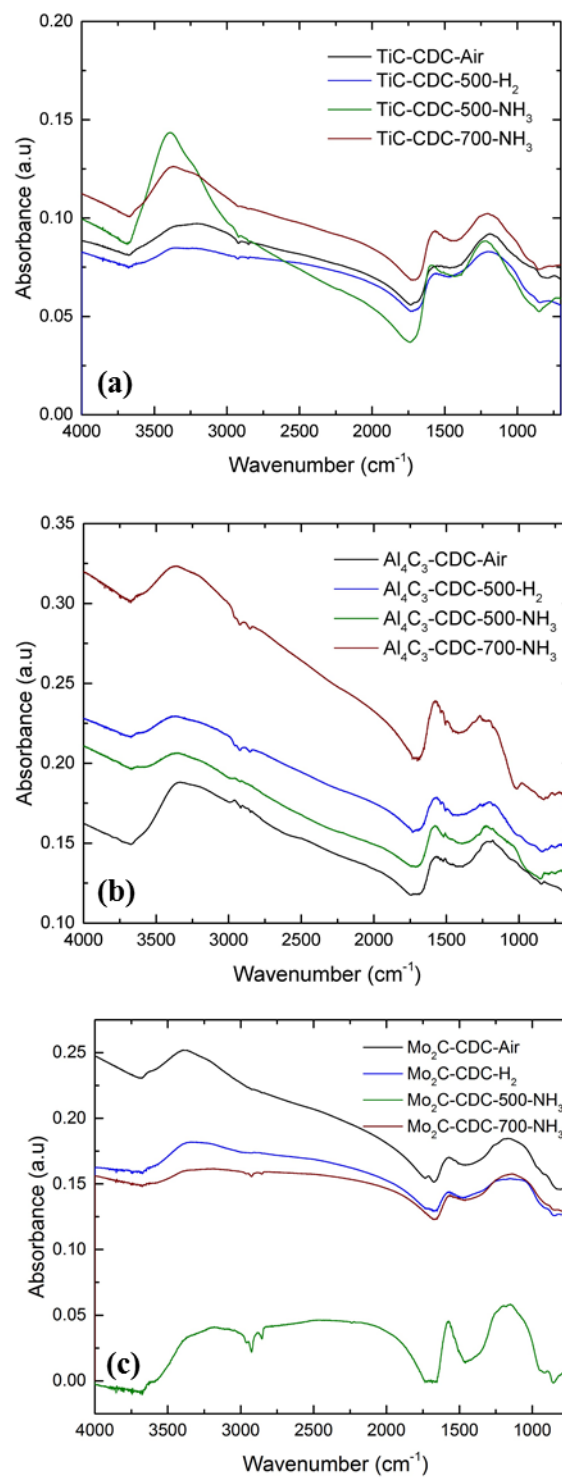


Figure A-36: Attenuated total reflectance data on all (a) Al_4C_3 -CDC, (b) TiC-CDC, and (c) Mo_2C -CDC

A.5 Chapter 7: Structured Growth of Metal-Organic Framework MIL-53(Al) from Solid Aluminum Carbide Precursor

Reproduced (adapted) from Moran C.M., et al., *Structured Growth of Metal–Organic Framework MIL-53(Al) from Solid Aluminum Carbide Precursor*. Journal of the American Chemical Society (2018) 29, p. 9148-9153

A.5.1 Supplemental and Raw Data for Chapter 7

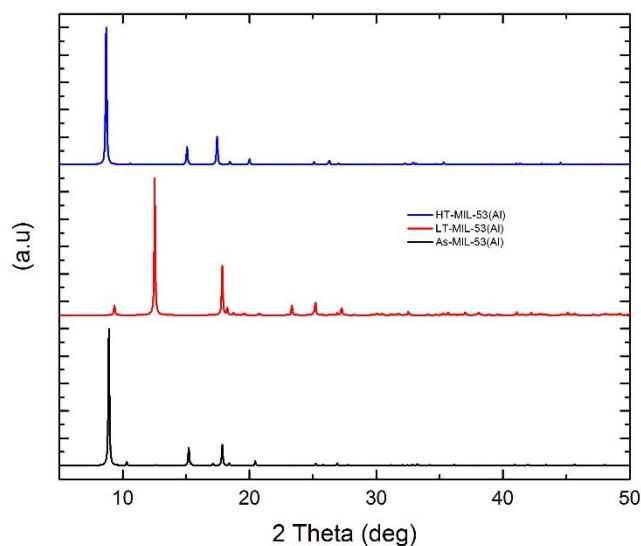


Figure A-37: Simulated MIL-53(Al) patterns¹

Table A-9: BET surface area and pore volume ($P/P_0 = 0.8$) of $\text{Al}_4\text{C}_3\text{-BDC-XX}$ materials.

Sample	$S_{\text{BET}}(\text{m}^2 \text{ g}^{-1})$	$V_{\text{P}}(\text{cm}^3 \text{ g}^{-1})$
Al₄C₃-BDC-1h	-	-
Al₄C₃-BDC-2h	-	-
Al₄C₃-BDC-3h	26	0.03
Al₄C₃-BDC-4h	400	0.17
Al₄C₃-BDC-6h	942	0.39
Al₄C₃-BDC-12h	1134	0.47
Al₄C₃-BDC-24h	1205	0.51
Al₄C₃-BDC-72h	1206	0.51

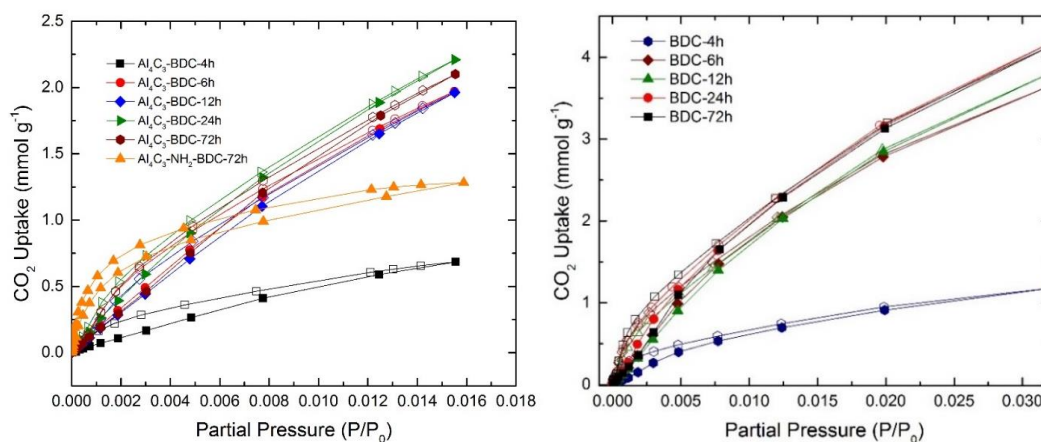


Figure A-38: (a) CO₂ adsorption isotherms at 25°C up to 1 bar and (b) CO₂ adsorption isotherms at 0°C.

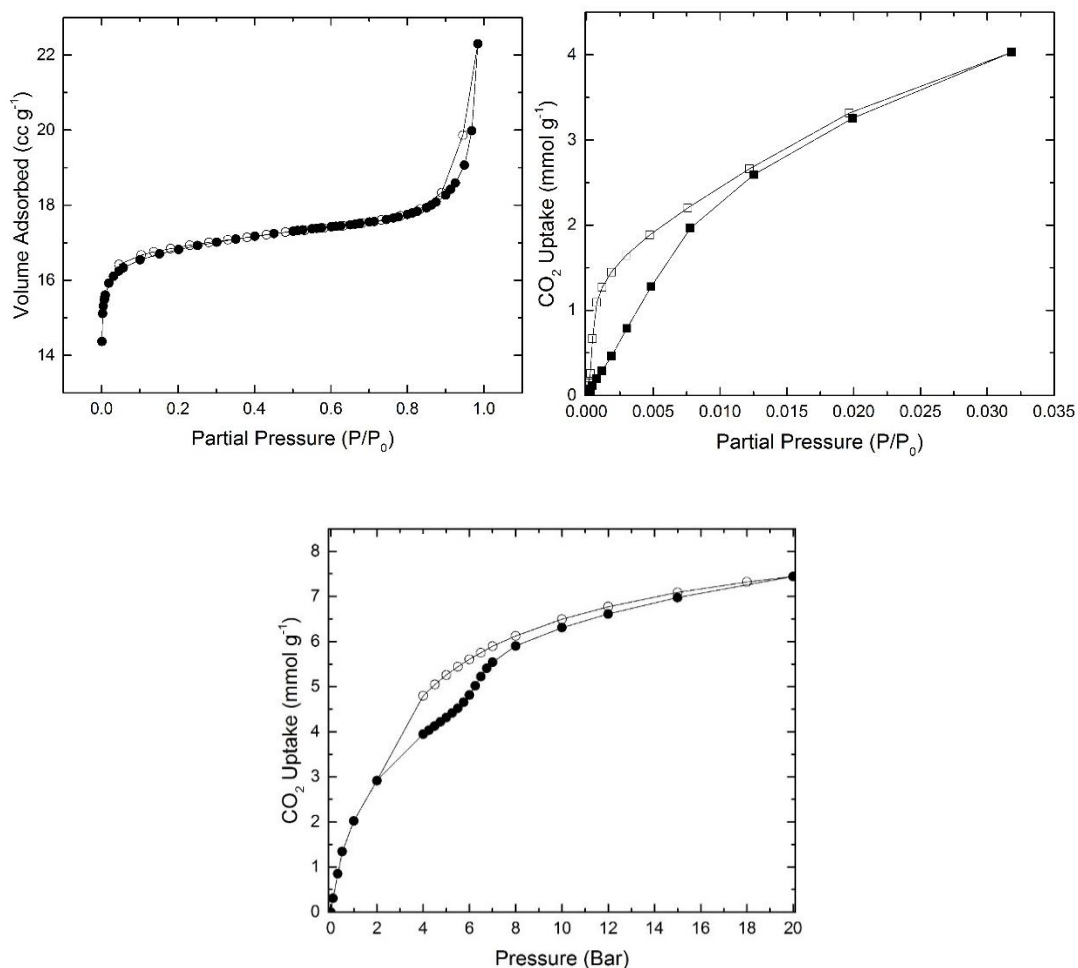


Figure A-39: MIL-53(Al) from Al(H₂O)₆Cl₃ (a) N₂ physisorption isotherm, (b) CO₂ adsorption at 0°C and (c) CO₂ adsorption at 25°C on Al₄C₃-BDC-72h from 0-20 bar.

Table A-10: EDS results from points taken from Al₄C₃-BDC-72h and theoretical percentages for MIL-53(Al).²

Species	Element	Weight %	Atomic %
Al ₄ C ₃ -BDC-72h	C	52.84	61.64
	O	38.92	34.08

	Al	8.24	4.28
MIL-53-as	C	51.84	60.71
	O	39.60	34.82
	Al	8.56	4.46
MIL-53-HT	C	47.32	57.14
	O	35.71	35.71
	Al	13.29	7.14



Figure A-40: Images of $\text{Al}_4\text{C}_3\text{-BDC-72h}$ (left) and unreacted Al_4C_3 (right).

Table A-11: Elemental composition results from XPS survey scan on Al₄C₃-BDC-72h

Elemental Species	Atomic Percent (%)
Al	8.93
O	33.81
C	57.26

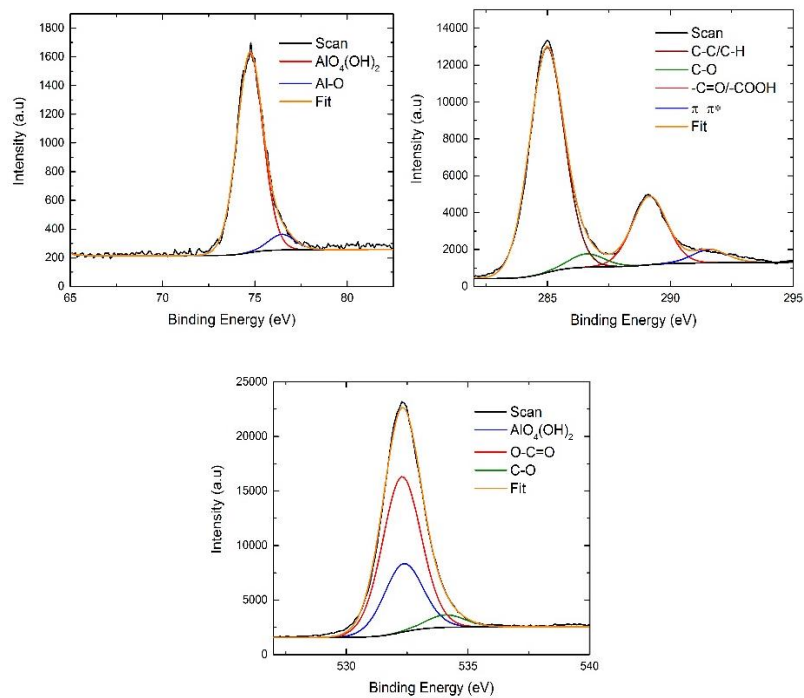


Figure A-41: High resolution XPS scans of (a) Al 2p (b) C 1s and (c) O 1s

The survey scan for $\text{Al}_4\text{C}_3\text{-BDC-72h}$ reveals atomic percentages close that of HT-MIL-53(Al) which is expected after the material was activated and put under vacuum for XPS analysis. The high resolution Al 2p peak at 74.74 and the O 1s peak at 532.35 eV can be assigned to the coordination of the Al cations with the oxygen anion of the BDC linker. Trace amounts of Al-O by-product material that is not the octahedral metal center was also detected at 76.46 eV as seen in Figure A-41. Interestingly the absence of an O 1s peak at 533.7 eV reveals there was no free BDC on the surface of $\text{Al}_4\text{C}_3\text{-BDC-72h}$ for the areas that were analyzed.

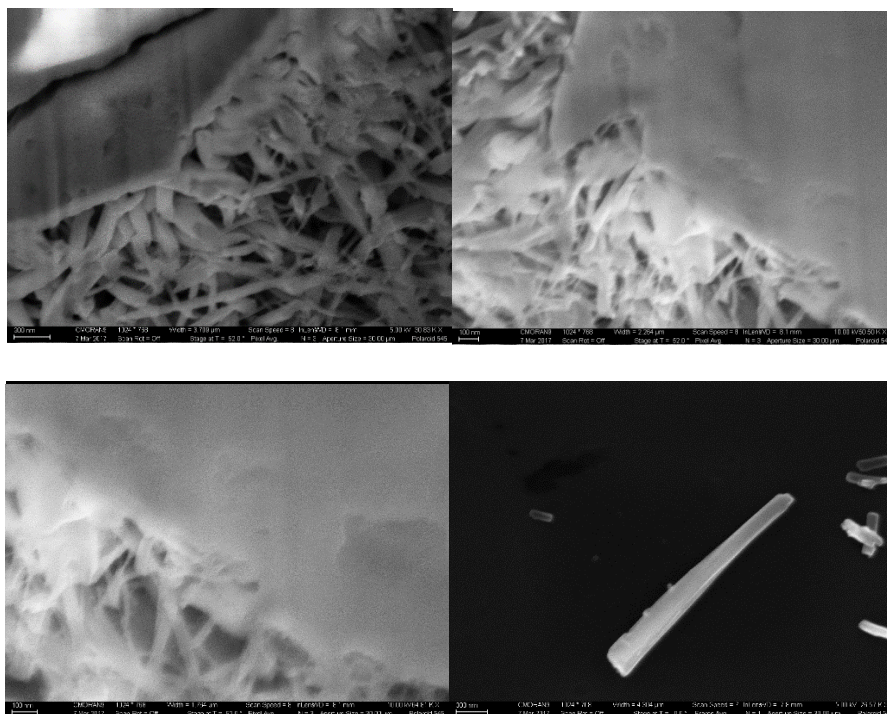


Figure A-42: $\text{Al}_4\text{C}_3\text{-BDC-4h}$ FIB-SEM images.

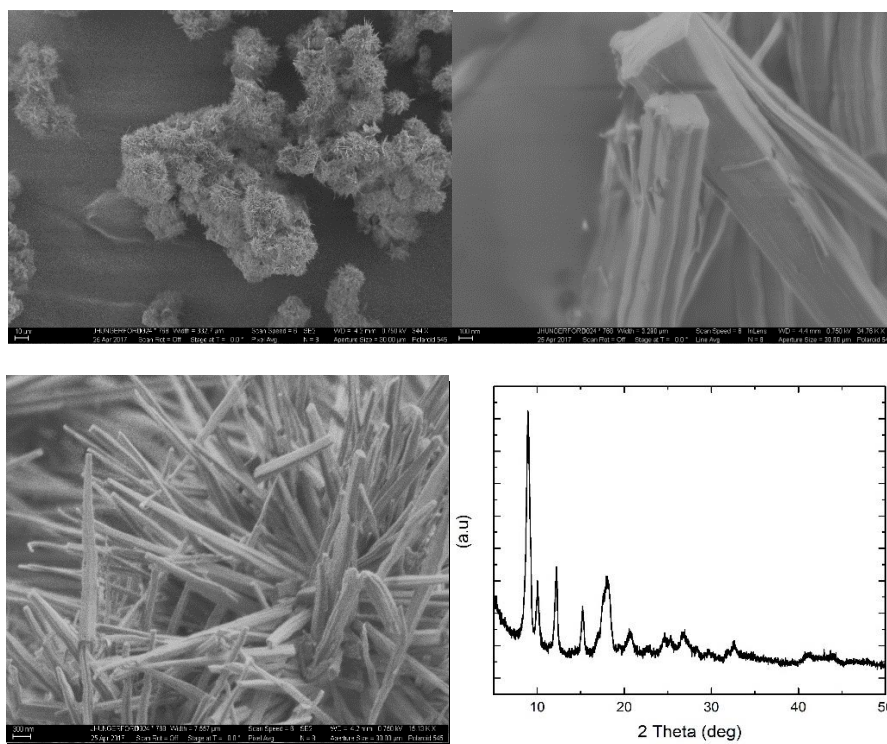


Figure A-43: (a-c) SEM images and (d) PXRD of Al₄C₃-NH₂-BDC-72h

Table A-12: N₂ Physisorption data on temperature trials.

Species	S _A BET (m ² g ⁻¹)	PV (cc g ⁻¹)
Al ₄ C ₃ -BDC-210	1163	0.50
Al ₄ C ₃ -BDC-190	1098	0.48

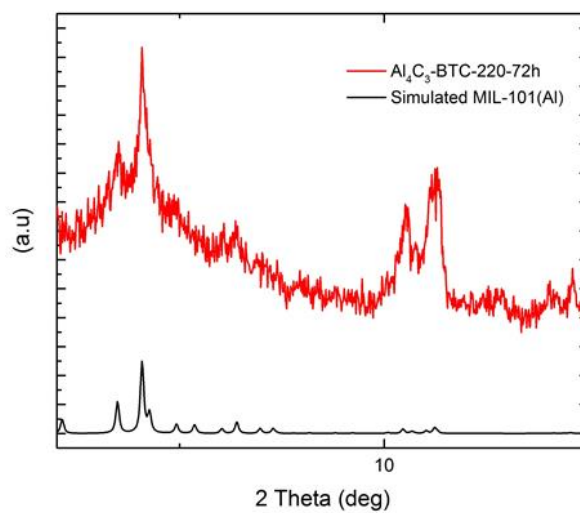
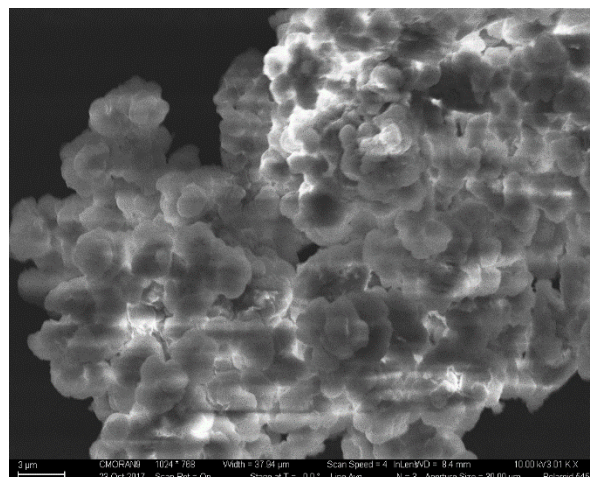


Figure A-44: SEM (a) and PXRD (b) on $\text{Al}_4\text{C}_3\text{-BTC-220-72h}$.

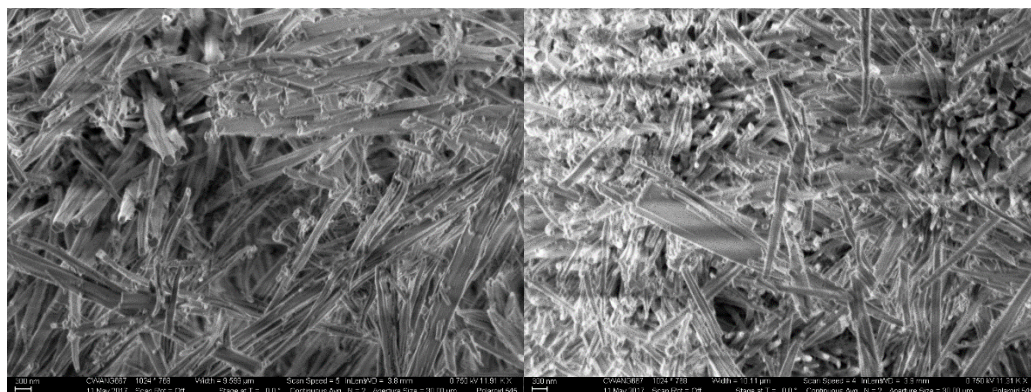


Figure A-45: SEM on (a) $\text{Al}_4\text{C}_3\text{-BDC-210-24h}$ (b) $\text{Al}_4\text{C}_3\text{-BDC-190-24h}$.

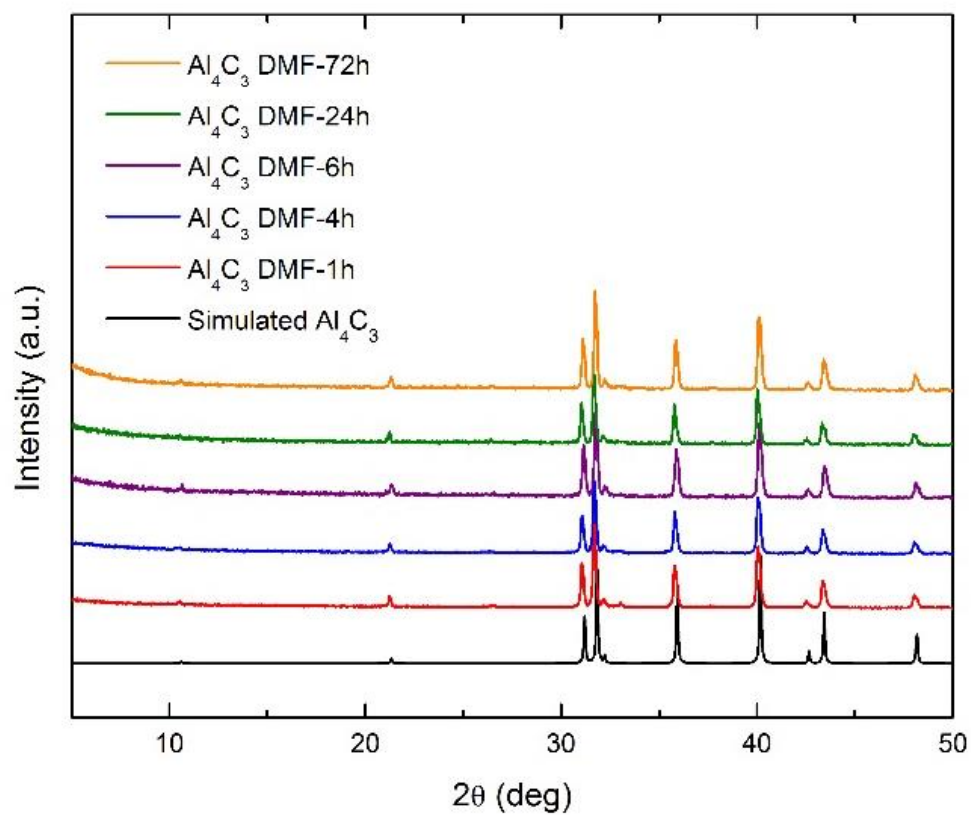


Figure A-46: Al_4C_3 in DMF from 1-72h.

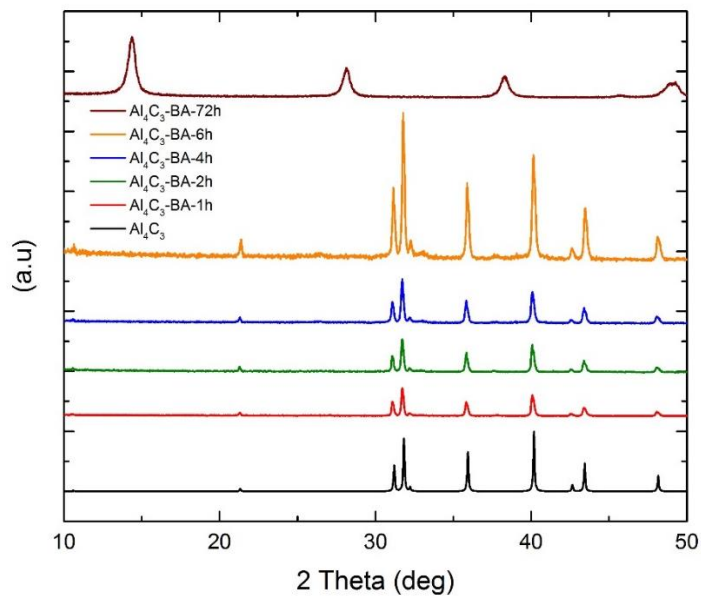


Figure A-47: PXRD on time trials for $\text{Al}_4\text{C}_3\text{-BA-XXh}$.

Table A-13: Rietveld results for post heated $\text{Al}_4\text{C}_3\text{-BDC-72h}$

Formula	HT-MIL-53 (Al)
Crystal system	orthorhombic
Space group	Imma (74)
a	6.639501
b	17.02673
c	12.55413
alpha/beta/gamma°	90
Cell volume (Å ³)	1420
Number of reflections	191
R _{exp}	3.16
R _{wp}	14.4
R _p	15.3

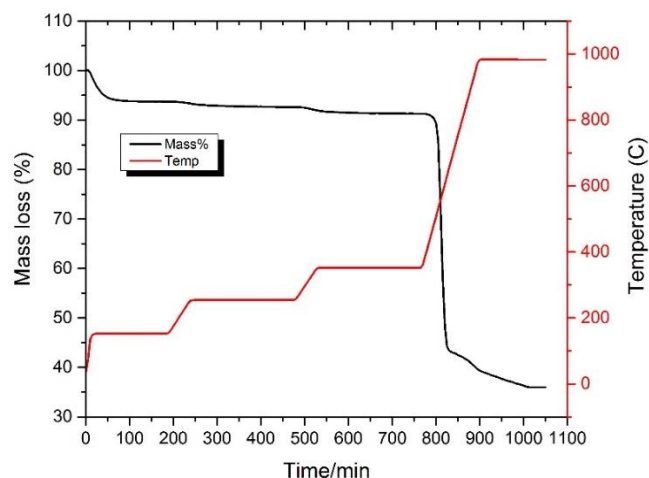


Figure A-48: TGA of Al₄C₃-BDC-72h.

Further analysis of Al₄C₃-BDC-72h was pursued with TGA measurements, provided in Figure A-48. Upon simulating activation temperatures of 150°C, the material displayed an immediate mass loss of 5%, which can be attributed to water. A 3% drop during incremental heating to 380°C, is attributed to trace amounts of residual uncoordinated BDC not removed through normal activation, leaving the 1D channels. Al₄C₃-BDC-72h displayed high thermal stability up to 500°C, correlating well with traditional MIL-53(Al).² Interestingly, upon heating to 1000°C the Al₄C₃-BDC-72h retained 36% of its mass, where literature reports for MIL-53(Al) display 20% retention.^{2,3} The mass loss of coordinated BDC was used to calculate the weight percent of MIL-53(Al) for the materials based on the HT-MIL-53(Al) composition, which revealed a MOF compositions range of ~24 and 75wt% for Al₄C₃-BDC-4h and Al₄C₃-BDC-72h, respectively. After the release of coordinated BDC, the materials continue to lose mass for a period of time while being held at 1000°C. These results would suggest unreacted precursor or intermediate species are present in the material up to 72h of reaction.

Table A-14: N₂ physisorption data before and after water exposure.

Sample	S_{BET} (m ² g ⁻¹)	V_{P} (cm ³ g ⁻¹)
Al₄C₃-BDC-72h	1206	0.51
Al₄C₃-BDC-72h- (50% RH for 3 months)	1204	0.51
Al₄C₃-BDC-72h- 90% RH	1196	0.51

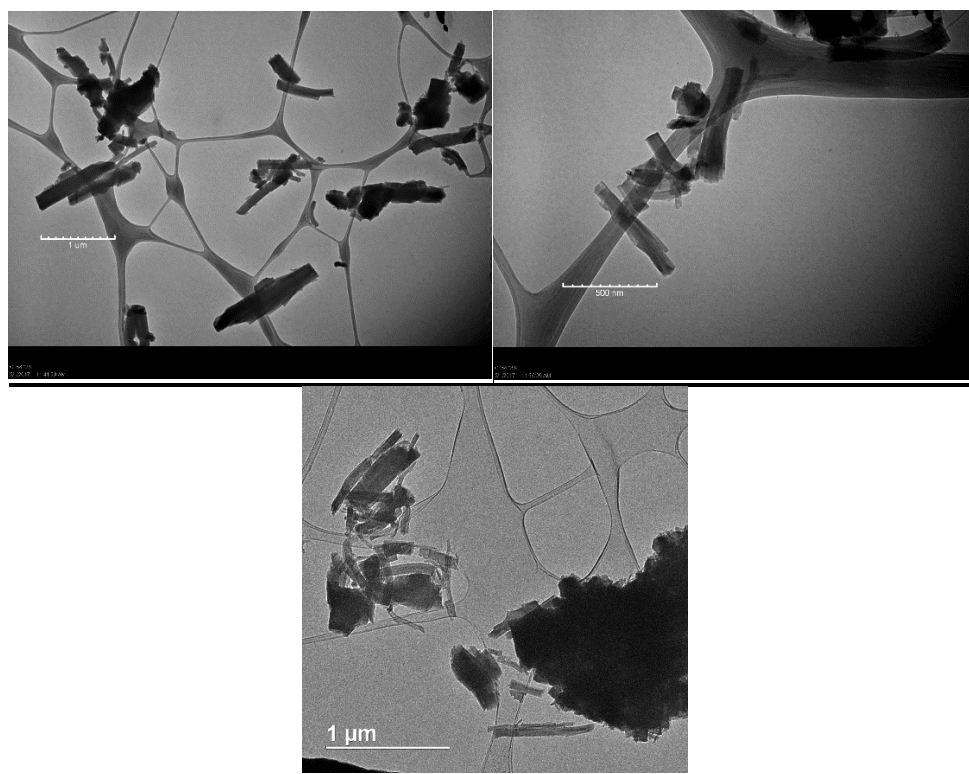


Figure A-49: TEM Images of Al₄C₃-BDC-72h

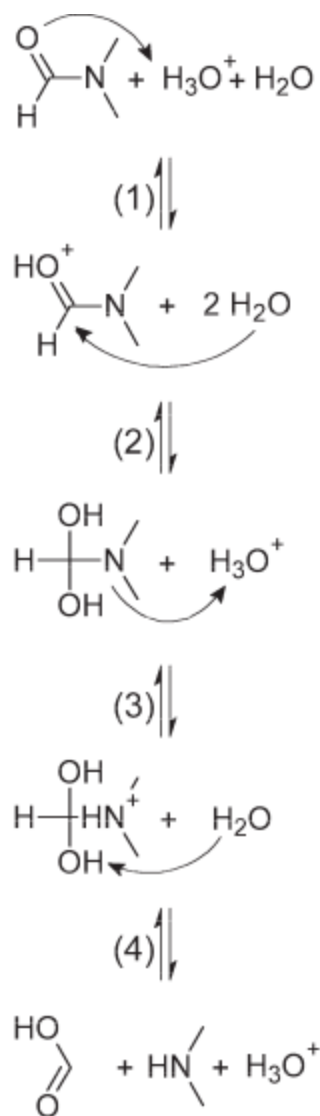


Figure A-50: Protonation and hydrolysis of DMF adapted from Cottineau et al.¹¹

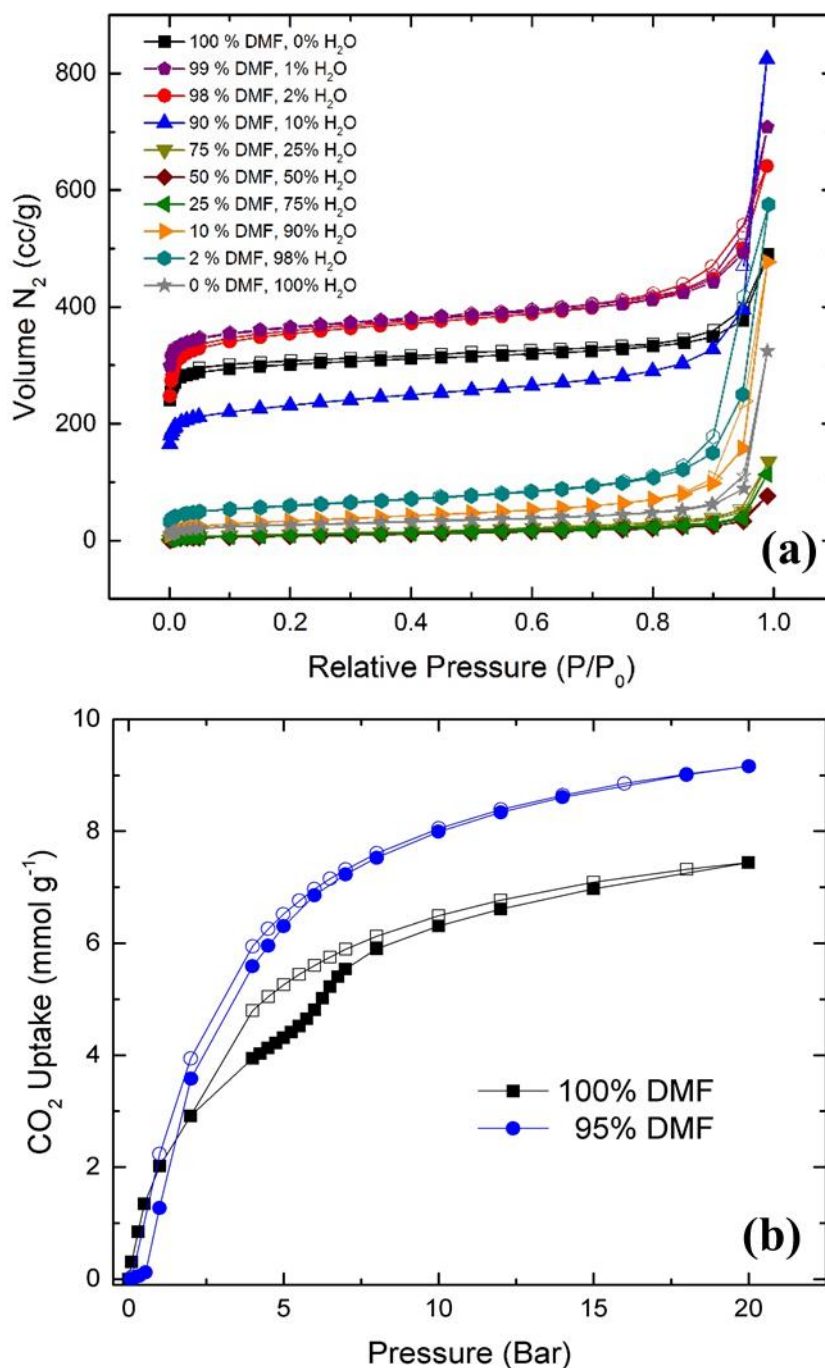


Figure A-51: Nitrogen sorption isotherms at 77 K for Al₄C₃-MIL-53(Al) samples synthesized with different DMF/H₂O solvent ratios and (b) CO₂ adsorption at 25°C up to 20 bar for Al₄C₃-BDC-24h samples with pure DMF and a 95/5 DMF to water ratio

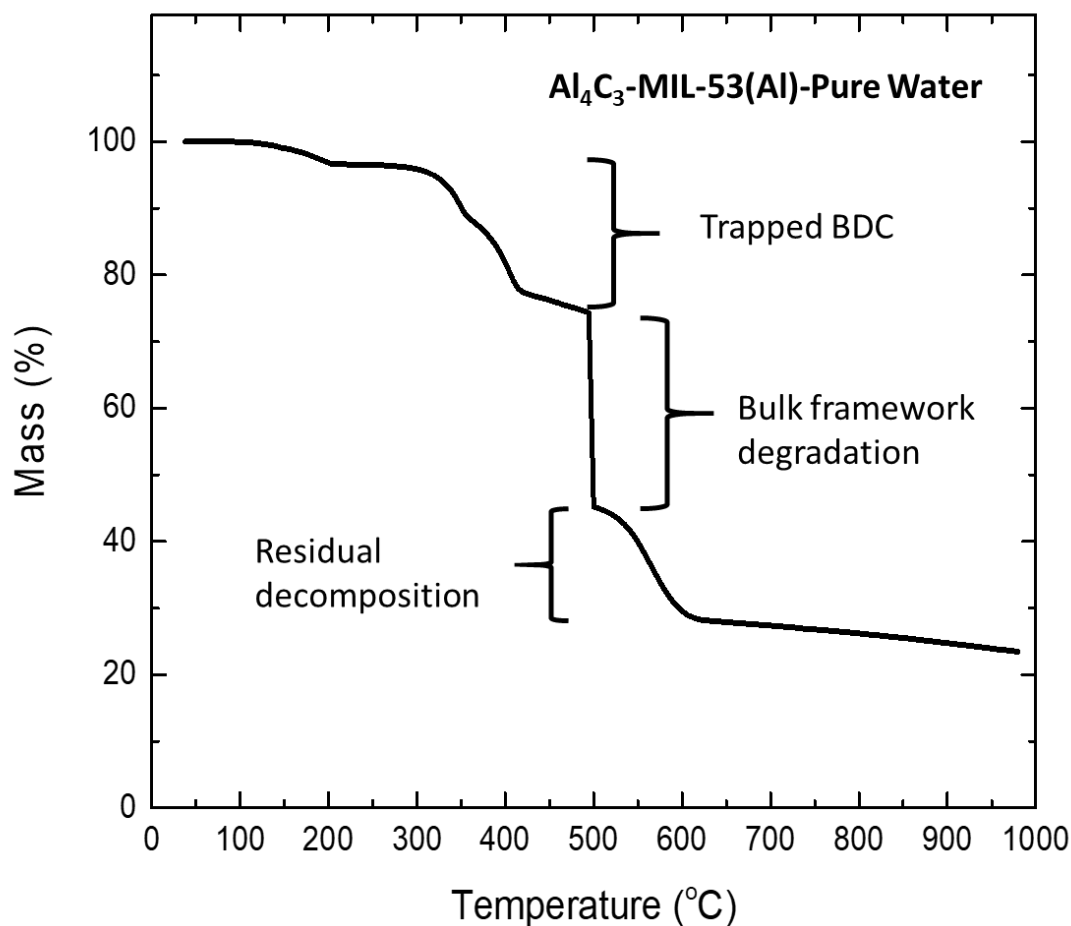


Figure A-52: TGA on Al_4C_3 derived MIL-53(Al) in pure water

References

1. Balan, E.; Blanchard, M.; Hochepped, J.-F.; Lazzeri, M., Surface modes in the infrared spectrum of hydrous minerals: the OH stretching modes of bayerite. *Physics and Chemistry of Minerals* **2008**, 35 (5), 279-285.
2. Barroso-Bogeat, A.; Alexandre-Franco, M.; Fernández-González, C.; Gómez-Serrano, V., FT-IR Analysis of Pyrone and Chromene Structures in Activated Carbon. *Energy & Fuels* **2014**, 28 (6), 4096-4103.

3. Wang, D.-W.; Wu, K.-H.; Gentle, I. R.; Lu, G. Q., Anodic chlorine/nitrogen co-doping of reduced graphene oxide films at room temperature. *Carbon* **2012**, 50 (9), 3333-3341.
4. Sweeting, L. M., Organic Structural Spectroscopy (Lambert, Joseph B.; Shurvell, Herbert F.; Lightner, David A.; Cooks, R. Graham). *Journal of Chemical Education* **1998**, 75 (10), 1218.
5. Arsyad, N. A. S.; Razab, M. K. A. A.; An'amt Mohamed Noor, M. H.; Amini, M.; Yusoff, N. N. A. N.; Halim, A. Z. A.; Yusuf, N. A. A. N.; Masri, M. N.; Sulaiman, M. A.; Abdullah, N. H., Effect of Chemical Treatment on Production of Activated Carbon from *Cocos nucifera* L.(Coconut) Shell by Microwave Irradiation Method. *J. Trop. Resour. Sustain. Sci* **2016**, 4, 112-116.
6. Terzyk, A. P., The influence of activated carbon surface chemical composition on the adsorption of acetaminophen (paracetamol) in vitro. *Colloids and Surfaces A: Physicochemical and Engineering Aspects* **2001**, 177 (1), 23-45.
7. Mawhinney, D. B.; Yates, J. T., FTIR study of the oxidation of amorphous carbon by ozone at 300 K — Direct COOH formation. *Carbon* **2001**, 39 (8), 1167-1173.
8. Shin, S.; Jang, J.; Yoon, S. H.; Mochida, I., A study on the effect of heat treatment on functional groups of pitch based activated carbon fiber using FTIR. *Carbon* **1997**, 35 (12), 1739-1743.
9. Zhou, J.-Y.; Wang, Z.-W.; Zuo, R.; Zhou, Y.; Cao, X.-M.; Cheng, K., The surface structure and chemical characters of activated carbon fibers modified by plasma. *Asia-Pacific Journal of Chemical Engineering* **2012**, 7, S245-S252.
10. Al-Abadleh, H. A.; Grassian, V. H., FT-IR Study of Water Adsorption on Aluminum Oxide Surfaces. *Langmuir* **2003**, 19 (2), 341-347.
11. Cottineau, T.; Richard-Plouet, M.; Mevellec, J.-Y.; Brohan, L., Hydrolysis and Complexation of N , N -Dimethylformamide in New Nanostructured Titanium Oxide Hybrid Organic–Inorganic Sols and Gel. *The Journal of Physical Chemistry C* **2011**, 115 (25), 12269-12274.